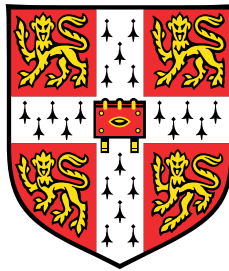


Stability of Topological States and Crystalline Solids



Bartholomew Andrews

Department of Physics
University of Cambridge

This dissertation is submitted for the degree of
Doctor of Philosophy

Jesus College

October 2018

Dla moich rodziców: Iwona i Wojciech.

Preface

The first three chapters of this dissertation provide an introduction to topological states and crystalline solids, while the final chapter presents the conclusion. Intermediate chapters contain original material that is published, or in preparation for submission, as follows:

Chapter 4: “Stability of fractional Chern insulators in the effective continuum limit of Harper-Hofstadter bands with Chern number $|C| > 1$ ”, B. Andrews and G. Möller, *Phys. Rev. B* **97**, 035159 (2018) [1].

In this project, I was responsible for the data collection, processing, and a large part of the analysis. I additionally produced the figures, including on-line interactive supplementary material, and drafted the manuscript. This project was carried out under the supervision of Gunnar Möller, who, in addition to his role as the project supervisor, made significant contributions by editing sections of the code, and writing Sec. 4.2.2.

We acknowledge useful discussions with Nicolas Regnault, Nigel Cooper and Michael Zaletel as well as related collaborations with Nigel Cooper, Rahul Roy, and Antoine Sterdyniak. I also thank Chaitanya Mangla, Andrew Fowler, Philipp Verpoort, Michael Rutter, and Beñat Mencia for technical help with the computations. Our numerical results were produced using DiagHam. I acknowledge support from the Engineering and Physical Sciences Research Council under grant no. EP/M506485/1. Gunnar Möller acknowledges support from the Royal Society under grant no. UF120157 and from the University of Kent. He also thanks the TCM group, Cavendish Laboratory and Trinity Hall for their hospitality.

Chapter 5: “Direct evaluation of the force constant matrix in quantum Monte Carlo”, Y. Y. F. Liu, B. Andrews, and G. J. Conduit, *J. Chem. Phys.* **150**, 034104 (2019) – Editor’s Pick [2].

In this project, Yu Yang Liu was responsible for the low-level programming tasks, including implementing the matrix of force constants in the source code, as well as all of the data collection. My contribution was higher-level scripting for data analysis,

helping with the code patch, producing the figures, and writing the manuscript. This project was conducted under the supervision of Gareth Conduit.

We thank Andrew Fowler, Neil Drummond, Christian Carbogno, Ryan Hunt, Pablo López Ríos, John Trail, Thomas Gasenzer, and Lars Schonenberg for useful discussions. The QMC calculations in this chapter were performed using CASINO. Yu Yang Liu acknowledges support from the Agency for Science, Technology and Research; I acknowledge support from the Engineering and Physical Science Research Council under grant no. EP/M506485/1; and Gareth Conduit acknowledges support from the Royal Society.

Chapter 6: “Lattice stability of three-dimensional crystals”, B. Andrews and G. J. Conduit, in preparation (2019).

In this project, I was responsible for the data collection, producing the figures, and writing the manuscript. This project was carried out under the supervision of Gareth Conduit, who, in addition to his role as the project supervisor, made significant contributions to the construction of the tight-binding toy model in Sec. 6.4.

We thank Emilio Artacho, Edward Linscott, Chris Pickard, Daniel Rowlands, Beñat Mencia, Claudio Castelnovo, Yu Yang Liu and Pablo López Ríos for useful discussions. I acknowledge support from the Engineering and Physical Sciences Research Council under grant no. EP/M506485/1, and Gareth Conduit acknowledges support from the Royal Society.

This dissertation is the result of my own work and includes nothing which is the outcome of work done in collaboration except as declared in the Preface and specified in the text. It is not substantially the same as any that I have submitted, or, is being concurrently submitted for a degree or diploma or other qualification at the University of Cambridge or any other University or similar institution except as declared in the Preface and specified in the text. I further state that no substantial part of my dissertation has already been submitted, or, is being concurrently submitted for any such degree, diploma or other qualification at the University of Cambridge or any other University or similar institution except as declared in the Preface and specified in the text. This dissertation does not exceed 60,000 words, including summary/abstract, tables, footnotes and appendices, but excluding table of contents, photographs, diagrams, figure captions, list of figures/diagrams, list of abbreviations/acronyms, bibliography and acknowledgments.

Bartholomew Andrews
October 2018

Acknowledgments

This thesis would not have been possible without the patience, help and guidance of my supervisors: Dr Gareth Conduit and Dr Gunnar Möller. In particular, I am indebted to them for mentoring me, sharing their enthusiasm of the subject, and training me with the transferable skills needed to progress.

I am grateful to all of the staff in the Theory of Condensed Matter group who have advised me with my project, including Prof. Mark Warner, Prof. Chris Pickard, Prof. Benjamin Simons, Prof. Nigel Cooper, and Dr Michael Rutter.

I would like to thank Chaitanya Mangla for helping me on countless occasions, with all aspects of my work. His programming talent and problem solving ability will continue to be an inspiration to me in my future career.

I am grateful to Andrew Fowler for many hours of debugging, well into the early hours of the morning on several occasions, and for introducing me to the fine art of Blender. I thank Ryo Koblitz and Li Yifan for their hospitality and encouragement during the final months of the writing process; Philipp Verpoort for his C++ and Python expertise and camaraderie in the office; Dr Daniel Rowlands and Dr Yani Ioannou for proof-reading my introductory chapters; Dr Chau for fascinating discussions on a huge variety of topics and for motivating my trip to Japan; as well as Dr Tu-Kai Min and his family for an enjoyable tour of the sights in Kyoto – hopefully we will have a chance to meet in the near future.

Additionally, I am thankful for my friends from college, the department, and abroad, who have made my time in Cambridge an enjoyable and rewarding experience: Elise Hickey, John Dudley, May Hen, Sohaib Abdul Rehman, Victoria Tse, Ellie Brown, Dr Jack Thorley, Yu Yang Liu, Dr Hajime Shinohara, Natalie Sizer, Theresa Jakuszeit, Jonathan Wang, Janina Schupp, Martin Schlegel, Hippolyte Astier, Dédalo Sanz Hernández, Edward Linscott, Dr Jamie Wynn, Jackson Wo, Dr Jerónimo Terrones Portas, Chris Parmee, Beñat Mencia Uranga, Lilit Davtyan, Jakub Drapal, Patrick Jones, Elliott Bussell, Simon Wilkinson, Edward Lødøen Tasker, Dr Lars Schonenberg, Fahim Ahmed, Kevin Duff, Victor Jouffrey, Muhsin Ali, Dr Daniel Malz, Dr Adam Smith, as well as many others.

Finally, I would like to thank my family and girlfriend for their unconditional love and support.

Abstract

From the alignment of magnets to the melting of ice, the transition between different phases of matter underpins our exploitation of materials. Both a quantum and a classical phase can undergo an instability into another state. In this thesis, we study the stability of matter in both contexts: topological states and crystalline solids.

We start with the stability of fractional quantum Hall states on a lattice, known as fractional Chern insulators. We investigate, using exact diagonalization, fractional Chern insulators in higher Chern bands of the Harper-Hofstadter model, and examine the robustness of their many-body energy gap in the effective continuum limit. We report evidence of stable states in this regime; comment on two cases associated with a bosonic integer quantum Hall effect; and find a modulation of the correlation function in higher Chern bands.

We next examine the stability of molecules using variational and diffusion Monte Carlo. By incorporating the matrix of force constants directly into the algorithms, we find that we are able to improve the efficiency and accuracy of atomic relaxation and eigenfrequency calculation. We test the performance on a diverse selection of case studies, with varying symmetries and mass distributions, and show that the proposed formalism outperforms existing restricted Hartree-Fock and density functional theory methods.

Finally, we analyze the stability of three-dimensional crystals. We note that for repulsive Coulomb crystals of point nuclei, cubic systems have a zero matrix of force constants at second order. We investigate this by constructing an analytical model in the tight-binding approximation, and present a phase diagram of the most stable crystal structures, as we tune core and valence orbital radii. We reconcile our results with calculations in the nearly free electron regime, as well as current research in condensed matter and plasma physics.

Table of Contents

1	Introduction	1
2	Atoms, Molecules, and Crystalline Solids	5
2.1	Orbitals and Plane Waves	5
2.1.1	Hybrid functional method	9
2.2	Quantum Monte Carlo	12
2.2.1	Variational Monte Carlo	12
2.2.2	Diffusion Monte Carlo	16
2.3	Forces in Quantum Monte Carlo	20
2.4	Force Constants in Quantum Monte Carlo	22
2.4.1	Derivation omitting Pulay term	22
2.4.2	Derivation including Pulay term	23
2.5	Stability Criteria	25
3	Topological States of Matter	27
3.1	Landau Quantization	28
3.1.1	Landau gauge	29
3.1.2	Symmetric gauge	30
3.2	Geometry and Topology	32
3.2.1	Berry phase	32
3.2.2	Chern number	33
3.3	Integer Quantum Hall Effect	34
3.3.1	Mechanism	35
3.3.2	IQHE on a torus	37
3.4	Fractional Quantum Hall Effect	43
3.4.1	Mechanism	43
3.4.2	Laughlin ground states	44
3.4.3	Laughlin excited states	45

3.4.4	Non-Laughlin states	48
3.4.5	Composite fermion theory	49
3.5	Fractional Chern Insulators	51
3.5.1	Motivation	51
3.5.2	Numerical techniques	52
3.5.3	Generalizing the FQHE	53
4	Stability of Fractional Chern Insulators	55
4.1	Introduction	56
4.2	Model	58
4.2.1	Single-particle Harper-Hofstadter Hamiltonian	58
4.2.2	Hofstadter models and Chern insulators	59
4.2.3	Many-body Hamiltonian	60
4.2.4	Target FCI phases in general Chern bands	61
4.2.5	Scaling to the continuum limit at fixed aspect ratio	62
4.3	Results	63
4.3.1	FCIs in $ C = 1$ Harper-Hofstadter bands	63
4.3.2	FCIs in $ C = 2$ bands	74
4.3.3	FCIs in $ C = 3$ bands	87
4.4	Thermodynamic Limits and Scaling with Chern Number	91
4.5	Discussion & Conclusions	94
5	Stability of Molecules	97
5.1	Introduction	97
5.2	Formalism	98
5.2.1	Matrix of force constants	98
5.2.2	Variational Monte Carlo	100
5.2.3	Diffusion Monte Carlo	101
5.2.4	Contributions of the Hellmann-Feynman and Pulay terms	102
5.3	Applications of Force Constants	103
5.3.1	Atomic relaxation	103
5.3.2	Vibrational modes	104
5.4	Case Studies	104
5.4.1	Hydrogen atom and molecule	104
5.4.2	Hydrogen chloride	109
5.4.3	Carbon dioxide	111
5.4.4	Methane	112

5.5	Conclusion	112
6	Stability of Crystals	115
6.1	Introduction	115
6.2	Theory	116
6.3	Transient Coulomb Model	117
6.3.1	Analysis	117
6.3.2	Discussion	122
6.4	Tight-binding Model	123
6.4.1	Analysis	124
6.4.2	Discussion	128
6.5	Nearly Free Electron Model	129
6.6	Conclusion	133
7	Conclusion	135
Appendix A Topological States of Matter		137
A.1	Classical Hall Effect	137
A.2	Anyons	139
Appendix B Stability of Fractional Chern Insulators		141
B.1	Periodic Landau Gauge Vector Potential for Rectangular Lattices	141
B.2	Periodic Landau Gauge Transform in Fourier Space	142
B.3	Scaling to the Continuum Limit at Fixed Flux Density	145
B.4	Derivation of the Correlation Function	146
B.5	Accuracy of Correlation Functions	148
B.6	Error Analysis	150
Appendix C Stability of Molecules		153
C.1	Atomic Relaxation Calculation	153
C.1.1	Minimizing the energy	153
C.1.2	Correction for global translations	154
C.1.3	Correction for global rotations	154
C.1.4	Correction for anharmonicity	155
C.2	Vibrational Modes Calculation	157
C.2.1	Existing computational approaches	157
C.2.2	Matrix of force constants approach	157
C.2.3	Approaches based on derivatives of the force and energy	158

C.2.4	Correction for anharmonicity	159
C.2.5	Monte Carlo uncertainty	159
Appendix D	Stability of Crystals	161
D.1	Higher-order Derivative Test	161
D.2	Higher-order Matrices of Force Constants	162
D.3	Crystal Structures in the Periodic Table	163
D.4	Numerical Model	163
D.4.1	Cubic systems (cub, bcc, fcc, dia)	163
D.4.2	Hexagonal systems (hcp, dhcp)	165
D.4.3	Multi-parameter systems	168
D.5	Details of the Tight-binding Model	168
D.5.1	Definitions	168
D.5.2	Ion-ion contribution	173
D.5.3	Electron-ion contribution	174
D.5.4	Electron-electron contribution	175
D.5.5	Pauli repulsion	175
D.5.6	Crystal relaxation	177
D.6	Oscillatory Electron Density in the Nearly Free Electron Model	177
References		179

Chapter 1

Introduction

The study of collective behavior in many-body systems, or condensed matter physics, stands out in recent years, both in terms of academic and industrial impact. In academia, the field is responsible for the most Nobel prizes in physics, with four awarded in the last decade [3], as well as some of the most highly-cited papers, particularly in density functional theory [4]. In industry, condensed matter research has enabled ground-breaking advancements for existing products, such as energy-efficient LEDs [5], as well as completely new commercial technology, such as quantum dot displays [6] and superconducting quantum computers [7]. The energies and length scales at which typical condensed matter problems operate are in part the reason for its success. Fortunately, this clear applicability to real world has in many cases motivated increased investment and interest in the field [8].

Topological phases of matter is a prime example of a branch of condensed matter physics that has exploded in the last thirty years: from the three Nobel prizes for the integer quantum Hall effect [9], fractional quantum Hall effect [10], and the theory of topological phases [11], through to current research, with the experimental discovery of three-dimensional topological insulators [12], Weyl fermions [13], and Majorana zero-modes [14]. This progress has not gone unnoticed, as topological matter is having an increasing influence in academia and industry alike. Just over a decade ago, Microsoft founded the Station Q project, led by Michael Freedman, to accelerate the progress in topological quantum computing [15]. More recently, in 2016, the company made multi-million dollar investments in this area to found new international laboratories, such as Station Q Copenhagen [16]. Although the first topological qubit has not yet been experimentally constructed, researchers at Station Q Delft have recently published the first experimental evidence of quantized Majorana conductance [17, 18]. Furthermore, the discovery of topological phases has spawned several sub-fields of its own. For example, topomechanics, pioneered by Sebastian Huber [19], has highlighted the ubiquity of topological phases in the classical world, from acoustic [20] to

equatorial waves [21]. And skyrmionics - the study of non-volatile data storage devices using magnetic skyrmions - offers blueprints for the next generation of hard disk drives [22]. Overall, the possibilities for the field are far reaching, and the heavy involvement of industry and external investors is testament to its promise. We study the stability of topological phases on a lattice in Chapter 4.

In addition to accelerating computational performance through new types of architecture, many condensed matter theorists work simultaneously to exploit these advancements in their research. Building on the success of a large variety of density functional theory programs, e.g. CASTEP [23], an effort is now being made to solve quantum many-body problems with higher levels of precision, using classes of methods which were previously undesirable, or even inaccessible, due to computational expense. One example of such a class of methods is quantum Monte Carlo, which aims to provide state-of-the-art accuracy for the solutions to the quantum many-body problem, based on the optimization of an initial quantum state using stochastic sampling [24]. The past two decades have seen surge of activity on this topic, due to the rise of petascale computing, improvements to the algorithms [25], and particular interest in quantum spin liquids [26] and high-temperature superconductivity [27]. Notably, 2016 saw the publication of the seminal paper by Zen et al. on “Boosting the accuracy and speed of quantum Monte Carlo” [25], which has now become widely adopted as the cutting-edge implementation by the community [28]. Furthermore, progress in the development of initial variational states has led to the accurate modeling of more complicated systems, with multiple electron orbitals, disorder, and electron-phonon interactions¹ [24]. In contrast to the progress in applications to other branches of condensed matter physics, Federico Becca and Sandro Sorella bemoan in the preface of their 2017 book that “very few [quantum Monte Carlo] investigations have been performed in the lattice versions of the quantum Hall effect” e.g. in the Hofstadter model [24]. This thesis introduces both of these topics and so sets the scene to pursue this line of research. We enhance the efficiency and precision of quantum Monte Carlo algorithms in Chapter 5.

Not all discoveries in condensed matter physics are due to new technological advances or state-of-the-art algorithms, however. Some breakthroughs arise from re-interpretations or paradigm shifts in existing theory. Consider, for example, crystal structure and atomic packing, which has been an area of research in the field since its inception. Despite the topic’s long history, there are still major discoveries being made to this decade, such as the 2010 Nobel prize for the discovery of Graphene [30] - a two-dimensional hexagonal

¹Quantum Monte Carlo is not without its competitors, with density matrix renormalization group and tensor network approaches making equally impressive progress in recent years [29]. However, since these alternate approaches are unbiased in the sense that no initial wave function is required, the methods may be considered complementary [24].

lattice of Carbon atoms with zero band gap - or the 2011 Nobel prize for the discovery of quasicrystals [31] - crystals which are ordered but lack translational symmetry². These cases emphasize the importance of revisiting even well-established theories with new insight and tools. We contribute to the theory of crystal stability in Chapter 6.

Every advancement in the field of condensed matter physics emphasizes how much we have left to learn about the world around us, with theory providing a glimpse into what the future may hold. In this thesis, we present work spanning topological phases of matter, quantum Monte Carlo, and crystal structure, focusing on system stability in each case. We hope to instill a greater appreciation of the subtleties in these topics, as well as the scope for their potential unification in the future.

²Contrary to initial skepticism, the existence of these structures has now been experimentally verified multiple times [32] and is now paving the way to new areas of research, such as the first observation of quasicrystalline superconductivity in 2018 [33].

Chapter 2

Atoms, Molecules, and Crystalline Solids

Even plasma, the most abundant and disordered phase of matter in the universe, can form a crystal.

paraphrased from Thomas et al. [34]

Despite recent advances in experimental methods and materials science, electronic structure calculations remain, in many cases, the leading technique in which to accurately probe properties of a material. In fact, numerical implementations are often reliable enough to replace expensive experiments in industry, which is part of the reason for their commercial success [23, 35, 36]. In this chapter, we discuss the formalism of electronic structure calculations for atoms, molecules, and crystalline solids. We start by discussing how best to model atomic configurations from a theoretical perspective, motivated by numerical methods. We then proceed to detail two of the most powerful quantum Monte Carlo algorithms in the field: variational Monte Carlo and diffusion Monte Carlo. Finally, we outline the challenges of implementing forces and force constants in a quantum Monte Carlo scheme, and analyze the stability criteria for these systems. The formalism presented is general, and as alluded by the epigraph, has a larger scope than may first appear.

2.1 Orbitals and Plane Waves

This section is based on the lecture notes by Towler [37], Sherill [38], and Skylaris [39]. The molecular orbitals described are used to construct the trial wave function in Chapter 5.

When studying a material structure problem, either theoretically or computationally, one of the first quantities to formalize is the wave function. After all, the wave function

provides a complete quantum mechanical description of the system, from which it is possible to model the behavior of interest. In a numerical calculation, however, there is almost always a trade-off between accuracy and efficiency. The aim is to use approximations to construct accurate representations of the wave function, with minimal computational cost.

In the early years of computational electronic structure calculations, scientists used their intuition from calculations based on ‘Hydrogen-like’ atoms as the basis for orbital construction. This is in part due to the fact that the radial functions in these systems are analytic. Consider a Hydrogen-like atom with one electron and a point nucleus of charge $+Z$ at the origin. From an analysis of the radial function of this system, $R(r)$, we can see the wave function has a cusp at the origin, such that

$$\left. \frac{dR}{dr} \right|_{r=0} = -Z,$$

and the wave function decays exponentially outwards. For this reason, theorists sought to capture this exponential decay and cusp, and so they started constructing their orbitals using *primitive Slater-type orbitals* (STOs) of the form:

$$g^{\text{STO}}(r, \zeta, n) = A(n, \zeta) Y_{l,m}(\theta, \phi) r^{n-1} e^{-\zeta r},$$

where A is a normalization constant, $Y_{l,m}$ are the spherical harmonics, ζ is the exponent, and $\{n, m, l\}$ are the quantum numbers [40]. The initial problem with using such orbitals is the computational cost for multi-center integrals. Historically, the community started to switch to using *primitive Gaussian-type orbitals* (GTOs) in response to this issue [41]. The GTOs take a similar form:

$$g^{\text{GTO}}(\mathbf{r}) = B(l, \zeta) Y_{l,m}(\theta, \phi) r^l e^{-\zeta r^2},$$

where B is a normalization factor. The important differences being that Gaussians do not have a cusp at the origin and they decay faster. Since they give an incorrect short-distance and long-distance behavior, people believed that this was at best an approximation employed simply to speed up the computations. However, Gaussian orbitals worked surprisingly well, and this is due to several reasons:

1. In a Cartesian basis, GTOs are completely separable, which drastically simplifies the numerical integration.
2. It is true that point nuclei would have a cusp in theory, but for real nuclei with a finite radius, a Gaussian may be a more realistic model.

3. The cusp is often not necessary to accurately predict properties of the wave function in the vicinity of the nucleus.
4. Even though in principle an STO would be able to model the correct large-separation exponential decay, this only occurs for a specific value of the exponent, which is too restrictive for practical molecular or crystalline solid calculations.

For these reasons, GTOs are now a common starting point to construct accurate orbitals for electronic structure calculations.

At this stage, we note that a GTO on its own does not resemble an atomic orbital i.e. a solution to the electronic Schrödinger equation for the atom. For this, it is often necessary to take a linear combination of GTOs to create *contracted Gaussian basis functions* (CGFs) of the form:

$$G_{\alpha}(\mathbf{r}) = \sum_{v=1}^{N_{\alpha}} c_v g_v^{\text{GTO}}(\mathbf{r}),$$

where α is the atomic index, N_{α} is the number of GTOs in the contraction, c_v are the contraction coefficients, and ζ_v are the contraction exponents in the GTO¹. One may now in principle select the contraction coefficients and exponents to obtain the desired properties of the CGFs. In practice, however, the contraction coefficients and exponents for a particular atom are calculated using a self-consistent field (SCF) calculation and stored in a database [42, 43]. One of the main advantages of this formalism is that even though many GTOs may be required to accurately model an atomic orbital, the relative weights of these GTOs are virtually unchanged when the atoms form larger structures. Therefore when extending an atomic calculation to molecules or crystals, one only needs to change the scale factors of the CGFs.

Now that we have formed CGFs to start to model atomic orbitals, we have a couple of options. If we are interested in modeling molecules, we may now take a linear combination of these CGFs in order obtain a final model for our molecular orbital²:

$$\psi_i(\mathbf{r}) = \sum_{\alpha=1}^{N_{\text{BF}}} C_{\alpha,i} G_{\alpha}(\mathbf{r}), \quad (2.1)$$

where i is the molecular index, N_{BF} is the number of basis functions, and $C_{\alpha,i}$ is the coefficient, tuned using a SCF calculation (discussed in Sec. 2.1.1). On the other hand, if we are interested

¹Note that CGFs are often incorrectly referred to as "atomic orbitals" in the literature. Even if the CGFs are atom-centric, they are not precise solutions to the electronic Schrödinger equation for the atom and so this is a misnomer.

²Historically, this was referred to as the "linear combination of atomic orbitals" (LCAO) method, however this is again a misnomer for the same reason as in the previous footnote.

in modeling a crystalline solid, we may assign p CGFs to each of the atoms in the unit cell. These CGFs are associated with all N atoms in the crystal, separated from the unit cell by multiples of the translation vector \mathbf{t} . From these CGFs we may construct Gaussian-type Bloch functions (GTBFs) of the form

$$\tilde{G}_{0,\mathbf{k}}(\mathbf{r}) = \sum_{\mathbf{t}} G_0(\mathbf{r} - \mathbf{r}_0 - \mathbf{t}) e^{i\mathbf{k} \cdot \mathbf{t}},$$

where G_0 is the CGF, \mathbf{r}_0 is the coordinate of the basis atom, both associated to the zeroth unit cell; and \mathbf{k} is the momentum vector. Note that the contraction coefficients and exponents may differ from corresponding values for molecular calculations.

A popular alternative to using Gaussians for crystalline solid calculations is the use of plane waves. For this thesis, we tested both types of calculation and ultimately decided to use all-electron Gaussians. This decision was taken for several reasons, including the following advantages of the Gaussian method:

1. We are able to model both core and valence electronic orbitals accurately and simulate finite systems in an arbitrary number of dimensions.
2. The integrals are exactly solvable and so the method yields extremely precise total energies.
3. We can compute exact non-local exchange, which is required for DFT exchange-correlation functionals.

It is also known that Gaussians are more efficient than plane waves for quantum Monte Carlo, where accuracy is paramount.

There is freedom in how orbitals are constructed, determined by whether speed or accuracy is a priority. Usually the atomic orbitals are represented by several CGFs with a range of contraction exponents [44]. The CGFs with large contraction exponents are referred to as *core basis functions*, whereas the CGFs with small contraction exponents are more diffuse and are referred to as the *valence basis functions*³. The number of CGFs used to represent an atomic orbital (which historically was a Slater orbital, with exponent ‘zeta’) naturally dictates the accuracy of the representation. For example, a *single zeta* representation would not be as faithful to the real atomic orbital as a *triple zeta* representation; however, it would be faster to compute⁴. Furthermore, since valence electrons usually play the most important role in atomic bonding, it is common to use a larger number of CGFs to represent

³This is once again a reference to the incorrect notion of CGFs as ‘atomic orbitals’.

⁴The single-zeta representation uses only one CGF to represent an atomic orbital and hence is the minimal representation.

the valence orbitals than the core orbitals in an atom. For example, one would typically take one CGF to represent the core orbital and several for the valence orbital. This is known as a *split-valence basis*.

There are a couple more features commonly employed to improve the accuracy of basis set expansions. The first of these are *polarization functions*, which are functions of higher angular momentum quantum number than the highest occupied orbital in the configuration. The motivation behind these functions, stems from the fact that when an atom is in a background electric field its charge distribution becomes asymmetric i.e. the atom is polarized. This can occur for atoms in a molecule, for example, where they can experience a non-uniform electric field due to the other atoms present. Polarization functions added to the basis set expansion can accommodate for the increased angular momentum of the orbitals in this situation. This consequently gives the atomic orbital representation more flexibility, particularly when applied to molecules and crystalline solids.

The second feature commonly used to bolster the accuracy of atomic orbital representations are *diffuse functions*. These functions are typically employed in molecules, where the charge distribution of the atoms is expected to be much more diffuse than normal. Alternatively, they may be employed simply when a more accurate representation of the outer orbital distribution is desired. As the name suggests, they are functions with smaller contraction exponents than the usual valence basis functions. Note that diffuse functions are generally avoided when modeling crystalline solids.

Now that we have constructed the most realistic representation possible for our system, we are ultimately left with a wave function of the form of Eq. 2.1 for molecules. At this point we have selected the basis functions, which are now fixed, however the coefficients for our configuration are yet to be determined. To this end, we tune the coefficients in Eq. 2.1 using an SCF calculation. Traditionally, this is performed by deriving the Hartree equation as an approximate solution to the Schrödinger equation and then ensuring that the final field derived from the charge distribution is self-consistent with the initial field. However, nowadays, a popular alternative to Hartree-Fock calculations is to use *density functional theory* (DFT), which attempts to incorporate both exchange and correlation energies in the calculation. In this thesis, we will use a *hybrid functional method* which adopts aspects from both the traditional Hartree-Fock method and also DFT.

2.1.1 Hybrid functional method

The underlying concept of Kohn-Sham DFT comes from mapping an intractable interacting N-electron problem onto a set of tractable non-interacting one-electron problems. The initial problem may be a system of nuclei and electrons represented by the N-body Schrödinger

equation:

$$\left(-\frac{1}{2}\nabla^2 + \frac{1}{2}\sum_{i\neq j}\frac{1}{|\mathbf{r}_i - \mathbf{r}_j|} - \sum_{i,I}\frac{Z_I}{|\mathbf{r}_i - \mathbf{R}_I|} + \frac{1}{2}\sum_{I\neq J}\frac{Z_I Z_J}{|\mathbf{R}_I - \mathbf{R}_J|} \right) \Psi(\mathbf{r}_1, \mathbf{r}_2, \dots) = E\Psi(\mathbf{r}_1, \mathbf{r}_2, \dots),$$

where \mathbf{r}_i are the coordinates of electron i , \mathbf{R}_I are the coordinates of nucleus I , Z is the nuclear charge, and Ψ is the many-body wave function with corresponding eigenenergy⁵ E . From this, we know that the exact electronic density of the system is given as

$$n^{\text{exact}}(\mathbf{r}) = \int \dots \int \Psi^*(\mathbf{r}, \mathbf{r}_2, \dots) \Psi(\mathbf{r}, \mathbf{r}_2, \dots) d\mathbf{r}_2 d\mathbf{r}_3 \dots$$

Alternatively, we can represent these interacting electrons as a set of non-interacting Kohn-Sham quasi-particles, whose behavior is modeled by the *Kohn-Sham equations*:

$$\left(-\frac{1}{2}\nabla_i^2 + \frac{1}{2}\int \frac{n(\mathbf{r}')}{|\mathbf{r} - \mathbf{r}'|} d\mathbf{r}' - \sum_I \int \frac{Z_I n(\mathbf{r}')}{|\mathbf{r}' - \mathbf{R}_I|} d\mathbf{r}' + \frac{1}{2}\sum_{I\neq J} \frac{Z_I Z_J}{|\mathbf{R}_I - \mathbf{R}_J|} + \mu_{\text{XC}}[n(\mathbf{r})] \right) \psi_i(\mathbf{r}) = \varepsilon_i \psi_i(\mathbf{r}),$$

where we have replaced the electron sums with density integrals and introduced an exchange-correlation (XC) potential functional μ_{XC} [45, 46]. ψ_i is the Kohn-Sham eigenstate for electron i with corresponding eigenenergy ε_i . Here the electronic density is given simply as

$$n^{\text{DFT}}(\mathbf{r}) = \sum_i \psi_i^*(\mathbf{r}) \psi_i(\mathbf{r}).$$

Note that the electronic density is exactly preserved in this mapping.

The problem with the Kohn-Sham representation of the problem is that the exchange-correlation energy is unknown. Within DFT, we may write the exchange-correlation energy exactly as

$$E_{\text{XC}} = \frac{1}{2} \iint n(\mathbf{r}) \frac{n_{\text{XC}}(\mathbf{r}, \mathbf{r}')}{|\mathbf{r} - \mathbf{r}'|} d\mathbf{r} d\mathbf{r}'.$$

This is nothing more than the Coulomb interaction between an electron at position \mathbf{r} and an exchange-correlation hole at position \mathbf{r}' . However, the precise form of the exchange-correlation density hole, n_{XC} , is still unknown. The art of Kohn-Sham DFT is, therefore, accurately approximating the exchange-correlation energy.

⁵Here we set $\hbar = m \equiv 1$.

From Hartree-Fock theory, with the most basic assumptions of the antisymmetry of the many-body wave function, we may write the exact non-local exchange energy as

$$E_X^{\text{HF}} = -\frac{1}{2} \sum_{ij,kq} \iint \frac{\psi_{ik}^*(\mathbf{r}) \psi_{ik}(\mathbf{r}') \psi_{jq}^*(\mathbf{r}') \psi_{jq}(\mathbf{r})}{|\mathbf{r} - \mathbf{r}'|} d\mathbf{r} d\mathbf{r}'.$$

Taken on its own, the Hartree-Fock exchange energy is an overly simplified approximation and generally underestimates the binding energy [47].

Several attempts have been made, therefore, to model the exchange-correlation energy. The first and simplest of these models is the *local density approximation* (LDA), which takes the exchange-correlation energy to be of the form

$$E_{\text{XC}}^{\text{LDA}}[n(\mathbf{r})] = \int n(\mathbf{r}) \epsilon_{\text{XC}}^{\text{LDA}}[n(\mathbf{r})] d\mathbf{r},$$

where $\epsilon_{\text{XC}}^{\text{LDA}}$ is taken to be from the homogeneous electron gas [45]. However, this has several limitations including an overestimate of the binding energy. Subsequently, proposals have been introduced to construct a more accurate energy, including the next higher-order approximation known as the *generalized gradient approximation* (GGA) [48],

$$E_{\text{XC}}^{\text{GGA}}[n(\mathbf{r})] = \int n(\mathbf{r}) \epsilon_{\text{XC}}^{\text{GGA}}[n(\mathbf{r}), \nabla n(\mathbf{r})] d\mathbf{r},$$

or even higher-order approximations which follow in a similar fashion i.e. $\epsilon_{\text{XC}}[n(\mathbf{r}), \nabla n(\mathbf{r}), \nabla^2 n(\mathbf{r}), \dots]$ [49]. To a certain extent, all of these approximations suffer from similar problems to the LDA. However, these problems are the opposite to those that we encountered when taking the Hartree-Fock exchange functional alone [50]. Hence, it was subsequently realised that by taking a hybrid of the exact non-local Hartree-Fock exchange energy with the local energy approximations, it is possible to compensate for the limitations of the approximations [51, 52]. The underlying idea of the hybrid functional method is to build an exchange-correlation energy of the form

$$E_{\text{XC}} = \alpha E_X^{\text{HF}} + \sum_i \beta_i E_X^{\text{local}_i} + \sum_i \gamma_i E_C^{\text{local}_i},$$

where $\alpha \in [0, 1]$ is a tuning parameter, $\sum_i \beta_i = 1 - \alpha$ and $\sum_i \gamma_i = 1$. The index ‘local_{*i*}’ could be any of the local energy approximations mentioned above, e.g. LDA, GGA, or higher-order variants. For the simulations in this thesis, we tested a variety of approximations for the local exchange-correlation energy and we found that a mixture of LDA and GGA, known as the *Becke, three-parameter, Lee-Yang-Parr* (B3LYP) energy [53], worked best for our

systems. This functional uses a LDA exchange-correlation energy from Vosko-Wilk-Nusair (VWN) [54], a GGA exchange energy due to Becke [55], and a GGA correlation functional from Lee-Yang-Parr [56]. The complete expression for the functional is given as

$$E_{XC}^{B3LYP} = E_X^{LDA} + \alpha_0(E_X^{HF} - E_X^{LDA}) + \alpha_X(E_X^{GGA} - E_X^{LDA}) + E_C^{LDA} + \alpha_C(E_C^{GGA} - E_C^{LDA}),$$

where $\alpha_0 = 0.20$, $\alpha_X = 0.72$, and $\alpha_C = 0.81$ are the three parameters [57].

In summary, the coefficients in Eq. 2.1 are tuned using an SCF calculation, which in our case equates to minimizing the energies from the restricted Hartree-Fock⁶ and B3LYP hybrid functional method in the CRYSTAL program [58].

2.2 Quantum Monte Carlo

This section is based on the reviews by Toulouse et al. [59], Towler [60], Austin et al. [61], Foulkes et al. [62], Needs et al. [35], Kolorence & Mitas [63], the book chapter by Pederiva et al. [64], and the thesis chapters by Badinski [65] and Kent [66]. The original papers are by McMillan [67] and Ceperley & Alder [68]. The algorithms described in this section are used in conjunction for the simulations in Chapter 5.

Equipped with an accurate description of the underlying orbitals in our system, we may now construct the many-body wave function and use this to simulate the system's behavior. For this, we employ two leading quantum Monte Carlo (QMC) algorithms: variational Monte Carlo (VMC) and diffusion Monte Carlo (DMC).

2.2.1 Variational Monte Carlo

We start by constructing a trial fermionic many-body wave function for our system of Slater-Jastrow form:

$$\Psi_T = e^J D_\uparrow D_\downarrow, \quad (2.2)$$

where e^J is the Jastrow factor and $D_{\uparrow/\downarrow}$ is a Slater determinant of up/down-spin single-particle orbitals. The Jastrow factor incorporates a customizable function, J , which depends on inter-particle distance and thus encodes the electron correlation. The Hartree-Fock part of the trial wave function, $D_\uparrow D_\downarrow$, encodes Pauli exclusion.

⁶The restricted closed-shell Hartree-Fock method is applied to an atom or molecule where all orbitals are doubly occupied. The restricted open-shell Hartree-Fock method uses doubly-occupied orbitals as far as possible, and singly-occupied orbitals for the remaining electrons.

The most important quantity of interest is the energy of the system. From the Ritz variational principle, we know that the variational energy, E_v , is greater than or equal to the ground-state energy, E_0 , such that

$$E_v = \frac{\langle \Psi_T | \hat{H} | \Psi_T \rangle}{\langle \Psi_T | \Psi_T \rangle} \geq \frac{\langle \Psi_0 | \hat{H} | \Psi_0 \rangle}{\langle \Psi_0 | \Psi_0 \rangle} = E_0,$$

where \hat{H} denotes the Hamiltonian of the system, and Ψ_0 the true ground-state wave function. Hence, we know that by varying the energy of our trial system, we expect to approach the ground-state energy from above.

In an electron-position basis, we may write the variational energy as

$$E_v = \frac{\int d\mathbf{r} |\Psi_T|^2 E_L}{\int d\mathbf{r} |\Psi_T|^2} = \int d\mathbf{r} \rho E_L,$$

where $E_L \equiv \hat{H}\Psi/\Psi$ is the local energy and ρ is a normalized probability density function (PDF). The Hamiltonian and wave function are both functions of electron coordinates \mathbf{r} . The variational energy can then be approximated as the average of the local energy, such that

$$E_v \approx \bar{E}_L = \frac{1}{M} \sum_{k=1}^M E_L(\mathbf{r}_k), \quad (2.3)$$

where the selection of M points, \mathbf{r}_k , have been sampled from the PDF, $\rho(\mathbf{r})$, using the Metropolis-Hastings algorithm [69, 70] (discussed later in the Sampling section).

When using a stochastic scheme, such as VMC, a careful analysis of the uncertainty is of paramount importance. In this case we have a systematic uncertainty in the way we have constructed our trial wave function (which may even be at the orbital level), and so this ultimately places a restriction on the accuracy of our result. More easy to quantify, however, is the statistical uncertainty of our Monte Carlo run. It is this statistical uncertainty that is generally quoted together with Monte Carlo results in the literature.

According to the central limit theorem, if the sample of local energies in Eq. 2.3 are random variables that are independent and identically distributed, with finite expectation value $E[E_L]$, and variance $\text{Var}[E_L]$, then in the limit as $M \rightarrow \infty$ the mean local energy \bar{E}_L converges to a Gaussian with expectation value $E[E_L]$, and variance⁷ $\text{Var}[E_L]/M$. Hence, in a statistical sense, the mean of the local energy is an *estimator* of the variational energy.

⁷The law of large numbers guarantees the convergence of \bar{E}_L to $E[E_L]$ in the limit as $M \rightarrow \infty$ when the expectation value is finite but the variance is infinite, however the variance then converges more slowly.

Blocking

However, since the PDF is sampled in a non-independent way, using the Metropolis-Hastings algorithm, we cannot apply the central limit theorem to the whole sample M . Instead, we use the *blocking* technique to split the sample up into M_b independent blocks of size M_s . The Metropolis-Hastings algorithm is based on a Markov chain process, where the probability of the sampling the next point is conditional on the previous point. Within this framework, we may define a timescale over which the points decorrelate, which is known as the *autocorrelation time*. For the blocking technique to work, we need to use a block size which is greater than or equal to the autocorrelation time.

Here we may define a block average for the local energy as

$$\bar{E}_{L,b} = \frac{1}{M} \sum_{k=1}^{M_s} E_{L,k},$$

which is the average within a block, and the global average

$$\bar{E}_L = \frac{1}{M_b} \sum_{b=1}^{M_b} \bar{E}_{L,b}$$

which is the average of the blocks themselves. If the blocks are independent, we may then write the variance of the global average in the large M limit as

$$\text{Var}[\bar{E}_L] = \frac{\text{Var}[\bar{E}_{L,b}]}{M_b}.$$

Note that the samples within a block are not independent, and so the inter-block variance $\text{Var}[\bar{E}_{L,b}]$ involves covariances between the variables. Upon simplification we find that

$$\text{Var}[\bar{E}_{L,b}] = T_c \frac{\text{Var}[E_L]}{M_s},$$

where the autocorrelation time is defined as

$$T_c = 1 + \frac{2}{\text{Var}[E_L]M_s} \sum_{k < l} \text{Cov}[E_{L,k}, E_{L,l}].$$

Hence the final form of the statistical uncertainty for our VMC run takes the form

$$\sigma[\bar{E}_L] = \sqrt{\frac{\text{Var}[E_L]}{M_{\text{eff}}}},$$

where $M_{\text{eff}} = M/T_c$ is the number of effectively independent sample points. This formula implies that the statistical error has an inverse square root relationship with the number of iteration steps⁸.

Sampling

As mentioned in the previous section, the Metropolis-Hastings algorithm is used to sample the PDF, $\rho(\mathbf{r})$. This sampling algorithm uses a Markov chain, which is a memoryless stochastic process, whereby the probability of sampling the next point only depends on the previous point sampled. In this framework, we denote the transition probability of going from an initial point \mathbf{r}_i to a final point \mathbf{r}_f as $P(\mathbf{r}_f|\mathbf{r}_i)$. For the discrete Markov chain, this transition probability is a matrix, called a *Markov matrix*.

The Markov matrix has several important properties:

1. *Stochasticity* – The Markov matrix is non-negative and has normalized columns, which implies that it is possible to select the initial point again on the next step.
2. *Ergodicity* – Since it is possible to move between any initial point \mathbf{r}_i and final point \mathbf{r}_f in a finite number of steps, all states can be selected during a Markov process, and so the chain converges to a unique PDF, $\rho(\mathbf{r})$.
3. *Reversibility* – The Markov matrix is constructed subject to the detailed balance condition $P(\mathbf{r}_f|\mathbf{r}_i)\rho(\mathbf{r}_i) = P(\mathbf{r}_i|\mathbf{r}_f)\rho(\mathbf{r}_f)$ which implies that the probability flux is the same in both directions.

After a few equilibration steps of the random walk of the Markov chain (which are usually discarded), the walk samples from the unique stationary distribution $\rho(\mathbf{r})$ and the observables of interest can be calculated.

In the Metropolis-Hastings algorithm [69, 70], a random walk from \mathbf{r}_i to \mathbf{r}_f is constructed based on the two events: proposal and acceptance. If a candidate point \mathbf{r}'_f is proposed and accepted, it becomes \mathbf{r}_f , whereas if it proposed and rejected it remains \mathbf{r}_i . The Markov matrix in this case may be written as

$$P(\mathbf{r}_f|\mathbf{r}_i) = P_{\text{acc}}(\mathbf{r}_f|\mathbf{r}_i)P_{\text{prop}}(\mathbf{r}_f|\mathbf{r}_i) + \left[1 - \sum_{\mathbf{r}'_f} P_{\text{acc}}(\mathbf{r}'_f|\mathbf{r}_i)P_{\text{prop}}(\mathbf{r}'_f|\mathbf{r}_i) \right] \delta(\mathbf{r}_i - \mathbf{r}_f), \quad (2.4)$$

⁸Various tricks have been applied to manipulate the probability distribution so as to minimize the error. One of the most well known is to add a quantity to the PDF with a smaller variance but zero expectation value [71–73].

where P_{prop} denotes the proposal, and P_{acc} the acceptance, probabilities. The key question is then to determine the optimal choices for these proposal and acceptance probabilities.

Determining the optimal acceptance probability is the easier of the two problems and has already been solved by Metropolis et al. [69]. They derive an optimal acceptance probability of the form:

$$P_{\text{acc}}(\mathbf{r}_f|\mathbf{r}_i) = \min \left\{ 1, \frac{P_{\text{acc}}(\mathbf{r}_f|\mathbf{r}_i)}{P_{\text{acc}}(\mathbf{r}_i|\mathbf{r}_f)} \right\} = \min \left\{ 1, \frac{P_{\text{prop}}(\mathbf{r}_i|\mathbf{r}_f)\rho(\mathbf{r}_f)}{P_{\text{prop}}(\mathbf{r}_f|\mathbf{r}_i)\rho(\mathbf{r}_i)} \right\},$$

where the second equality is due to detailed balance⁹.

An optimal proposal probability, however, is not as clear-cut. The aim is to use a proposal probability that minimizes the autocorrelation time, whilst giving reasonable acceptance ratios and satisfying all of the conditions for the Markov matrix stated before. In this thesis, we use the CASINO program [35], where the proposal is the original configuration plus a Gaussian-distributed random displacement of variance, τ , and a wave function drift term, $\mathbf{v}\tau$, where $\mathbf{v} = \nabla\Psi/\Psi$. Hence, the proposal probability takes the form

$$P_{\text{prop}}(\mathbf{r}_f|\mathbf{r}_i) = \frac{1}{(2\pi\tau)^{3N/2}} \exp\left(-\frac{(\mathbf{r}_f - \mathbf{r}_i - \mathbf{v}(\mathbf{r}_i)\tau)^2}{2\tau}\right).$$

This is an isotropic Gaussian diffusion process, known as a *Wiener process*, with the addition of a drift term which biases the random walk towards higher probability amplitudes.

2.2.2 Diffusion Monte Carlo

Once we have optimized our trial wave function from Eq. 2.2 using VMC, we make further improvements using the more expensive, and accurate [74], DMC algorithm. Using VMC and DMC in combination in this way is a standard technique in the QMC electronic structure community [65].

One of the greatest limitations of the VMC algorithm is the form of the trial wave function. No matter how well the statistical uncertainty is minimized, the method will always be limited by the systematic uncertainty of the initial wave function ansatz. DMC, on the other hand, manages to overcome this issue. It does so by sampling from a *mixed distribution*, $f = \Psi_0\Psi$, which takes both the VMC-optimized wave function, Ψ , and the exact ground-state wave

⁹Note that the acceptance probability does not need to be an ergodic matrix [59].

function, Ψ_0 , into account¹⁰. In DMC, the ground-state energy is written as

$$E_0 = \frac{\langle \Psi_0 | \hat{H} | \Psi \rangle}{\langle \Psi_0 | \Psi \rangle},$$

which in an electron position basis may be written in similar way:

$$E_0 = \frac{\int d\mathbf{r} \Psi_0 \Psi E_L}{\int d\mathbf{r} \Psi_0 \Psi} = \int d\mathbf{r} \rho E_L.$$

By implementing the exact ground-state wave function, we can overcome the inaccuracies of the optimized trial wave function. The question then shifts to how to obtain the exact ground-state wave function¹¹. For this, we evolve the trial wave function (or, in principle, any arbitrary wave function not orthogonal to the ground state) using the $t \rightarrow -it$ imaginary time Schrödinger equation to filter out the ground state. In real space, the evolution of the mixed distribution may be written as

$$f(\mathbf{r}_f, t) = \int d\mathbf{r}_i \tilde{G}(\mathbf{r}_f | \mathbf{r}_i; t) \Psi(\mathbf{r}_i)^2, \quad (2.5)$$

where we define the *importance-sampled Green's function* as

$$\tilde{G}(\mathbf{r}_f | \mathbf{r}_i; t) = \Psi(\mathbf{r}_f) G(\mathbf{r}_f | \mathbf{r}_i; t) \frac{1}{\Psi(\mathbf{r}_i)}.$$

In this context, ‘importance sampling’ means we are sampling according to the mixed PDF. At large imaginary times this will tend to the aforementioned stationary distribution $f = \Psi_0 \Psi$.

However, since an analytical expression for the Green's function of the form of Eq. 2.5 is only known in the limit of short times, we iterate the process over many short times to obtain the stationary distribution. This introduces what is known as a *time-step error* into the calculation, which may be eliminated by extrapolating to $\tau \rightarrow 0$ [75–77].

Fixed Node Approximation

The problem with using this mixed distribution as our PDF however, is that for fermions it can take positive and negative values. As a consequence, this means that although the DMC algorithm can achieve arbitrary accuracy for the ground-state energy of bosonic systems, it

¹⁰For simplicity, both wave functions in this section are assumed to be real.

¹¹Calculating the action of the Hamiltonian directly on Ψ_0 is in most cases too expensive to be computationally feasible.

suffers from the sign problem for fermions¹². In order to circumvent this issue, we fix the nodes of the "exact" ground-state wave function to be the same as those for the trial wave function. This ensures that the mixed PDF is non-negative and is known as the *fixed node approximation* [79–81].

Formally speaking, this is achieved by adding infinite potential delta functions to the true Hamiltonian to form the fixed node Hamiltonian, \hat{H}_{FN} . This extra potential does not contribute to the energy, E_{FN} , of course because the wave function, Ψ_{FN} , is zero at the nodes. Position space is now divided into *nodal pockets* where the wave function has a fixed sign.

The analogous importance-sampled Green's function is of the form

$$\tilde{G}_{\text{FN}}(\mathbf{r}_f|\mathbf{r}_i;t) = \Psi(\mathbf{r}_f)G_{\text{FN}}(\mathbf{r}_f|\mathbf{r}_i;t)\frac{1}{\Psi(\mathbf{r}_i)},$$

which confines moves to a nodal pocket. As before, a short-time approximation needs to be taken. The tiling theorem states that for ground-state calculations it is sufficient to sample only one nodal pocket. In short, the accuracy of a DMC result depends on the quality of the nodal surface of the trial wave function¹³.

Sampling

Unfortunately, it is not possible to use the importance-sampled Green's function to construct a Markov chain directly since it is not a stochastic matrix (i.e. it is not normalized). Instead we use it to form a *weighted random walk* by writing

$$\tilde{G}(\mathbf{r}_f|\mathbf{r}_i;\tau) = P(\mathbf{r}_f|\mathbf{r}_i)W(\mathbf{r}_f|\mathbf{r}_i),$$

where τ is a small time increment, P is a stochastic matrix, and W is a weight matrix. The process starts with a distribution (or *walker*) with a position \mathbf{r}_1 and weight $w_1 = 1$, and then we sample subsequent positions \mathbf{r}_i with probability $P(\mathbf{r}_i|\mathbf{r}_{i-1})$ and weight $w_i = W(\mathbf{r}_i|\mathbf{r}_{i-1})w_{i-1}$. As before, the weighted random walk samples the stationary distribution after the equilibration phase.

At this point, we run into another obstacle, which is that the weights are expensive to compute, and the observable averages are only dominated by the points with largest weight anyway. The answer is use a *branching process* for the walkers in the system. This process works by assigning, at each iteration k , a population of walkers with positions $\mathbf{r}_{k,\alpha}$ and

¹²This sign problem originates from topological properties of the configuration [78].

¹³Accurately approximating the nodal surface is notoriously difficult for solid-state systems, and hence alternative approaches have been developed, such as full configuration interaction quantum Monte Carlo, in order to reliably benchmark quantum chemistry results in these cases [82].

weights $w_{k,\alpha}$ with $\alpha = 1, 2, \dots, M_k$, which each perform a random walk. This results in drastically smaller change in the weights from their initial value. Various algorithms exist for this purpose, including the split-join [83] and stochastic reconfiguration algorithms¹⁴ [84, 85].

In order to sustain a finite walker population, the trial energy, E_T , in the Green's function, $G(\mathbf{r}_f|\mathbf{r}_i;t) = \langle \mathbf{r}_f | e^{-(\hat{H}-E_T)t} | \mathbf{r}_i \rangle$, is set as a function of the weight of the walkers. In turn, this implies that E_T fluctuates with respect to the ground-state energy on each iteration, which introduces what is known as *population control error*. The net effect is an overestimate of the energy¹⁵.

The Metropolis-Hastings algorithm is used, similarly to VMC, for the weighted random walk in DMC. The transition probability matrix may be written in an analogous form to Eq. 2.4, where we use a Metropolis acceptance probability and a drifting Wiener proposal probability. Consequently, the finite time-step error is eliminated in the transition probability matrix (but remains for the weight matrix). The DMC algorithm now takes the form of a diffusion process with a time-scale¹⁶, τ . A small time step must be used for DMC to minimize time-step error, with a large number of walkers to minimize population control error.

As before, the ground-state energy is estimated by an average of the local energy with respect to the normalized mixed PDF. Post equilibration phase this may be written as

$$E_0 \approx \bar{E}_L = \frac{\sum_{k=1}^M \sum_{\alpha=1}^{M_k} w_{k,\alpha} E_L(\mathbf{r}_{k,\alpha})}{\sum_{k=1}^M \sum_{\alpha=1}^{M_k} w_{k,\alpha}}.$$

This estimator has the same or analogous statistical properties as those discussed for VMC.

In cases where the observable of interest, \hat{O} , does not commute with the Hamiltonian, we may use the *extrapolation formula* to reduce the error by one order in $\|\Psi - \Psi_0\|$ [87]. The extrapolation formula is given as

$$\langle \hat{O} \rangle = 2 \langle \hat{O} \rangle_{\text{DMC}} - \langle \hat{O} \rangle_{\text{VMC}} + \mathcal{O}(\|\Psi - \Psi_0\|^2),$$

where $\langle \rangle_{\text{DMC}}$ denotes the average over the mixed DMC distribution and $\langle \rangle_{\text{VMC}}$ denotes the average within VMC. There are also many other techniques used to generate pure distributions from local operators [88], such as the future walking method [89].

¹⁴Bias may be eliminated by tuning the population of walkers between each iteration, and controlling the weight distribution among the walkers.

¹⁵The population control error scales inversely with the number of walkers and can be effectively eliminated by not controlling the population on the last few iterations of the DMC algorithm [83, 86].

¹⁶Note that the variance in the drifting Wiener proposal probability for the VMC algorithm is often also referred to as a time-scale by analogy, even though it has no relation to physical time.

2.3 Forces in Quantum Monte Carlo

This section is based on the thesis by Badinski [65], as well as the papers by Assaraf & Caffarel [90], Moroni et al. [91], and Badinski et al. [92]. Finite-difference derivatives of forces are used as a benchmark for the force constant calculations in Chapter 5.

The advantages of incorporating forces (i.e. derivatives of the energy with respect to nuclear displacements) into solid-state simulations are undisputed for both atomic relaxation and molecular dynamics, however, in many cases, they are notoriously difficult to compute. Even at the level of basis functions, scientists were, for many years, reluctant to use Gaussian basis sets over plane waves due to the difficulty of computing forces. CRYSTAL, for example, only included forces for the first time in its fifth release: CRYSTAL03. For QMC, the inability to compute forces was listed as the number one reason on Ceperley's "Top Ten List of reasons why quantum Monte Carlo is not used in chemistry" published in 1996 [93]. Of course, times have moved on since then, and progress has been made in this area. However, the topic of forces is just as influential today and still remains a subject of active research.

At present, atomic relaxation is generally performed using DFT, where the QMC simulations are then used to accurately calculate the energy in the Born-Oppenheimer approximation, i.e. with stationary nuclei. However, methods have been proposed to incorporate the force directly. These may be split into two types:

1. analytic derivatives [94, 95]
2. finite differences [96]

In this thesis, we shall focus on the analytical derivatives approach, since this is the method pursued in most modern literature.

As discussed in the previous section, the energy of a system may be written in an electron position basis as

$$E = \frac{\int \Psi^* \hat{H} \Psi \, d\mathbf{r}}{\int |\Psi|^2 \, d\mathbf{r}}, \quad (2.6)$$

where the many-body wave function, Ψ , and Hamiltonian, \hat{H} , are functions of all particle positions. From this, we may take the derivative of the energy with respect to the displacement

of the I^{th} nucleus, \mathbf{R}_I , to yield¹⁷

$$\frac{dE}{d\mathbf{R}_I} = \frac{\int \Psi^* \frac{d\hat{H}}{d\mathbf{R}_I} \Psi d\mathbf{r}}{\int |\Psi|^2 d\mathbf{r}} + \frac{\int \frac{d\Psi^*}{d\mathbf{R}_I} \hat{H} \Psi + \Psi \hat{H} \frac{d\Psi}{d\mathbf{R}_I} d\mathbf{r}}{\int |\Psi|^2 d\mathbf{r}} - \frac{\int \Psi^* \hat{H} \Psi d\mathbf{r}}{\int |\Psi|^2 d\mathbf{r}} \frac{\int \frac{d\Psi^*}{d\mathbf{R}_I} \Psi + \Psi^* \frac{d\Psi}{d\mathbf{R}_I} d\mathbf{r}}{\int |\Psi|^2 d\mathbf{r}}.$$

Identifying the energy (Eq. 2.6) in the above expression, and rearranging, leads to an expression for the force composed of two parts:

$$F = F_{\text{HF}} + F_{\text{Pulay}}, \quad (2.7)$$

where the Hellmann-Feynman term is given as

$$F_{\text{HF}} = \frac{\int \Psi^* \frac{d\hat{H}}{d\mathbf{R}_I} \Psi d\mathbf{r}}{\int |\Psi|^2 d\mathbf{r}}, \quad (2.8)$$

and the Pulay term takes the form

$$F_{\text{Pulay}} = \frac{\int \frac{d\Psi^*}{d\mathbf{R}_I} (\hat{H} - E) \Psi d\mathbf{r}}{\int |\Psi|^2 d\mathbf{r}} + \text{c.c.}$$

The problem with evaluating the force in QMC naively, just as we did with the energy in the previous section, is that the force does not satisfy the *zero-variance property*.

In Sec. 2.2.1, we showed that, for VMC, the variational energy could be estimated by the statistical mean of the local energy, where the mean is sampled from the PDF $|\Psi_T|^2$. Similarly, for DMC, we showed that the exact energy could be estimated from a statistical mean of the local energy sampled over the (fixed-node) mixed distribution, $\Psi\Psi_T$. In both cases, we see that the uncertainty in the energy result is related to the fluctuations in the local energy. When the variance in the local energy goes to zero, then so too will the uncertainty in our result. The issue with applying the same technique to forces is that the bare force has infinite variance. Since $F \sim r^{-2}$ at short distances, then we can clearly see that $\langle F^2 \rangle \rightarrow \infty$.

In the last two decades, several attempts have been suggested to overcome the obstacle of infinite variance. Of particular focus for this thesis are the studies of the *heavy tails* of the force distribution. The term "heavy tails" is given to a power-law decay, rather than an exponential decay, at large distances, giving rise to infinite variance. For the local Hellmann-Feynman force, these heavy tails were found to decay with the fourth power, such that

¹⁷The input wave functions are generally unnormalized, with normalization factors that depend on the ion displacements \mathbf{R} , and so we include all normalization factors in these derivations. This also shows the derivatives exactly as they are implemented in the CASINO code.

$\sim |F - F_0|^{-4}$, where F_0 is a constant. It has also been shown that singularities in the energy landscape (at the nodal surface of Ψ_T) would lead to heavy tails of the same form.

Nowadays, many of the technical difficulties arising from force calculations have been circumvented for both VMC and DMC, which puts QMC in the limelight as a competitive electronic structure technique.

2.4 Force Constants in Quantum Monte Carlo

In this thesis, we propose further improving the accuracy and efficiency of QMC calculations by incorporating the matrix of force constants.

2.4.1 Derivation omitting Pulay term

When the wave function is an exact eigenstate of the Hamiltonian ($\hat{H}\Psi = E\Psi$), the Pulay term in Eq. 2.7 vanishes. Hence, the total force is given simply as the Hellmann-Feynman force in Eq. 2.8.

In order to simplify the following algebra, we take Ψ to be real and we drop the ion subscripts. Furthermore, we write the force in terms of local quantities and probability densities, so as to mimic the quantities computed in CASINO. Our initial expression for the force is therefore written as

$$F_{\text{HF}} = \frac{\int \Psi^2 \left(\frac{\hat{H}'\Psi}{\Psi} \right) d\mathbf{r}}{\int \Psi^2 d\mathbf{r}}, \quad (2.9)$$

where the dash indicates a derivative with respect to nuclear configuration. Taking the derivative of Eq. 2.9 with respect to nuclear configuration then yields

$$F'_{\text{HF}} = \frac{\int \left[2\Psi^2 \frac{\Psi'}{\Psi} \right] \left(\frac{\hat{H}'\Psi}{\Psi} \right) d\mathbf{r}}{\int \Psi^2 d\mathbf{r}} + \frac{\int \Psi^2 \left[\left(\frac{\hat{H}''\Psi}{\Psi} \right) + \left(\frac{\hat{H}'\Psi'}{\Psi} \right) - \frac{\Psi'}{\Psi} \left(\frac{\hat{H}'\Psi}{\Psi} \right) \right] d\mathbf{r}}{\int \Psi^2 d\mathbf{r}} - 2 \frac{\int \Psi^2 \left(\frac{\hat{H}'\Psi}{\Psi} \right) d\mathbf{r}}{\int \Psi^2 d\mathbf{r}} \frac{\int \Psi^2 \frac{\Psi'}{\Psi} d\mathbf{r}}{\int \Psi^2 d\mathbf{r}}. \quad (2.10)$$

Identifying the Hellmann-Feynman force (Eq. 2.9) in the above expression and simplifying gives

$$F'_{\text{HF}} = \frac{\int \Psi^2 \left(\frac{\hat{H}''\Psi}{\Psi} \right) d\mathbf{r}}{\int \Psi^2 d\mathbf{r}} + \frac{2}{\int \Psi^2 d\mathbf{r}} \left[\frac{1}{2} \int \Psi^2 \frac{\Psi'}{\Psi} \left(\frac{\hat{H}'\Psi}{\Psi} \right) d\mathbf{r} + \frac{1}{2} \int \Psi^2 \left(\frac{\hat{H}'\Psi'}{\Psi} \right) d\mathbf{r} \right] - 2F_{\text{HF}} \frac{\int \Psi^2 \frac{\Psi'}{\Psi} d\mathbf{r}}{\int \Psi^2 d\mathbf{r}}. \quad (2.11)$$

At this point, we note that although the Hamiltonian does not commute with the wave function, the derivative of the Hamiltonian with respect to nuclear configuration does commute. The only non-commuting part of the Hamiltonian is the kinetic energy, which is the total kinetic energy of the electrons. Once the derivative is taken with respect to nuclear configuration, the kinetic energy term goes and we are left with a commuting \hat{H}' . We use this fact to combine the terms in the square brackets of Eq. 2.11, such that

$$F'_{\text{HF}} = \frac{\int \Psi^2 \left(\frac{\hat{H}''\Psi}{\Psi} \right) d\mathbf{r}}{\int \Psi^2 d\mathbf{r}} + 2 \frac{\int \Psi^2 \frac{\Psi'}{\Psi} \left(\frac{\hat{H}'\Psi}{\Psi} - F_{\text{HF}} \right) d\mathbf{r}}{\int \Psi^2 d\mathbf{r}}.$$

Extending this derivation to complex Ψ and general ion elements is trivial, and the final result for the matrix of force constants is given as

$$\frac{d^2E}{d\mathbf{R}_I d\mathbf{R}_J} = \frac{\int \Psi^* \frac{d^2\hat{H}}{d\mathbf{R}_I d\mathbf{R}_J} \Psi d\mathbf{r}}{\int |\Psi|^2 d\mathbf{r}} + \frac{\int \Psi^* \left[\frac{d\Psi}{d\mathbf{R}_I} \left(\Psi^{-1} \frac{d\hat{H}}{d\mathbf{R}_J} \Psi - \frac{dE}{d\mathbf{R}_J} \right) + (I \leftrightarrow J) \right] d\mathbf{r}}{2 \int |\Psi|^2 d\mathbf{r}} + \text{c.c.}$$

We approximate the pure expectation value of the matrix of force constants in DMC using the extrapolation formula. We compute this expression directly in QMC and have submitted a patch so that this capability is incorporated in the latest version of CASINO.

2.4.2 Derivation including Pulay term

In practice, however, the wave functions are not exact in VMC or DMC and so the initial assumption in Sec. 2.4.1 does not precisely hold. In this case, the total force is given by Eq. 2.8 and in simplified form may be written as

$$F = \underbrace{\frac{\int \Psi^2 \left(\frac{\hat{H}'\Psi}{\Psi} \right) d\mathbf{r}}{\int \Psi^2 d\mathbf{r}}}_{F_{\text{HF}}} + 2 \underbrace{\frac{\int \Psi^2 \frac{\Psi'}{\Psi} \left[\left(\frac{\hat{H}'\Psi}{\Psi} \right) - E \right] d\mathbf{r}}{\int \Psi^2 d\mathbf{r}}}_{F_{\text{Pulay}}}. \quad (2.12)$$

Taking the derivative of the Hellmann-Feynman force with respect to nuclear configuration yields Eq. 2.10, however now identifying the total force (Eq. 2.12) in this expression gives

$$F'_{\text{HF}} = \frac{\int \Psi^2 \left(\frac{\hat{H}'\Psi}{\Psi} \right) d\mathbf{r}}{\int \Psi^2 d\mathbf{r}} + 2 \frac{\int \Psi^2 \frac{\Psi'}{\Psi} \left(\frac{\hat{H}'\Psi}{\Psi} - F \right) d\mathbf{r}}{\int \Psi^2 d\mathbf{r}} + 4 \frac{\int \Psi^2 \frac{\Psi'}{\Psi} \left[\left(\frac{\hat{H}\Psi}{\Psi} \right) - E \right] d\mathbf{r}}{\int \Psi^2 d\mathbf{r}} \frac{\int \Psi^2 \frac{\Psi'}{\Psi} d\mathbf{r}}{\int \Psi^2 d\mathbf{r}}. \quad (2.13)$$

Taking the derivative of the Pulay term with respect to nuclear configuration yields

$$\begin{aligned} F'_{\text{Pulay}} = & 2 \frac{\int \left[2\Psi^2 \left(\frac{\Psi'}{\Psi} \right)^2 + \Psi^2 \frac{\Psi''}{\Psi} - \Psi^2 \left(\frac{\Psi'}{\Psi} \right)^2 \right] \left[\left(\frac{\hat{H}\Psi}{\Psi} \right) - E \right] d\mathbf{r}}{\int \Psi^2 d\mathbf{r}} \\ & + 2 \frac{\int \Psi^2 \frac{\Psi'}{\Psi} \left[\left(\frac{\hat{H}'\Psi}{\Psi} \right) + \left(\frac{\hat{H}\Psi'}{\Psi} \right) - \frac{\Psi'}{\Psi} \left(\frac{\hat{H}\Psi}{\Psi} \right) - F \right] d\mathbf{r}}{\int \Psi^2 d\mathbf{r}} \\ & - 4 \frac{\int \Psi^2 \frac{\Psi'}{\Psi} \left[\left(\frac{\hat{H}\Psi}{\Psi} \right) - E \right] d\mathbf{r}}{\int \Psi^2 d\mathbf{r}} \frac{\int \Psi^2 \frac{\Psi'}{\Psi} d\mathbf{r}}{\int \Psi^2 d\mathbf{r}}, \end{aligned}$$

which after simplification, and using the commutation relation $[\hat{H}', \Psi] = 0$, becomes

$$\begin{aligned} F'_{\text{Pulay}} = & \frac{2}{\int \Psi^2 d\mathbf{r}} \int \Psi^2 \left[\frac{\Psi'}{\Psi} \left(\frac{\hat{H}'\Psi}{\Psi} \right) + \frac{\Psi''}{\Psi} \left(\frac{\hat{H}\Psi}{\Psi} - E \right) \right. \\ & \left. + \frac{\Psi'}{\Psi} \left(\frac{\hat{H}\Psi'}{\Psi} \right) - E \left(\frac{\Psi'}{\Psi} \right)^2 - F \frac{\Psi'}{\Psi} \right] d\mathbf{r} \\ & - 4 \frac{\int \Psi^2 \frac{\Psi'}{\Psi} \left[\left(\frac{\hat{H}\Psi}{\Psi} \right) - E \right] d\mathbf{r}}{\int \Psi^2 d\mathbf{r}} \frac{\int \Psi^2 \frac{\Psi'}{\Psi} d\mathbf{r}}{\int \Psi^2 d\mathbf{r}}. \end{aligned} \quad (2.14)$$

Note that the term in square brackets in Eq. 2.14 may of course be expressed as a total derivative ($[\Psi'(\hat{H} - E)\Psi]'$), since the second term in Eq. 2.14 is the derivative of the denominator of the Pulay term.

Finally, adding the Hellmann-Feynman (Eq. 2.13) and Pulay (Eq. 2.14) contributions together we obtain the final expression for the matrix of force constants:

$$\begin{aligned} F' = & \frac{\int \Psi^2 \left(\frac{\hat{H}'\Psi}{\Psi} \right) d\mathbf{r}}{\int \Psi^2 d\mathbf{r}} + 2 \frac{\int \Psi^2 \frac{\Psi'}{\Psi} \left(\frac{\hat{H}'\Psi}{\Psi} - F \right) d\mathbf{r}}{\int \Psi^2 d\mathbf{r}} \\ & + \frac{2}{\int \Psi^2 d\mathbf{r}} \int \Psi^2 \left[\frac{\Psi'}{\Psi} \left(\frac{\hat{H}'\Psi}{\Psi} \right) + \frac{\Psi''}{\Psi} \left(\frac{\hat{H}\Psi}{\Psi} - E \right) + \frac{\Psi'}{\Psi} \left(\frac{\hat{H}\Psi'}{\Psi} \right) - E \left(\frac{\Psi'}{\Psi} \right)^2 - F \frac{\Psi'}{\Psi} \right] d\mathbf{r}. \end{aligned}$$

The matrix of force constants including Pulay term has not been implemented in this thesis due to: results showing that the Pulay contribution is minimal close to equilibrium (see Chapter 5), the difficulty in evaluating the second derivative of the wave function in CASINO, and the time required for a careful analysis of the Hellmann-Feynman contribution. However, computing and analyzing the effect of the Pulay contribution to the matrix of force constants is a promising avenue for future research.

2.5 Stability Criteria

The implications of directly implementing the matrix of force constants within a QMC framework are numerous. Having access to this harmonic term would allow direct computations of atomic vibrations in molecules or phonons in crystals. Moreover, the matrix of force constants would improve the accuracy of higher-order anharmonic corrections to these vibrations, such as the Morse correction. However, the benefits of studying the matrix of force constants transcends the QMC framework, as this term plays a fundamental role in physics.

When studying the energy of a system at equilibrium, we find that

$$E(\mathbf{R}) = E(\mathbf{R}_0) + \frac{dE}{d\mathbf{R}_I} \mathbf{R}_{0,I} + \frac{1}{2} \frac{d^2E}{d\mathbf{R}_I d\mathbf{R}_J} \mathbf{R}_{0,I} \mathbf{R}_{0,J} + \dots,$$

where \mathbf{R}_0 denotes the equilibrium displacement. Hence, at equilibrium, the force is zero, and the sign of the matrix of force constants determines whether the equilibrium is stable or unstable, by the multi-variate derivative test¹⁸. A positive-definite matrix of force constants is a sufficient condition for system stability. Therefore, not only would a computation of the force constants bring with it the expected accuracy benefits of calculating a higher-order term, it would also allow us to directly study properties of fundamental interest to the community, and specifically comment on stability.

¹⁸If the 2nd-order term is also zero, then higher-order terms may be used to determine the nature of the turning point (see Appendix D.1).

Chapter 3

Topological States of Matter

The Earth is a Chern insulator of Chern number two.

paraphrased from Delplace et al. [97]

Consider electrons confined to a two-dimensional sample in a perpendicular magnetic field. When a longitudinal current is driven through the sample, a transverse voltage is produced [98]. This is the classical Hall effect¹. In strong magnetic fields and at low temperatures, the transverse conductivity of the system is quantized, which is the quantum Hall effect (QHE). If the sample is sufficiently *impure*² and the Landau levels are fully filled, then its transverse conductivity is quantized in *integer* steps [99]. This is the integer quantum Hall effect (IQHE). If the sample is sufficiently *pure* and the Landau levels are only partially filled, then its transverse conductivity is quantized in *rational* steps [100]. This is the fractional quantum Hall effect (FQHE).

In this chapter, we provide an overview of the key concepts and derivations in the field of topological matter. We begin, in Secs. 3.1 and 3.2, by explaining Landau quantization and the connection between geometry and topology, through the use of simple examples. In Sec. 3.3, we discuss the mechanism of the IQHE, as well as its applications on tori, culminating in an exposition of the Thouless-Kohmoto-Nightingale-den Nijs (TKNN) formula [101]. In Sec. 3.4, we transition to the FQHE and touch on fractional statistics, topological order, and composite fermion theory. Finally, in Sec. 3.5, we bring these ideas together to motivate the study of fractional Chern insulators, and set the scene for modern research.

¹See Appendix A.1 for a derivation.

²In this context, impurity refers to the impurity of the conducting material; for example, due to lattice dislocations and imperfections.

3.1 Landau Quantization

This section is based on the notes by Huber [102], Tong [103], and Goerbig [104]; and the books by Jain [105], Janßen et al. [106], Wen [107], and Phillips [108]. The original theory is by Landau [109].

Consider an electron, of mass m_e and charge $-e$, confined to a two-dimensional sample in a perpendicular magnetic field $\mathbf{B} = \nabla \times \mathbf{A}$, where \mathbf{A} is the gauge potential. The quantum Hamiltonian³ for an electron⁴ with canonical momentum \mathbf{p} is

$$H = \frac{1}{2m_e}(\mathbf{p} + e\mathbf{A})^2, \quad (3.1)$$

with canonical commutation relations

$$\begin{aligned} [x_i, p_j] &= i\hbar\delta_{ij}, \\ [x_i, x_j] &= [p_i, p_j] = 0. \end{aligned}$$

Using a suitable choice of ladder operators, a, a^\dagger , the Hamiltonian takes the form of the harmonic oscillator. Hence, the Hilbert space may be defined as

$$\begin{aligned} a^\dagger |n\rangle &= \sqrt{n+1} |n+1\rangle, \\ a |n\rangle &= \sqrt{n} |n-1\rangle, \quad a |0\rangle = 0, \end{aligned}$$

with eigenenergies $E_n = \hbar\omega_B(n + 1/2)$, where ω_B is the cyclotron frequency and $n \in \mathbb{Z}$ is the principal quantum number. The energy levels of an electron in a magnetic field are called *Landau levels*. They are equally spaced with an energy gap proportional to the field strength. Unlike the harmonic oscillator, Landau levels are *degenerate*.

Let us now, more specifically, consider an electron in the xy-plane with a perpendicular magnetic field $\mathbf{B} = B\hat{\mathbf{e}}_z$. The gauge potential associated with this magnetic field is not unique. Although the magnetic field has a translational and rotational symmetry in the xy-plane, the gauge potential is necessarily in a subgroup of the physical symmetry [103], and hence we have a gauge choice.

³In this chapter, the hats on quantum operators are implicit.

⁴In a magnetic field, there is a Zeeman splitting of energy levels for the up- and down-spin electrons. At low temperatures, the electrons do not have enough energy to jump the Zeeman gaps, and hence may be treated as spinless [103].

3.1.1 Landau gauge

Let us choose *Landau gauge*:

$$\mathbf{A} = \begin{pmatrix} 0 \\ xB \\ 0 \end{pmatrix}.$$

This choice of gauge breaks translational symmetry in the x-direction. The Hamiltonian in Eq. 3.1 becomes

$$H = \frac{1}{2m_e} (p_x^2 + (p_y + eBx)^2).$$

Translational invariance in the y-direction motivates a plane-wave ansatz of the form

$$\psi_k(x, y) = e^{iky} f_k(x),$$

where $f_k(x)$ is a function of x for a state with momentum $k \in \mathbb{R}$. Inserting this ansatz into the Schrödinger equation yields

$$H_k \psi_{n,k} = E_n \psi_{n,k},$$

with Hamiltonian

$$H_k = \frac{p_x^2}{2m_e} + \frac{m_e \omega_B^2}{2} (x + kl_B^2)^2$$

and eigenenergies

$$E_n = \hbar \omega_B \left(n + \frac{1}{2} \right). \quad (3.2)$$

This corresponds to a harmonic oscillator, centered on $\langle x \rangle = -kl_B^2$, with characteristic *magnetic length*

$$l_B \equiv \sqrt{\frac{\hbar}{eB}}.$$

Consequently, the wave functions take the form

$$\psi_{n,k}(x, y) \propto e^{iky} H_n(x + kl_B^2) \exp \left[-\frac{1}{2l_B^2} (x + kl_B^2)^2 \right],$$

where H_n denotes the n^{th} Hermite polynomial. The degeneracy of the wave functions is now manifest.

Consider a finite rectangular sample of dimensions \mathcal{L}_x , \mathcal{L}_y , and area $A_{\text{sample}} = \mathcal{L}_x \mathcal{L}_y$. The finite extent in the y-direction implies that momentum is quantized such that

$$k_{\mathcal{N}} = \frac{2\pi \mathcal{N}}{\mathcal{L}_y}, \quad \mathcal{N} \in \mathbb{Z}. \quad (3.3)$$

The finite extent in the x-direction restricts the wave functions to be centered inside the sample, and hence imposes a further condition on the momenta:

$$-\frac{\mathcal{L}_x}{l_B^2} \leq k_{\mathcal{N}} \leq 0. \quad (3.4)$$

Combining Eqs. 3.3 & 3.4, we find that the total number of states in the sample

$$\mathcal{N} = \frac{\mathcal{L}_y}{2\pi} \int_{-\mathcal{L}_x/l_B^2}^0 dk = \frac{\mathcal{L}_x \mathcal{L}_y}{2\pi l_B^2} = \frac{BA_{\text{sample}}}{h/e} \equiv \frac{\Phi}{\Phi_0},$$

where $\Phi = BA_{\text{sample}}$ is the total flux through the sample and $\Phi_0 \equiv h/e$ is the *flux quantum*. Hence, the flux quantum is interpreted as the flux through an area of $2\pi l_B^2$, which is the area that a state must occupy in each Landau level⁵. The total number of filled Landau levels, or *filling factor*, is therefore

$$\nu \equiv \frac{n_e}{n_B},$$

where n_e is the electron density and $n_B = 1/2\pi l_B^2$ is the state density.

3.1.2 Symmetric gauge

Let us choose *symmetric gauge*:

$$\mathbf{A} = \frac{1}{2} \begin{pmatrix} -yB \\ xB \\ 0 \end{pmatrix}.$$

This choice of gauge breaks translational symmetry in the x- and y-directions. However, rotational symmetry about the origin is preserved.

In symmetric gauge, we can define two types of momenta, to track the Landau level n , and the degeneracy m , respectively:

$$\begin{aligned} \boldsymbol{\pi} \equiv \mathbf{p} + e\mathbf{A} &\Rightarrow a \equiv \frac{1}{\sqrt{2e\hbar B}} (\pi_x - i\pi_y), \\ \tilde{\boldsymbol{\pi}} \equiv \mathbf{p} - e\mathbf{A} &\Rightarrow b \equiv \frac{1}{\sqrt{2e\hbar B}} (\tilde{\pi}_x + i\tilde{\pi}_y). \end{aligned}$$

With this choice of ladder operators, the eigenstates are

$$|n, m\rangle \propto a^{\dagger n} b^{\dagger m} |0, 0\rangle,$$

⁵More precisely, $2\pi l_B^2$ is the minimum uncertainty product for the x- and y-coordinates of the electron.

with the usual eigenenergies, given in Eq. 3.2.

Consider the *lowest Landau level* (LLL). The states in the LLL satisfy

$$a|0, m\rangle = 0. \quad (3.5)$$

Defining

$$\begin{aligned} z &\equiv x - iy, \\ \partial &\equiv (\partial_x + i\partial_y)/2, \end{aligned} \quad (3.6)$$

yields

$$\begin{aligned} a &= -i\sqrt{2} \left(l_B \bar{\partial} + \frac{z}{4l_B} \right), \\ b &= -i\sqrt{2} \left(l_B \partial + \frac{\bar{z}}{4l_B} \right). \end{aligned}$$

Equation 3.5 is therefore a differential equation which may be solved to yield

$$\Psi_{\text{LLL},m}(z) = f_m(z) e^{-|z|^2/4l_B^2},$$

for any holomorphic⁶ function $f_m(z)$. The lowest state in the LLL is annihilated by both a and b . Hence, it is directly proportional to $e^{-|z|^2/4l_B^2}$. All higher LLL states are constructed by acting with b^\dagger on the lowest state, which implies

$$\Psi_{\text{LLL},m}(z) \propto \left(\frac{z}{l_B} \right)^m e^{-|z|^2/4l_B^2}.$$

Similarly, all higher Landau-level wave functions are constructed by acting with a^\dagger on the LLL. Due to the rotational symmetry of the gauge, the wave functions are all eigenfunctions of the angular momentum operator.

⁶The unconventional definition of z in Eq. 3.6 was chosen to ensure holomorphic, rather than antiholomorphic, wave functions [103, 106].

3.2 Geometry and Topology

This section is based on the notes by Tong [103], Huber [102], and Witten [110]; and the books by Bernevig [111], and Jain [105]. The original paper is by Berry [112].

Consider the Hamiltonian $H(x^a; \lambda^i)$, which depends on degrees of freedom x^a and parameters λ^i . Initially, the system is in the unique⁷ ground state $|\psi\rangle$. As we vary the parameters slowly, the ground state becomes $|\psi(\lambda(t))\rangle$.

The *adiabatic theorem* states that if a system is in an energy eigenstate and the parameters of the system are varied sufficiently slowly, then the system will remain in that energy eigenstate. The rate at which you need to vary the parameters is dependent on the energy gap to the nearest neighboring eigenstate [113].

3.2.1 Berry phase

For our first example, let us slowly vary the parameters, such that we form a closed path in parameter space, Γ . For each parameter choice, let us define a reference ground state with a fixed choice of phase $|n(\lambda)\rangle$. The adiabatic theorem allows us to write the ground state as

$$|\psi(t)\rangle = U(t) |n(\lambda(t))\rangle,$$

where $U(t)$ is a time-dependent phase which satisfies $U(0) = 1$. Every energy eigenstate has a *dynamical phase* $e^{-i \int dt E_0(t)/\hbar}$, regardless of whether the parameters are varied. We set $E_0 = 0$, $\forall t$, to focus on the effect of the parameter evolution. Substituting our ground state into the time-dependent Schrödinger equation and taking the overlap with $\langle\psi|$, yields

$$\dot{U} = -i \mathcal{A}_i \dot{\lambda}^i U, \quad (3.7)$$

where the *Berry connection* is defined as

$$\mathcal{A}_i(\lambda) \equiv -i \left\langle n \left| \frac{\partial}{\partial \lambda^i} \right| n \right\rangle.$$

Equation 3.7 can be integrated to find

$$U(t) = \exp \left(-i \oint_{\Gamma} \mathcal{A}_i(\lambda) d\lambda^i \right),$$

⁷A unique ground state results in the Abelian case, which is sufficient to introduce the key concepts of Berry phase and Chern number. However, a degenerate ground state needs to be considered in order to analyze non-Abelian systems.

which is known as the *Berry phase*. Note that the Berry phase depends on the integral of the closed path taken through parameter space and hence, is gauge-invariant and physical.

Due to the arbitrary choice of fixed phase in $|n(\lambda)\rangle$, there is a redundancy in our definition of the Berry connection. All physics remains invariant if we use a different fixed phase, or even a different phase for every choice of parameters. In analogy to electromagnetism, we can extract the physical information from this vector potential (over the space of all parameters), by considering the gauge-invariant quantity

$$\mathcal{B}_{ij} = \frac{\partial \mathcal{A}_i}{\partial \lambda^j} - \frac{\partial \mathcal{A}_j}{\partial \lambda^i},$$

which is known as the *Berry curvature*. Finally, using Stokes' theorem, we may write the Berry phase as

$$U(t) = \exp\left(-i \iint_S \mathcal{B}_{ij} dS^{ij}\right),$$

where S is a two-dimensional surface in parameter space bounded by the curve Γ . Note that there is freedom in choosing the surface S .

3.2.2 Chern number

For our second example, let us consider an electron in a magnetic field \mathbf{B} and focus only on its spin. The Hilbert space of this system has two states: $|\uparrow\rangle$ and $|\downarrow\rangle$. The Hamiltonian is

$$H = -\mathbf{B} \cdot \boldsymbol{\sigma}_P + B,$$

where $\boldsymbol{\sigma}_P$ is the triplet of Pauli matrices, and satisfies

$$\begin{aligned} H|\uparrow\rangle &= 2B|\uparrow\rangle, \\ H|\downarrow\rangle &= 0. \end{aligned}$$

The magnetic field is a tunable external parameter, and hence we will work over the space of magnetic fields $\lambda^i \equiv B^i$. The Berry curvature in this scenario is

$$\mathcal{B}_{ij} = -\varepsilon_{ijk} \frac{B^k}{2|\mathbf{B}|^3},$$

which is a monopole, with charge $g_m = -1/2$, in the space of magnetic fields (see [114] for the original monopole quantization argument by Dirac, and [103] for a derivation of the Berry curvature). Note that the Berry curvature is singular when $\mathbf{B} = \mathbf{0}$, and therefore when

the ground state $|\downarrow\rangle$ is degenerate with $|\uparrow\rangle$. The Abelian theory breaks down under these conditions.

As in the previous section, we now take a closed path Γ in parameter space. Let the surface S , bounded by Γ , make a solid angle Ω . Since $\iint_{S^2} \mathcal{B}_{ij} dS^{ij} = 4\pi g_m$, the Berry phase may be written as

$$U(t) = \exp\left(-i \iint_S \mathcal{B}_{ij} dS^{ij}\right) = \exp(-i\Omega g_m). \quad (3.8)$$

However, if we chose a surface S' which went around the other side of the monopole (i.e. opposite orientation), then it would make a solid angle $\Omega' = 4\pi - \Omega$. In that case, the Berry phase would be

$$U'(t) = \exp\left(-i \iint_{S'} \mathcal{B}_{ij} dS^{ij}\right) = \exp(i\Omega' g_m),$$

which agrees with Eq. 3.8, as it should, since the Berry phase is gauge-invariant and physical. However, note that these two expressions for the Berry phase are only equal if the monopole charge satisfies $2g_m \in \mathbb{Z}$. This simple example illustrates an important general result. Quantization of the monopole charge implies that

$$\oint \mathcal{B}_{ij} dS^{ij} = 2\pi C,$$

where $C \in \mathbb{Z}$ is known as the *Chern number*.

3.3 Integer Quantum Hall Effect

This section is based on the books by Janßen et al. [106], Phillips [108], Jain [105], Wen [107], and Bernevig [111]; the notes by Tong [103], Huber [102], Goerbig [104] and Nayak [115]; and the review by Girvin [116]. The original paper is by Klitzing et al. [99], for which Klitzing was awarded the Nobel Prize in Physics in 1985 [9].

For the theory of the IQHE, we do not need to take interactions between electrons into account and hence, for the purposes of this discussion, we may assume that the results derived for single particles generalize to many particles. The Pauli exclusion principle is the only many-body effect that comes into play⁸ [103].

⁸Historically, this is how the theory of the quantum Hall effect developed, however, as we shall discuss in Sec. 3.4, this is now known not to be the case.

3.3.1 Mechanism

In the classical Hall effect, it was shown that for electrons confined to a two-dimensional sample in a perpendicular magnetic field, a longitudinal current produces a transverse voltage [98]. This phenomenon can be explained treating electron dynamics classically (see Appendix A.1). Almost a century later, it was observed that at fully-filled Landau levels, low temperatures, high magnetic fields, and with a sufficiently impure sample, the transverse Hall conductivity plateaus in integer steps. This phenomenon can be explained using the quantum mechanics of non-interacting electrons.

Two main questions are addressed in this section:

1. Why is the Hall conductivity quantized in integer steps?
2. Why does this quantization manifest itself as extended plateaus?

1. To answer the first question, consider an electron confined to the xy -plane in the presence of a longitudinal electric field $\mathbf{E} = E\hat{\mathbf{x}}$ and a perpendicular magnetic field $\mathbf{B} = B\hat{\mathbf{z}}$. In Landau gauge, the Hamiltonian is

$$H = \frac{1}{2m_e} (p_x^2 + (p_y + eBx)^2) - eEx. \quad (3.9)$$

Following the same derivation as in Sec. 3.1.1, we find that the wave functions corresponding to Eq. 3.9 are of the form

$$\psi_{n,k}(x,y) \propto e^{iky} H_n \left(x - \frac{m_e E}{eB^2} + kl_B^2 \right) \exp \left[-\frac{1}{2l_B^2} \left(x - \frac{m_e E}{eB^2} + kl_B^2 \right)^2 \right],$$

which implies that the oscillator states are centered on

$$\langle x \rangle = \frac{m_e E}{eB^2} - kl_B^2. \quad (3.10)$$

In terms of the canonical momentum and vector potential, we may write the mechanical velocity of the electron as $\mathbf{v} = (\mathbf{p} + e\mathbf{A})/m_e$. Hence, the total current is

$$\mathbf{I} = -e\mathbf{v} = -\frac{e}{m_e} \sum_{n=0}^{\nu} \sum_k \langle -i\hbar\nabla + e\mathbf{A} \rangle,$$

where we are summing over all filled states. Using Landau gauge, together with the result in Eq. 3.10, we find that the current density $\mathbf{J} = -(e\nu E/\Phi_0)\hat{\mathbf{y}}$. Finally, applying Ohm's law,

we find that the transverse conductivity is quantized in integer steps:

$$\sigma = \frac{e\nu}{\Phi_0} \begin{pmatrix} 0 & 1 \\ -1 & 0 \end{pmatrix}, \quad \nu \in \mathbb{Z}.$$

2. To answer the second question, we need to study the potential landscape of the sample and how the current flows within it. Consider an electron in a pure rectangular sample which is finite in the x -direction, with Hamiltonian

$$H = \frac{1}{2m_e} (p_x^2 + (p_y + eBx)^2) + V(x),$$

where $V(x)$ rises steeply at the edges of the sample. Taylor expanding the potential in the vicinity of the electron's location X , we find that

$$V(x) \approx \frac{\partial V}{\partial x}(X - x),$$

which implies that the group velocity of the electron is given by

$$v_y = -\frac{1}{eB} \frac{\partial V}{\partial x}.$$

In general, it can be shown that the electrons drift along equipotentials in a direction perpendicular to ∇V [102]. The *edge modes* are chiral and modes on opposite edges travel in opposite directions. If we just have a magnetic field, then only the edge modes contribute to the current, since the potential is flat in the bulk. If we add a background electric field, then the Landau levels are tilted slightly and so all modes contribute to the current.

Let us now introduce *disorder* in the sample, which is small relative to the splitting of the Landau levels⁹. The potential still rises steeply at the edges of the sample, but is now random in the bulk. From perturbation theory, we know that since these perturbations do not preserve a symmetry, they necessarily break degeneracies [103]. Second, since electrons drift along equipotentials, we expect certain quantum states to become localized.

In terms of conductivity, only extended states can transport charge from one side of the sample to the other. As we decrease the magnetic field, each Landau level can accommodate fewer electrons and so the Fermi energy will increase. However, if all the extended states are already filled in a given Landau level, then before jumping to the next Landau level, all the localized states in that Landau level need to be populated. These localized states have a slightly

⁹Disorder in the sample is a necessary feature of the IQHE. Increased disorder increases the precision of the integer quantum Hall effect, but only up to the splitting of the Landau levels [102].

higher energy than the extended states, and so are populated last. Naturally, localized states do not contribute to the conductivity, and so until all of the localized states are filled, the conductivity remains constant. The more disordered the sample (up to the splitting of the Landau levels), the more prominent the plateaus of conductivity.

There is now a discrepancy. The way that we derived the quantization of conductivity, in answer to question 1, assumed that all modes contribute to the current. However, in a disordered sample many modes are localized and so do not contribute to the current. In fact, Laughlin showed precisely in 1981, by considering a Corbino ring geometry in a charge pumping thought experiment, that the current carried by the extended states increases to compensate for the lack of current carried by the localized states [117]. Halperin later refined these ideas and published the theory of extended states in 1982 [118].

3.3.2 IQHE on a torus

This section is based on the book by Fradkin [119] and the notes by Tong [103]. The original papers are by Laughlin [117] and Thouless et al. [101], for which Thouless was awarded the Nobel Prize in Physics in 2016 [11].

To illustrate the connection between the IQHE and topology, it is instructive to examine the IQHE on a torus. This is also faithful to the theory's historical development [101]. In this section, we examine tori in both real and momentum space.

Torus: \mathbf{T}^2 in real space

In the first scenario, we consider a rectangular quantum Hall system in a uniform magnetic field B with sides of length \mathcal{L}_x , \mathcal{L}_y , and periodic boundary conditions.

Let us introduce operators which translate the wave function by some position vector \mathbf{d} . We define these *magnetic translation operators* as

$$T(\mathbf{d}) \equiv e^{-i\mathbf{d}\cdot(m\hat{\mathbf{x}})/\hbar+i\phi'} = e^{-i\mathbf{d}\cdot(i\nabla+e\mathbf{A}/\hbar)+i\phi'},$$

with auxiliary phase¹⁰ ϕ' and boundary conditions

$$\begin{aligned} T_x \psi(x, y) &\equiv T(\mathbf{d} = (\mathcal{L}_x, 0)) \psi = \psi(x, y), \\ T_y \psi(x, y) &\equiv T(\mathbf{d} = (0, \mathcal{L}_y)) \psi = \psi(x, y). \end{aligned}$$

¹⁰Mathematically, an auxiliary phase is necessary to ensure the magnetic translation operators form a group; however, this does not effect the physics. The precise form of this auxiliary phase is given in the original paper by Zak [120].

Note that the magnetic translation operators are not gauge-invariant, and so the final wave functions will only agree up to a gauge transformation. In Landau gauge, we find that

$$T_y T_x = e^{-ieB\mathcal{L}_x\mathcal{L}_y/\hbar} T_x T_y.$$

Hence, for periodic boundaries we demand the *Dirac quantization condition*

$$\frac{\Phi}{\Phi_0} \in \mathbb{Z}.$$

This is an example of how the quantization condition manifests itself from the topology of the system.

Consider the fluxes Φ_x and Φ_y threaded through the x- and y-cycles of the torus, respectively. In Landau gauge, the vector potential becomes

$$\mathbf{A} = \begin{pmatrix} \frac{\Phi_x}{\mathcal{L}_x} \\ \frac{\Phi_y}{\mathcal{L}_y} + Bx \\ 0 \end{pmatrix},$$

which perturbs the Hamiltonian by

$$\Delta H = -\mathbf{J} \cdot \mathbf{A} = - \sum_{i=x,y} \frac{J_i \Phi_i}{\mathcal{L}_i}.$$

Using 1st-order perturbation theory, under an infinitesimal change of Φ_i , the ground state $|\psi_0\rangle$ changes by

$$\left| \frac{\partial \psi_0}{\partial \Phi_0} \right\rangle = -\frac{1}{L_i} \sum_{n \neq \psi_0} \frac{\langle n | J_i | \psi_0 \rangle}{E_n - E_0} |n\rangle. \quad (3.11)$$

In linear response theory, it can be shown that the *Kubo formula* [119] for the Hall conductivity is

$$\sigma_{xy} = i\hbar \sum_{n \neq 0} \frac{\langle 0 | J_y | n \rangle \langle n | J_x | 0 \rangle - \langle 0 | J_x | n \rangle \langle n | J_y | 0 \rangle}{(E_n - E_0)^2}.$$

Hence, using Eq. 3.11,

$$\sigma_{xy} = i\hbar \left[\frac{\partial}{\partial \Phi_y} \left\langle \psi_0 \left| \frac{\partial \psi_0}{\partial \Phi_x} \right\rangle - \frac{\partial}{\partial \Phi_x} \left\langle \psi_0 \left| \frac{\partial \psi_0}{\partial \Phi_y} \right\rangle \right]. \quad (3.12)$$

Note that Φ_i appear as parameters in the Hamiltonian, yet the energy spectrum only depends on $\Phi_i \bmod \Phi_0$. Hence, the space of flux parameters is also a torus \mathbf{T}_{Φ}^2 .

For clarity, let us define dimensionless angular variables

$$\theta_i = 2\pi(\Phi_i \bmod \Phi) \quad : \quad \theta_i \in [0, 2\pi).$$

The Berry connection over \mathbf{T}_Φ^2 is then

$$\mathcal{A}_i(\Phi) = -i \left\langle \psi_0 \left| \frac{\partial}{\partial \theta_i} \right| \psi_0 \right\rangle,$$

with transverse Berry curvature

$$\mathcal{B}_{xy} = -i \left[\frac{\partial}{\partial \theta_y} \left\langle \psi_0 \left| \frac{\partial \psi_0}{\partial \theta_x} \right\rangle - \frac{\partial}{\partial \theta_x} \left\langle \psi_0 \left| \frac{\partial \psi_0}{\partial \theta_y} \right\rangle \right].$$

This is directly proportional to the Hall conductivity in Eq. 3.12:

$$\sigma_{xy} = -\frac{e^2}{\hbar} \mathcal{B}_{xy}.$$

If we now average over all fluxes,

$$\sigma_{xy} = -\frac{e^2}{\hbar} \iint_{\mathbf{T}_\Phi^2} \frac{d^2\theta}{(2\pi)^2} \mathcal{B}_{xy}$$

and recall that the (first) Chern number is identified as

$$C = \frac{1}{2\pi} \iint_{\mathbf{T}_\Phi^2} d^2\theta \mathcal{B}_{xy},$$

we obtain the *TKNN invariant* [101, 121]

$$\sigma_{xy} = -\frac{e^2}{h} C, \quad C \in \mathbb{Z}.$$

We have derived the familiar expression for the Hall conductivity in the IQHE; except, in this case, we have identified the quantum number as the Chern number. The remarkable fact is that a directly measurable physical quantity, such as the Hall conductivity, is directly proportional to a topological quantum number. This is the first indication that topology plays a key role in understanding the theory of quantum Hall systems.

Lattice: \mathbf{T}^2 in momentum space

In the second scenario, we consider a quantum Hall system confined to a rectangular lattice, with lattice spacings a , b , and primitive lattice vectors $\mathbf{e}_x = (a, 0)$, $\mathbf{e}_y = (0, b)$. Assume a simple lattice in an insulating state, such that the single-particle energy spectra form gapped band structures. The multi-particle spectrum is then obtained by filling up the single-particle spectra subject to the Pauli exclusion principle.

Bloch's theorem states that wave functions in a given band are periodic on the unit cell:

$$\psi_{\mathbf{k}}(\mathbf{x}) = e^{i\mathbf{k}\cdot\mathbf{x}} u_{\mathbf{k}}(\mathbf{x}),$$

where $u_{\mathbf{k}}(\mathbf{x} + \mathbf{e}) = u_{\mathbf{k}}(\mathbf{x})$, and the momentum is confined to the *Brillouin zone*:

$$\begin{aligned} -\frac{\pi}{a} < k_x \leq \frac{\pi}{a}, \\ -\frac{\pi}{b} < k_y \leq \frac{\pi}{b}, \end{aligned}$$

which is a torus \mathbf{T}^2 in momentum space. In analogy to Sec. 3.3.2, we may analyze the topology over this torus. However, on this occasion the torus is over the space of states rather than the space of parameters. Nevertheless, the basic topological properties still hold. The Chern number is now given by an integral over the Brillouin zone (BZ),

$$C = \frac{1}{2\pi} \oint_{\mathbf{T}_{\text{BZ}}^2} d^2k \mathcal{B}_{xy},$$

where the Berry curvature, \mathcal{B}_{xy} , is defined in terms of the periodic functions $u_{\mathbf{k}}$. This means that we can assign a Chern number C_n to each band n . Hence, it may be shown that the Hall conductivity is given by the *TKNN formula* [101]

$$\sigma_{xy} = -\frac{e^2}{h} \sum_n C_n.$$

This is essentially the TKNN invariant for a non-interacting band insulator, where the Chern number is now replaced by the sum of the Chern numbers over all of the bands. Note that there also exist band insulators with non-trivial Chern numbers, even in the absence of a magnetic field [103]. Band insulators which have a single-particle spectrum that yields a finite Chern number are known as *Chern insulators*.

Initially, let us examine a particle hopping on a lattice in the absence of a magnetic field. For simplicity, we restrict ourselves to the special case of a square lattice with $a = b$. In the

tight-binding model, the positions of the eigenstates $|\mathbf{x}\rangle$ are restricted to the lattice sites, and hence the Hamiltonian is

$$H = -t \sum_{\mathbf{x}} \sum_{j=1,2} |\mathbf{x}\rangle \langle \mathbf{x} + \mathbf{e}_j| + \text{H.c.},$$

where the lattice momenta lie in the Brillouin zone and t is the hopping parameter. If we consider a finite sample with x and y -dimensions given by \mathcal{L}_1 and \mathcal{L}_2 , respectively, then k_i is quantized into units of $1/2\pi\mathcal{L}_i$. This implies that the total number of states in the Brillouin zone is given by A_{sample}/a^2 , where $A_{\text{sample}} = \mathcal{L}_1\mathcal{L}_2$ is the area of the sample¹¹.

Now, let us introduce a gauge field $A_j(\mathbf{x})$ on the links between lattice sites, where $A_1(\mathbf{x})$ is to the right of point \mathbf{x} and $A_2(\mathbf{x})$ is above. This additional field may be incorporated into the Hamiltonian¹² such that

$$H = -t \sum_{\mathbf{x}} \sum_{j=1,2} |\mathbf{x}\rangle e^{-ieaA_j(\mathbf{x})/\hbar} \langle \mathbf{x} + \mathbf{e}_j| + \text{H.c.} \quad (3.13)$$

So far, our topological arguments have relied on the existence of a Brillouin zone. However, in the presence of a magnetic field, the gauge choice breaks the translational invariance which allowed us to construct the Brillouin zone. We can remedy this by defining an analogous Brillouin zone in the presence of magnetic fields.

Define gauge-invariant magnetic translation operators

$$T_j \equiv \sum_{\mathbf{x}} |\mathbf{x}\rangle e^{-ieaA_j(\mathbf{x})/\hbar} \langle \mathbf{x} + \mathbf{e}_j|,$$

such that the Hamiltonian in Eq. 3.13 becomes

$$H = -t \left(\sum_{j=1,2} T_j + T_j^\dagger \right),$$

where T_j and T_j^\dagger move states vertically and horizontally by one lattice site, respectively. As a particle moves anticlockwise around a plaquette, to leading order in t , it can be shown that it picks up an Aharonov-Bohm phase with flux $\Phi = Ba^2$ [103]. Hence, these magnetic translation operators obey a discrete version of the magnetic translation algebra

$$T_2 T_1 = e^{ie\Phi/\hbar} T_1 T_2. \quad (3.14)$$

¹¹This ratio gives the number of sites in the lattice, which is manifestly the number of states in the Hilbert space.

¹²The energy spectrum for this Hamiltonian is the Hofstadter butterfly [122, 123].

However, it is possible to construct magnetic translation operators which commute with the Hamiltonian:

$$\tilde{T}_j \equiv \sum_{\mathbf{x}} |\mathbf{x}\rangle e^{-iea\tilde{A}_j(\mathbf{x})/\hbar} \langle \mathbf{x} + \mathbf{e}_j|,$$

where we have defined a new gauge field \tilde{A}_j : $\partial_k \tilde{A}_j = \partial_j A_k$. Although these operators commute with the Hamiltonian, among themselves they satisfy the discrete magnetic translation algebra given in Eq. 3.14. Hence, we cannot yet simultaneously label an eigenstate by the eigenvalues of both of the magnetic translation operators.

To remedy this, we consider fluxes at rational multiples of the flux quantum

$$\frac{\Phi}{\Phi_0} = \frac{p}{q},$$

where p and q are co-prime integers. In this case, we can construct commuting operators

$$[\tilde{T}_1^{n_1}, \tilde{T}_2^{n_2}] = 0, \quad \forall \frac{p}{q} n_1 n_2 \in \mathbb{Z}.$$

Hence, it is now possible to simultaneously label each eigenstate with, for example, eigenvalues of \tilde{T}_1^q and \tilde{T}_2 .

For example, defining states $|\mathbf{k}\rangle$ satisfying

$$\begin{aligned} \tilde{T}_1^q |\mathbf{k}\rangle &= e^{iqk_1 a} |\mathbf{k}\rangle, \\ \tilde{T}_2 |\mathbf{k}\rangle &= e^{ik_2 a} |\mathbf{k}\rangle, \end{aligned}$$

such that $H |\mathbf{k}\rangle = E(\mathbf{k}) |\mathbf{k}\rangle$, we find that the momenta on the torus are:

$$\begin{aligned} -\frac{\pi}{qa} < k_1 \leq \frac{\pi}{qa}, \\ -\frac{\pi}{a} < k_2 \leq \frac{\pi}{a}, \end{aligned}$$

which is known as the *magnetic Brillouin zone*. This magnetic Brillouin zone is q -times smaller than the original Brillouin zone and hence contains A_{sample}/qa^2 states. Consequently, the spectrum decomposes into q bands, each with a different range of energies. Furthermore, any eigenenergy in a given band is q -fold degenerate. We have freedom in how the magnetic Brillouin zone (or equivalently, magnetic unit cell) is defined.

3.4 Fractional Quantum Hall Effect

This section is based on the books by Fradkin [119], Jain [105], Wen [107], and Phillips [108]; the notes by Tong [103], and Nayak [115]; and the review by Girvin [116]. The original papers are by Tsui et al. [100] and Laughlin [124], for which Laughlin, Störmer and Tsui were awarded the Nobel Prize in Physics in 1998 [10].

For the theory of the FQHE, we need to take interactions between electrons into account. In fact, it is the plethora of electron-electron interactions that dominates the physics in this phenomenon [105].

3.4.1 Mechanism

In the previous section, we saw how if we performed the Hall experiment with fully-filled Landau levels, at sufficiently low temperatures and high magnetic fields ($k_B T \ll \hbar \omega_B$), and with a sufficiently impure sample ($0 \ll V_{\text{disorder}} \ll \hbar \omega_B$), the Hall conductivity is quantized in integer steps. However, all of the arguments in the previous section made at least one of two assumptions:

1. The electrons do not interact with each-other, other than via Pauli exclusion.
2. The ground state is unique.

In this section, we discuss the regime where these approximations break down, resulting in a rational quantization of the Hall conductivity¹³.

We consider a Hall experiment with partially-filled Landau levels, at even lower temperatures and stronger magnetic fields than the IQHE, such that the interactions between electrons become significant. In this chapter, we shall model the electron-electron interactions using the Coulomb potential, V_{Coulomb} . In order for the electron-electron interactions to play a significant role, we require that

$$\hbar \omega_B \gg V_{\text{Coulomb}} \gg V_{\text{disorder}},$$

which is achieved by taking a relatively pure sample to these extreme conditions [100].

The analysis of the FQHE presents one major difficulty. For the IQHE, we assumed that the ground state is unique. However, we know that in a partially-filled Landau level ($\nu < 1$) there are ${}^N C_{\nu N}$ ways of filling the states, which is far from unique. In fact, the ground states

¹³Since the number of fractions increases as we make the sample purer, in the limit of a perfectly pure sample, we would expect to recover the direct proportionality that we saw for the classical Hall effect.

of these systems are so degenerate that using perturbation theory would be impossible by hand. Numerically this can be solved, as demonstrated in Chapter 4, but still only for ~ 10 particles. Hence, analysis of the FQHE cannot be performed exactly in an analytical way. Instead, in this section, we focus on a variety of approximations and analogies to best capture the physics.

3.4.2 Laughlin ground states

Laughlin explained the physics at fractional increments of

$$\nu = \frac{1}{m}, \quad \text{where } m \text{ is an odd integer (for fermions).}$$

These are known as *Laughlin states*.

Instead of solving the problem exactly, Laughlin simply wrote down an ansatz for the wave function based on angular momentum arguments in symmetric gauge [124]. Recall that in the LLL, the wave functions take the form

$$\psi_{\text{LLL}}(z_1, \dots, z_N) = \tilde{\psi}(z_1, \dots, z_N) e^{-\sum_{i=1}^N |z_i|^2 / 4l_B^2},$$

where the holomorphic function $\tilde{\psi}$ must be antisymmetric under the exchange of two particles, so that the wave function obeys Fermi-Dirac statistics. Laughlin's ansatz for the ground-state wave function is

$$\tilde{\psi}(z_1, \dots, z_N) = \prod_{i < j} (z_i - z_j)^m,$$

where m is an odd integer, as before. There are two things to note about this ansatz. First, this is indeed antisymmetric when m is an odd integer. Second, the magnitude of the wave function vanishes when the electrons are too close together or far apart, and hence it is peaked at a certain radius.

From analysis of the angular momentum eigenvalues, we find that m denotes the relative angular momentum of the particles [103]. For example, if we consider the first particle z_1 , we find that there are $m(N-1)$ powers of z_1 in the pre-factor, which corresponds to the maximum angular momentum of the particle. This implies that the particle is at a radius $R = \sqrt{2m(N-1)}l_B$, tracing out an area $A = \pi R^2$. Hence, the number of states in the entire Landau level is

$$\mathcal{N} = \frac{\Phi}{\Phi_0} = \frac{A}{2\pi l_B^2} = m(N-1),$$

which correctly reproduces the required filling fraction $\nu \approx 1/m$.

Another useful check we can perform on the Laughlin ansatz, is to verify that it agrees with the expected wave function for a fully-filled Landau level. The many-body wave function for N non-interacting electrons is given by the *Slater determinant*. Applying this to the LLL wave functions of the electrons

$$\psi_{\text{LLL},m}(z) \propto z^{m-1} e^{-|z|^2/4l_B^2}, \quad m = 1, \dots, N,$$

yields the general form of the many-body LLL wave functions, with the function $\tilde{\psi}$ given by the *Vandermonde determinant*

$$\tilde{\psi}(z_i) = \begin{vmatrix} z_1^0 & z_2^0 & \cdots & z_N^0 \\ z_1^1 & z_2^1 & \cdots & z_N^1 \\ \vdots & \vdots & \ddots & \vdots \\ z_1^{N-1} & z_2^{N-1} & \cdots & z_N^{N-1} \end{vmatrix} = \prod_{i < j} (z_i - z_j),$$

which indeed corresponds to the Laughlin ansatz for $\nu = 1$.

Numerically, the Laughlin wave function agrees well with the ground state for few particles. For many particles, it is expected to diverge wildly [103]. However, the Laughlin ansatz remains in the same *universality class* as the true ground state, which means it retains the same topological properties. In fact, the Laughlin states have the properties of a new phase of matter, with topological order and fractional statistics¹⁴. It is this feature of the Laughlin wave function, rather than precise agreement with certain configurations, that makes the ansatz so intriguing.

3.4.3 Laughlin excited states

Building on this, we now consider excitations of the LLL Laughlin wave function. The excitations may be categorized into two forms: neutral excitations and charged excitations.

Neutral excitations come in form of collective *density waves*, where the density of the electrons ripples through space; reminiscent of phonons in superfluids [125]. However, these collective excitations do not vanish with the momentum, due to the incompressibility of the states. In analogy with superfluids, the minimum of the dispersion relation of the collective modes is known as the *magneto-roton* [125]. It is even possible to observe more than one minimum, at more unusual filling fractions [105].

Charged excitations may be categorized into *quasi-holes* and *quasi-particles*. For example, consider a quasi-hole at position $\eta \in \mathbb{C}$. We require that the electron density vanishes

¹⁴In simple cases, Laughlin states may be thought of as a Fermi liquid, with a competing solid phase known as the *Wigner crystal*. However, the solid phase is only observed at sparse filling $\nu \leq 1/7$ [103].

at the point η . Hence the simplest way to introduce M quasi-holes into the system of N electrons is to write

$$\tilde{\Psi}_{\text{holes}}(z_i; \eta_j) = \prod_{j=1}^M \prod_{i=1}^N (z_i - \eta_j) \prod_{k<l} (z_k - z_l)^m. \quad (3.15)$$

Alternatively, consider placing all M quasi-holes at the same point η such that

$$\tilde{\Psi}_{\text{holes}}(z_i; \eta) = \prod_{i=1}^N (z_i - \eta)^m \prod_{k<l} (z_k - z_l)^m.$$

This wave function now describes the absence of an electron at η . Hence, m holes is the equivalent to the deficit of a single electron and so holes are considered to have fractional charge $e^* = e/m$. Conversely, the charged excitations described by quasi-particles carry charge $e^* = -e/m$.

Naturally, the fractional charge carried by these excitations does not contradict any physical laws because the total charge in a sample will always be an integer multiple of e . However, within the sample, these fractionally charged objects act as independent particles. This has been measured experimentally using shot-noise experiments [126].

We can apply the concept of fractionally charged excitations to re-derive the Hall conductivity. The simplest method is to consider the Corbino ring geometry with central flux $\Phi(t) = 0 \rightarrow \Phi_0$. As the flux is adiabatically increased, spectral flow is induced so that, by the end of the process, the angular momentum of the electrons is increased by one quantum. Therefore, the new wave function is obtained by multiplying through by $\prod_i z_i$. In the limit of vanishing radii, this yields the quasi-hole wave function with a quasi-hole at the origin. Hence, during this process a quasi-particle is transferred from the inner to outer ring. Therefore, a whole electron is only transferred when the flux is increased to $m\Phi_0$, which implies that

$$\sigma_{xy} = \frac{e^2}{h} \nu,$$

where the filling factor is given by $\nu = 1/m$, as expected.

As in the IQHE, it is natural now to perform Berry analysis on these charged excitations. Considering a fractional quantum Hall system with N electrons and M quasi-holes, described by the wave function in Eq. 3.15, the Berry connection [103] may be evaluated as

$$\mathcal{A}_{\eta_i} = -\frac{i}{2m} \sum_{j \neq i} \frac{1}{\eta_i - \eta_j} + \frac{i\bar{\eta}_i}{4ml_B^2}. \quad (3.16)$$

Fractional charge

We are now in the position to compute the charge of these quasi-holes. Consider a quasi-hole which is taken on a closed path Γ in position space, which does not enclose any other quasi-holes. In this case, only the second term in Eq. 3.16 contributes to the Berry phase, and so we find that

$$U(t) = \exp \left(-i \oint_{\Gamma} (\mathcal{A}_{\eta} d\eta + \mathcal{A}_{\bar{\eta}} d\bar{\eta}) \right) = e^{ie^* \Phi / \hbar},$$

where $e^* = e/m$. Notice that this corresponds to the Aharonov-Bohm phase of a particle with charge e^* .

Fractional statistics

Consider now that the closed path Γ taken by the quasi-hole η_1 encloses one other quasi-hole η_2 . In this case, both terms in Eq. 3.16 contribute to the Berry phase. As we have already seen, the second term yields the Aharonov-Bohm phase. However, the first term yields

$$U_1(t) = \exp \left(-\frac{1}{2m} \oint_{\Gamma} \frac{d\eta_1}{\eta_1 - \eta_2} + \text{H.c.} \right) = e^{2\pi i/m}.$$

Hence, the phase picked up by exchanging two quasi-holes is $e^{2\pi i \alpha_s}$ with $\alpha_s = 1/m$. In conclusion, quasi-charges obey Abelian anyonic¹⁵ statistics with statistical parameter $\alpha_s = 1/m$.

Topological order

Now, let us consider a quasi-particle–quasi-hole pair on a spatial torus. We apply the translation operator T_1 to the quasi-particle and T_2 to the quasi-hole, so they both end up in the same place. Since both quasi-charges are anyons, the translation operators must obey

$$T_1 T_2 = e^{2\pi i/m} T_2 T_1,$$

yet this is incompatible with a unique ground state. Hence, the Laughlin ground state must be m -fold degenerate, simply due to the topology.

Laughlin states, therefore, can be characterized as a new type of matter with *topological order*. This paradigm is centered around characterizing states based on their ground-state degeneracy and operator algebra.

¹⁵See Appendix A.2 for further details.

3.4.4 Non-Laughlin states

This section is based on the notes by Tong [103] and the books by Jain [105] and Fradkin [119]. The original paper is by Haldane [127]. Haldane was awarded the Nobel Prize in Physics 2016 for his contribution to the field [11].

In the Corbino ring example from Sec. 3.4.3, we saw how increasing the flux through the flux tube creates a quasi-particle and reproduces the expected Hall conductivity at $\nu = 1/m$ filling. Consider now a change in the external magnetic field, so that we move away from $\nu = 1/m$ filling. We find that when the system is close to Laughlin filling, the quasi-particles themselves are able to form quantum Hall systems. This in turn produces secondary quasi-particles, which are also able to form quantum Hall systems, ad infinitum.

In the Laughlin wave function, the choice of m being odd was motivated by Fermi-Dirac statistics. Quasi-particles, however, obey anyonic statistics with a statistical parameter α_s . In order to preserve these statistics, the Laughlin ansatz must therefore take the form

$$\tilde{\psi} = \prod_{i < j} (\eta_i - \eta_j)^{2p + \alpha_s}, \quad p \in \mathbb{Z}^+.$$

Around the Laughlin state, we have $\alpha_s = \pm 1/m$ for quasi-holes and quasi-particles, respectively. The maximum momentum of a quasi-charge is $N(2p + \alpha_s)$, which implies a radius of $R \approx \sqrt{N(2p + \alpha_s)} ml_B$. The area of the droplet is therefore $A = \pi R^2 = 2\pi(2p + \alpha_s)N(ml_B^2)$. Since electrons are composed of m quasi-charges, the total number of quasi-charges is

$$N_{\text{quasi}} = m \frac{\Phi}{\Phi_0} = \left(2p \pm \frac{1}{m}\right) m^2 N \Rightarrow \nu_{\text{quasi}} = \mp \frac{1}{2pm^2 \pm m},$$

where the top sign is for quasi-holes and the bottom sign for quasi-particles. Hence, the total filling fraction is the sum of the filling fraction due to the electrons ($\nu = 1/m$) and the filling fraction due to the quasi-charges:

$$\nu_{\text{total}} = \frac{1}{m \pm \frac{1}{2p}}.$$

Assuming that these quasi-charges themselves form quantum Hall states, and their secondary quasi-charges do the same ad infinitum, the total filling fraction is

$$\nu_{\text{total}} = \frac{1}{m \pm \frac{1}{2p_1 \pm \frac{1}{2p_2 \pm \dots}}}. \quad (3.17)$$

This continued filling fraction reproduces the vast majority of observed fractional quantum Hall states [127].

3.4.5 Composite fermion theory

In this section, we introduce an alternative interpretation of fractional quantum Hall physics, inspired by the Laughlin ansatz, which allows us to reproduce the sequence in Eq. 3.17 and also explain more exotic states [105, 128].

Let us introduce a *vortex* which represents the winding in the phase of a wave function. For example, consider the factor $\prod_i (z_i - \eta)$ in the quasi-hole wave function. Naturally, this gives the wave function zero charge at η . However, there is also an angular dependence, which means that the phase of the wave function changes by 2π as any particle wraps around η . In this way, the quasi-hole may be interpreted as a vortex. In general, the quasi-charges may be interpreted as vortices.

The Laughlin wave function for electrons comes with a pre-factor $\prod_{i < j} (z_i - z_j)^m$, where m is odd. We justified this choice in Sec. 3.4.2 by saying that the wave function goes to zero when two electrons are close together or far apart. However, note that this choice does not just give us one zero as the electrons are brought close together, it gives us m . One of the zeros may be attributed to the Pauli exclusion principle, and so we can interpret this as each electron carrying one vortex by default. The other $m - 1$ zeros are open to interpretation, and we denote them as $k \equiv m - 1$ (not to be confused with momentum).

Let us define a *composite fermion* to be an electron-vortex pair bound to k further vortices. The electrons therefore carry an extra emergent flux with them, due to the vortices. This is known as *flux attachment*, and is completely separate to the background magnetic flux [129, 130].

Jain states

Let us consider a quantum Hall system with a composite fermion density n_{CF} . As before, we may now perform our usual Berry analysis. We take the composite fermion on a closed path

Γ , which encloses an area A . The Berry phase is

$$U(t) = \exp \left(2\pi i \left(\Phi / \Phi_0 - \underbrace{kn_{\text{CF}}A}_{\text{vortices contribution}} \right) \right),$$

where Φ / Φ_0 corresponds to the usual Aharonov-Bohm contribution. In Sec. 3.4.3, when we found an unusual Berry phase for the quasi-charges, we interpreted this as an Aharonov-Bohm phase with an effective fractional charge for the quasi-charges. In composite fermion theory, we interpret the unusual Berry phase as an Aharonov-Bohm phase with an effective magnetic field $B^* = B - kn_{\text{CF}}\Phi_0$, for the composite fermions. The composite fermion density is manifestly equivalent to the electron density, however they experience different magnetic fields, and hence different filling fractions, r , in this interpretation. This yields the equality

$$\frac{rB^*}{\Phi_0} = \frac{\nu B}{\Phi_0},$$

which may be rearranged into the form

$$\nu = \frac{r}{kr + 1}. \quad (3.18)$$

Notice that a composite fermion filling fraction of one, corresponds to the Laughlin filling fraction for electrons. Hence, the FQHE may be interpreted as an IQHE for composite fermions. Indeed, the Laughlin ansatz may be factorized into fully-filled LLL and flux attachment factors, such that $\tilde{\Psi} = \prod_{k < l} (z_k - z_l) \prod_{i < j} (z_i - z_j)^k$.

Building on this, we now examine the higher IQHE states for composite fermions. In the case of $m = 3$, this yields the same sequence of filling fractions as we observed in Eq. 3.17. Motivated by this, we write down a new ansatz for the wave function in terms of composite fermions:

$$\tilde{\Psi}_\nu(z) = P_{\text{LLL}} \left[\prod_{i < j} (z_i - z_j)^k \Psi_{\nu^*}(z) \right] P_{\text{LLL}},$$

where P_{LLL} is the LLL projection operator and Ψ_{ν^*} is the composite fermion wave function for integer filling. These are known as *Jain states*.

One of the main successes of composite fermion theory is an explanation for why there are no observed plateaus at half filling [131]. In this case $m = 2$ and $n = B/2\Phi_0$, which implies that the composite fermions do not experience any effective magnetic field: $B^* = 0$.

3.5 Fractional Chern Insulators

This section is based on the reviews by Parameswaran et al. [132], Neupert et al. [133], and Bergholtz [134]; and the presentation by Neupert [135]. The prominent paper is by Regnault & Bernevig [136].

As opposed to Chern insulators which have fully-filled Landau-levels, as we saw in Sec. 3.3.2, *fractional Chern insulators* (FCIs) have fractionally-filled Landau levels. In general, FCIs may be defined as two-dimensional lattice systems of interacting particles whose gapped many-body ground states, in the Landau-limit, share the same universal topological properties of the FQHE. These properties include:

- quantized fractional Hall conductivity,
- universal quasi-particle excitations,
- topological ground-state quasi-degeneracy given by $\nu^{-g_{\text{gs}}}$, where g_{gs} is the genus of the ground-state manifold [132].

In this case, the Landau-level limit requires flat bands and unit Chern number¹⁶. However, the main advantage of FCIs is that, away from the Landau-level limit, they generalize the Hamiltonians of the FQHE to lattice-based systems [138].

3.5.1 Motivation

There are three main motivations for the study of FCIs:

1. In order to properly understand the mechanism of the FQHE, we need to uncover the *universal* features specific to the topological phases. FCIs have much less symmetry than Landau-level Hamiltonians or Laughlin wave functions, for example. Therefore, they can be tuned to **discern the true topological properties of the FQHE**.
2. FQHE states are interesting because they allow for non-Abelian anyon braiding, which may potentially be used to construct topological quantum computers [139]. From an experimental perspective, it would be advantageous to be able to produce these states in **common operating conditions**. Chern insulators already have the advantage that they exhibit these phenomena without the need for a strong magnetic field [134]. Furthermore, the energy scales in FCIs are predicted to be large, and so we could also potentially produce FQHE states at room temperature [135].

¹⁶This is independent of whether the FCI is in an external magnetic field (producing *Hofstadter bands* [101]) or in the absence of an external magnetic field (producing *Haldane bands* [137]).

3. At full magnetization and half filling, FCIs spontaneously exhibit the anomalous quantum Hall effect, which could be used to produce **highly efficient room-temperature conductors** [133]. Naturally, the measured conductivity would be lower than that of comparable superconductors. However, the relaxed operating conditions make FCIs an attractive option.

3.5.2 Numerical techniques

The discovery of FCIs was predominantly due to numerical exact diagonalization [136]. As mentioned in Sec. 3.4.1, the degeneracy of the ground states in FQHE systems is so high that perturbation theory can only be performed numerically, and even then only for a relatively small number of particles (see Chapter 4). These restrictions meant that observing FCI states, and furthermore verifying the FCI states, was a formidable numerical challenge. As a result, several numerical techniques developed, which are now widely used to study FCIs [140–142]. The general procedure is to exactly diagonalize the flat-band Hamiltonian for a small number of particles, and carefully extrapolate the results to the case for large particle number: the *thermodynamic limit*.

There are a wide variety of checks that can be performed to verify the existence of fractional quantum Hall (FQH)-like states in FCIs, including the following facts [132]:

- FQH states are usually incompressible liquids, therefore the particle densities should be uniform.
- The overlap of the FCI ground state with particular FQH wave functions should be close to unity.
- Adiabatic continuity between FQH Hamiltonians, which are the ground states of model pseudopotential Hamiltonians, and the numerical Hamiltonian is sufficient to determine topological order.
- The fractional statistics of quasi-particle excitations in FQH systems follows a generalized Pauli exclusion principle, which influences the spectrum of low-lying eigenstates.

There are numerous further checks which can be performed, however, we shall focus on the following two in more detail.

Spectral flow

Spectral flow was one of the first of the techniques employed to verify topological states in FCIs [136, 143]. Consider a FQH system on a spatial torus in the thermodynamic

limit¹⁷. This system has a quasi-degenerate ground-state manifold, with a many-body wave function that converges to a constant value in the thermodynamic limit. From Sec. 3.3.2, we know that if we insert a flux tube through the hole in the torus, the system exhibits spectral flow. Numerically, this can be achieved by diagonalizing the Hamiltonian with twisted-phase boundary conditions. Hence, we expect to see that if the ground states are indeed topologically ordered, then they should flow into each other as we twist the boundary conditions. Furthermore, this spectral flow should be periodic. Using this data, a Hall conductance can also be computed, which should match that of the FQH system [132].

Entanglement

A more sophisticated technique that is now widely used is the analysis of the ground-state particle entanglement. The resulting particle entanglement spectra reveal many aspects of underlying topological phases [134].

Consider a wave function $|\psi\rangle \in \mathcal{H}$. If we split the Hilbert space $\mathcal{H} = \mathcal{H}_A \otimes \mathcal{H}_B$, such that the particle number is divided into subspaces A and B , then the wave function has a Schmidt decomposition

$$|\psi\rangle = \sum_{k,n} \lambda_{k,n} |\psi_{k,n}^A\rangle \otimes |\psi_{k,n}^B\rangle,$$

where $\lambda_{k,n} > 0$ are the Schmidt coefficients. The (von Neumann) entropy may therefore be written as

$$S_{\text{vN}} = -\sum_{\alpha} \lambda_{\alpha}^2 \ln \lambda_{\alpha}^2 \equiv \sum_{\alpha} \lambda_{\alpha}^2 \xi_{\alpha},$$

where the entanglement energy is defined as $\xi \equiv -\ln \lambda^2$.

In most cases, the insight gained from the entanglement energy spectrum and the entanglement entropy are equivalent. However, the entanglement spectra may show additional information provided that the splitting of the Hilbert space commutes with a fundamental symmetry of the system [132]. As we shall see in Chapter 4, it also proves useful to compute the entanglement spectra to check for topological order and verify how close a state lies to the Landau level continuum.

3.5.3 Generalizing the FQHE

As mentioned before, the special property of FCIs is not simply that we can recover FQH physics, but rather that we can generalize it. In this section, we discuss how the FQH states persist even when the band structure deviates significantly from the Landau-level limit.

¹⁷A spatial torus is considered, since FQHE bands on a spatial torus are directly comparable to Chern bands on a spatial lattice [132].

To begin, we summarise the Landau limit as

$$\text{Landau-level limit} \Rightarrow \begin{cases} g_{\mu\nu}(\mathbf{k}) = \text{const.}, \\ \mathcal{A}_{\mu\nu}(\mathbf{k}) = \text{const.}, \\ \varepsilon(\mathbf{k}) = \text{const.}, \\ |C| = 1, \end{cases}$$

where $g_{\mu\nu}$ is the Fubini-Study metric¹⁸, and $\varepsilon(\mathbf{k})$ is the energy dispersion of a Chern band. It has been shown that any of these four properties can be significantly violated in FCIs and the FQHE still holds [133].

1. $g_{\mu\nu}(\mathbf{k}) \neq \text{const.}$ and $\mathcal{A}_{\mu\nu}(\mathbf{k}) \neq \text{const.}$ Numerous theories which support stable FCI phases have zero Fubini-Study metric or Berry connection for some momentum values [133]. This implies that there are strong fluctuations present in the curvature and metric.
2. $\varepsilon(\mathbf{k}) \neq \text{const.}$ The Chern band under consideration does not, in fact, need to be flat or energetically isolated to exhibit fractional statistics. FCIs prevail simply if the interactions are large in comparison to the bandwidth, regardless of the exact nature of the band spectrum [144, 145].
3. $|C| > 1$ FCIs have been observed in bands with higher Chern number [138]. In these cases, the states occur at filling factors

$$\nu = \frac{r}{kr|C| + 1}, \quad r \in \mathbb{Z},$$

where $k = 1, 2$ for fermions and bosons, respectively, and r corresponds to the number of filled composite fermion bands¹⁹. These states are not analogous to Landau-level states, which have $|C| = 1$. In fact, they are even distinct from multi-layer FQH states due to their modified exclusion statistics. Furthermore, FCIs can also arise in bands with zero Chern number [133].

¹⁸The quantum geometry of a Chern band is characterized by its Fubini-Study metric and Berry connection. The precise form of the quantum geometry is derived by identifying the projected density algebra as the Girvin-MacDonald-Platzman algebra. See the review by Parameswaran for a full derivation [132].

¹⁹This is the higher Chern band generalization of Eq. 3.18.

Chapter 4

Stability of Fractional Chern Insulators in the Effective Continuum Limit of Harper-Hofstadter Bands with Chern Number $|C| > 1$

We study the stability of composite fermion fractional quantum Hall states in Harper-Hofstadter bands with Chern number $|C| > 1$. From composite fermion theory, states are predicted to be found at filling factors $\nu = r/(kr|C| + 1)$, $r \in \mathbb{Z}$, with $k = 1$ for bosons and $k = 2$ for fermions. Here, we closely analyze these series in both cases, with contact interactions for bosons and nearest-neighbor interactions for (spinless) fermions. In particular, we analyze how the many-body gap scales as the bands are tuned to the effective continuum limit of Chern number $|C|$ bands, realized near flux density $n_\phi = 1/|C|$. Near these points, the Hofstadter model requires large magnetic unit cells that yield bands with perfectly flat dispersion and Berry curvature. We exploit the known scaling of energies in the effective continuum limit in order to maintain a fixed square aspect ratio in finite-size calculations. Based on exact diagonalization calculations of the band-projected Hamiltonian for these lattice geometries, we show that for both bosons and fermions, the vast majority of finite-size spectra yield the ground-state degeneracy predicted by composite fermion theory. For the chosen interactions, we confirm that states with filling factor $\nu = 1/(k|C| + 1)$ are the most robust and yield a clear gap in the thermodynamic limit. For bosons with contact interactions in $|C| = 2$ and $|C| = 3$ bands, our data for the composite fermion states are compatible with a finite gap in the thermodynamic limit. We also report new evidence for gapped incompressible states stabilized for fermions with nearest-neighbor interactions in $|C| > 1$ bands. For cases with a clear gap, we confirm that the thermodynamic limit commutes with the effective

continuum limit within finite-size error bounds. We analyze the nature of the correlation functions for the Abelian composite fermion states and find that the correlation functions for $|C| > 1$ states are smooth functions for positions separated by $|C|$ sites along both axes, giving rise to $|C|^2$ sheets; some of which can be related by inversion symmetry. We also comment on two cases which are associated with a bosonic integer quantum Hall effect (BIQHE): For $\nu = 2$ in $|C| = 1$ bands, we find a strong competing state with a higher ground-state degeneracy, so no clear BIQHE is found in the band-projected Harper-Hofstadter model; for $\nu = 1$ in $|C| = 2$ bands, we present additional data confirming the existence of a BIQHE state.

4.1 Introduction

New realizations of artificial gauge fields can be achieved by light-matter coupling in cold atoms [146–153], by more general Floquet systems with periodically modulated Hamiltonians [154–156], or possibly by exploiting spin-orbit coupling in two-dimensional materials [157, 158]. In conjunction with repulsive interactions, they provide exciting opportunities to observe interesting flavors of fractional quantum Hall physics [159–164]. The recurring motif in these systems, called “fractional Chern insulators” (FCIs) [165], is the existence of topological flat bands with nonzero Chern numbers that mimic the topological properties of the lowest Landau level (LLL) of particles in a magnetic field [158, 165–172]. Although, for unit Chern number, the physics of FCIs is continuously connected to Landau level physics [173–175], this connection is no longer possible for $|C| > 1$, resulting in a series of *lattice-specific* fractional quantum Hall states [160–163]. Furthermore, FCIs in higher Chern number bands have the potential for exotic physical phenomena, such as hosting lattice defects carrying non-Abelian statistics [176–178].

The Harper-Hofstadter model [179–181] has played a special role in the study of quantum Hall effects. It was the first model in which the Chern number was identified as the topological invariant determining the quantization of the Hall conductance in integer quantum Hall states [182]. The first theory of FCIs, or fractional quantum Hall states on lattices, was formulated by Kol and Read in the context of the Hofstadter model [159], generalizing early notions [183–185] and using the framework of composite fermion theory [186]. Furthermore, the Hofstadter model has provided the basis for the first proposals for FCIs in optical lattice realizations of cold atomic gases [160, 161, 187, 188]. More recently, the Hofstadter model represents one of the first examples for experimental realizations of artificial gauge fields in cold atomic gases [147, 148, 150, 189], although access to highly entangled low-temperature phases will require further advances in cooling or adiabatic state preparation [190–192].

The Harper-Hofstadter model provides bands of any Chern number $C \in \mathbb{Z}$, with varying magnitudes of the single-particle gap. In this model, it is well understood how to construct isolated Chern bands of any Chern number that can support fractional quantum Hall liquids [163]. However, numerical studies have been challenging, since finite-size systems have to simultaneously satisfy several integer relations between the number of particles, the number of flux quanta and the number of sites – which are incommensurable in general. Hence, having chosen a specific flux density and filling factor, one is led to study a series of systems with varying aspect ratios. Here, we would instead like to take a proper two-dimensional thermodynamic limit for the system while keeping the aspect ratio fixed and square, since it is expected that square Hofstadter lattices are especially stable [193]. It is possible to identify finite-size geometries which are exactly or almost square, by considering large magnetic unit cells (MUCs) [163, 194]. Moreover, the limit of large MUCs is appealing, as it provides Chern bands with a flat dispersion and additionally a perfectly flat band geometry [163, 194]. Hence, the Hofstadter model allows one to optimize the criteria of band flatness and flat geometry, shown to be correlated with the stability of fractional Hall liquids for the $|C| = 1$ cases [194–200]. We refer to the limit of $n_\phi \rightarrow 1/|C|$ as the effective continuum limit, to distinguish it from the continuum limit $n_\phi \equiv p/q \rightarrow 0$. The continuum limit is expected to exist, as $n_\phi \rightarrow 0$ implies that the magnetic length $\ell_0 \gg a$, where a is the lattice constant, so the discreteness of the lattice should be irrelevant and the continuum physics is recovered. For our numerical analyses, we further define the thermodynamic (effective) continuum limit as the (effective) continuum limit subsequently taken to large particle number ($N, q \rightarrow \infty$).¹

In this chapter, we study the stability of quantum Hall states of the Abelian composite fermion series $\nu = r/(|kC|r + 1)$ [163], with $k = 1(2)$ for bosons (fermions), in Chern bands with $|C| = 1, 2, 3$ in the Hofstadter model, focusing on finite-size square systems. To find such configurations, we vary the flux density while moving within a series of single-particle bands with fixed Chern number, allowing us to find finite-size configurations with an aspect ratio of (approximately) one, as well as matching a target filling factor. The results from such different realizations of Chern bands can be combined into a single measure for the stability of the phase, owing to the known scaling of the many-body gap with the number of sublattices [194].

The ground-state degeneracy of these states agrees with the predictions of composite fermion theory. As expected, we find that states with filling factor $\nu = 1/(k|C| + 1)$ are the most robust, with the effective continuum limit remaining approximately independent of N and inversely proportional to $|C|$. Our results show considerable finite-size effects for

¹The (effective) continuum limit at fixed aspect ratio is denoted as $\lim_{N, q \rightarrow \infty}(q\Delta) = \lim_{N \rightarrow \infty}(\lim_{q \rightarrow \infty}(q\Delta))$, and is distinguished from the limit at fixed flux density: $\lim_{q, N \rightarrow \infty}(q\Delta) = \lim_{q \rightarrow \infty}(\lim_{N \rightarrow \infty}(q\Delta))$.

most other filling fractions, leaving the behavior in the thermodynamic limit indeterminate. While taking the thermodynamic effective continuum limit does not generally alleviate these finite-size effects, we find some system sizes where competing states are eliminated when square geometries are considered.

To further characterize the target composite fermion states or their competing phases, we analyze their two-particle correlation functions, and for select examples also their particle entanglement spectra (PES). In our microscopic model, we find that correlation functions are modulated with a period of $|C|$ sites along both the x- and y-axes of the square Hofstadter model, yielding the visual appearance of $|C|^2$ smooth correlation functions.

This chapter is organized as follows: In Sec. 4.2, we introduce the Harper-Hofstadter Hamiltonian and explain how to obtain finite-size geometries with approximately square aspect ratio for the desired filling factors. In Sec. 4.3, we present our numerical evidence for FCI phases of bosons in $|C| = 1, 2, 3$ Hofstadter bands and fermions in $|C| = 1, 2$ Hofstadter bands, including many-body spectra, ground-state correlation functions, and particle entanglement spectra. In Sec. 4.4, we comment on the overall trends regarding the thermodynamic effective continuum limits and analyze the role that the Chern number plays in the scaling. Finally, in Sec. 4.5, we provide conclusions on the stability of FCI phases in the effective continuum limit of $|C| > 1$ Harper-Hofstadter bands and suggest avenues for future research.

4.2 Model

4.2.1 Single-particle Harper-Hofstadter Hamiltonian

The single-particle Hamiltonian for the Harper-Hofstadter model [179] was obtained as the tight-binding representation of a single-orbital lattice model subject to Peierls' substitution for a homogeneous magnetic field $\mathbf{B} = B\hat{\mathbf{e}}_z$ (with $\mathbf{B} = \nabla \times \mathbf{A}$), giving²

$$H_0 = - \sum_{i,j} t_{ij} e^{i\phi_{ij}} c_j^\dagger c_i + \text{H.c.}, \quad (4.1)$$

with complex hoppings of phase ϕ_{ij} relating to the vector potential \mathbf{A} such that

$$\phi_{ij} = \frac{e}{\hbar} \int_{\mathbf{r}_i}^{\mathbf{r}_j} \mathbf{A} \cdot d\mathbf{l} + \delta\phi_{ij}. \quad (4.2)$$

In the Landau gauge $\mathbf{A} = Bx\hat{\mathbf{e}}_y$, and for rational flux density $n_\phi = Ba^2 = p/q$ (with p and q coprime), the phases ϕ_{ij} naturally repeat under translations $T_{qa\hat{\mathbf{e}}_x}$ by $qa\hat{\mathbf{e}}_x$, and also under

²The hopping parameters are given as $t_{ij} \equiv 1$ for nearest-neighbor bonds, and zero otherwise.

the translation $T_{a\hat{e}_y}$. This corresponds to a MUC of $q \times 1$ sites. (For simplicity, we set $a = 1$, below.) However, other choices for MUC geometries $l_x \times l_y = q$ with the same area can be made, and thus enclosing the same number of magnetic flux quanta. These choices correspond to a gauge freedom in the problem, encoded in terms of additional phase factors $\delta\phi_{ij}$ occurring in the tight-binding model. These phase factors can be thought of as an additional phase generated by magnetic translations for hopping terms crossing the MUC boundary, or alternatively the tight-binding parameters can be expressed in terms of a vector potential in a periodic gauge, with $\mathbf{A}(\mathbf{r} + l_\mu \hat{\mathbf{e}}_\mu) = \mathbf{A}(\mathbf{r})$ [201]. For an explicit construction of the periodic gauge, see Appendix B.1. We further note that the choice of the MUC affects the definition of the momenta for single-particle eigenstates, and in Appendix B.2, we provide an additional note expanding on how the states are remapped throughout the Brillouin zone under such gauge transformations.

Within the Hofstadter spectrum, band gaps of any cumulative Chern number can be found. In order to facilitate our numerical work, we closely examine specific flux densities at which the lowest band has Chern number $|C|$ and remains well separated from higher excited bands of the Harper-Hofstadter model. Following Möller and Cooper [163], such cases are realized when the density of states $n_s(n_\phi = p/q) = 1/q$, corresponding to flux densities

$$n_\phi = \frac{p}{|C|p - \text{sgn}(C)} \equiv \frac{p}{q}, \quad p \in \mathbb{N}. \quad (4.3)$$

In this chapter, we will focus on the cases (Eq. 4.3) in the limit of large q and consider flux densities in the close vicinity of points $n_\phi = 1/|C|$. At other nearby flux densities, we would find a low-energy manifold made up of several bands with the same cumulative Chern number C . However, we do not explore such cases here in order to maximize the number of k points in the Brillouin zone in our numerics.

4.2.2 Hofstadter models and Chern insulators

Given some hesitations in the literature, let us discuss whether (partially) filled bands of the Harper-Hofstadter Hamiltonian (Eq. 4.1) should be considered (fractional) Chern insulators. One of the superficial reasons why Chern insulators might be dissociated from the Harper-Hofstadter model is that the latter represents a homogeneous magnetic field, or constant flux per plaquette, while the former is simply defined as having bands with finite Chern numbers arising from complex hopping phases. It could further be argued that the Hofstadter model is characterized by a finite flux per MUC, while the flux averages to zero in Chern insulators like the Haldane model [166]. However, in existing cold-atom realizations of the Hofstadter model, there is no physical magnetic field present – rather, these experiments

realize the model directly as a tight-binding lattice with complex hopping terms induced by laser-assisted hoppings or more general time-modulated Floquet-Hamiltonians [152, 202] in order to mimic the Aharonov-Bohm effect of a magnetic field.

The overall flux threading the lattice is also not a good distinction of Hofstadter models from generic cases, given that flux is defined only modulo the flux quantum Φ_0 in a lattice geometry and so any integer number of flux quanta can be inserted within a given plaquette of the lattice without altering the physics. A finite-size realization of the Hofstadter model requires an integer number of flux quanta per MUC; thus it can always be interpreted as a model without net flux: Any excess flux can be neutralized by adding an opposite flux through one of the plaquettes in a unit cell [203]. Indeed, one could argue that any finite-size implementation of the complex hopping phases (Eq. 4.2) that is compatible with periodic boundary conditions effectively corresponds to such an insertion of neutralizing flux, which gives rise to the $\delta\phi_{ij}$ term in Eq. 4.2.

Comparing the translational symmetries of Hofstadter models with other general tight-binding models with Chern bands [158, 165, 168, 169], we can finally find one formal distinction between these cases. The translational symmetry group of the Harper-Hofstadter Hamiltonian is smaller than the translation symmetry of the underlying lattice potential due to the commensurability of the two length scales in the problem. By contrast, generic models typically have a full translational symmetry group identical to that of the lattice potential. Inversely, we could say that the translational symmetry group of the Hofstadter lattice can be enhanced if we allow simultaneous translations and gauge transformations (effectively translating the origin of the MUC), while no additional symmetries can be found in generic models.

As the terminology of (fractional) Chern insulators focuses on the topological properties, it seems natural to include those states realized in the Chern bands of the Hofstadter model. Conversely, since the Hofstadter model is closely related to physical magnetic fields, the terminology of lattice fractional quantum Hall states is also appropriate for these models.

4.2.3 Many-body Hamiltonian

We study the many-body physics of interacting particles in the Harper-Hofstadter model, described by the Hamiltonian

$$H = H_0 + P_{\text{LB}} \left[\sum_{i < j} V(\mathbf{r}_i - \mathbf{r}_j) : \rho_i \rho_j : \right] P_{\text{LB}}, \quad (4.4)$$

where P_{LB} denotes the lowest band projection operator and $:\rho_i\rho_j:$ indicates the normal ordering of the density operators, with site labels i, j .

In this chapter, we extend the work of Möller and Cooper [163] on bosonic contact interactions ($V_{ij} = U\delta_{ij}$) as well as considering the case of fermions with nearest-neighbor (NN) interactions ($V_{ij} = V\delta_{\langle i,j \rangle}$). In both cases, we target a number of known candidate phases for incompressible quantum Hall states.

We explore the spectrum of the many-body Hamiltonian (Eq. 4.4) using exact diagonalization calculations and identify incompressible states by means of their ground-state degeneracy, many-body gap Δ , as well as the correlations and entanglement properties of the corresponding ground-state wave functions. The incompressible phases which we find show a clear quasi-degenerate ground state, such that the gap Δ to the excited states is much larger than the splitting between states in the ground-state manifold or the typical level spacing among higher lying excitations. We quote the gap in units of the interaction strength U (V), implicitly setting $U = V = 1$, below.

4.2.4 Target FCI phases in general Chern bands

Several families of incompressible quantum Hall states have been proposed to occur in Chern bands with higher Chern numbers $|C| > 1$, most importantly including generalizations of the Jain states [162, 204, 205], an Abelian series of states arising from the composite fermion construction [159, 161] and generalizations of the non-Abelian Read-Rezayi states [206] to higher Chern bands [162]. There were also reports of states that simultaneously break translation symmetries while displaying a quantized Hall response [164].

The incompressible character of these phases is expressed by a preferred density of particles, measured in terms of the number density per unit area of accessible single-particle states. While this manifold of single-particle states is trivially given by the continuum Landau levels in continuum fractional quantum Hall states, the relevant low-energy subspace for Chern insulators is set by a single-particle gap of the single-particle dispersion in a tight-binding model that is large compared to the dispersion of the low-lying band(s).

From composite fermion theory, one predicts a series of Abelian quantum liquids [159, 161] at filling factors

$$\nu(k, r, C) = \left| \frac{n}{n_s} \right| = \frac{r}{|kC|r + 1}, \quad (4.5)$$

where k is the number of flux quanta attached to the particles, $|r|$ is the number of bands filled in the composite fermion spectrum, and its sign indicates the relative sign of the

Chern number C^* for the composite fermion band relative to the Chern number C of the low-energy manifold [163]. The states (Eq. 4.5) carry a ground-state degeneracy of $d = |kCr + 1|$ [159, 163].

Where required, we consider a number of other competing phases. Prominently, this includes the states of the bosonic Read-Rezayi series, found at filling factors $\nu = \kappa/2$ in $C = 1$ bands [206] (with $\kappa \in \mathbb{Z}^+$) which carry a ground-state degeneracy $d_{\text{RR}} = \kappa + 1$. The generalizations of the Read-Rezayi states to higher Chern bands [162] do not generically occur at the same filling factors as the composite fermion states in Eq. 4.5, so we do not encounter them explicitly. At sufficiently weak interactions, generically one may find competition with condensed phases [207–210]. These may survive up to large values of the interaction at time-reversal symmetric points of the Hofstadter spectrum, but are likely less competitive elsewhere. Further instabilities include density-wave or crystalline orders. These were found to be stabilized in related time-reversal symmetric flat band models [211], and are generically expected to be among the competing phases in Chern insulator models.

4.2.5 Scaling to the continuum limit at fixed aspect ratio

Finite-size geometries of the square Harper-Hofstadter model are determined by the number of sites in the x - and y -directions N_x, N_y , and the total number of flux quanta N_ϕ piercing the system. Each geometry may allow an additional gauge choice for the shape of the MUC given by l_x and l_y sites, and the number of repetitions L_x and L_y of the MUC within the simulation cell along these axes. In this chapter, we shall be looking at square systems in terms of the total number of sites, hence systems with a unit aspect ratio:

$$R = \frac{N_x}{N_y} = \frac{L_x l_x}{L_y l_y} = 1.$$

Note that the spectra are gauge-invariant and depend only on the total system size, but not on the shape of the MUC. However, the definition of momentum depends on the choice of MUC, as further discussed in Appendix B.2.

We examine the filling factors (Eq. 4.5) for Chern bands $|C| = 1, 2, 3$ with $|r| = 1, 2, 3$ and a finite particle number N set by the available Hilbert space sizes, typically ranging up to about 10–20 particles. For each case, we generate a sample of finite-size systems including all possible square geometries in a specified range of effective flux densities $n_\phi = p/q$ subject to Eq. 4.3. A restriction is placed on the numerator such that $2 \lesssim p \lesssim 1000$, where low p value configurations are excluded because they may correspond to band gaps with a lower Chern number, and the upper bound is determined by the computational cost and numerical accuracy of our calculations of the single-particle spectrum.

For certain cases, the restriction on the numerator of the effective flux density does not yield any square configurations. In these situations, we look for approximately square configurations, with a fixed maximum error $\varepsilon \approx 1\%$ such that

$$\delta R = \left| \frac{N_x}{N_y} - 1 \right| \leq \varepsilon,$$

taking $N_x > N_y$ by convention. In practice, the allowable deviation of the aspect ratio from one is adjusted slightly so that we obtain a comparable sample size, or number of geometries, for each filling factor ν .

In Ref. 194, Bauer et al. undertook a similar study for models with short-range repulsive interactions in the $C = 1$ bands of the Hofstadter model. Using geometric considerations for the Laughlin and Moore-Read states for $N = 8$ particles, they found that the many-body gap scales as $\Delta \sim 1/q$ for bosons and $\Delta \sim 1/q^2$ for fermions. They also found approximate continuum limits for $n_\phi \rightarrow 0$ for the three phases they considered.

As shown below, we find that the (effective) continuum limit is helpful for examining the stability of candidate incompressible Hall states, as it improves the effectiveness of finite-size scaling analyses. For comparison, we also undertake the conventional finite-size scaling at fixed flux density n_ϕ , as previously considered by Möller and Cooper [163]. An extract of our additional data for this thermodynamic limit is shown in Appendix B.3.

4.3 Results

We present results on fractional quantum Hall states in Harper-Hofstadter bands with higher Chern number. However, to establish our methodology, we first review the case of $|C| = 1$ bands. Our results reproduce the known continuum limit, i.e. the well-known quantum Hall physics of the LLL of a homogeneous magnetic field. Our results go beyond previous studies on the Hofstadter lattice in that we study fermionic quantum Hall states in addition to bosonic ones, and we consider the thermodynamic limit in addition to the continuum limit.

4.3.1 FCIs in $|C| = 1$ Harper-Hofstadter bands

Bosonic states

We first review the case of bosons in Chern number $|C| = 1$ bands, which are well known to support fractional quantum Hall states in the continuum LLL [167, 212, 213]. We consider states of the Jain series (Eq. 4.5) with $|C| = 1$, $|r| = 1, 2, 3$ and we restrict ourselves to Hilbert space dimensions $\dim\{\mathcal{H}\} < 10^7$, which typically allows us to consider particle numbers

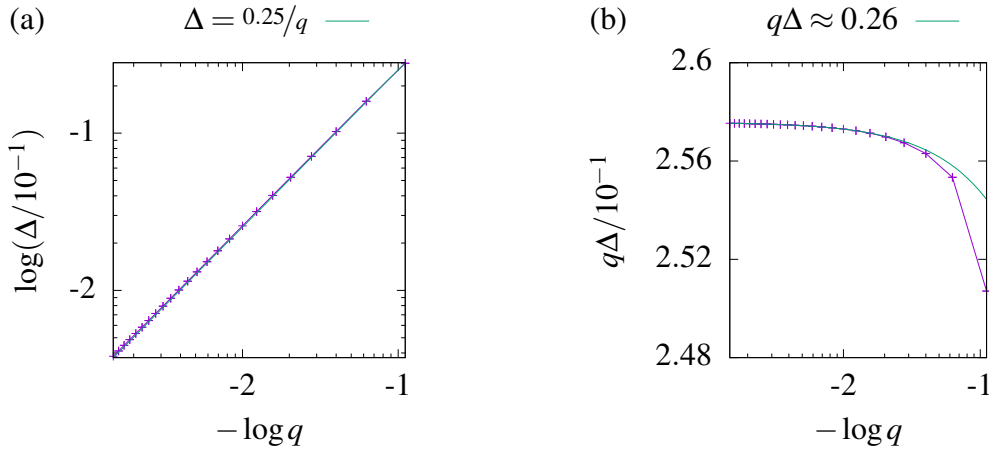


Fig. 4.1 Magnitude of the gap for the bosonic 12-particle $\nu = 3/4$ state in the $|C| = 1$ band, as a function of MUC size, q . (a) Log-log plot of Δ vs q^{-1} . (b) Scaling of $q\Delta$ to a constant value in the continuum limit $n_\phi \rightarrow 0$.

$N \lesssim 12$.³ Furthermore, there are no states corresponding to $r = -1$, as Eq. 4.5 is undefined for this value. Overall, we have considered 24 different combinations of particle size and filling factor, with an average of ~ 38 different geometries for each, giving a total of 921 different exact diagonalization calculations. Apart from exceptional cases that we discuss in detail below, we found that all candidate states show a degenerate ground-state manifold composed of $|krC + 1|$ states, in line with the predictions of composite fermion theory. For each system that we examine, we have plotted the energy gap above the ground-state manifold, Δ , against the MUC size, q , to test whether the expected *reciprocal* scaling [194] is realized. An example scaling for an $r = 3$ state with $\nu = 3/4$ is shown in Fig. 4.1a.

Next, we test the scaling hypothesis and extract the coefficient for $\Delta \propto q^{-1}$ at large MUC size, shown in Fig. 4.1b. For $|C| = 1$, this is the continuum limit. Theoretically, the large- q limit of $q\Delta$ should be independent of q , while finite-size effects imply variations for small q . When establishing the continuum limit, we thus neglect small- q outliers to take account of this fact. Notice that, as a result, the line of best fit in Fig. 4.1a does not exactly correspond to the $q\Delta$ limit in Fig. 4.1b. Using this procedure, we find agreement with the value of the many-body gap for the bosonic Laughlin state calculated by Bauer et al. [194] and we now go beyond their work by considering the thermodynamic limit, as well as the continuum limit, for a large sample of systems.

We collect the continuum limit of $q\Delta$ for the various filling factors under consideration at all available particle numbers ($6 \leq N \lesssim 12$). In Fig. 4.2, we plot how the limiting value $\lim_{q \rightarrow \infty} q\Delta(N, q)$ varies with particle number for each filling factor. We attempt to proceed

³Here we neglect trivially small particle numbers and cases where finite-size effects are clearly dominant.

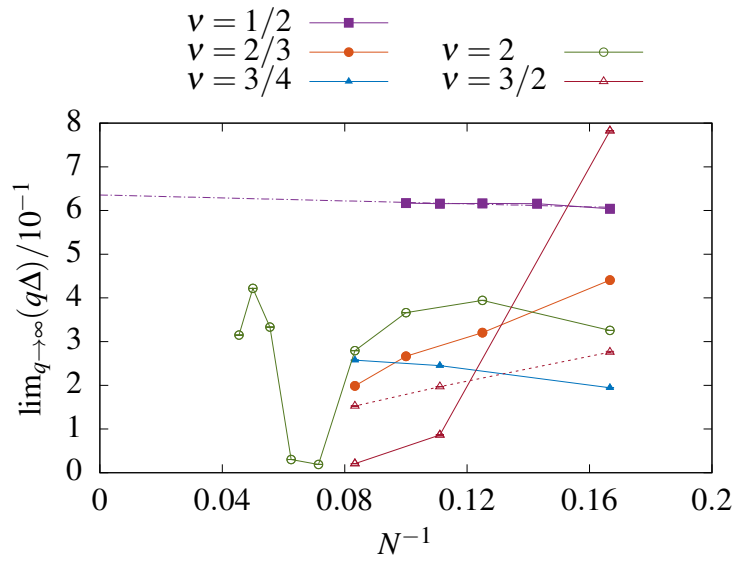


Fig. 4.2 Finite-size scaling of the gap to the thermodynamic continuum limit at fixed aspect ratio, for bosonic states in the $|C| = 1$ band. The extrapolation to the y-axis is shown for the robust $\nu = 1/2$ states. The dashed line for the $\nu = 3/2$ series corresponds to the scaling behavior given a ground-state degeneracy of $d = 4$, as predicted by Read-Rezayi theory. Squares, circles, and triangles denote states with $|r| = 1, 2, 3$, respectively, where the filled (hollow) symbols correspond to positive (negative) r . All of the error bars are smaller than the data points on the scale of the plot.

with a scaling extrapolation to the thermodynamic continuum limit on the basis of an inverse regression for $\lim_{q \rightarrow \infty} q\Delta$ against N^{-1} . Using this approach, we examine, for each filling factor, the $\lim_{q \rightarrow \infty} q\Delta$ limit as $N^{-1} \rightarrow 0$.

Figure 4.2 shows the continuum limits for the five filling factors under consideration. Note that the error bars due to the extrapolation in $q \rightarrow \infty$ are negligible for these points on the scale of the plot. We have also verified that these data agree with many-body gaps of the corresponding states in the continuum LLL on the torus. We include data on a comparison of the correlation functions, below.

The results are insightful in that they illustrate the caveats of interpreting data on finite-size geometries. Composite fermion theory suggests that the stability of states in the Jain series decreases with $|r|$. However, this is only partially borne out by the data.

First, we find that the Laughlin state corresponding to $r = 1$ has the largest gap and has negligible finite-size corrections for the gap in the continuum limit. In this case, we also see close agreement of the limiting value obtained from a finite-size scaling at fixed flux density. The corresponding data are shown in Appendix B.3, Fig. B.1a. We extrapolate a thermodynamic continuum limit of $\lim_{N, q \rightarrow \infty} (q\Delta) = 0.64 \pm 0.01$ in this case, where the error given is the asymptotic standard error in the linear regression¹.

For the next states in the series, we find that the $r = 2$, $\nu = 2/3$ state has a gap that reduces approximately linearly with inverse system size, while the $r = 3$, $\nu = 3/4$ state appears more stable. By contrast, analyses of continuum quantum Hall states in the LLL (on the sphere) show that both of these states are stable and the latter has the smaller gap [213]. Owing to the higher symmetry, continuum calculations enable slightly larger system sizes to be calculated, resulting in more accurate estimates for the gap by including larger system sizes. Note also that we have not considered data beyond Hilbert space sizes of 10^7 for our comprehensive sampling of different geometries, while larger Hilbert spaces can be considered for single cases. Despite the fact that our data are not sufficient to ascertain the size of the gap in the thermodynamic continuum limit for these states, reassuringly, all of our simulations at these filling factors did identify the expected ground-state degeneracies (with $d = 3$ or $d = 4$, respectively) and a clear separation of scales for the gap.

For the states at negative effective flux [214, 215], we see an interesting competition with the Read-Rezayi series, in line with the results for the continuum LLL [167, 216]. The $r = -2$ state is interesting in that it occurs at the integer filling factor $\nu = 2$, so it is a potential example of a bosonic integer quantum Hall effect (BIQHE) [161, 163, 191, 217, 218]. As the BIQHE is not a fractionalized phase, it is associated with a singly degenerate ground state. However, our exact diagonalization calculations show higher ground-state degeneracies for our target Hamiltonian (Eq. 4.4), consisting of onsite repulsions projected to the lowest

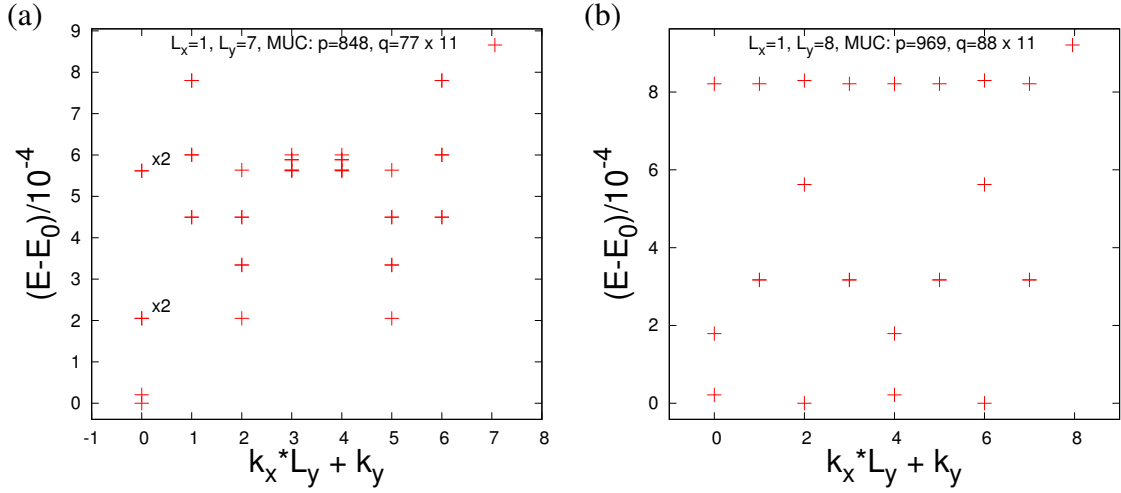


Fig. 4.3 Energy spectra for bosonic states in the $|C| = 1$ band. (a) The 14-particle $\nu = 2$ state with $p = 848$, resolved to $n = 6$ states per sector. (b) The 12-particle $\nu = 3/2$ state with $p = 969$, resolved to $n = 3$ points per sector.

Hofstadter band. In particular, we find ground-state degeneracies of $d_{N=14} = 2$ and $d_{N=16} = 2$ or 6 for the $N = 14$ and $N = 16$ particle systems, respectively, while other system sizes are compatible with an interpretation as a singly degenerate ground state. The $N = 14$ spectrum is shown in Fig. 4.3a. The realized degeneracies are inconsistent with the interpretation as a BIQHE state. The $k = 4$ Read-Rezayi state could be an alternative candidate for this filling, but it would have a $d = 5$ -fold degeneracy for N divisible by 4 [206]. In this context, we note that in order to stabilize the Read-Rezayi state in the continuum LLL, a small amount of dipolar interaction is required [216]. At any rate, our findings suggest that unlike the BIQHE in $|C| = 2$ bands (see Sec. 4.3.2), the $\nu = 2$ state is not realized in the single $|C| = 1$ band of the band-projected Harper-Hofstadter-Hubbard Hamiltonian (Eq. 4.4). It therefore seems likely that the $\nu = 2$ BIQHE state reported in a recent DMRG study for hardcore bosons requires at least the two lowest bands to be stabilized, which would be quite similar to the situation in two-flavor quantum Hall states [218] or Chern number $|C| = 2$ bands [161, 163, 219].

Finally, for the $r = -3$ series with $\nu = 3/2$, we find a marked reduction of the gap above the second-lowest state, so the degeneracy of $d = 2$ predicted by composite fermion theory does not describe this phase well. As observed in the continuum LLL [220], the $k = 3$ Read-Rezayi state appears to be a good candidate for this filling, as a stable gap appears to form above the lowest $d = 4$ states, in line with the expected ground-state degeneracy for this Read-Rezayi state. A full spectrum for the $N = 12$ particle state is given in Fig. 4.3b, and the finite-size scaling of the gap inferred for the Read-Rezayi states is shown as dotted

lines in Fig. 4.2 – these data are consistent with a finite gap in the thermodynamic continuum limit, even without the addition of long-range interactions [220].

In order to further characterize the different candidate states, we calculate the density-density correlation functions $g(\mathbf{r}) = \langle \rho(\mathbf{r})\rho(\mathbf{0}) \rangle$ for the different ground states, as explained in Appendix B.4. In order to establish the accuracy of our code, we have further verified that correlations approach the exact continuum result for the corresponding state in the continuum Landau level on a torus (see Appendix B.5). Our results show close agreement at short distances, while there are slight deviations at larger separations. We interpret these findings as being most likely a consequence of finite precision floating point arithmetic, as discussed in Appendix B.5.

Correlation functions for all available filling factors are shown in Fig. 4.4, based on the lowest-lying ground state at zero momentum. Note that the Laughlin state in Fig. 4.4a displays a correlation function that has saturated to a nearly constant value at large distances, with a zero correlation hole at zero separation. This is the expected form of the Laughlin correlation function and may be solved analytically for the torus, as discussed in Appendix B.5. For all other states, we find oscillations that are generally stronger for the states with higher $|r|$ values. The relatively small isotropic fluctuations of the correlation profile in Fig. 4.4a may be an artifact of finite-size effects. However, the remaining oscillations in Figs. 4.4c, 4.4d, & 4.4e are indicative of either states with longer correlation lengths, or potentially competing density wave instabilities. For example, the most marked oscillations are seen for the $N = 9$, $\nu = 3/4$ state in Fig. 4.4e. These oscillations also break the rotational symmetry as they occur predominantly along the x-axis for this geometry, which may be a signature of an instability toward charge density wave formation. For the states at $\nu = 3/2$ and $\nu = 2$, the correlations show a local maximum at zero separation, followed by a shallow correlation hole, which could be consistent with the interpretation as clustered Read-Rezayi states.

To summarize, the $|C| = 1$ boson data yields well-defined continuum limits $q \rightarrow \infty$, with negligible errors due to the extrapolation to large MUCs. From the cases considered, we can conclude that bosons in the $|C| = 1$ Chern number bands obey the expected scaling relations for the gap, and we obtain a well-converged continuum limit with no exceptions. However, extrapolation of these values to the thermodynamic limit remains difficult to achieve, and is prone to finite-size effects. The predictions of composite fermion theory apply only to a subset of possible composite fermion states, due to both finite-size effects and the apparent competition with states of the Read-Rezayi series or other competing phases such as density wave instabilities.

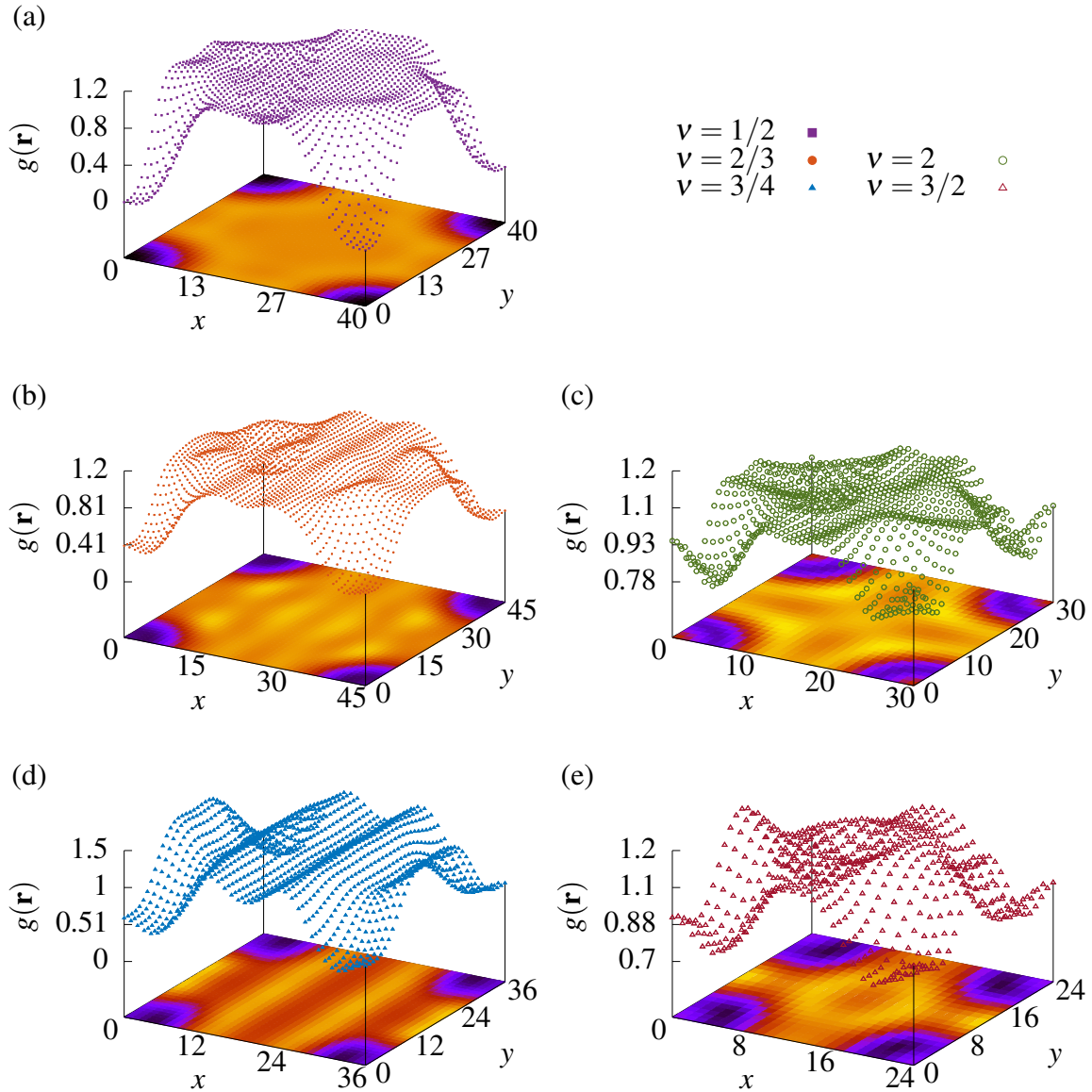


Fig. 4.4 Density-density correlation functions for bosonic states in the $|C| = 1$ band. The plots are shown for lowest-lying ground state in the $(k_x, k_y) = (0, 0)$ momentum sector, with (a) $r = 1$: $\nu = 1/2$, $N = 8$, $p = 99$; (b) $r = 2$: $\nu = 2/3$, $N = 10$, $p = 134$; (c) $r = -2$: $\nu = 2$, $N = 20$, $p = 91$; (d) $r = 3$: $\nu = 3/4$, $N = 9$, $p = 107$; and (e) $r = -3$: $\nu = 3/2$, $N = 9$, $p = 97$.

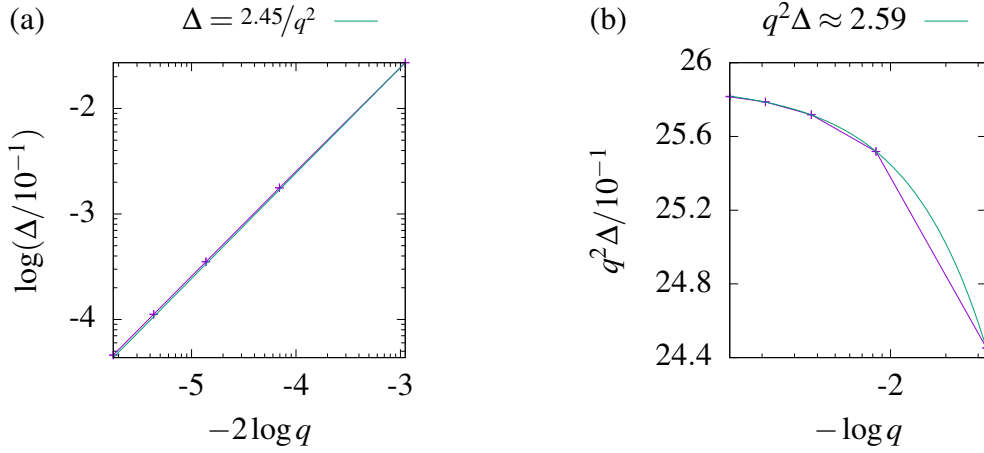


Fig. 4.5 Magnitude of the gap for the fermionic 20-particle $\nu = 2/3$ state in the $|C| = 1$ band, as a function of MUC size, q . (a) Log-log plot of Δ vs q^{-1} . (b) Scaling of $q^2 \Delta$ to a constant value in the continuum limit $n_\phi \rightarrow 0$.

Fermionic states

Building on our analysis for bosonic states, we carry out a corresponding study for fermions in the $|C| = 1$ band. As before, we consider cases with $|r| = 1, 2, 3$ and typical values of $6 \leq N \lesssim 12$ arising from the constraint on the Hilbert space dimension $\dim\{\mathcal{H}\} < 10^7$. Note the Hilbert space of N bosons in a $|C| = 1$ band with N_ϕ flux maps to the Hilbert space of fermions at $N + N_\phi - 1$ flux in the continuum, so the Hilbert space dimensions for the Jain states are identical for bosons at fermionic states of a given r value. They are essentially the same on the lattice also, up to different numbers of conserved momenta. Hence, we are able to obtain a comparable sample of geometries as in the previous section. The $r = -1$ series is omitted because this corresponds to a band insulator, so composite fermion theory is not relevant. Overall, we have considered 18 different combinations of particle number and filling factor, with an average of ~ 28 different geometries for each, and a total of 498 different exact diagonalization calculations underlying the data in this section.

For each filling factor, we plot the energy gap, Δ , against the MUC size, q , which reproduces the *inverse-square* relation $\Delta \propto q^{-2}$ expected for fermions [194], as illustrated in Fig. 4.5 for the 20-particle $\nu = 2/3$ data point.

From composite fermion theory, the expected ground-state degeneracy is $|krC + 1|$ with $k = 2$ for fermionic systems. This is indeed realized in all the observed energy spectra. As before, we find agreement with the value of the many-body gap in the continuum limit for the $N = 8$ fermionic Laughlin state considered by Bauer et al. [194].

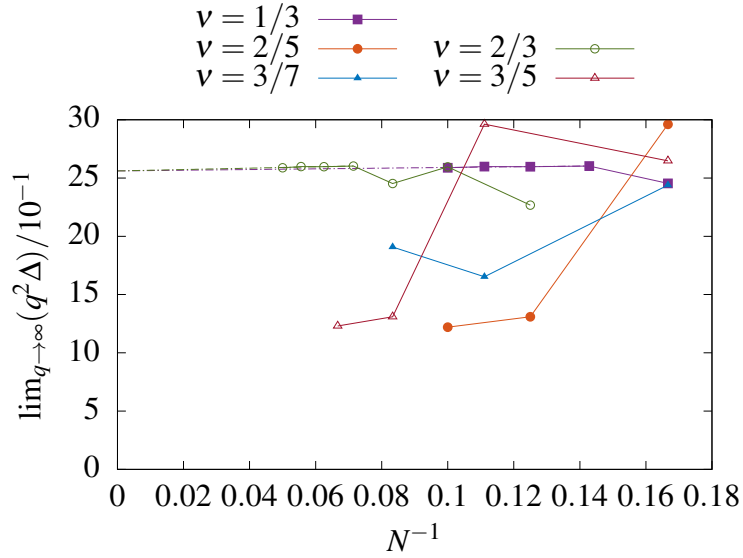


Fig. 4.6 Finite-size scaling of the gap to the thermodynamic continuum limit at fixed aspect ratio, for fermionic states in the $|C| = 1$ band. The extrapolation to the y-axis is shown for the robust $\nu = 1/3$ and $\nu = 2/3$ states. Squares, circles, and triangles denote states with $|r| = 1, 2, 3$, respectively, where the filled (hollow) symbols correspond to positive (negative) r . All of the error bars are smaller than the data points on the scale of the plot.

For all fermionic candidate states, we examine the continuum limit of $q^2\Delta$ at large MUC size, as demonstrated in Fig. 4.5b. As seen previously, finite-size effects may result in fluctuations at small q , so we neglect outliers at small q when determining the continuum limit.

Figure 4.6 shows the thermodynamic continuum limiting behavior for the five filling factors under consideration. The sample size shown is comparable to that in Fig. 4.2. Notice that the $r = 1$ series (this time corresponding to $\nu = 1/3$) displays very minor finite-size effects. In Appendix B.3, we also compare this limit against the finite-size scaling at fixed flux density, followed by extrapolation of the thermodynamic values to the continuum limit. Both orders of limits agree well, as shown in Fig. B.1b. Compared to the data for bosons in Fig. B.1a, we note that finite-size corrections are more noticeable for smaller system sizes. The gap in the continuum limit oscillates for small particle number but gradually settles to a well-defined thermodynamic continuum limit, which we extrapolate to be $\lim_{N, q \rightarrow \infty} (q\Delta) = 2.56 \pm 0.02^1$. This nicely illustrates the dissipation of finite-size effects as system sizes exceed the correlation length.

The $\nu = 2/3$ series also exhibits noteworthy behavior. We find that the many-body gaps are closely related to the values for $\nu = 1/3$ states by particle-hole symmetry, via $\Delta(N) =$

$\Delta(N_\phi - N)$, although lattice models typically break this symmetry [221]. Clearly, the particle-hole symmetry re-emerges as an exact symmetry in the limit of continuum Landau levels, so it is reassuring that it is also approximated closely for finite flux densities. In this case, we also extrapolate the thermodynamic continuum limit to be $\lim_{N,q \rightarrow \infty}(q\Delta) = 2.56 \pm 0.02$ to two decimal places, perfectly matching the result for $\nu = 1/3$ ¹.

For the $\nu = 2/5$ state, we again find a particle-hole symmetric partner at $\nu = 3/5$ with similar gaps. In both cases, the finite-size gap appears strongly enhanced for small system sizes, but settles to a relatively flat plateau for the last two system sizes that we have evaluated. These data are indicative of a gap in the thermodynamic continuum limit, in accordance with established numerical results for the LLL. Likewise, the $\nu = 3/7$ state also yields finite gaps that are consistent with a nonzero thermodynamic continuum limit.

Density-density correlation functions for the ground states of the considered range of fillings are shown in Fig. 4.7. As expected for spinless fermions, the correlation at zero separation is identically zero due to Pauli exclusion. We note that the Laughlin state in Fig. 4.7a, as well as the particle-hole symmetry-related $\nu = 2/3$ state in Fig. 4.7c, tend to a constant correlation at large distances. However, the zero-separation correlation hole is more distinct for the Laughlin state in Fig. 4.7a, analogous to that observed for the bosonic Laughlin state in Fig. 4.4a. As for $|C| = 1$ bosons, the $r = 2$ fermion state shows minor isotropic fluctuations at large distances, as shown in Fig. 4.7b, which may be due to finite-size effects. The density-density correlation functions for the $|r| = 3$ states in Figs. 4.7d & 4.7e, however, show large anisotropic oscillations in the y -direction. For the $\nu = 3/7$ state in Fig. 4.7d, for example, we observe a global maximum of almost double the constant value at large distance observed for the Laughlin state in Fig. 4.7a. Again, these directional oscillations in the $|r| = 3$ states may be indicative of a charge density wave instability.

Overall, obtaining the fermion data is more computationally expensive than the corresponding data for bosons due to the higher ground-state degeneracies. However, for $|C| = 1$, the Hilbert space dimensions are nearly identical, allowing a large number of geometries and system sizes. As before, we conclude that the scaling relations for the gap yield a well-defined continuum limit for large q in all cases. As for bosons, the composite fermion prediction for the stability hierarchy is not observed, as the $\nu = 3/7$ state appears to have a larger gap than the $\nu = 2/5$ state, possibly signaling a different intervening phase. However, to the extent that our data are conclusive, they indicate that all examined states can have a finite gap in the thermodynamic continuum limit.

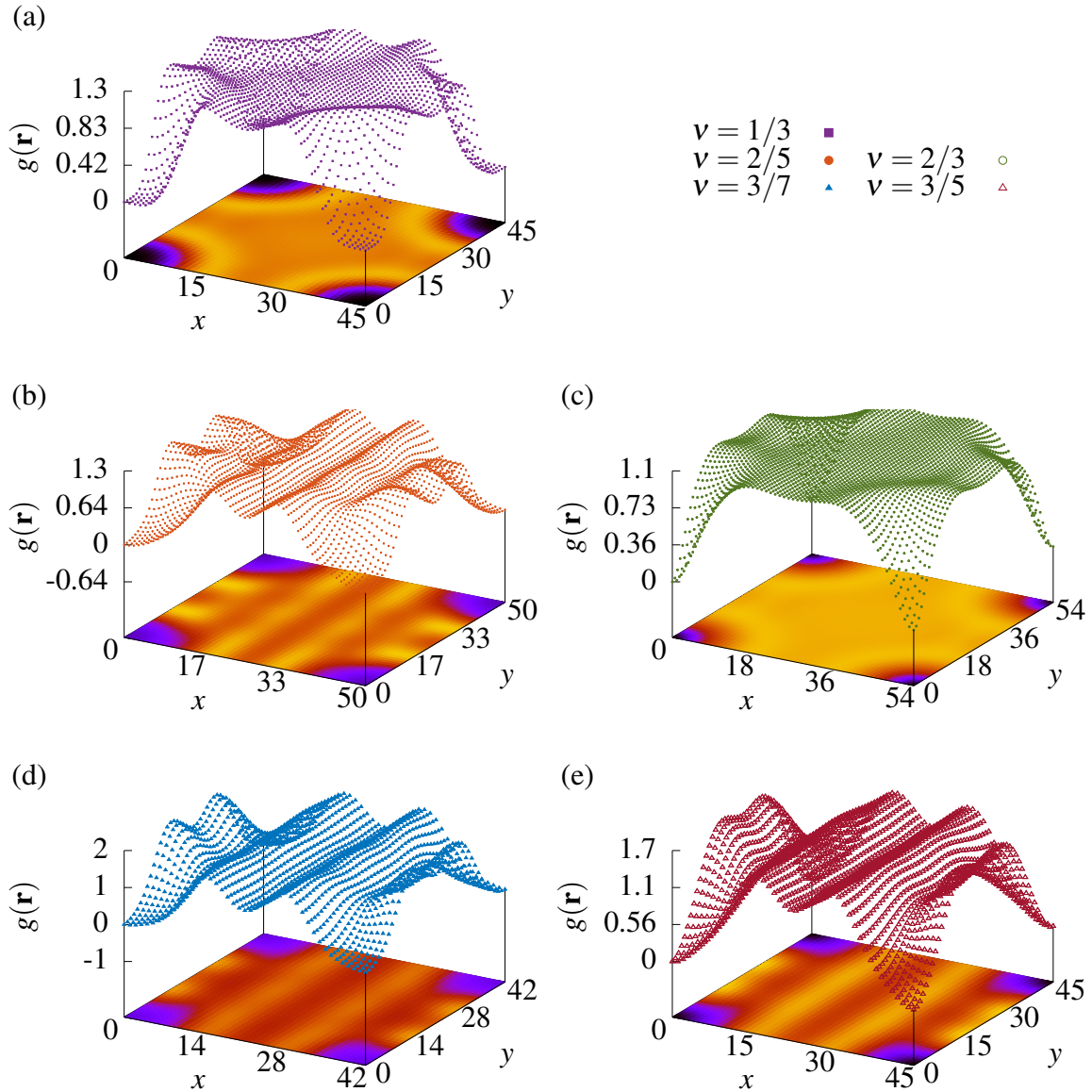


Fig. 4.7 Density-density correlation functions for fermionic states in the $|C| = 1$ band. The plots are shown for the lowest-lying ground state in the $(k_x, k_y) = (0, 0)$ momentum sector, with (a) $r = 1$: $\nu = 1/3$, $N = 9$, $p = 76$; (b) $r = 2$: $\nu = 2/5$, $N = 8$, $p = 124$; (c) $r = -2$: $\nu = 2/3$, $N = 18$, $p = 107$; (d) $r = 3$: $\nu = 3/7$, $N = 9$, $p = 85$; and (e) $r = -3$: $\nu = 3/5$, $N = 9$, $p = 134$.

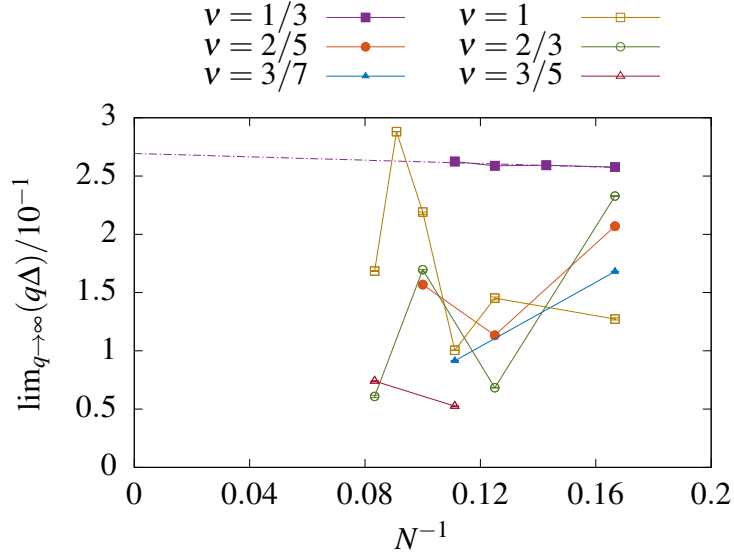


Fig. 4.8 Finite-size scaling of the gap to the thermodynamic effective continuum limit at fixed aspect ratio, for bosonic states in the $|C| = 2$ band. The extrapolation to the y-axis is shown for the robust $\nu = 1/3$ states. Squares, circles, and triangles denote states with $|r| = 1, 2, 3$, respectively, where the filled (hollow) symbols correspond to positive (negative) r . All error bars due to the effective continuum limit are smaller than the symbols on the scale of the plot.

4.3.2 FCIs in $|C| = 2$ bands

The preceding study of $|C| = 1$ bands in the continuum limit provides a solid foundation from which to explore higher Chern number bands. However, naively extending the analysis in Sec. 4.3.1 presents two major challenges. First, the Hilbert space dimension for systems with a higher Chern number is considerably larger, since the filling factor is reduced, and thus calculations at the same particle numbers are exponentially more expensive. Additionally, the systematic process of obtaining square configurations, outlined in Sec. 4.2.5, is often too constricting to yield an adequate number of square configurations for higher Chern numbers. This is a geometric problem, which can be overcome by finding approximately square configurations for the problem cases.

Bosonic states

As before, we start with bosonic systems with onsite interactions, considering filling factors of the series (Eq. 4.5) with $|r| = 1, 2, 3$. Again, we include particle numbers with Hilbert space dimensions of $\dim\{\mathcal{H}\} < 10^7$. Overall, we have considered 23 different combinations of particle number and filling factor, with an average of ~ 22 different geometries for each,

and a total of 510 different exact diagonalization calculations underlying the data in this section. The final data for the effective continuum limiting behavior for the six filling factors under consideration are shown in Fig. 4.8. Notice that the $q\Delta$ values are smaller than in the corresponding cases for $|C| = 1$ bands in Fig. 4.2. The $r = 1$ series is again almost completely unaffected by finite-size scaling, with an extrapolated thermodynamic effective continuum limit of $\lim_{N,q \rightarrow \infty}(q\Delta) = 0.27 \pm (4.4 \times 10^{-3})^1$. Finite-size effects are noticeable for all other series. We will first discuss the scaling to the effective continuum limit and then provide further discussion of the finite-size scaling for the different states.

We find that the many-body gap scales inversely with q for the $|C| = 2$ bands, also. However, we find stronger fluctuations of the scaled gap around the limiting value, which is partly related to the absence of square geometries. We illustrate common behaviors by examining three examples in detail.

In Figs. 4.9a & 4.9b, we display the 12-particle $\nu = 1$ state. We choose this state as it has a high particle number and behaves in the familiar and expected way; i.e. it produces an adequate number of square configurations and its energy gap can be determined without any ambiguity.

In Figs. 4.9c & 4.9d, we display the six-particle $\nu = 1$ state. We choose this state as an example of a case which does not produce an adequate number of (or, indeed, any) square configurations, in accordance to our systematic method (see Sec. 4.2.5). Therefore, for this case, we consider all configurations which are within an error $\varepsilon \leq 2\%$ of being square, as this gives an adequate and comparable sample size of ~ 10 configurations. This is noticeable by the deviations from a straight line in Fig. 4.9c and in the clear oscillations in Fig. 4.9d. The various rectangular configurations obey slightly different scaling relations with MUC size, which results in noticeable oscillations in the plots (note, however, the small scale on the y-axes). In the cases where we use approximately square configurations, the error in the effective continuum limit is no longer negligible on the scale of the thermodynamic limit plot and so must be taken into account. The precise determination of errors for the effective continuum limit of $q \rightarrow \infty$ is discussed in Appendix B.6.

Finally, in Figs. 4.9e & 4.9f, we display the 12-particle $\nu = 2/3$ state. We choose this state as a case of interest because it is the largest system size for the $\nu = 2/3$ state, shown in Fig. 4.8. Yet, it retains a strong geometry dependency. Note that these data are based on configurations which are within $\varepsilon \leq 1\%$ of being square. Figure 4.9e shows the overall reciprocal scaling of the many-body gap with MUC size. However, from Fig. 4.9f, we can see that there seem to be two different rectangular configurations which have distinct scaling behaviors. By closely examining the energy spectra, this is indeed the case. Figures 4.10a & 4.10b show the spectra for the two distinct rectangular configuration geometries present in

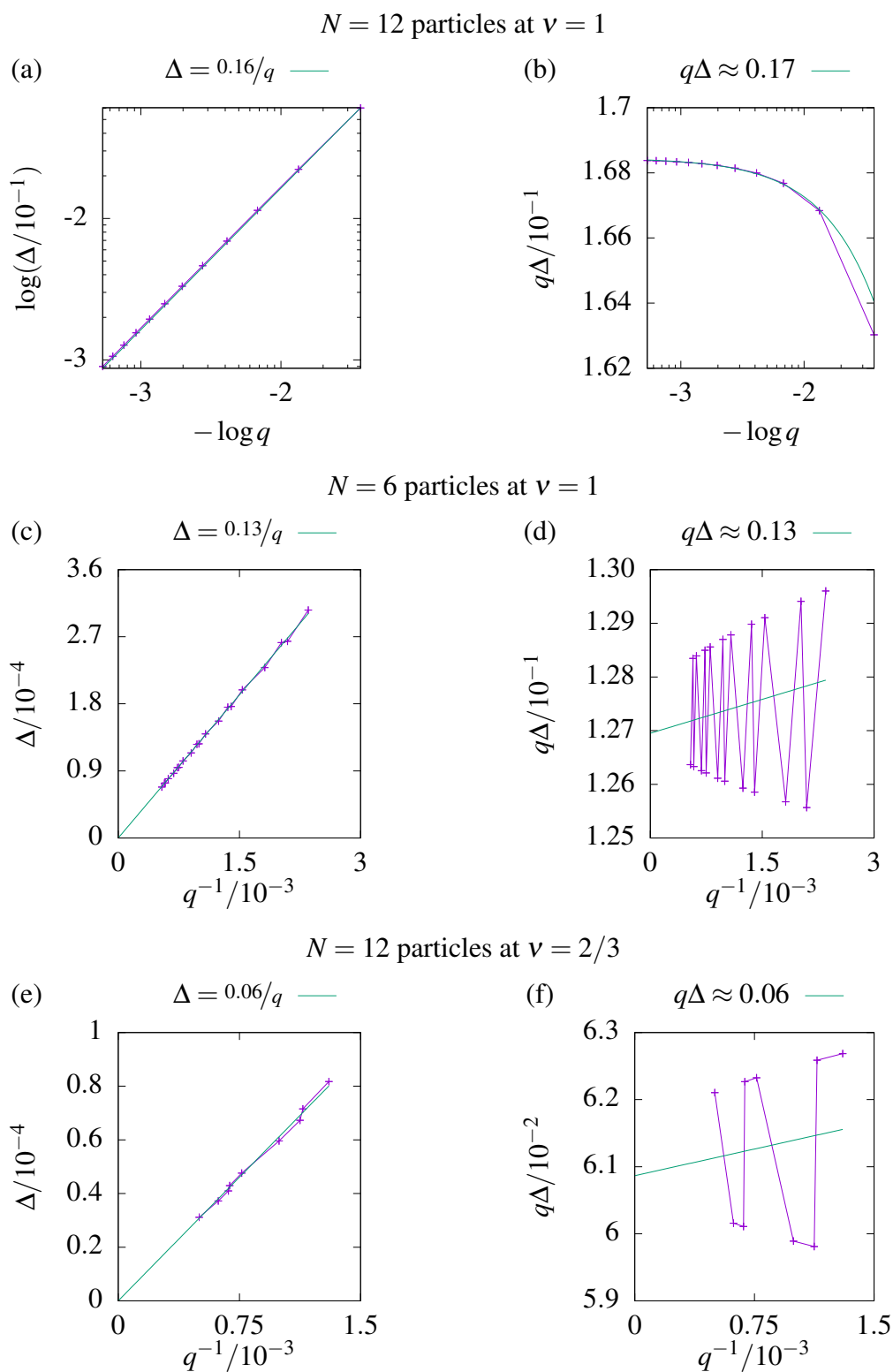


Fig. 4.9 Magnitude of the gap for bosonic states in the $|C| = 2$ band, as a function of MUC size, q .

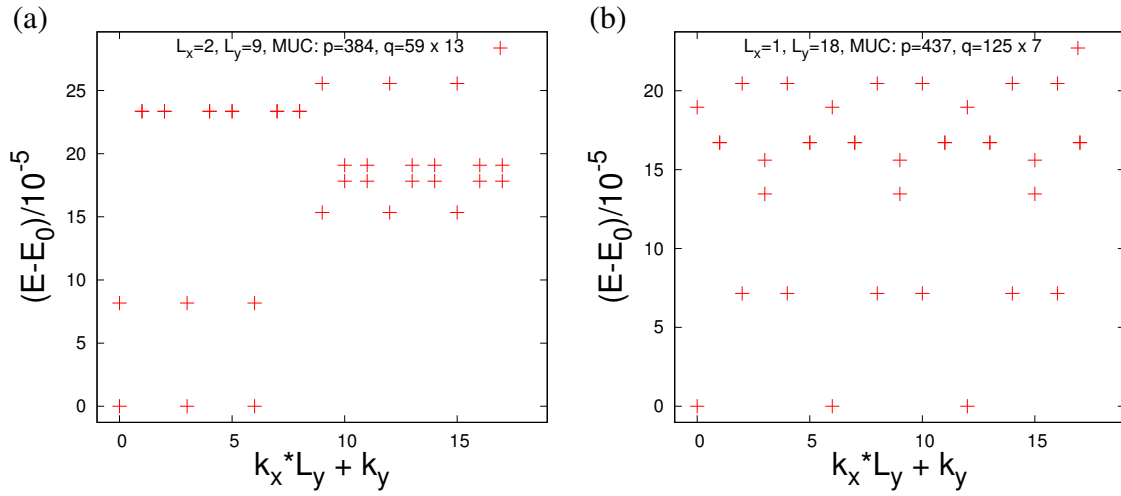


Fig. 4.10 Energy spectra for the bosonic 12-particle $\nu = 2/3$ state in the $|C| = 2$ band, at (a) $p = 384$, and (b) $p = 437$. The plots are resolved to $n = 2$ points per sector.

the sample: the $L_x \times L_y = 2 \times 9$ and $L_x \times L_y = 1 \times 18$ cases (taking MUCs with the largest possible L_y extension). In addition, the density-density correlation function corresponding to the $L_x \times L_y = 2 \times 9$ case is presented in Fig. 4.11d. From composite fermion theory, we expect the degeneracy of the ground state to be $d = 3$, which is indeed what we observe; and the degeneracy is even clearly visible in the spectra, since the ground states happen to be in different momentum sectors. Yet, there is a discrepancy between the energy gaps for the two rectangular configurations, which is larger than the fluctuations of the previously discussed data at $\nu = 1$ with $\varepsilon \leq 2\%$ deviations from square geometries, in Fig. 4.9d. Nonetheless, any errors from the extrapolation to the effective continuum limit remain small compared to the finite-size fluctuations of the gap visible in Fig. 4.8.

Overall, the $\nu = 2/3$ state has the strongest finite-size effects, with smaller gaps for configurations with N divisible by four: In its finite-size scaling, we see clear oscillations of the many-body gap under addition of pairs of particles. The next larger system size at $N = 14$ was found to have a larger gap in the previous study at fixed flux density [163]. Hence, the low value at $N = 12$ should not be taken as an indication of the vanishing of the gap in the thermodynamic effective continuum limit. The correlation function for the 12-particle $\nu = 2/3$ state corresponding to Fig. 4.10a is shown in Fig. 4.11d. Here we observe that charge density wave instabilities may also play a role.

The $|C| = 2$, $\nu = 1$ state is the second candidate for a BQHE state within the series (Eq. 4.5). Here, we consistently find a nondegenerate ground state in our numerical analysis, as predicted by composite fermion theory. The many-body gap in Fig. 4.8 shows significant finite-size effects, precluding us from taking a quantitative extrapolation to the thermody-

dynamic effective continuum limit. However, its magnitude is consistently nonzero for all available system sizes. We further note that the realizations of the BIQHE in $|C| = 2$ optical flux lattices were likewise found to have a significant geometry dependency of the many-body gaps [222]. Notwithstanding these finite-size effects, we stress that all geometries allow for a clear identification of a singly degenerate ground state. This is unlike the case of the potential $\nu = 2$ BIQHE state in the lowest $|C| = 1$ Hofstadter bands, where competing phases appear to dominate, as we have discussed in Sec. 4.3.1.

The $\nu = 2/5$ state demonstrates a robust many-body gap for the states considered. The Hilbert space dimension of $|C| = 2$ bosons is comparable to that of $|C| = 1$ fermions in Fig. 4.6 and so the data are limited due to computational expense. Nevertheless, the remaining filling factor series show the potential for a robust thermodynamic effective continuum limit. We note the lack of particle-hole symmetry for the $\nu = 2/5$ and $\nu = 3/5$ filling factor series, visible in Fig. 4.8, unlike for the $|C| = 1$ fermions in Fig. 4.6. Additionally, we observe approximately the predicted composite fermion hierarchy of gaps for $r = -1, -2, -3$, as well as for $r = 1, 2, 3$. Unfortunately, finite-size effects dominate extrapolation errors from $q \rightarrow \infty$, and so preclude a clear extrapolation to the thermodynamic effective continuum limit.

The correlation functions for the six filling factors under consideration are shown in Fig. 4.11. Notice the appearance of four distinct correlation sheets. We differentiate between the sheets by labeling them corresponding to the $|C|^2$ possible solutions for $(x \bmod |C|, y \bmod |C|)$, where x and y denote the x - and y -axis lattice positions. Hence, the modulation along the x - and y -axes of period $|C|$ leads to the appearance of $|C|^2$ smooth correlation sheets. However, in a finite-size system, some of these sheets may be related by inversion symmetries of the type $x_i \leftrightarrow L_i - x_i$ whenever $L_i \bmod C \neq 0$. This observation seems to contradict models of higher Chern number $|C|$ bands as effective multilayer fractional quantum Hall systems composed of $|C|$ layers [160, 203, 223–225]. It is unclear at present how to reconcile this view with our observations, as the conventional multilayer view allows for no more than $|C|$ distinct correlation functions. Although it is possible that a suitable basis could be found in which the number of sheets decreases, this would likely require a nonlocal transformation mixing several sites within the unit cell. On the other hand, it is plausible that a $|C|$ -fold periodicity should appear along each axis, given that the single-particle wave functions of Harper's equation show such behavior [179, 203, 223, 225]. For this single-particle problem in the Landau gauge, one singles out one of the axes for momentum conservation, so that $|C|$ -fold oscillations in the eigenstates occur only in the perpendicular direction. However, as the problem is gauge-invariant, either permutation of the two axes could be chosen to exhibit these behaviors. Furthermore, the correlation function should be isotropic in space in

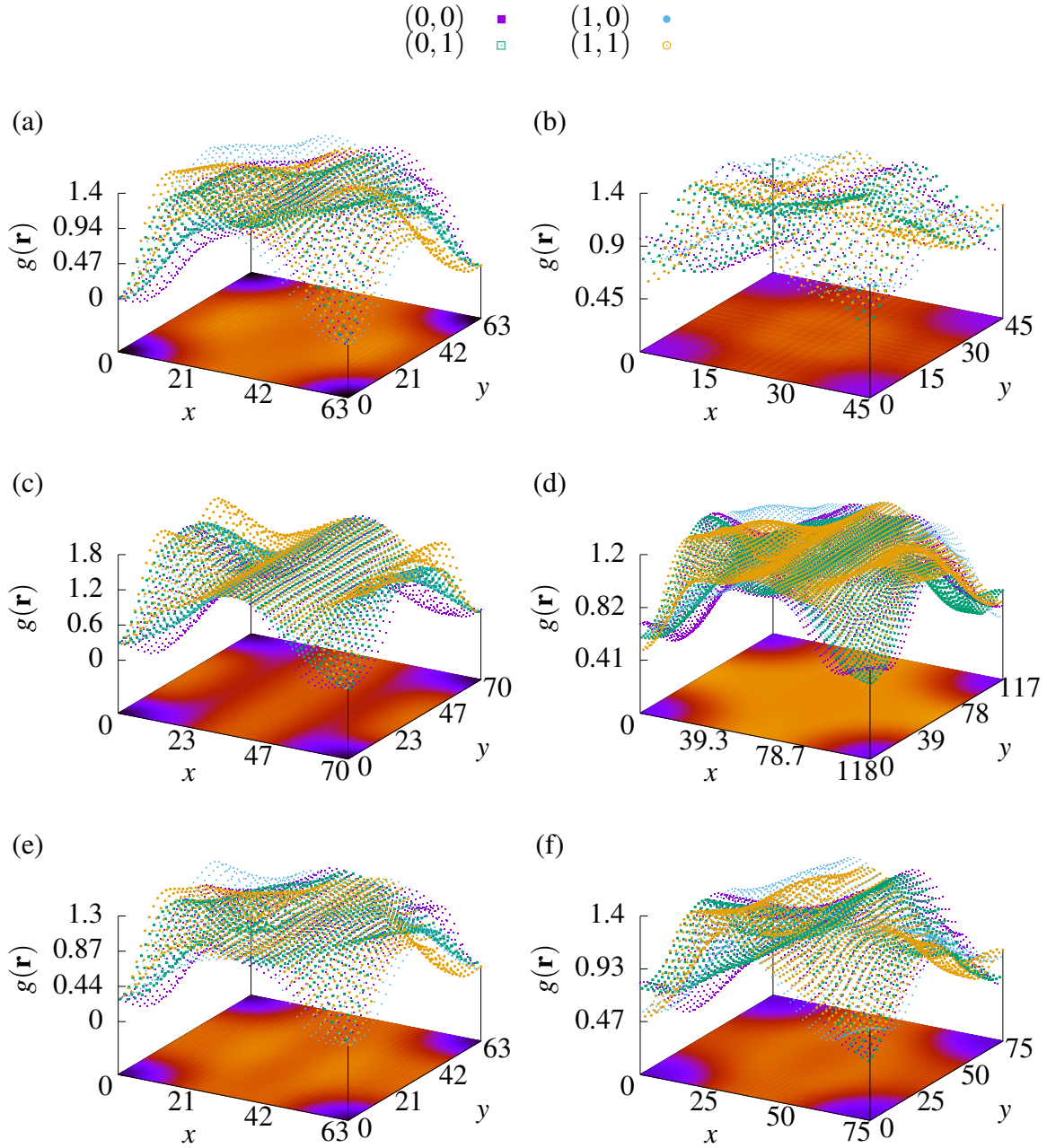


Fig. 4.11 Density-density correlation functions for bosonic states in the $|C| = 2$ band. The plots are shown for the lowest-lying ground state in the $(k_x, k_y) = (0, 0)$ momentum sector. The legend differentiates between the correlation functions at lattice positions $(x \bmod 2, y \bmod 2)$, as explained in the main text. We show data for (a) $r = 1$: $\nu = 1/3$, $N = 7$, $p = 94$; (b) $r = -1$: $\nu = 1$, $N = 9$, $p = 112$; (c) $r = 2$: $\nu = 2/5$, $N = 8$, $p = 123$; (d) $r = -2$: $\nu = 2/3$, $N = 12$, $p = 384$; (e) $r = 3$: $\nu = 3/7$, $N = 9$, $p = 94$; and (f) $r = -3$: $\nu = 3/5$, $N = 9$, $p = 188$.

the infinite system. Hence, it appears natural that the correlation functions display $|C|$ -fold periodicity along both axes.

The state at $\nu = 1/3$ in Fig. 4.11a shows features reminiscent of the Laughlin states in the $|C| = 1$ band, since this state also has positive flux attachment with one filled band in the composite fermion spectrum ($r = 1$). We refer to such states as primary composite fermion states. The zero-separation correlation hole is most pronounced here and converges to zero for all of the correlation sheets; this is observed for all of the states with positive r in Fig. 4.11. Furthermore, the isotropic fluctuations at large distances show signs of settling, although it is hard to discern the limiting value of the correlation function in this case. Note that pairs of sheets are related by inversion symmetry for the specific geometry shown in the figure. This is a recurring feature for higher Chern bands. In the present case, we see that the $\{(0,0), (1,0)\}$ and $\{(0,1), (1,1)\}$ pairs are related along the x-axis; and the $\{(0,0), (0,1)\}$ and $\{(1,0), (1,1)\}$ pairs are related along the y-axis. Due to the large number of data points and intricacy of these figures, the data are available, along with this chapter, to view interactively on-line as Supplementary Material⁴.

The correlation functions for the $\nu = 1$ and $\nu = 2/3$ fillings in Figs. 4.11b & 4.11d are similarly isotropic at large distances with comparable global maxima. However, the correlation sheets for these separate cases do not converge to a unique value at the correlation hole. In contrast, the correlation functions for the $\nu = 2/5$, $\nu = 3/7$, and $\nu = 3/5$ filling factor series, in Figs. 4.11c, 4.11e, & 4.11f, show signs of anisotropy with directional oscillations, which may be indicative of competing charge density wave instabilities. Note that signs of charge density waves were also observed for the corresponding r values ($r = -3, 2, 3$) for fermions in $|C| = 1$ bands, shown above in Fig. 4.7.

Next, we examine the particle entanglement spectra of the examined quantum liquids. In general, the PES for these series are gapped confirming the existence of a topological phase. For instance, the PES for the selected states in Fig. 4.11 have principal entanglement gaps, Δ_ξ , of (a) 14.25, (b) 1.37, (c) 4.09, (d) 1.12, and (e) 1.85, after tracing out $\lfloor N/2 \rfloor$ particles. The count of eigenstates below the principal entanglement gaps for these states, in each of the momentum sectors, are (a) 31, 30, 30 (repeated for 21 sectors), (b) 53 (repeated for 9 sectors), (c) 441, 430, 430, 430 (repeated for 20 sectors), (d) 5605, 5586, 5601, 5583, 5601, 5583 (repeated for 18 sectors), (e) 504 (repeated for 21 sectors), and (f) 198 (repeated for 15 sectors), respectively. The spectra corresponding to the correlation functions in Figs. 4.11a & 4.11c are shown in Fig. 4.12. Here, the primary composite fermion $\nu = 1/3$ state in Fig. 4.12a shows the largest and clearest gap by a significant margin, as expected. All other

⁴Supplemental Material includes the original data for the correlation functions and instructions to view these interactively [1].

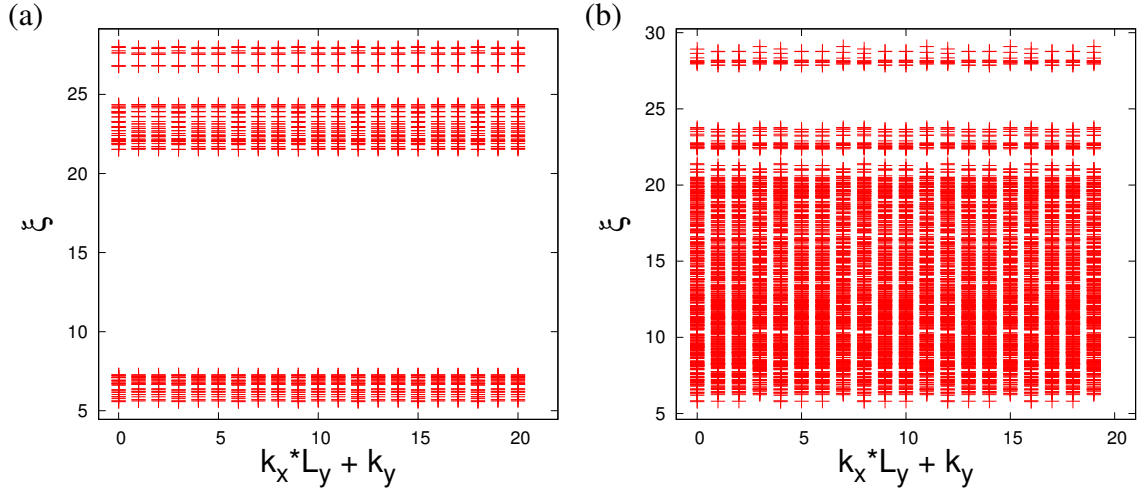


Fig. 4.12 PES for bosonic states in the $|C| = 2$ band. We show data for: (a) $r = 1$: $\nu = 1/3$, $N = 7$, $p = 94$; and (b) $r = 2$: $\nu = 2/5$, $N = 8$, $p = 123$. In both cases we take $N_A = \lfloor N/2 \rfloor$. The counts of eigenstates from the bottom of the spectra up to the principal entanglement gaps, in each of the momentum sectors, is (a) 31, 30, 30 (repeated for 21 sectors), and (b) 441, 430, 430, 430 (repeated for 20 sectors), respectively.

states have a smaller principal entanglement gap higher in the spectrum, as in Fig. 4.12b. Unlike the primary composite fermion states, other states of the composite fermion series (Eq. 4.5) are not characterized by a generalized exclusion principle [226], so they obey no simple counting rule for these numbers of quasi-particle states.

Overall, the bosonic series for the second Chern band presented some of the expected difficulties owing to the commensurability of several constraints on the geometries; however, these problems were largely overcome by allowing for a scaling in q . The only noticeable drawbacks, compared to the $|C| = 1$ band, are the reduced number of data points, particularly for higher particle numbers, and the correspondingly larger uncertainty in the extrapolation as $q \rightarrow \infty$. As emphasized in the previous discussion, although considering approximately square configurations undoubtedly introduces error bars in the data, the deviation from square systems is not directly proportional to the error observed in the effective continuum limit. Rather, the subsequent error in the effective continuum limit is principally determined by the specific variation in the spectra for a given state.

Fermionic states

We now extend our analysis to fermions with NN interactions. For $|C| > 1$, the Hilbert space dimensions for fermionic states are higher than those of the corresponding bosonic states due

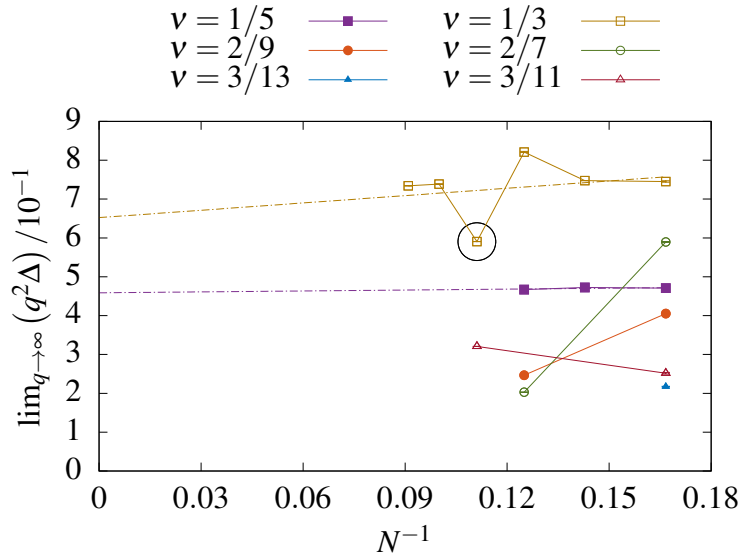


Fig. 4.13 Finite-size scaling of the gap to the thermodynamic effective continuum limit at fixed aspect ratio, for fermionic states in the $|C| = 2$ band. The extrapolation to the y-axis is shown for the robust $\nu = 1/5$ and $\nu = 1/3$ states. The $N = 9$ data point for the $\nu = 1/3$ series is circled to indicate that there is a competing topological phase present with $d = 2$. Squares, circles, and triangles denote states with $|r| = 1, 2, 3$, respectively, where the filled (hollow) symbols correspond to positive (negative) r . All error bars are smaller than the data points on the scale of the plot.

to the smaller filling factors and we thus expect to be able to compute fewer fermion states due to computational limitations.

Figure 4.13 shows the data for the gap in the effective continuum limit for the six filling factors under consideration as a function of the inverse system size. Because of computational limitations, substantial data were only obtained for the $|r| = 1$ series, while we have few data points for the other filling factors. Again, the $r = 1$ primary composite fermion state shows the smallest finite-size effects on the many-body gap, and we extrapolate the thermodynamic effective continuum limit to be $\lim_{N, q \rightarrow \infty} (q^2 \Delta) = 0.46 \pm 0.02^1$. Note also that the magnitude of $q^2 \Delta$ values is lower than in the corresponding $|C| = 1$ fermion plot in Fig. 4.6. Finite-size effects are noticeable for all series and the $q \rightarrow \infty$ extrapolation errors are much larger compared to the $|C| = 2$ boson data. All of the fermion data was obtained using systems which were within $\delta R \leq 1\%$ of square simulation cells. Some of these systems were exactly square, but no filling fraction yields enough such geometries to use exact square systems exclusively, throughout the scaling procedure. More specifically, we have considered 18 different combinations of particle number and filling factor, with an average of ~ 24 different

geometries for each. There are a total of 433 different exact diagonalization calculations underlying the data in this section.

Figures 4.14a & 4.14b show the plots for the six-particle $\nu = 2/9$ state. This is selected as an example of a state which has a clean scaling limit. The plots of Δ and $q^2\Delta$ for the eight-particle $\nu = 1/3$ state in Figs. 4.14c & 4.14d show slight oscillations due to the $\delta R \leq 1\%$ approximation in square configurations, similar to the bosonic states in Figs. 4.9c & 4.9d. However, these deviations are not as large as in the $|C| = 2$ bosonic problem case in Fig. 4.9f. The effective continuum limit can be determined with a reasonable error. The spectra in Figs. 4.15a & 4.15b show the origin of the oscillations in Fig. 4.14d. As with the $|C| = 2$ bosons in Figs. 4.10a & 4.10b, we see a competition between two distinct rectangular geometries. The higher lying bands are more densely packed for the $L_x \times L_y = 3 \times 8$ system in Fig. 4.15a than for the $L_x \times L_y = 2 \times 12$ spectrum in Fig. 4.15b.

The $\nu = 1/3$ series obtained for negative flux attachment ($r = -1$) has an exceptionally large gap with moderate finite-size effects and allows for a clear scaling of the many-body gap to the thermodynamic effective continuum limit. We extrapolate a limit of $\lim_{N,q \rightarrow \infty} (q\Delta) = 0.65 \pm 0.16$ in this case¹. Note that at this filling factor, for $N = 9$ we find that some lattice geometries realize a competing phase with $d = 2$ instead of the degeneracy $d = 3$ predicted by composite fermion theory. This competing phase appears to be topological, with a large entanglement gap of $\Delta_\xi = 6.40$ for $p = 73$ ($N_A = 4$), for example, and a corresponding eigenstate count of 385 (repeated for 27 sectors). As we find only few lattice geometries at this single system size showing this behavior, we do not attempt to further characterize this competing state. For the purposes of the effective continuum limit shown in Fig. 4.13, only the geometries with the predicted threefold degeneracy were taken into account.

The data series for the remaining filling factors in Fig. 4.13 show few points due to the steep Hilbert space dimension scaling with particle number for $|C| = 2$ fermions. However, these series produce the correct ground-state degeneracies and the initial data have the potential for a robust gap in the thermodynamic effective continuum limit.

The correlation functions for the available filling factors are shown in Fig. 4.16. We note a few repeating characteristics that resemble features of states for the $|C| = 1$ bands in Figs. 4.4 & 4.7, as well as the $|C| = 2$ bosons in Fig. 4.11. The primary composite fermion state in Fig. 4.16a shows a pronounced correlation hole at zero separation and isotropic fluctuations at large distances. The fluctuations in this case are, however, larger than those in the corresponding boson plot in Fig. 4.11a. The correlation plots for the flux densities at $r = -1$ and $r = -2$ in Figs. 4.16b & 4.16d again show some degree of rotational symmetry and isotropy at large distances, whereas the plots with $r = -3, 2, 3$ in Figs. 4.16f, 4.16c, & 4.16e show directional oscillations, potentially indicative of an instability due to charge

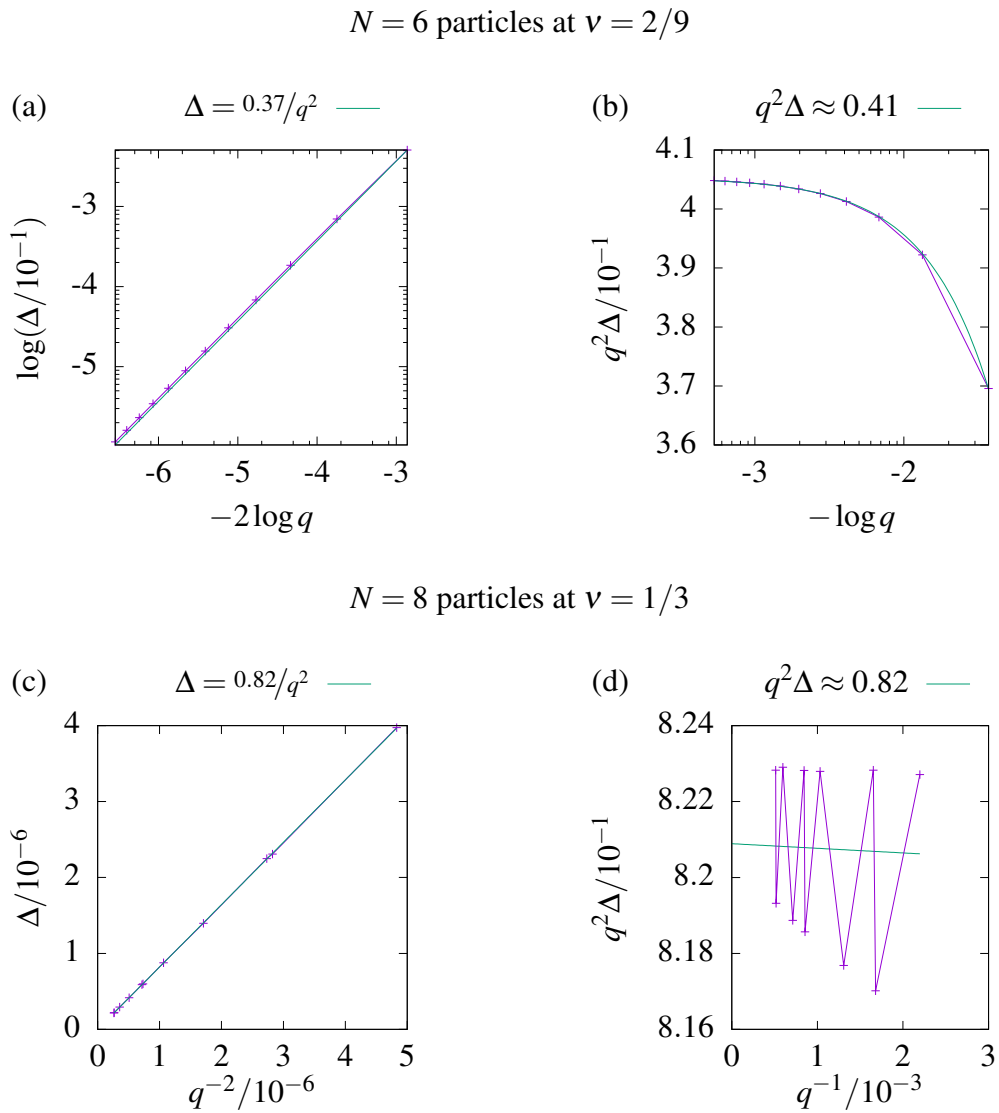


Fig. 4.14 Magnitude of the gap for fermionic states in the $|C| = 2$ band, as a function of MUC size, q .

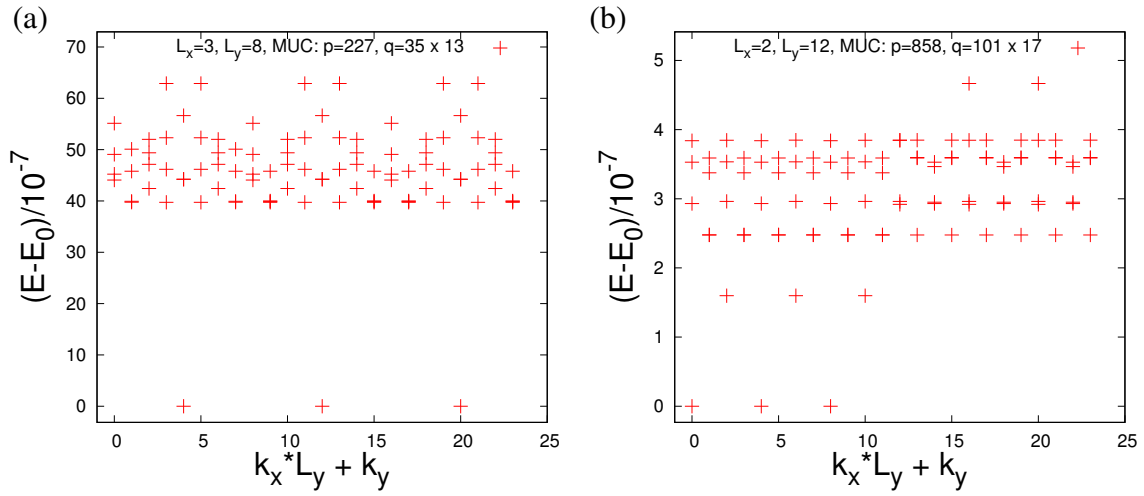


Fig. 4.15 Energy spectra for the fermionic eight-particle $\nu = 1/3$ state in the $|C| = 2$ band, at (a) $p = 227$, and (b) $p = 858$. The plots are resolved to $n = 4$ points per sector.

density wave order. Recall that this was also observed for the $|C| = 2$ bosons in Fig. 4.11 and the $|C| = 1$ fermions in Fig. 4.7. The smooth correlation functions are again visibly split into $|C|^2$ sheets.

The PES for the fermionic series have notably large and clear gaps overall. For example, the spectra for the states in Fig. 4.16 have Δ_ξ values of (a) 13.76, (b) 7.58, (c) 0.82, (d) 6.06, (e) 9.46, and (f) 10.84, after tracing out $\lfloor N/2 \rfloor$ particles. The corresponding eigenstate counts from the bottom of the spectra up to the principal entanglement gaps, in each of the momentum sectors, are (a) 77 (repeated for 35 sectors), (b) 385 (repeated for 27 sectors), (c) 1117, 1110, 1118, 1110 (repeated for 36 sectors), (d) 445, 440, 446, 440 (repeated for 28 sectors), (e) 77 (repeated for 26 sectors), and (f) 51 (repeated for 22 sectors), respectively. The PES corresponding to Figs. 4.16a & 4.16f are shown in Fig. 4.17. Each of the fermionic states, with the exception of the PES corresponding to Fig. 4.16c, show PES with large gaps and relatively uniform eigenstate counts across the momentum sectors. These are features which we otherwise found to be realized only for the primary composite fermion state within the bosonic series. For the fermionic series under examination, the primary composite fermion $\nu = 1/5$ state remains distinguished predominantly by the magnitude of the gap.

Overall, the $|C| = 2$ fermion series produces robust results for the gaps of the states (Eq. 4.5). While we have not generated enough data to ascertain a nonzero gap in the thermodynamic limit for all members of the family, all observed finite-size gaps are nonzero, and we find a clear thermodynamic effective continuum limit for the $r = \pm 1$ states. Several high-particle-number points are omitted but the error bars in the data obtained are reasonable.

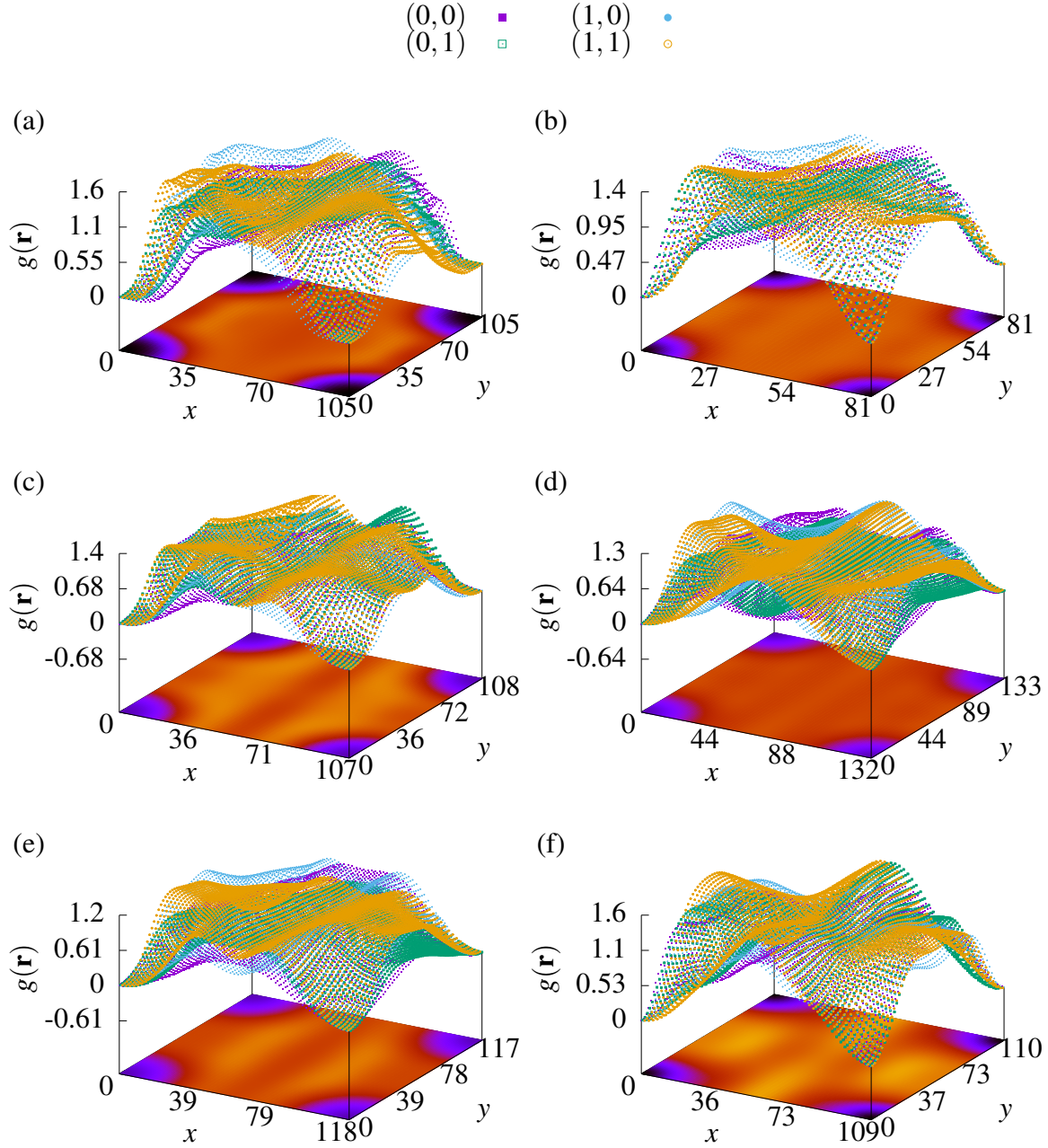


Fig. 4.16 Density-density correlation functions for fermionic states in the $|C| = 2$ band. The plots are shown for the lowest-lying ground state in the $(k_x, k_y) = (0, 0)$ momentum sector, with sheets colored as in Fig. 4.11. We show data for (a) $r = 1$: $\nu = 1/5$, $N = 7$, $p = 157$; (b) $r = -1$: $\nu = 1/3$, $N = 9$, $p = 121$; (c) $r = 2$: $\nu = 2/9$, $N = 8$, $p = 160$; (d) $r = -2$: $\nu = 2/7$, $N = 8$, $p = 313$; (e) $r = 3$: $\nu = 3/13$, $N = 6$, $p = 265$; and (f) $r = -3$: $\nu = 3/11$, $N = 6$, $p = 272$.

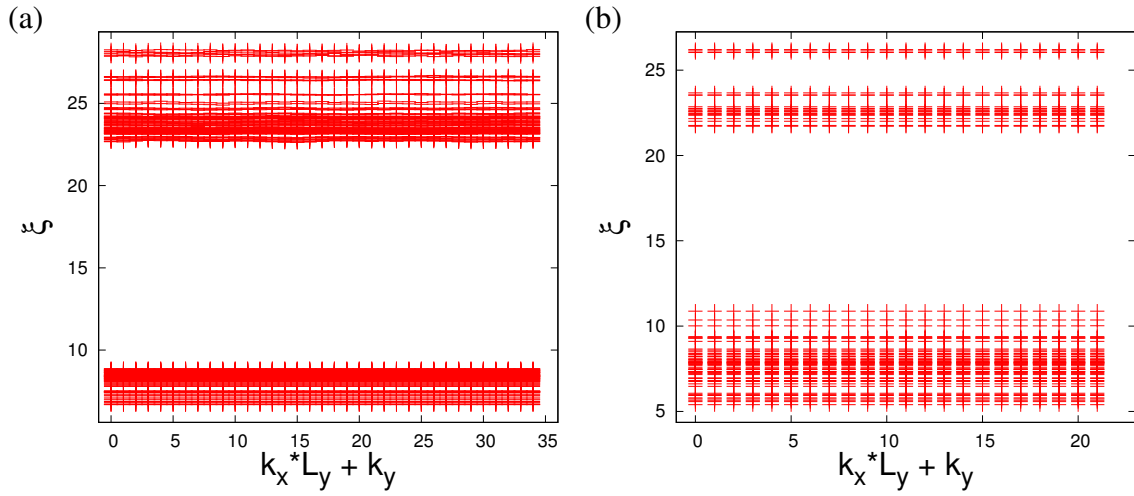


Fig. 4.17 PES for fermionic states in the $|C| = 2$ band. We show data for (a) $r = 1$: $\nu = 1/5$, $N = 7$, $p = 157$; and (b) $r = -3$: $\nu = 3/11$, $N = 6$, $p = 272$. In both cases, we take $N_A = \lfloor N/2 \rfloor = 3$. The counts of eigenstates from the bottom of the spectrum up to the principal entanglement gap, in each of the momentum sectors, are (a) 77 and (b) 51.

The $r = 1$ series is again the most stable and the range of $q^2\Delta$ limits is lower than in Fig. 4.6. With the exception of one competing topological phase at $\nu = 1/3$, the ground-state degeneracy follows the predictions of composite fermion theory throughout.

4.3.3 FCIs in $|C| = 3$ bands

For $|C| = 3$, we find stronger finite-size effects than in $|C| = 2$ bands. The Hilbert space dimension of the states is higher still for given N and thus, fewer high-particle-number systems are computationally accessible. Coupled with this, the energy spectra are difficult to analyze. Not only is the ground-state gap often ambiguous, but the spectra in general are complex, showing a plethora of competing geometric and topological physical effects. For these reasons, the analysis of the $|C| = 3$ fermionic states is omitted and we focus on the bosonic systems with contact interactions. Note that, just as in Sec. 4.3.2, all the systems in this section are within 1% of square geometries. Some of the systems were exactly square, but all filling factors required the use of some approximately square geometries within the scaling procedure.

Bosonic states

As in Secs. 4.3.1 and 4.3.2, we continue our analysis in a similar fashion and examine the effective continuum limit, followed by finite-size scaling to the thermodynamic limit

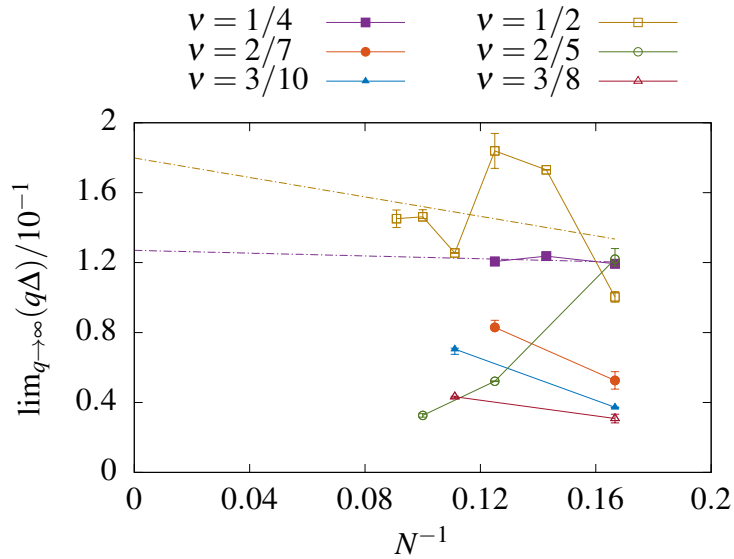


Fig. 4.18 Finite-size scaling of the gap to the thermodynamic effective continuum limit at fixed aspect ratio, for bosonic states in the $|C| = 3$ band. The extrapolation to the y-axis is shown for the robust $\nu = 1/4$ and $\nu = 1/2$ states. Squares, circles, and triangles denote states with $|r| = 1, 2, 3$, respectively, where the filled (hollow) symbols correspond to positive (negative) r .

where possible. Figure 4.18 shows the effective continuum limiting behavior for the six filling factors under consideration. As expected, due to computational limitations, fewer high-particle-number states are analyzed, compared to the $|C| = 2$ boson data in Fig. 4.8. Nevertheless, a reasonable sample is obtained, comparable to that of the $|C| = 2$ fermion data in Fig. 4.13. Overall, we have considered 18 different combinations of particle number and filling factor, with an average of ~ 25 different geometries for each. There are a total of 460 different exact diagonalization calculations underlying the data in this section.

We find smaller values for the $q\Delta$ limits, when compared to the lower Chern number ($|C| = 2$) scaling shown in Fig. 4.11. This is a general trend with increasing Chern number, which we discuss later.

A stable $r = 1$ series with $\nu = 1/4$ is observed. In this case, the thermodynamic effective continuum limit is extrapolated to be $\lim_{N, q \rightarrow \infty} (q\Delta) = 0.13 \pm 0.01^1$. The corresponding negative flux attached version of this series with $\nu = 1/2$ at $r = -1$ is also found to be exceptionally stable, with the gap exceeding that for $\nu = 1/4$, extrapolated as $\lim_{N, q \rightarrow \infty} (q\Delta) = 0.18 \pm 0.07^1$. The error bars due to the effective continuum limit are significant yet adequate, and more noticeable than those in Fig. 4.8.

The remaining data series are insufficient to make any comments on scaling to the thermodynamic effective continuum limit; however, the predicted ground-state degeneracies from composite fermion theory are observed at our finite N , and the finite many-body gaps show the potential for a robust gap in the thermodynamic effective continuum limit.

Figure 4.19 shows the plots for the six-particle $\nu = 3/8$ state. This system is selected as a case of interest, since it has a large ground-state degeneracy, and we obtain significant error bars for its effective continuum limit. The plot of the scaling of the gap in Fig. 4.19a shows the expected reciprocal relation, with some slight deviations due to the 1% square approximation of configurations. The plot of $q\Delta$ vs $1/q$ given in Fig. 4.19b shows these deviations in more detail. As previously mentioned, the small- q deviations may be attributed to finite-size effects and they stabilize as the MUC size is increased.

Four distinct energy spectra for different geometries realizing the six-particle $\nu = 3/8$ state are shown in Figs. 4.19c, 4.19d, 4.19e, & 4.19f. These cases differ in the realized shape of the MUC. Notice that the spectra shown in Figs. 4.19c & 4.19d correspond to the same $L_x \times L_y = 4 \times 4$ square configuration, and yield similar spectra. The other two spectra in Figs. 4.19e & 4.19f correspond to geometries with $L_x \times L_y = 1 \times 16$ and $L_x \times L_y = 2 \times 8$ MUCs, respectively, and yield qualitatively distinct features. (Again, these geometries are chosen with the maximum possible value of L_y consistent with the lattice size.) As a result of such distinct geometries, the fluctuations of the gap persist up to large values of q in the scaling shown in Fig. 4.19b. Geometric effects such as this give rise to the significant error bars in Fig. 4.18. The entanglement gaps for these systems are shown in Fig. 4.20. While the numerical value of Δ_ξ is relatively small, the opening of the gap confirms the topological nature of this state.

Correlation functions for the discussed filling factors are shown in Fig. 4.21. As for the bosons in the $|C| = 1, 2$ bands (Figs. 4.4a & 4.11a), only the primary composite fermion state with a flux attachment of $r = 1$ in Fig. 4.21a has a fully-formed correlation hole at zero separation. The correlation functions are again modulated by the Chern number, giving rise to $|C|^2$ sheets, which now is visible even in the color plots of our figures, for example, in Fig. 4.21f. In this Chern band, all of the correlation functions seem to show isotropy in the large-distance limit. However, small scale features are hard to discern. As with the $|C| = 2$ bosons in Fig. 4.11, for the cases with negative flux attachment ($r < 0$) the correlation function sheets do not converge to the same value at zero separation. This is shown in Figs. 4.21b, 4.21d, & 4.21f for this Chern band, mirroring the behaviors seen in Figs. 4.11b, 4.11d, & 4.11f for $|C| = 2$.

The PES for the remaining bosonic series in the $|C| = 3$ band have small but distinct gaps. Considering the spectra for the states in Fig. 4.21, we find Δ_ξ values of (a) 12.84, (b) 1.02,

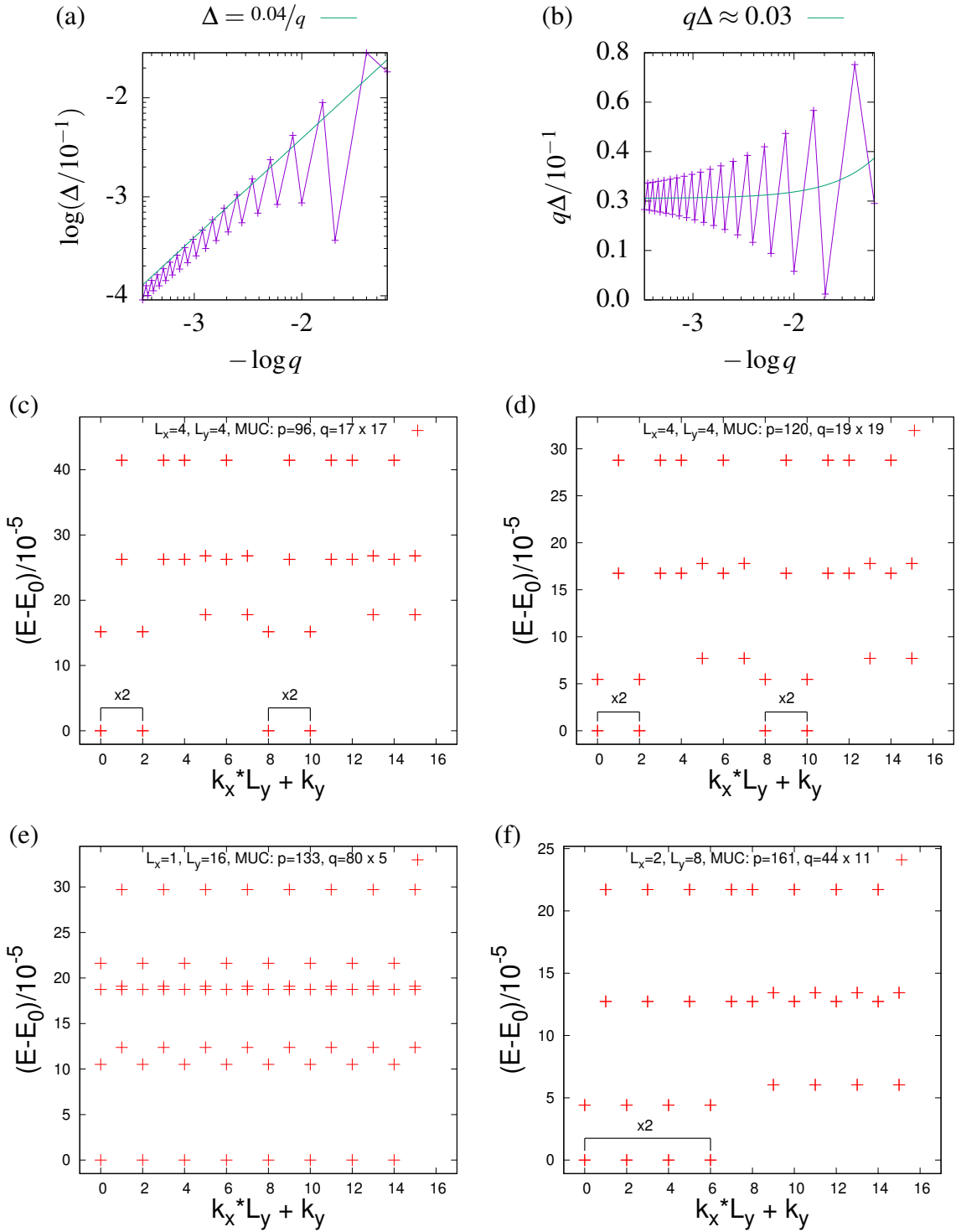


Fig. 4.19 [(a), (b)] Magnitude of the gap for bosonic six-particle $\nu = 3/8$ states in the $|C| = 3$ band, as a function of MUC size, q . [(c)–(f)] Energy spectra for the bosonic six-particle $\nu = 3/8$ state in the $|C| = 3$ band, at (c) $p = 96$, (d) $p = 120$, (e) $p = 133$, and (f) $p = 161$. The plots are resolved to $n = 4$ points per sector.

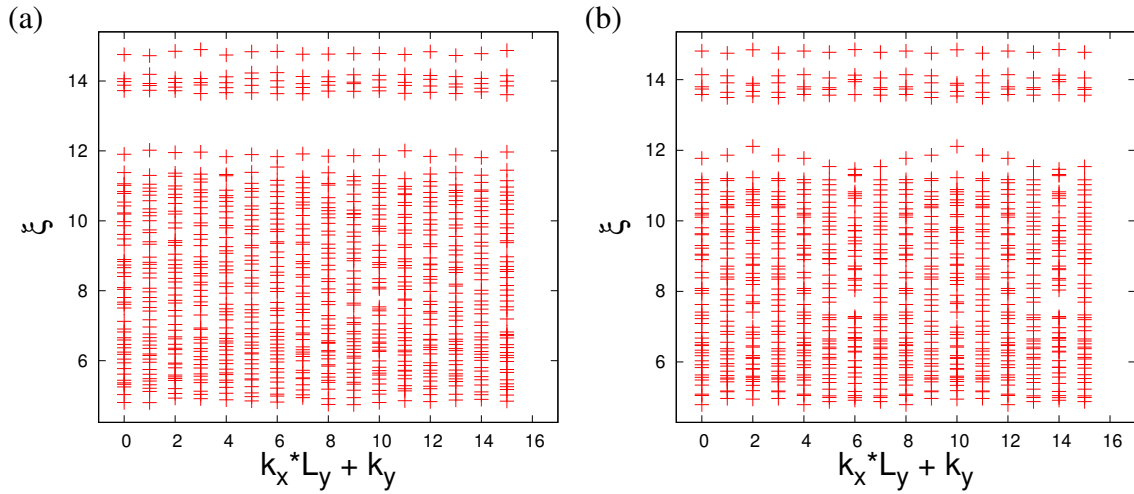


Fig. 4.20 PES for the bosonic six-particle $\nu = 3/8$ state in the $|C| = 3$ band with $N_A = \lfloor N/2 \rfloor = 3$, at (a) $p = 120$, and (b) $p = 133$. The count of eigenstates from the bottom of the spectrum up to the principal entanglement gap is 46 per momentum sector.

(c) 1.49, (d) 1.71, (e) 1.41, and (f) 1.92, after tracing out $\lfloor N/2 \rfloor$ particles. The corresponding eigenstate counts from the bottom of the spectra up to the principal entanglement gaps, in each of the momentum sectors, are (a) 51 (repeated for 28 sectors), (b) 323, 323, 323, 318, 318 (repeated for 18 sectors), (c) 1127, 1112, 1112, 1112 (repeated for 28 sectors), (d) 438, 432, 437, 432 (repeated for 20 sectors), (e) 1364, 1364, 1364, 1356, 1356, 1356 (repeated for 30 sectors), and (f) 46 (repeated for 16 sectors), respectively. In addition, these spectra typically show several smaller gaps higher in the spectrum. The primary composite fermion $\nu = 1/4$ state is again the largest and most distinct, with a uniform count of eigenstates below the principal entanglement gap, across the momentum spectrum.

4.4 Thermodynamic Limits and Scaling of the Effective Continuum Limit with Chern Number

In this section, we consolidate our analyses of the $|C| = 1, 2, 3$ bands in order to comment on the behavior of the thermodynamic limits that we could extrapolate from the effective continuum limits at finite system sizes.

Extrapolated thermodynamic limits for bosons are presented in Table 4.1a. One overarching characteristic of the plots in Figs. 4.2, 4.8, & 4.18 is the robust $r = 1$ series. The corresponding gaps are extracted and shown in Fig. 4.22a. Up to the $|C| = 3$ system, we find that $\lim_{q \rightarrow \infty} (q\Delta)$ for $N = 6$ scales approximately inversely with Chern number, as seen in

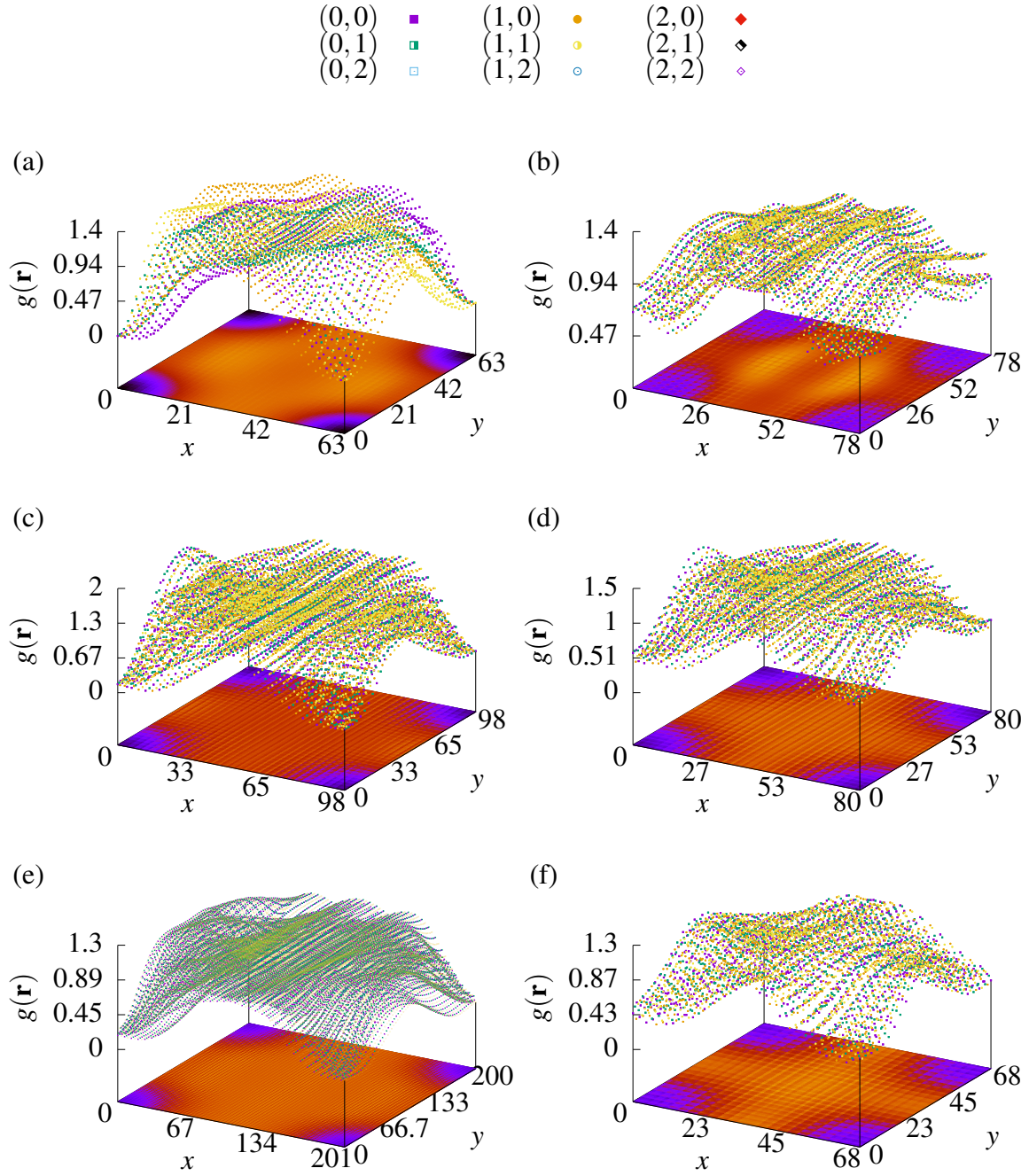


Fig. 4.21 Density-density correlation functions for bosonic states in the $|C| = 3$ band. The plots are shown for the lowest-lying ground state in the $(k_x, k_y) = (0, 0)$ momentum sector. The legend differentiates between correlation functions at lattice positions $(x \bmod 3, y \bmod 3)$, as explained in the main text. We show data for (a) $r = 1$: $\nu = 1/4$, $N = 7$, $p = 114$; (b) $r = -1$: $\nu = 1/2$, $N = 9$, $p = 113$; (c) $r = 2$: $\nu = 2/7$, $N = 8$, $p = 114$; (d) $r = -2$: $\nu = 2/5$, $N = 8$, $p = 107$; (e) $r = 3$: $\nu = 3/10$, $N = 9$, $p = 447$; and (f) $r = -3$: $\nu = 3/8$, $N = 6$, $p = 96$.

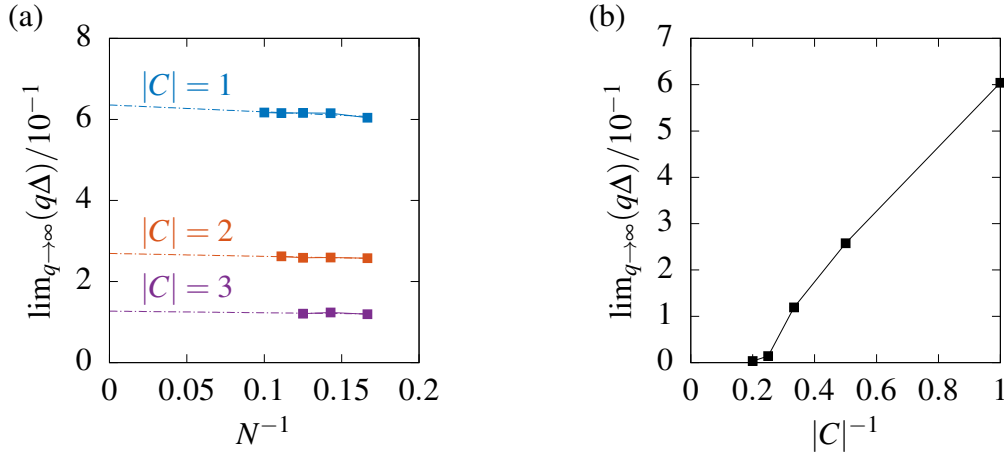


Fig. 4.22 (a) Finite-size scaling of the gap to the thermodynamic (effective) continuum limit at fixed aspect ratio, for robust $r = 1$ bosonic states. The filling factors are $\nu = 1/2, 1/3, 1/4$ for Chern numbers $|C| = 1, 2, 3$, respectively. (b) Finite-size scaling of the (effective) continuum limit of the gap at fixed aspect ratio, against Chern number, for robust $r = 1$ bosonic states with $N = 6$ particles. In both cases, all of the error bars are smaller than the data points on the scale of the plots.

Fig. 4.22b. In addition, we show that this (approximate) reciprocal relation does not hold precisely for the $|C| = 4, 5$ bands. However, we caution that our data are very limited in those cases.

We also highlight again the stable $r = -1$ series with filling $\nu = 1/2$ in $|C| = 3$ bands for which the gap is extrapolated to the thermodynamic effective continuum limit in Fig. 4.18. Since the larger- N systems should intuitively be given more weight when taking the limit, this value is perhaps an overestimate of the true thermodynamic effective continuum limit. This is captured by the larger error bars.

The thermodynamic effective continuum limits for the gaps of fermionic states are summarized in Table 4.1b. As for bosons, we find that the gap decreases with Chern number. However, due to computational expense, we did not consider enough Chern numbers to postulate a scaling relation. As seen before in Fig. 4.6, the $\nu = 1/3$ and $\nu = 2/3$ series yield the same thermodynamic effective continuum limit due to particle-hole symmetry. For the $\nu = 1/3$ series in the $|C| = 2$ band, shown in Fig. 4.6, we note intuitively that the extrapolated limit is perhaps an underestimate since larger- N systems should be given greater weight. Again, this is accounted for in the uncertainty.

Our studies of the density-density correlation functions for the higher Chern bands show some common features for the states with successful thermodynamic extrapolations. Compared to the other states, the correlation functions corresponding to the suc-

cessfully extrapolated series, shown in Figs. 4.4a, 4.11a, 4.21a, & 4.21b for bosons and in Figs. 4.7a, 4.7c, 4.16a, & 4.16b for fermions are characterized by smaller oscillations in the large distance limit and are more likely to be fully isotropic. This is consistent with small correlation lengths for these cases, as plausibly expected for states with small composite fermion filling factors $|r|$. In addition, the correlation functions of higher $|r|$ values also show some of the features expected for quantum Hall liquids such as a small-distance correlation hole. Most series for which we could not find a satisfactory thermodynamic (effective) continuum limit show visible oscillations throughout the simulation cell, which may be either indications of finite-size effects, or competing charge density wave orders.

All of the correlation functions for higher Chern bands show a characteristic modulation of the magnitude of correlations as a function of x - and y -positions modulo the Chern number and so give the appearance of $|C|^2$ correlation sheets. This modulation may also explain the continued sensitivity of the states to the geometry of the system, as simulation cell sizes which are multiples of the Chern number, i.e. geometries $N_x \bmod |C| = 0$ and $N_y \bmod |C| = 0$, are special but are generally difficult to realize in conjunction with all other constraints.

4.5 Discussion & Conclusions

In this chapter, we have quantitatively analyzed the composite fermion series of states for higher Chern number bands in the Harper-Hofstadter model [159, 161, 163]. Exact diagonalization calculations of these fractional quantum Hall liquids in the Hofstadter model are challenging, owing to numerous Diophantine constraints relating filling factor, flux density, and lattice geometry. We exploit the scaling of the energy scales in the size of the MUC, first observed by Bauer et al. [194], to resolve some of these commensuration issues. We are thus able to extract finite-size data exclusively for nearly square systems, leading to more reliable determination of the many-body gaps as compared to finite-size scaling at fixed flux density.

(a) bosons				(b) fermions			
$ C $	r	ν	$\lim_{N,q \rightarrow \infty}(q\Delta)$	$ C $	r	ν	$\lim_{N,q \rightarrow \infty}(q^2\Delta)$
1	1	1/2	0.64 ± 0.01	1	1	1/3	2.56 ± 0.02
2	1	1/3	0.27 ± 0.004		-2	2/3	2.56 ± 0.02
3	1	1/4	0.13 ± 0.01	2	1	1/5	0.46 ± 0.02
	-1	1/2	0.18 ± 0.07		-1	1/3	0.65 ± 0.16

Table 4.1 Summary of states with (effective) continuum limits that could be extrapolated to the thermodynamic limit, given to two decimal places, for (a) bosons and (b) fermions. The uncertainty quoted for the limit is the asymptotic standard error from a linear regression of $q\Delta$ against $1/N$.

We confirm that the prediction of composite fermion theory for the ground-state degeneracy is correct at all filling factors that we examined, with few exceptions due to competing phases. Several states were shown to have stable gaps in the thermodynamic (effective) continuum limit. Among these – as expected – the primary composite fermion states with filling factor $\nu = 1/(k|C| + 1)$ are the most robust, and we find that they have an (effective) continuum limit that is largely independent of particle number. We found several other states that allow for a reliable finite-size scaling of the gap, as summarized in Table 4.1. However, for many candidate phases predicted by composite fermion theory, we have found that scaling toward the (effective) continuum limit does not sufficiently alleviate finite-size effects to draw firm conclusions about their stability in the thermodynamic (effective) continuum limit. In part, this is due to the system-size limitations used in our study. The topological character of the different target phases has been clearly shown through the use of entanglement spectroscopy, which reveals the existence of entanglement gaps.

Our data also shed light on the fate of two potential BIQHE states in the Hofstadter model. A first candidate arises in $|C| = 1$ bands at filling $\nu = 2$, for $r = -2$ filled composite fermion levels. However, this state is clearly not realized within the lowest-band-projected Harper-Hofstadter model examined in this chapter, as we do not find the correct ground-state degeneracy of one for all system sizes. We therefore conjecture that the recently reported $\nu = 2$ state of hardcore bosons [191] likely requires filling of (at least) the lowest two Landau levels, which would bring it in line with other realizations of the BIQHE that require two flavors of bosons. The second candidate is the $\nu = 1$ state in $C = 2$ bands. Here, we find conclusively a large gap above a nondegenerate ground state for all system sizes. While the magnitude of the gap shows important variations with system size even after taking the

effective continuum limit, our data are consistent with the existence of a gapped phase in the thermodynamic effective continuum limit, subject to the known generic caveats [227].

In addition to spectral properties, we have studied the two-particle correlation functions of the Hofstadter model, revealing their unexpected structure which resembles a total of $|C|^2$ continuous sheets. This result is in disagreement with suggestions that Chern number C bands can be regarded as $|C|$ -layer quantum Hall systems. In this multilayer picture, we would only expect $|C|$ distinct correlation functions, so we hope that our results will stimulate further research that will clarify the origin of this discrepancy.

We have shown that approximately square geometries stabilize some of the expected isotropic quantum liquid phases predicted by composite fermion theory. In general, we find that variations of the gap due to a small change in aspect ratio are smaller than the finite-size effects but still remain significant. Hence, the sensitivity of the problem to details of the geometry seems to indicate that competing phases are likely to exist. Indeed, in addition to the isotropic quantum Hall liquids discussed in our work, several candidates for symmetry broken phases [208, 209] or phases combining a broken symmetry and topological response [164] have recently been proposed. We hope that the rich interplay of these competing phases will stimulate further active research in the physics of fractional topological insulators in Hofstadter models. Future research should focus on experimental probes for these regimes, as well as on specific realizations that can favor the various candidate phases, for example, via the effect of longer-range interactions or anisotropy.

Chapter 5

Direct Evaluation of the Force Constant Matrix in Quantum Monte Carlo

We develop a formalism to directly evaluate the matrix of force constants within a quantum Monte Carlo calculation. We utilize the matrix of force constants to accurately relax the positions of atoms in molecules and determine their vibrational modes, using a combination of variational and diffusion Monte Carlo. The computed bond lengths differ by less than 0.007 Å from the experimental results for all four tested molecules. For hydrogen and hydrogen chloride, we obtain fundamental vibrational frequencies within 0.1% of experimental results and ~ 10 times more accurate than leading computational methods. For carbon dioxide and methane, the vibrational frequency obtained is on average within 1.1% of the experimental result, which is at least three times closer than results using restricted Hartree-Fock and density functional theory with a PBE functional and comparable or better than density functional theory with a semi-empirical functional.

5.1 Introduction

Quantum Monte Carlo (QMC) is a leading class of approaches used to establish and study the electronic ground state of molecules and solids. Specifically, diffusion Monte Carlo (DMC) is widely used to project out the exact electronic ground-state wave function of a system, subject only to the fixed node approximation, fully accounting for correlation effects such as van der Waals interactions [228, 229]. Although DMC is an ideal tool for studying the electronic wave function of the system [230], the determination of the wave function of the atoms – their expected positions and energy landscape – remains a challenge for the method. Several approaches have been put forward to calculate the force acting on the atoms with

DMC [65, 91, 92, 231–235], but a more comprehensive characterization of the atomic wave function requires the second derivative of the energy – the matrix of force constants – to both efficiently relax atomic positions and calculate vibrational modes.

We propose a method to directly calculate the matrix of force constants, $d^2E/d\mathbf{R}_I d\mathbf{R}_J$, where \mathbf{R}_I is the position of the I th, and \mathbf{R}_J the J th, atom in the system. The energy, $E = \langle \hat{H} \rangle$, is calculated in the Born-Oppenheimer approximation of Hamiltonian \hat{H} ; that is with the electrons always in their ground state for the respective atomic configuration. The calculation is implemented in QMC through a new quantum mechanical expectation value, $d^2\langle \hat{H} \rangle/d\mathbf{R}_I d\mathbf{R}_J$, meaning that it can be evaluated with one configuration of the atoms to recover the entire matrix of force constants. The matrix of force constants allows us to efficiently relax atomic positions and determine the vibrational modes.

We start by introducing the formalism and the QMC methods in Sec. 5.2. We subsequently outline the applications and implementation of the matrix of force constants in Sec. 5.3, followed by a series of case studies in Sec. 5.4. We begin with atomic and diatomic hydrogen, and then move on to hydrogen chloride, carbon dioxide, and methane. For each molecule we derive the matrix of force constants, relax the positions of the atoms, and determine the vibrational modes. We critically evaluate the results with respect to existing computational methods: restricted Hartree-Fock (RHF) [236–238] and density functional theory (DFT) [45, 239]. Finally, in Sec. 5.5 we summarize the results and discuss future opportunities for the new formalism.

5.2 Formalism

In this section, we present the matrix of force constants. We then outline the numerics by discussing how the electronic orbitals are generated and the details of the QMC algorithms.

5.2.1 Matrix of force constants

We consider many-body quantum systems comprised of N_n nuclei and N_e electrons. The three-dimensional position vectors are denoted as \mathbf{R}_I for nuclei and \mathbf{r}_i for electrons, with $I = 1, \dots, N_n$ and $i = 1, \dots, N_e$. These are used to construct the corresponding multi-dimensional vectors in configuration phase space: $\mathbf{R} \equiv (\mathbf{R}_1, \dots, \mathbf{R}_{N_n})$ and $\mathbf{r} \equiv (\mathbf{r}_1, \dots, \mathbf{r}_{N_e})$.

We use the non-relativistic Hamiltonian [62]

$$\hat{H} = -\frac{1}{2} \sum_{i=1}^{N_e} \nabla_{\mathbf{r}_i}^2 + \sum_{i < j}^{N_e} \frac{1}{|\mathbf{r}_i - \mathbf{r}_j|} - \sum_{i=1}^{N_e} \sum_{I=1}^{N_n} V_I(\mathbf{R}_I - \mathbf{r}_i) + \sum_{I < J}^{N_n} \frac{Z_I Z_J}{|\mathbf{R}_I - \mathbf{R}_J|},$$

which is comprised of the electron kinetic energy, as well as the electron-electron, electron-ion, and ion-ion interactions¹. V_I and Z_I represent the electron-ion pseudopotential and full nuclear charge, of atom I , respectively. We use a Hartree-Fock average effective Trail-Needs pseudopotential [240], which has been specifically optimized for DMC calculations, to screen the effects of the core electrons and nucleus on the valence electrons.

In an electron position basis, the expectation value of the energy [92] may be written as

$$E = \frac{\int \Psi^* \hat{H} \Psi \, d\mathbf{r}}{\int |\Psi|^2 \, d\mathbf{r}},$$

where the many-body wave function, Ψ , and Hamiltonian, \hat{H} , are both functions of nucleus configuration, \mathbf{R} , and electron configuration, \mathbf{r} .

The force acting on ion I is defined as the negative total derivative of the energy with respect to the nuclear coordinates. Taking the first derivative of the energy with respect to atom position [92] yields

$$\frac{dE}{d\mathbf{R}_I} = \frac{\int \Psi^* \frac{d\hat{H}}{d\mathbf{R}_I} \Psi \, d\mathbf{r}}{\int |\Psi|^2 \, d\mathbf{r}} + \left[\frac{\int \frac{d\Psi^*}{d\mathbf{R}_I} (\hat{H} - E) \Psi \, d\mathbf{r}}{\int |\Psi|^2 \, d\mathbf{r}} + \text{c.c.} \right],$$

which is decomposed into Hellmann-Feynman and Pulay terms, respectively. When the wave functions are exact eigenstates of the Hamiltonian, such that $(\hat{H} - E)\Psi = 0$, the Pulay term vanishes. However in practice, the wave functions are not exact in variational Monte Carlo (VMC) or DMC, so the Pulay term needs to be included to obtain the total force.

In this chapter, we derive the matrix of force constants from the second derivative of the energy, which takes the form of

$$\begin{aligned} \frac{d^2E}{d\mathbf{R}_I d\mathbf{R}_J} = & \frac{\int \Psi^* \frac{d^2\hat{H}}{d\mathbf{R}_I d\mathbf{R}_J} \Psi \, d\mathbf{r}}{\int |\Psi|^2 \, d\mathbf{r}} + \frac{\int \Psi^* \left[\frac{d\Psi}{d\mathbf{R}_I} \left(\Psi^{-1} \frac{d\hat{H}}{d\mathbf{R}_J} \Psi - \frac{dE}{d\mathbf{R}_J} \right) + (I \leftrightarrow J) \right] \, d\mathbf{r}}{2 \int |\Psi|^2 \, d\mathbf{r}} \\ & + \frac{\int \left[\frac{d}{d\mathbf{R}_J} \left[\frac{d\Psi}{d\mathbf{R}_I} (\hat{H} - E) \Psi \right] + (I \leftrightarrow J) \right] \, d\mathbf{r}}{2 \int |\Psi|^2 \, d\mathbf{r}} + \text{c.c.} \end{aligned}$$

This comprises one component of the matrix of force constants, so we must cycle over all atom pairs $\{I, J\}$ to determine the entire matrix. The second derivative of the Hamiltonian with respect to atom position does not commute with the Hamiltonian, hence we approximate the pure expectation value of the force constants in the DMC procedure, as discussed in

¹We work with Hartree atomic units $\hbar = m_e = e \equiv 1$.

Sec. 5.2.3. The first two terms of the matrix of force constants stem from the Hellmann-Feynman force, whereas the third is due to the Pulay force.

To calculate the entire matrix of force constants using the Monte Carlo algorithm, we need to compute the ion-ion and electron-ion components at a cost of at most $O(N_n^3 N_e) + O(N_n^2 N_e^2)$. This leads to an overall dominant scaling of $O(N_n^4)$ assuming $O(N_n) \propto O(N_e)$.

Having evaluated the matrix of force constants and implemented the formalism we can then use it to study atomic relaxation and vibrational modes.

5.2.2 Variational Monte Carlo

For the fermionic many-body trial wave function in the VMC method [67], we take a Slater-Jastrow wave function of the form [62]:

$$\Psi_T = e^J D_\uparrow D_\downarrow,$$

where $D_\uparrow(D_\downarrow)$ denotes the Slater determinant of the molecular spin-up(down) orbitals. Here, the usual Hartree-Fock ansatz, $\Psi_{\text{HF}} = D_\uparrow D_\downarrow$, which encodes Pauli exclusion through the anti-symmetry of the Slater determinant, is multiplied by a Jastrow factor, e^J , which is an optimizable function used to impose further constraints on Ψ_T .

Initially, we compute the VMC energy, which is the expectation value of the Hamiltonian operator with respect to the trial wave function [92]:

$$E_{\text{VMC}} = \frac{\int |\Psi_T(\mathbf{r})|^2 E_L(\mathbf{r}) \, d\mathbf{r}}{\int |\Psi_T(\mathbf{r})|^2 \, d\mathbf{r}},$$

where $E_L = \Psi_T^{-1}(\mathbf{r}) \hat{H} \Psi_T(\mathbf{r})$ is the local energy, $d\mathbf{r}$ is the infinitesimal hypervolume element in electron configuration phase space, and the integrals are performed using Monte Carlo² in the CASINO program [35].

Single-particle orbitals for the different molecular structures were calculated using the CRYSTAL program [58]. The RHF and DFT calculations with two exchange-correlation functionals: the PBE [53] GGA containing no exact orbital exchange, and the B3LYP [241–243] hybrid functional containing a fixed amount of exact exchange were performed with triple- ζ -valence Gaussian basis sets, as well as polarization and diffuse basis functions [244]. The exact exchange-correlation functional is unknown and the choice of functional depends heavily on the system and the property of interest. PBE as a general functional was chosen for its greater predictive power across all simulations and properties [245], though it is less likely

²Specifically, the Metropolis algorithm is used to generate a set of configurations distributed according to the square modulus of a trial wave function over which the local energy is averaged.

to achieve the accuracy of a semi-empirical functional such as B3LYP, which was chosen in addition for its good agreement with post-DFT methods within its range of applicability on molecules [246, 247]. We use a Jastrow factor in its most general form comprising of an electron-electron term, an electron-nucleus term, and an electron-electron-nucleus term. The wave function parameters are optimized by using the variance minimization method [248] first, followed by the energy minimization method [249–251].

5.2.3 Diffusion Monte Carlo

DMC evolves a wave function, Φ , according to the imaginary-time Schrödinger equation, in order to project out the lowest energy eigenstate, Φ_0 , with the same nodal surface as the trial wave function [62].

The efficiency of the DMC algorithm is improved by importance sampling [68]. By multiplying the wave function, Φ , by a trial wave function, Ψ_T from VMC, we may solve the Schrödinger equation for the mixed distribution $f(\mathbf{r}, \tau) = \Phi(\mathbf{r}, \tau)\Psi_T(\mathbf{r})$, where τ denotes imaginary time. We found negligible error with time-steps of $\tau = 0.01$ a.u., and so this is used throughout [252]. The fixed-node approximation [79, 80] is introduced to overcome the fermion sign problem by constraining the nodal surface of Φ_0 to match that of Ψ_T .³

The expectation value of the energy in the DMC method [92] is given by

$$E_{\text{DMC}} = \frac{\int \Phi(\mathbf{r})\Psi_T(\mathbf{r})E_L(\mathbf{r}) \, d\mathbf{r}}{\int \Phi(\mathbf{r})\Psi_T(\mathbf{r}) \, d\mathbf{r}}.$$

This is an unbiased estimator, up to the approximations made, since E_{DMC} does not depend on the trial wave function used. However, the mixed expectation value of an operator that does not commute with the Hamiltonian is biased. In these cases, we approximate the pure expectation value of an operator \hat{O} with the extrapolation formula [253]

$$O = 2O_{\text{DMC}} - O_{\text{VMC}} + \mathcal{O}[(\Phi - \Psi_T)^2].$$

Alternatively, the future-walking method may be used, for example, to obtain an exact pure estimator [89]. Although the extrapolation formula improves the results, this procedure depends on an almost complete error cancellation and is strongly dependent on the quality of the wave function employed. We run the simulations for longer to systematically reduce the statistical error associated with variational techniques.

³The fixed-node approximation is the only uncontrolled approximation in a DMC simulation of all-electron systems.

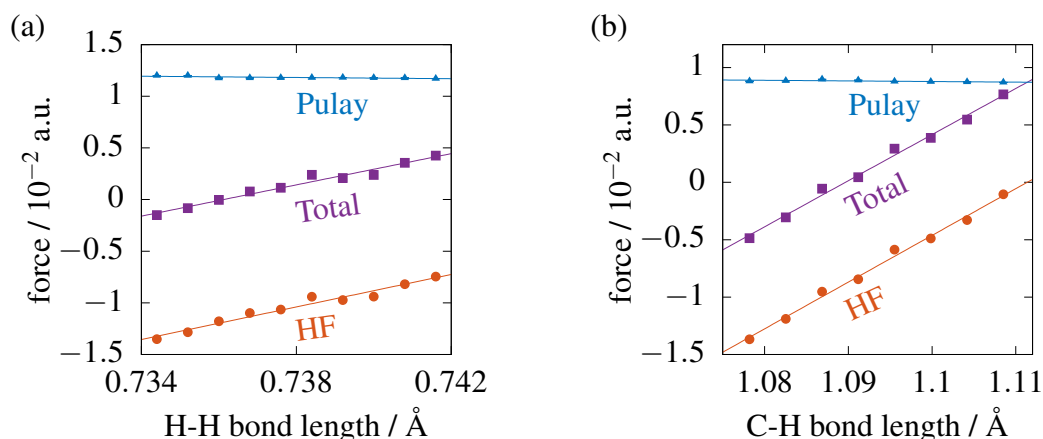


Fig. 5.1 Interatomic force estimates for the molecules (a) H₂ and (b) CH₄. The red dots correspond to the Hellmann-Feynman (HF) force, the blue triangles to the Pulay force, and the magenta squares to the total force. Error bars for all of the data are given – some error bars are smaller than the data points on the scale of the plot.

5.2.4 Contributions of the Hellmann-Feynman and Pulay terms

Both the Hellmann-Feynman and Pulay terms contribute to the force and matrix of force constants, and both Pulay terms are zero at the exact electronic ground state. However, the Pulay contribution to the matrix of force constants contains a second derivative of the wave function with respect to atom position, and so is more susceptible to steep gradients due to an incorrect trial wave function. Therefore, when using the electronic structure methods, it is useful to determine the relative contributions of the Hellmann-Feynman and Pulay terms so that we can gauge the importance of refining the electronic wave function.

The interatomic force in a hydrogen molecule and methane molecule is shown in Fig. 5.1. Different bond lengths within the vicinity of the equilibrium were chosen and forces were evaluated using the methods described in Secs. 5.2.2 and 5.2.3. The addition of the Pulay force to the Hellmann-Feynman force shifts the equilibrium bond length by 2% in both examples, therefore the Pulay force is crucial for finding the correct equilibrium geometry.

We now turn to consider the calculation of the matrix of force constants – the gradient of the force. We first note from Fig. 5.1 that the Pulay force is remarkably constant with respect to bond length across all molecules tested in this chapter, regardless of the molecular geometry. This means that the gradient of the force is negligible, and therefore does not significantly contribute to the matrix of force constants. We find that, when directly evaluated, the value of the Pulay term in the matrix of force constants is smaller than its standard error, as well as the standard error of the contribution from the Hellmann-Feynman term. Furthermore,

based on the analysis of variance at the $\alpha = 0.05$ level, the gradient of the Pulay force does not significantly deviate from zero. This means that the change in vibrational frequency due to the Pulay force gradient is just 1% of that from the Hellmann-Feynman gradient for both hydrogen and methane. This conclusion is also backed up by independent studies: taking a numerical derivative of the results for H₂ and LiH reported by Casalegno et al. [254], CO₂ reported by Lee et al. [255], as well as adenine-thymine reported by Ruiz-Serrano et al. [256], confirms the small contribution of the Pulay term to the matrix of force constants.

The effect of the Pulay term in the force is significant for force analysis and, when suitably formulated, can reduce the statistical noise in the expectation value and improve the convergence of the optimization algorithm [256]. However, as the Pulay force is almost constant with interatomic bond length, its contribution to the matrix of force constants is negligible. Therefore, we expect the Pulay contribution to the matrix of force constants to be insensitive to the quality of the trial wave function. Another corollary is that for our zero-variance scheme [71, 257], the expected $-5/2$ power-law tail associated with infinite variance that could arise from Pulay terms [92, 258] will only make a limited contribution to the tail of the total probability distribution.⁴

5.3 Applications of Force Constants

5.3.1 Atomic relaxation

The primary requirement for a versatile geometry model, is the ability to minimize the energy of an arbitrary configuration of atoms [259]. For quantum mechanical simulations, this is often performed using VMC, due to the algorithm's efficiency. In this chapter, we relax the positions of the atoms first with VMC using the additional information provided by the matrix of force constants. The wave function from VMC is then optimized in DMC and we perform the same iteration steps using DMC to confirm convergence and further reduce the error [260–263].

Requiring that the energy of the system is constant up to quadratic order in atomic displacement, and explicitly correcting for global translation and rotation, we find that the atomic displacement, $\Delta\mathbf{R}$, is given by

$$\Delta\mathbf{R} = -2\mathbf{M}^{-1} \cdot \nabla_{\mathbf{R}} E - \frac{\sum_I m_I \mathbf{R}_I}{\sum_I m_I} - \mathbf{R} \times \boldsymbol{\theta}, \quad (5.1)$$

⁴As shown in Fig. 5.4, we have not been hindered by this problem in our practical application.

where $\mathbf{M} \equiv d^2E/d\mathbf{R}_I d\mathbf{R}_J$ is the matrix of force constants; $\nabla_{\mathbf{R}}E \equiv dE/d\mathbf{R}_I$ is the multi-particle gradient of the energy with respect to atom position; and θ is the three-dimensional global angular displacement vector for the configuration \mathbf{R} . On each step, we displace the atoms by $\Delta\mathbf{R}$ in order to compare with other methods in determining the minimum energy of the system. This yields the interatomic bond length at the minimum of the total potential. The details of the calculation are outlined in Appendix C.1.

Though $\langle \hat{\mathbf{R}} \rangle$ minimizes the total potential after the atomic relaxation procedure, if the potential is not symmetric then the expected separation of the atoms does not coincide with the minimum. We capture the lowest-order difference with the addition of an anharmonic correction term, outlined in Appendix C.1.4.

5.3.2 Vibrational modes

One main motivation for incorporating the matrix of force constants into the QMC procedure is the ability to calculate vibrational modes and frequencies directly. In this chapter, we use a variety of methods to calculate the vibrational frequency for a cross comparison.

Up to a simple mapping, the eigenvectors of the matrix of force constants correspond to the vibrational modes of the system, and the eigenvalues correspond to the vibrational frequencies. We can, therefore, use a complete diagonalization of the matrix of force constants to estimate the eigenmodes and frequencies. To benchmark the results, we also calculate the frequencies from a numerical second derivative of the energy with respect to bond length – referred to as the energy curvature (EC) method – and from a numerical derivative of the force – force gradient (FG) method.

A discussion of all of these methods, including the analysis of statistical uncertainty and the anharmonic correction, is detailed in Appendix C.2.

5.4 Case Studies

In this section, we evaluate the effectiveness of the matrix of force constants formalism for a selection of molecules. We first confirm the theory with the simplest possible molecules, before testing the generalizability of the formalism on molecules containing more atoms.

5.4.1 Hydrogen atom and molecule

We begin by analyzing the simplest physical system: the hydrogen atom. By performing a DMC calculation, we verify that the hydrogen atom obeys Newton's laws since it has a net force of $(3.68 \pm 5.17) \times 10^{-3} E_h \text{\AA}^{-1}$ acting on it, which is zero within standard error.

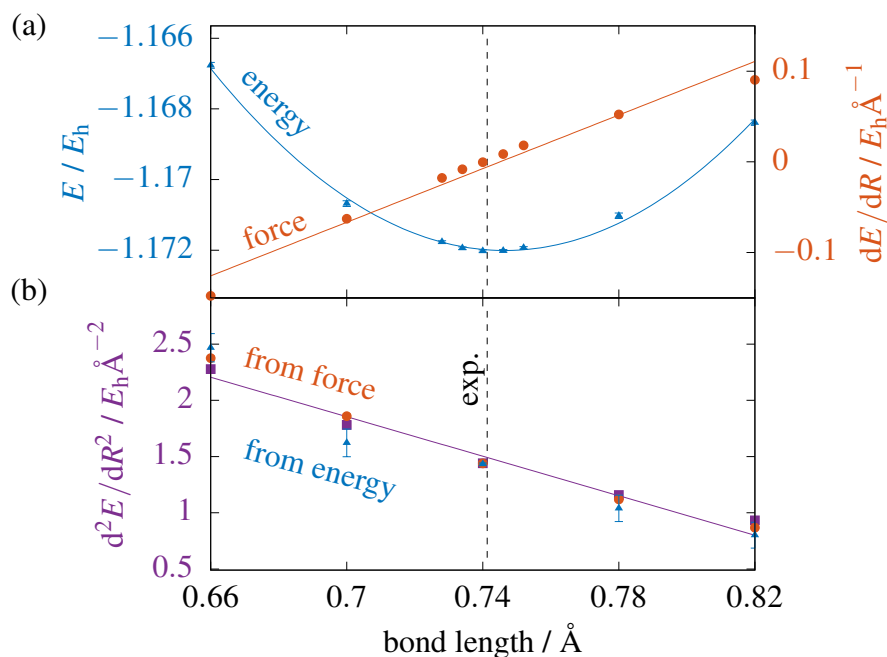


Fig. 5.2 (a) Energy, force, and (b) diagonal force constant against bond length, for the hydrogen molecule. For the energy and force plots, the parabolic and linear curves of best fit for the visible data, are overlaid. For the force constant plots, we show the diagonal force constant derived using the finite-difference method from the energy curvature, the force gradient, and the direct analytical evaluation of the matrix of force constants. The line of best fit for the visible MFC data is overlaid. The dashed line indicates the experimental equilibrium bond length. Error bars for all of the data are given – some error bars are smaller than the data points on the scale of the plot.

Furthermore, the hydrogen atom has a computed eigenfrequency of 0 cm^{-1} . This system behaves as expected and confirms the translational invariance.

From this, it is natural to increment the complexity by adding another hydrogen atom to form an H_2 molecule. This is the simplest physical example that allows us to verify the eigenfrequencies from our DMC method, which has no nodes and gives an exact wave function, by comparing them against both experimental results in the literature, and RHF/DFT predictions from the CRYSTAL program.

The energy, force, and diagonal elements of the matrix of force constants for the hydrogen atom are shown as a function of bond length in Fig. 5.2. We verify that the energy is at a minimum and the force is zero at the correct equilibrium bond length of 74.13 pm [264], within standard error. Furthermore, in Fig. 5.2b, we show that in the vicinity of the equilibrium bond length for the hydrogen molecule, the energy curvature, the force gradient, and the direct computation, all agree within error bounds. The entire matrix of force constants is sparse. If

we are only interested in the vibrational mode, it can be reduced to be a 2×2 matrix, with the off-diagonal force constants to be minus the diagonal elements within error, as required by symmetry⁵. Note that here the diagonal elements of the matrix of force constants are not constant across the range of bond lengths shown, as can also be seen in the slight curvature of the force in Fig. 5.2a. This is due to the anharmonicity of the potential in a diatomic molecule. We may use the gradient of the force constant to calculate the anharmonic constant, and correct for the anharmonicity, as discussed in Appendix C.1.4.

For the hydrogen molecule, it is possible to extract the matrix of force constants efficiently from the force, or energy, because the computational cost of obtaining the numerical derivatives is low. However, for more complicated molecules, where structural optimization is influential, using the matrix of force constants would be beneficial, as it provides both the movement direction and amplitude towards the minimum energy configuration. In these cases, the equivalent information would take considerably longer to extrapolate from either energy or force, if possible.

Equipped with reliable results for the matrix of force constants directly from DMC at each bond length, we may now exploit this information to efficiently relax the bond length of the molecule. The force tells us the direction to move the atoms, and the matrix of force constants additionally tells us how far to move them, on each step (Eq. 5.1). Owing to the anharmonicity of the potential, we must relax to the equilibrium bond length of 74.13 pm over several steps. The predicted bond length on the next atomic relaxation step as a function of initial bond length is shown in Fig. 5.3. We see that the PBE curve intersects the equilibrium line at 0.753 Å and the B3LYP curve intersects at 0.745 Å ; whereas our DMC calculation intersects at 0.7420 ± 0.0007 Å, in close agreement with the experimental value of 0.74130 Å [264].⁶ Furthermore, we note that PBE and B3LYP curves have a similar shape as a result of sharing the same optimization algorithm. However, both are steeper than the DMC curve in the vicinity of equilibrium and therefore converge more slowly, due to the fact that the DFT algorithm uses an inaccurate estimate for the force constant. The number of iteration steps reduced are particularly apparent when there are multiple atoms in a molecule, however the lower number of steps does not necessarily indicate a more efficient algorithm, as the complexity of each step needs to be taken into consideration. In some cases where complex molecules cannot be relaxed sufficiently for a long time using DFT, our approach may be more efficient in determining the ground-state geometry. In general, due to DFT's

⁵The diagonal elements of the matrix of force constants are the same for the hydrogen molecule, and hence no particular atom is specified when referring to d^2E/dR^2 in Figs. 5.2 & 5.4.

⁶Note that the turning points of the PBE, B3LYP and DMC curves in Fig. 5.3 do not correspond to fixed points, but rather the fixed points are given by the intersections of the curves with the equilibrium line.

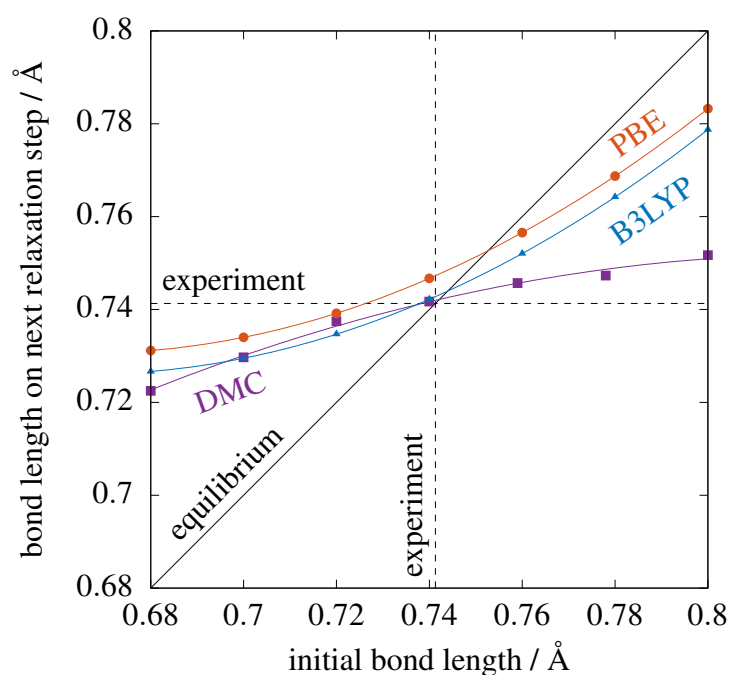


Fig. 5.3 Bond length on next step of atomic relaxation as a function of initial bond length, for the hydrogen molecule. The unconstrained parabolas of best fit, with respect to the visible DFT (PBE, B3LYP) and DMC data points, are overlaid. The dashed lines indicate the experimental equilibrium bond length, whereas the solid line indicates the equilibrium fixed points with respect to the plot. DMC error bars are smaller than the data points on the scale of the plot.

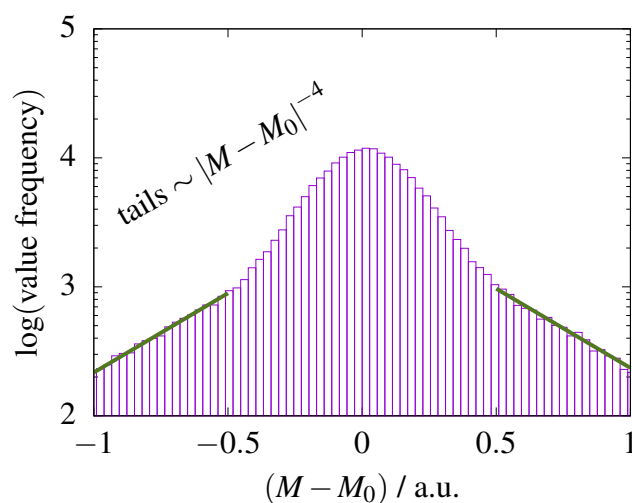


Fig. 5.4 Distribution of probability densities for the observed values of an element of the matrix of force constants from DMC, offset by the mean M_0 . Data are shown for the hydrogen molecule at the equilibrium bond length.

mode	ω_{RHF}	ω_{PBE}	ω_{B3LYP}	ω_{EC}	ω_{FG}	ω_{DMC}	$\omega_{\text{exp}}[265]$
stretch	4379	4116	4384	4170 ± 10	4180 ± 8	4166 ± 4	4161.1663 ± 0.0002

Table 5.1 Vibrational frequencies, evaluated at the computed equilibrium bond length, for the hydrogen molecule in units of cm^{-1} , where ω_{RHF} denotes the vibrational frequency obtained from a RHF calculation, ω_{PBE} and ω_{B3LYP} from DFT calculations with a PBE/B3LYP functional, ω_{EC} from the curvature of the DMC energy, ω_{FG} from the gradient of the DMC force, ω_{DMC} from the DMC matrix of force constants, and ω_{exp} from experiment. All values are presented at zero temperature and post anharmonic corrections. These quantities, as well as their associated errors, are discussed in Appendix C.2.

inaccurate estimate of the force constant, we observe at least a slight improvement for all molecules.

An additional important check, before we proceed, is an analysis of the probability distribution of the matrix of force constants generated by DMC. Fig. 5.4 shows the histogram of a force constant value for the DMC run at the computed equilibrium bond length. From this we can see that the force constant heavy tails decay with the same $\sim |M - M_0|^{-4}$ power law as the energy and Hellmann-Feynman force [92, 258]. This is as expected, since the effective remaining term is the Hellmann-Feynman term due to the quasi-constant Pulay contribution in proximity to the ground state, as seen in Sec. 5.2.4. Reassuringly, the expected value of the distribution is also the modal value.

Now that the configuration is relaxed, we may analyze the fundamental vibrational modes. For the hydrogen molecule, we obtain six eigenmodes, as expected for a diatomic molecule. Three modes correspond to global translation, two correspond to global rotation, and one corresponds to a symmetric stretch. The symmetric stretch mode has the largest eigenfrequency. We extract the frequency using a selection of methods, outlined in Appendix C.2, for a cross-comparison. In this case, we obtain a fundamental vibrational frequency of $\omega_{\text{DMC}} = 4166 \pm 4 \text{ cm}^{-1}$, compared to the experimental value of $\omega_{\text{exp}} = 4161.1663 \pm 0.0002 \text{ cm}^{-1}$, which is 4.83 cm^{-1} away. This is a firm statistical confirmation of the accuracy of DMC compared to RHF, PBE and B3LYP results, which have deviations of 218 cm^{-1} , 45 cm^{-1} and 223 cm^{-1} from experiment, respectively. All of our computational values for the vibrational frequency from DMC – matrix of force constants, force gradient, and energy curvature – agree with each other within standard error and show close agreement to experiment. The DMC procedure yields no translational or rotational modes, just as for the hydrogen atom. A summary of the results is shown in Table 5.1. Note that the less computationally expensive calculation of the energy was run for four times longer, compared to the force gradient and matrix of force constant methods, in order to give the error bars of the energy curvature eigenfrequency to a comparable value.

5.4.2 Hydrogen chloride

Now that we have verified that the matrix of force constants agrees with numerical estimates, and that by exploiting this information it is possible to relax the molecule more efficiently, and outperform RHF and DFT estimates for the fundamental vibrational frequency for the hydrogen case, we move onto a more complex molecule: hydrogen chloride. We increment the complexity of our case study in order to verify that our formalism can cope with an asymmetric system with unequal masses.

The hydrogen chloride molecule again relaxes quickly to equilibrium, with a computed bond length of $128.0 \pm 0.6 \text{ pm}$, which agrees with the experimental value of 127.5 pm within standard error. Both atoms have the appropriate displacement to ensure that the center of mass is stationary. We obtain six eigenmodes for the system, including one symmetric stretch mode with eigenfrequency $\omega_{\text{DMC}} = 2995 \pm 8 \text{ cm}^{-1}$. This result agrees with the experimental value of $\omega_{\text{exp}} = 2990.946 \pm 0.003 \text{ cm}^{-1}$ within standard error, whereas RHF, PBE, B3LYP methods are 107 cm^{-1} , 112 cm^{-1} , 50 cm^{-1} away, respectively. A summary of the results is shown in Table 5.2a.

(a) hydrogen chloride					
mode	ω_{RHF}	ω_{PBE}	ω_{B3LYP}	ω_{DMC}	$\omega_{\text{exp}}[266]$
stretch	3098	2879	2941	2995 ± 8	2990.946 ± 0.003
(b) carbon dioxide					
mode	ω_{RHF}	ω_{PBE}	ω_{B3LYP}	ω_{DMC}	$\omega_{\text{exp}}[267]$
sym. stretch	1468	1284	1325	1309 ± 5	1333 ± 6
antisym. stretch	2480	2297	2321	2312 ± 6	2349 ± 1
bending	766	634	664	662 ± 2	667 ± 1
(c) methane					
mode	ω_{RHF}	ω_{PBE}	ω_{B3LYP}	ω_{DMC}	$\omega_{\text{exp}}[267]$
sym. stretch	3101	3034	3074	2874 ± 8	2917 ± 1
scissor	1655	1496	1544	1534 ± 9	1534 ± 1

Table 5.2 Vibrational frequencies, evaluated at the computed equilibrium bond length, for (a) the hydrogen chloride, (b) carbon dioxide, and (c) methane molecules in units of cm^{-1} , where ω_{RHF} denotes the vibrational frequency obtained from a RHF calculation, ω_{PBE} and ω_{B3LYP} from DFT calculations with a PBE/B3LYP functional, ω_{DMC} from a DMC calculation, and ω_{exp} from experiment. All values are presented at zero temperature and post anharmonic corrections. These quantities, as well as their associated errors, are discussed in Appendix C.2.

molecule	x_0^{RHF}	x_0^{PBE}	x_0^{B3LYP}	x_0^{DMC}	$x_0^{\text{exp}} [264]$
H ₂	0.736	0.753	0.745	0.7420 ± 0.0007	0.74130
HCl	1.260	1.286	1.278	1.280 ± 0.006	1.275
CO ₂	1.145	1.182	1.171	1.167 ± 0.003	1.1598
CH ₄	1.089	1.104	1.098	1.097 ± 0.002	1.093

Table 5.3 Computed equilibrium bond lengths for the hydrogen, hydrogen chloride, carbon dioxide, and methane molecules, in units of Å, where x_0^{RHF} denotes the equilibrium bond length obtained from a RHF calculation, x_0^{PBE} and x_0^{B3LYP} from DFT calculations with a PBE/B3LYP functional, x_0^{DMC} from a DMC calculation, and x_0^{exp} from experiment. The details of the atomic relaxation calculation in DMC are discussed in Appendix C.1.

5.4.3 Carbon dioxide

In the previous two examples, we found that the matrix of force constants can correctly calculate the modes of a diatomic molecule. Building on this, we increment the complexity to carbon dioxide: a three-atom system with several non-trivial vibrational modes, some of which are in orthogonal directions.

In this case, the $\text{O}=\text{C}=\text{O}$ configuration is relaxed to an equilibrium $\text{C}=\text{O}$ bond length of 116.7 ± 0.3 pm along one axis, which is within three standard deviations of the experimental value of 115.98 pm. For carbon dioxide, we obtain nine vibrational modes: three of which correspond to global translations, two to global rotations, and four to vibrational modes. Of the vibrational modes, we obtain one symmetric stretch mode, one asymmetric stretch mode, and two bending modes along orthogonal axes.

The modes examined in this section show a consistent improvement over the RHF and PBE calculations, with DMC eigenfrequency deviations from experiment of -1.80% (symmetric), -1.58% (antisymmetric), and -0.75% (bending). The recovery of the non-trivial antisymmetric mode is our first example to break the underlying symmetry of the molecule, and the bending mode shows that our formalism can extend to atoms moving in orthogonal directions. On average, our DMC result is 22 cm^{-1} away from the experimental value, which is an improvement over the RHF results (on average 122 cm^{-1} away) and PBE results (on average 45 cm^{-1} away). We note that in this particular case the B3LYP results are on average 13 cm^{-1} away from the experimental results, which is why this semi-empirical functional is a popular choice for non-metal-containing molecules [268].

It is worthwhile to mention that the experimental results come with a larger error for carbon dioxide when compared to smaller molecules, as shown in Table 5.2b. The symmetric stretch mode is Raman active and infrared inactive, whereas for the other modes, the opposite is true [267]. The Raman measurement typically comes with a larger uncertainty than infrared spectroscopy in this case, complicating the comparison to DMC. Additionally, for these larger molecules, as the number of modes increases, the chances of eigenfrequency interference is increased. Here we notice that the symmetric stretch mode eigenfrequency is quasi-degenerate with twice the bending mode eigenfrequency in Table 5.2b, which could also potentially contribute to the increased uncertainty of the symmetric stretch mode [269]. Finally, we note that the precise eigenfrequencies for arbitrarily large molecules have not been studied as extensively. In contrast, the eigenfrequency calculation for hydrogen especially, as well as for other common diatomic molecules, is often used as an experimental benchmark [265]. Together these factors motivate the need for improving the accuracy and precision of electronic structure calculations, such as QMC.

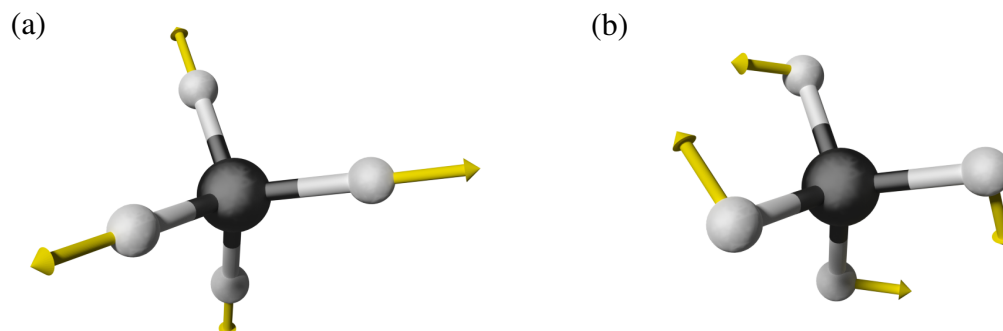


Fig. 5.5 (a) The symmetric stretch, and (b) scissor, vibrational modes of methane.

5.4.4 Methane

For the last example, we extend our formalism to a three-dimensional molecule containing five atoms: methane, to demonstrate that the formalism can be applied to diverse configurations of atoms.

We find that the configuration relaxes to a C – H bond length of 109.7 ± 0.2 pm, within two standard deviations of the experimental value of 109.3 pm, in fewer iterations than existing methods. The equilibrium bond lengths for all case studies are summarized in Table 5.3. In this case, we obtain fifteen eigenmodes of the system: three corresponding to global translation, three corresponding to global rotation, and nine corresponding to non-trivial vibrational modes. Of the vibrational modes, we select two modes to examine in detail: the symmetric stretch and scissor modes, as summarized in Table 5.2c and illustrated in Fig. 5.5.

An analysis of these modes yields a DMC deviation from experiment of -1.47% for the symmetric stretch mode and an expected agreement for the scissor mode, which is generally comparable to the results for carbon dioxide i.e. still of the order of 1% from the experimentally measured values. The successful recovery of these modes demonstrates that the formalism holds in three dimensions, and the excellent agreement for the scissor mode demonstrates that we are able to capture a non-trivial symmetry for this molecule. The symmetric stretch DMC eigenfrequency is 43 cm^{-1} away from experiment, whereas the RHF, PBE and B3LYP results are 184 cm^{-1} , 117 cm^{-1} and 157 cm^{-1} away, respectively.

5.5 Conclusion

In this chapter, we have developed and implemented a formalism to evaluate the matrix of force constants in QMC. We calculated vibrational frequencies and improved estimates for

the atomic displacements on each relaxation step, as well as correcting for anharmonicity. We report statistically significant improvements over RHF and DFT methods in the vast majority of cases, both in terms of the vibrational frequency and the efficiency of the atomic relaxation, for the hydrogen, hydrogen chloride, carbon dioxide, and methane molecules.

The ability to calculate the matrix of force constants within DMC, in particular, makes us well-positioned to calculate vibrational modes where high accuracy is a necessity and relax atomic positions in complex systems with many degrees of freedom where the extrapolation from energy or force is difficult, if not impossible, to optimize the geometry. The approach applies to both molecules and periodic configurations. This will be especially beneficial in systems with heavy atoms that are challenging to analyze accurately with DFT, systems with significant anharmonic corrections, and also those with strong van der Waals interactions, such as layered materials and surfaces.

Chapter 6

Lattice Stability of Three-dimensional Crystals

We perform a detailed study of the zero-temperature stability of the most common crystal structures in the periodic table in three different regimes: transient Coulomb, tight-binding, and nearly free electron. In the transient Coulomb model, we verify that cubic crystal structures are unstable at fourth order, whereas all other crystal structures are unstable at second order, in accordance with Gauss' law. For the tight-binding regime, we construct an analytical toy model and present a phase diagram as we tune the core and valence electron radial parameters away from the tight-binding limit. We verify that the presence of electron orbitals stabilizes the system, and show that, in the extreme tight-binding approximation, there is competition between the body-centered cubic and face-centered cubic phases. This result accords with analogous theoretical studies of the unconfined three-dimensional Yukawa crystal. We report that the hexagonal close-packed structure is the secondary dominant phase as we tune away from the tight-binding limit, which we reconcile with analytical calculations of the matrices of force constants in the nearly free electron model.

6.1 Introduction

The classical theory of crystal stability was extensively studied by Born in the first half of the 20th Century [270]. This seminal work predominantly focused on deriving the Born stability criteria based on the elasticity constants, as well determining the scope of the Cauchy-Born rule of crystal deformation [271]. Since this time, the topic of crystal stability has been revisited from numerous perspectives [272]: from the historic models of ionic matter by Born-Landé [273], Born-Mayer [274], and Kapustinskii [275]; through to sophisticated quantum

Monte Carlo simulations in current research [276, 277]. However, none of these works have addressed the precise *order* of stability in prototypical models, which are currently of increasing interest to the plasma physics [278] and astrophysics [279] communities.

In this chapter, we analyze the total potential energy for transient Coulomb, tight-binding, and nearly free electron crystal models. In each case, we examine the matrix of force constants, and higher-order equivalents. We comment on, and generalize, the criteria typically used to define crystal stability. By looking at a variety of crystal lattices, motivated by the periodic table, we draw comparisons between the stability of specific crystal structures. We ultimately stabilize all crystal structures through the inclusion of electron clouds in our model, and we study the stability transition.

We first introduce the underlying theory and stability criteria in Sec. 6.2. We then proceed to examine the transient Coulomb, tight-binding, and nearly free electron regimes in Secs. 6.3, 6.4, & 6.5, respectively. Finally, we summarize the conclusions and implications of the results in Sec. 6.6.

6.2 Theory

We consider an infinite crystal of atoms in three-dimensions and at zero temperature. Each unit cell of the crystal, I , has an atom at the origin of the cell with position \mathbf{R}_I . There may also be additional atoms in the unit cell with displacement vectors $\mathbf{r}_i^{\text{c.s.}}$ relative to \mathbf{R}_I , where c.s. denotes the crystal structure under consideration. We consider instantaneously displacing an atom in the crystal by a small and finite displacement $\mathbf{R} = (X, Y, Z)$. The total potential energy of the system is given by $E_{\text{c.s.}} = \sum_I V_{\text{c.s.}}(\mathbf{R}_I - \mathbf{R})$, where we sum over all distinct pairs. The crystal unit cell potential, $V_{\text{c.s.}}$, is a function of atomic potentials, V , such that $V_{\text{c.s.}}(\mathbf{R}) = f[V(\mathbf{R})]$, corresponding to the number of atoms per unit cell. By analyzing the resulting total potential function we are able to comment on the stability of the system.

Taylor expanding the potential of the system about its equilibrium, we can use the multivariate higher-order derivative test to determine the equilibrium's nature i.e. whether the equilibrium is stable: a minimum; the equilibrium is unstable: a maximum; or a mixture: a saddle point (see Appendix D.1). Typically, the crystal stability is discriminated by the second derivative of the potential, the matrix of force constants, however in this chapter we generalize this definition to the symmetry-contracted higher-order derivative tensors, which we refer to as higher-order matrices of force constants (see Appendix D.2)¹.

¹Note that higher-order (in)stabilities are, in all cases, weaker than at lower orders.

6.3 Transient Coulomb Model

In the transient Coulomb model, we consider a one-component crystal of Coulomb point charges of equal sign². We define the Coulomb potential as $V(\mathbf{R}) = \pm|\mathbf{R}|^{-1}$ corresponding to repulsive and attractive interactions, respectively³. We test the effect of perturbing a single point ion on the system, and hence discern the order and magnitude of the instability.

In order to perform the summation over lattice sites in this section, we use a rotationally-symmetric summation scheme. We start by defining all unit cells with an atom at the origin and then incrementally add atoms in concentric shells. We compute this summation until convergence to the desired precision. The full details of the numerical model are discussed in Appendix D.4.

In Sec. 6.3.1, we begin by analyzing the results, and then subsequently discuss their wider context in Sec. 6.3.2.

6.3.1 Analysis

For simplicity, we start our analysis by examining the Bravais lattices with only one free parameter: the lattice constant, a . These Bravais lattices are the: simple cubic (cub), body-centered cubic (bcc), and face-centered cubic (fcc) structures. Additionally, we study the diamond (dia) lattice structure, from the fcc family, separately, as it is of special interest due to its extreme physical properties, such as hardness and thermal conductivity. We also include the hexagonal close-packed (hcp) and double hexagonal close-packed (dhcp) structures in our initial analysis, from the hexagonal Bravais lattice family, due their ubiquity in nature (see Appendix D.3).

The matrices of force constants, minimizing directions, and minimal values for these crystals are shown in Table 6.1. In this model, the cubic systems (cub, bcc, fcc, dia) have no harmonic term in their potential energy expansion, which renders the derivative test inconclusive to this order. The hexagonal systems (hcp, dhcp) have indefinite matrices of force constants, which implies the system is at a saddle point. We see that the system is stable to perturbations in the xy -plane, but unstable to perturbations in the z -direction. These hexagonal systems are most unstable in the $\pm\hat{e}_z$ directions, as illustrated in Fig. 6.1a. The dhcp system is more unstable than the hcp system in this model due to the higher density of ions.

²Note that in the infinite case, this system is stable by symmetry.

³Throughout this chapter, we use Hartree atomic units ($m_e = e = \hbar = k_e = 1$).

crystal	$a \frac{d^2 E_{i-i}}{d\mathbf{R}^2}$	${}_{i-i}\hat{\mathbf{m}}_2$	${}_{i-i}\hat{\mathbf{m}}_2^\top \cdot \left(a \frac{d^2 E_{i-i}}{d\mathbf{R}^2} \right) \cdot {}_{i-i}\hat{\mathbf{m}}_2$
cub	$\mathbf{0}$	—	0
bcc	$\mathbf{0}$	—	0
fcc	$\mathbf{0}$	—	0
dia	$\mathbf{0}$	—	0
hcp	$0.16 \begin{pmatrix} 1 & 0 & 0 \\ 0 & 1 & 0 \\ 0 & 0 & -2 \end{pmatrix}$	$\pm \hat{\mathbf{e}}_z$	-0.33
dhcp	$0.4 \begin{pmatrix} 1 & 0 & 0 \\ 0 & 1 & 0 \\ 0 & 0 & -2 \end{pmatrix}$	$\pm \hat{\mathbf{e}}_z$	-0.8

Table 6.1 Matrices of force constants and minimizing directions for the ion-ion interaction expansion about equilibrium, at second order, with lattice spacing a . $d^2 E/d\mathbf{R}^2$ is the Hessian; $\hat{\mathbf{m}}_2$ is the normalized eigenvector corresponding to the lowest eigenvalue of the Hessian; and $\hat{\mathbf{m}}_2^\top \cdot (d^2 E/d\mathbf{R}^2) \cdot \hat{\mathbf{m}}_2$ is the projection of the Hessian in the minimizing direction. All values are given to the precision up to which they have converged, or three significant figures, whichever is lower.

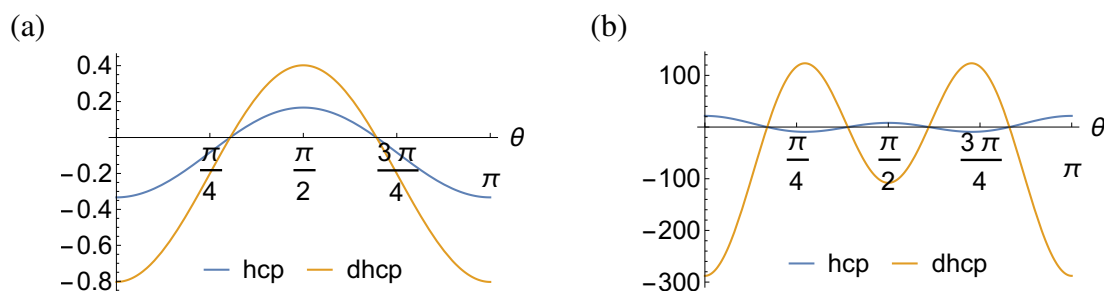


Fig. 6.1 Angular variation in the magnitude of the matrices of force constants, at unit radius, in units of a^{-1} . Plots are shown for the (a) 2nd-order, and (b) 4th-order terms for the hcp and dhcp crystal structures. Note that the magnitude of the higher-order matrices of force constants is azimuthally symmetric for these systems. The minimizing directions are recorded in Tables 6.1 & 6.2.

crystal	$a \frac{d^4 E_i}{d\mathbf{R}^4}$	$\hat{\mathbf{m}}_4$	$\hat{\mathbf{m}}_4^{\circ 2\text{T}} \cdot \left(a \frac{d^4 E_i}{d\mathbf{R}^4} \right) \cdot \hat{\mathbf{m}}_4^{\circ 2}$
cub	$74.6 \begin{pmatrix} 1 & -1.5 & -1.5 \\ -1.5 & 1 & -1.5 \\ -1.5 & -1.5 & 1 \end{pmatrix}$	$\frac{1}{\sqrt{3}}(\pm \hat{\mathbf{e}}_x \pm \hat{\mathbf{e}}_y \pm \hat{\mathbf{e}}_z)$	-49.7
bcc	$-74.6 \begin{pmatrix} 1 & -1.5 & -1.5 \\ -1.5 & 1 & -1.5 \\ -1.5 & -1.5 & 1 \end{pmatrix}$	$\{\pm \hat{\mathbf{e}}_x, \pm \hat{\mathbf{e}}_y, \pm \hat{\mathbf{e}}_z\}$	-74.6
fcc	$-181 \begin{pmatrix} 1 & -1.5 & -1.5 \\ -1.5 & 1 & -1.5 \\ -1.5 & -1.5 & 1 \end{pmatrix}$	$\{\pm \hat{\mathbf{e}}_x, \pm \hat{\mathbf{e}}_y, \pm \hat{\mathbf{e}}_z\}$	-181
dia	$-2570 \begin{pmatrix} 1 & -1.5 & -1.5 \\ -1.5 & 1 & -1.5 \\ -1.5 & -1.5 & 1 \end{pmatrix}$	$\{\pm \hat{\mathbf{e}}_x, \pm \hat{\mathbf{e}}_y, \pm \hat{\mathbf{e}}_z\}$	-2570
hcp	$8.1 \begin{pmatrix} 1 & 1 & 0 \\ 1 & 1 & 0 \\ 0 & 0 & 0 \end{pmatrix} + 21.6 \begin{pmatrix} 0 & 0 & -1.5 \\ 0 & 0 & -1.5 \\ -1.5 & -1.5 & 1 \end{pmatrix}$	$\theta = 0.857, \pi - 0.857$	-9.3
dhcp	$-108 \begin{pmatrix} 1 & 1 & 0 \\ 1 & 1 & 0 \\ 0 & 0 & 0 \end{pmatrix} - 288 \begin{pmatrix} 0 & 0 & -1.5 \\ 0 & 0 & -1.5 \\ -1.5 & -1.5 & 1 \end{pmatrix}$	$\pm \hat{\mathbf{e}}_z$	-288

Table 6.2 Matrices of force constants and minimizing directions for the ion-ion interaction expansion about equilibrium, at fourth order, with lattice spacing a . $d^4 E/d\mathbf{R}^4$ is the 4th-order Hessian; $\hat{\mathbf{m}}_4$ is the normalized eigenvector corresponding to the lowest eigenvalue of the 4th-order Hessian; and $\hat{\mathbf{m}}_4^{\circ 2\text{T}} \cdot (d^4 E/d\mathbf{R}^4) \cdot \hat{\mathbf{m}}_4^{\circ 2}$ is the projection of the 4th-order Hessian in the minimizing direction. Fourth-order tensors are contracted to matrices as described in Appendix D.2. All values are given to the precision up to which they have converged, or three significant figures, whichever is lower.

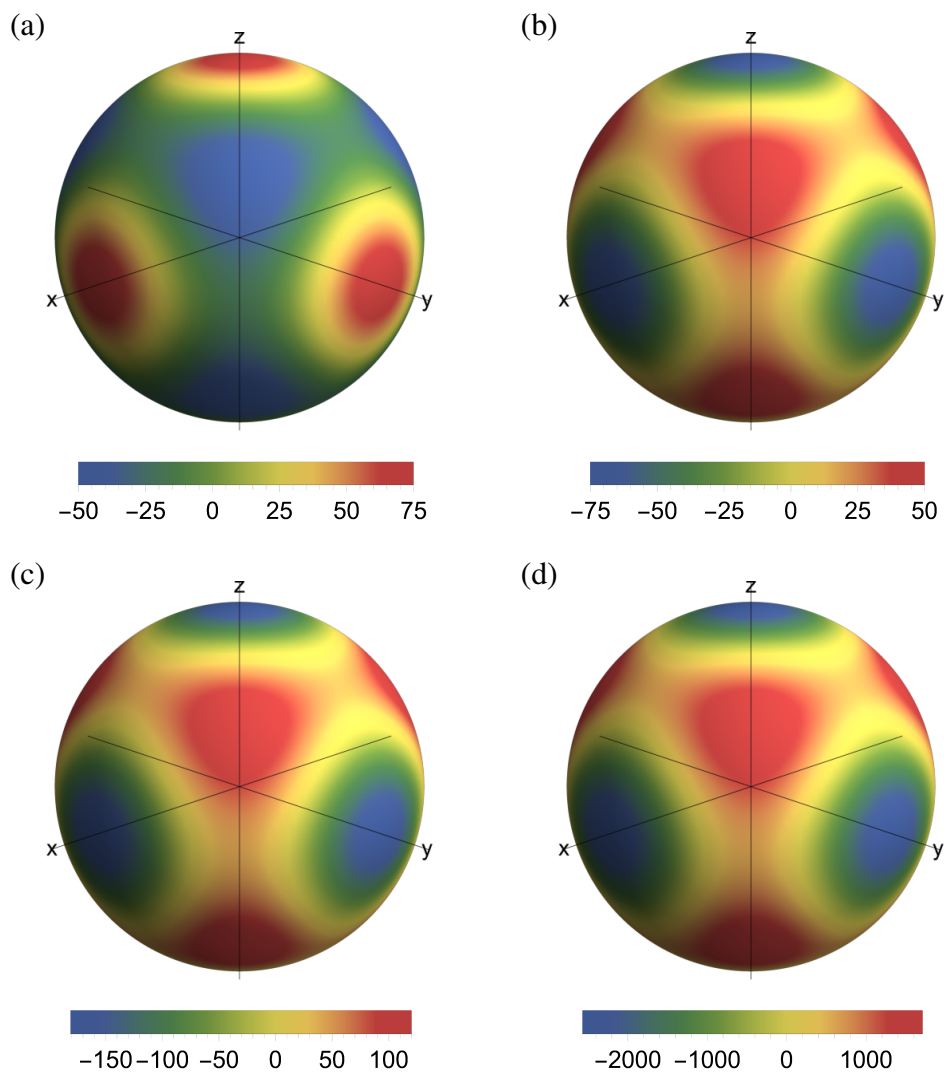


Fig. 6.2 Angular variation in the magnitude of the 4th-order matrices of force constants, at unit radius, in units of a^{-1} . Plots are shown for the (a) cub, (b) bcc, (c) fcc, and (d) dia crystal structures. The minimizing directions are recorded in Table 6.2.

An analogous table for the 4th-order generalized matrices of force constants is shown in Table 6.2.⁴ At this order, the cubic systems do not have vanishing contributions, instead they demonstrate a 4th-order instability. Note that the form of the higher-order matrices is the same in each case, with a varying pre-factor. Plots of the angular variation of these 4th-order matrices are shown in Fig. 6.2. As for the hexagonal systems at second order, the system is again at a saddle point. In this case, the configuration is stable to perturbations in the Cartesian basis directions for cub; and in the diagonal directions for bcc, fcc and dia crystals, and visa versa. For completeness, we show that the 4th-order matrices for the hexagonal systems are also indefinite. Plots of the angular variation for these systems are shown in Fig. 6.1b. In the dhcp case, the minimizing directions are again $\pm\hat{e}_z$, whereas for the hcp system the minimizing directions have now shifted to $\theta = 0.857, \pi - 0.857$. The angular variation for the hexagonal systems is rotationally symmetric about the z-axis, since the x and y eigenvalues are the same. Note that since higher-order (in)stabilities are always weaker than lower orders, it is unnecessary to examine the higher-order terms for these hexagonal systems. As seen for the 2nd-order case, the magnitude of the instabilities is determined by the ion density.

Finally, we extend our analysis to all other Bravais lattice structures in the periodic table (see Appendix D.3), in terms of the x-direction lattice constant a , and using examples to set the additional free parameters (see Appendix D.4.3). Table 6.3 shows the eigenvalues of the matrices of force constants for a selection of elements. We find that for the parameters of all other elements in the periodic table, a selection of which are shown in Table 6.3, the matrices of force constants are indefinite and the structures are at saddle points of stability. From this, we rule out the possibility that the 2nd-order term vanishes simply due to orthogonal basis vectors and conclude that this observation is unique to cubic systems. For example, the face-centered orthorhombic (fco) lattice has a 2nd-order term, yet the fcc lattice does not.

The explanation for this phenomenon is due to the Poisson equation $\nabla^2 V_{c.s.} = 0$ from Gauss' theorem. Cubic systems are the only systems for which the x-, y-, and z-directions are identical and hence Gauss' theorem dictates that each component of the matrix of force constants must be identically zero. For the 4th-order terms, Poisson's equation now takes the form $\nabla^2(\nabla^2 V_{c.s.}) = 0$ which produces mixed terms on the left-hand side and so the same argument does not hold.

Note that in this section we have considered a one-component ionic crystal *without* a neutralizing background. If a constant neutralizing background were to be introduced, then this would provide a quadratic restoring potential for the central ion, which would render the system stable. This would be true even for non-cubic systems, since it can be shown

⁴Odd power terms in the potential trivially vanish due to symmetry.

element	crystal	eigenvalues of $a^3 \frac{d^2 E_{i,i}}{d\mathbf{R}^2}$
B	rhom	5.95, -3.65, -2.29
Ga	bsco	-1.45, 0.809, 0.638
O	bscm	-21.7, 13.0, 8.70
In	bct	-0.721, 0.361, 0.361
Pu	mono	6.07, -5.55, -0.521
H	hex	6.57, -6.28, -0.28
P	tri	33.2, -17.3, -15.9
S	fco	-4.50, 2.77, 1.73
Np	orth	-6.68, 4.16, 2.52

Table 6.3 Eigenvalues of the matrices of force constants, $d^2E/d\mathbf{R}^2$, for a selection of elements with multi-parameter crystal structures in the periodic table, with lattice spacing a . The Bravais lattices, listed in order of ubiquity, are: simple rhombohedral (rhom), base-centered orthorhombic (bsco), base-centered monoclinic (bscm), body-centered tetragonal (bct), simple monoclinic (mono), hexagonal (hex), triclinic (tri), face-centered orthorhombic (fco), and simple orthorhombic (orth). All values are given for systems summed up to one shell, as described in Appendix D.4.

that the stabilizing contribution to the matrix of force constants from the constant uniform background is greater than the destabilizing contribution from the purely repulsive ionic crystal (see Sec. 6.5 for further analysis).

6.3.2 Discussion

Coulomb crystals are defined by the dominant role of the Coulomb interaction and simple form of their constituents [280]. In this chapter, we consider a special type of transient Coulomb crystal, categorized as an unconfined, one-component system with repulsive interactions. However, the study of Coulomb crystals extends beyond this limiting case and has a history spanning over a century [281]. In this section, we briefly summarize and comment on the key developments in the field, in order to provide context for our results.

The earliest study of a one-component system was by Madelung in 1918, where he showed that an infinite array of point charges can form an ordered state [281]. Two decades later, Wigner predicted, in his seminal paper, that the electron jellium in metals can form a bcc crystal at sufficiently low densities [282, 283]. The subsequent numerical and experimental confirmation of Wigner crystals sparked interest in the condensed matter community, and a plethora of papers on the general theory [284–290] and stability [291–294] of these systems followed, including detailed quantum Monte Carlo simulations [68, 295–300]. From the

plasma physics perspective on the other hand, interest in strongly coupled plasmas, i.e. plasmas where the average Coulomb energy of a particle is much greater than its average kinetic energy [301], led to the prediction that three-dimensional, one-component Coulomb plasmas can also form a bcc crystal at sufficiently *high* densities and/or low temperatures [302]. It was subsequently realized that these two conclusions could be reconciled as opposite density limits of the same problem⁵. All of these models, however, include a homogeneous positive background of charges to stabilize the system. Indeed, there are two main ways to stabilize a repulsive Coulomb crystal: using a homogeneous oppositely-charged background, or confining the system [280].

Work on confined plasmas has been performed in a variety of contexts [301]. Most notably, the structure and Madelung energy [303], as well as the melting of ordered states [304] in spherical Coulomb crystals has been studied in the last thirty years. These systems can also be probed and manipulated experimentally using ions confined to Penning [305] or Paul [306] traps, with motivation provided by the recent discovery of crystalline plasmas of dust particles in astrophysics [279]; as well as the industrial success of quantum dot technology [307]. For all of these confined systems, however, the resulting crystal structure is strongly dependent on the shape of the trap [304]. Therefore, no general statements can be made about the equilibrium structure.

In this section, we have examined a type of transient “Coulomb exploding” crystal to show that the cubic structures have the weakest (4th-order) instability in this regime. This result may accord with the analysis of stable systems in the literature [283, 289, 302], however further work (in the following sections) is needed to analyze the system’s stability transition.

6.4 Tight-binding Model

In the tight-binding model, we assume a crystal of localized atoms at each site. The electrons are tightly bound to each (point) nucleus with a spherical effective charge density parameterized by core and valence orbital radii.

In this section, we use the same rotationally-symmetric summation scheme for the crystal introduced in Sec. 6.3. The full details of the numerical model are discussed in Appendix D.4.

We start by analyzing the model and phase diagram in Sec. 6.3.1, and then discuss the interpretation in Sec. 6.3.2.

⁵Additionally, the successful quest to determine the intermediate physics arguably inspired the first application of importance-sampled diffusion Monte Carlo [68].

6.4.1 Analysis

In the previous section, we considered crystal lattices composed purely of ions interacting through a Coulomb potential. We now build on this foundation by introducing electrons. In the tight-binding limit, the electrons are situated directly on top of the ions, which yields an infinite crystal of neutral particles and hence zero potential energy. However, in the tight-binding approximation, we perturb around this limit to investigate the resulting behavior. For our toy model, we consider ions that have only spherically symmetric (s-type) orbitals, where the electron density obeys the distribution:

$$\rho_E(\mathbf{r}; c, a_e) \propto \frac{1}{1 + \exp\left(\frac{2(|\mathbf{r}|-c)}{a_e}\right)}.$$

Here \mathbf{r} denotes the displacement of the electron relative to the origin of its associated ion. c and a_e characterize the core and valence orbital radii, respectively. The factor of two ensures that the associated wave function, defined by $\rho = |\Psi|^2$, reduces to the hydrogenic atom solution $\exp(-|\mathbf{r}|/a_e)$ in the extreme tight-binding approximation: $c \ll a_e \ll a$. We choose this form of the electron orbital density, as opposed to simpler forms in the literature [299], because it is analytically well behaved for the required derivation (see Appendix D.5). Throughout our calculations, we work to leading order in the tight-binding approximation. In practice, this implies results up to first order in the small parameter (c/a_e) and second order in (a_e/a) .

We calculate the ion-ion, electron-ion, and electron-electron contributions to the potential energy based on the electron orbital ansatz up to the approximations detailed above. We subsequently add on the contribution to the energy due to the Pauli repulsion of the overlapping electron orbitals, evaluated at the optimal effective radius of atoms in a spherical packing. Finally, we relax the crystal structure to find the optimal lattice constant. We are left with a total potential energy of the crystal as a function of a_e and c . We perform this procedure for each of the crystal structures in the set {cub,bcc,fcc,dia,hcp,dhcp}. The full details of this calculation are shown in Appendix D.5.

In Fig. 6.3a, we show the phase diagram of the stable crystal structure with the lowest energy out of the cub, bcc, fcc, dia, hcp, and dhcp lattices. As can be seen from the diagram, the hcp, fcc, and bcc structures dominate the plot. Since we are working in the tight-binding approximation, the region of validity is where $c < a_e$ (indicated by the dashed black line in the diagram). However, we show results for $c > a_e$ to gain a broader understanding of the model. Additionally, we present a higher-resolution close-up of the tricritical point in Fig. 6.3b to analyze the features of interest. The tricritical point is at $(\log a_e, \log c) = (-2.69, -2.67)$ with

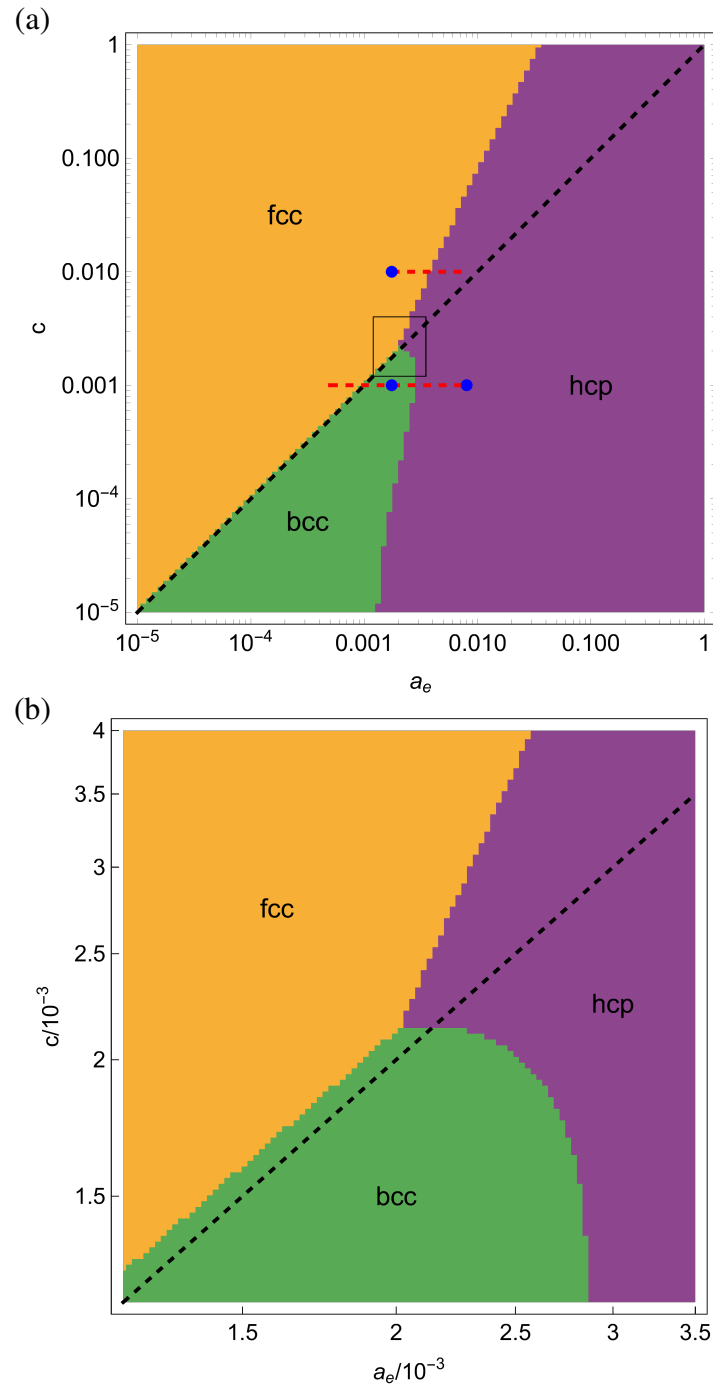


Fig. 6.3 (a) Phase diagram of the lowest energy crystal structure out of $\{\text{cub}, \text{bcc}, \text{fcc}, \text{dia}, \text{hcp}, \text{dhcp}\}$ at the optimum lattice constant, summed out to five shells. The black dashed line separates the valid region for the tight-binding model: $c < a_e$. The blue points, $\{(4 \times 10^{-4}, 10^{-3}), (1.75 \times 10^{-3}, 10^{-3}), (8 \times 10^{-3}, 10^{-3})\}$, are analyzed in Fig. 6.4, and the red dashed lines, $\{c = 10^{-2}, c = 10^{-3}\}$, indicate the cross sections analyzed in Fig. 6.5. (b) Higher-resolution plot of the region enclosed by the black square in (a), highlighting the tricritical point. The diagrams are plotted to a resolution of 100^2 points.

three transition lines: fcc-bcc at $\log c = \log a_e + 0.023$; fcc-hcp at $\log c = 2.5 \log a_e + 4.07$; and bcc-hcp at $\log c = -2.67 - 61.4 \exp(39.1 \log a_e + 93.8)$ in the vicinity of the tricritical point. Since all phase transitions between allotropes of crystal structures are first order, the tricritical point is valid with respect to the vertex rule. Note that other than the restriction imposed by the tight-binding approximation, in this context $c < a_e$, the phase diagram may be extended in both directions.

Now that we have constructed the phase diagram, we verify the convergence of our calculations. Figure 6.4 shows a detailed analysis of the blue points depicted in Fig. 6.3a. Most importantly, we see from plots of the total energy against number of summed shells, in Figs. 6.4a, 6.4c, & 6.4e, that convergence is reached at approximately five shells. Since the energies fluctuate considerably with a small number of shells, summing to the appropriate number is critical⁶. Moreover, these plots show that the hcp, bcc, and fcc crystal structures are grouped with comparable yet noticeably lower total energy than the cub, dia, and dhcp structures. On average, the {cub,dia,dhcp} energies are larger than the {bcc,fcc,hcp} energies by factors of 2.37×10^3 , 2.54×10^3 , and 3.45×10^2 , for Figs. 6.4a, 6.4c, & 6.4e, respectively. For comparison, the corresponding average *intra*-group total energy differences are smaller than this by factors of 2.16×10^5 , 2.44×10^5 , and 3.46×10^5 , averaged over both groups. It is also worth noting that the hcp crystal structure emerges as the lowest energy structure fastest, after only two shells, compared to the bcc structure (after five shells), and the fcc structure (after four shells). This is due to the statistical advantage of having a higher number of atoms in the unit cell. For instance, the dia and dhcp crystal structures also reached convergence after two shells, owing to the comparatively large number of atoms in their unit cells.

Figures 6.4b, 6.4d, & 6.4f show the breakdown of the contributions to the total energy at each of these points. From these plots, we can see that the ion-ion and electron-electron repulsive contributions to the potential are approximately of equal sign and magnitude. Furthermore, these contributions are almost balanced by the electron-ion attractive contribution, which is of negative sign and approximately twice the magnitude. As we increase the number of shells, these contributions continue to increase linearly, as expected. The Pauli contribution to the energy and the total energy, however, reach convergence after about five shells. Furthermore, we note that the differences between the various energy contributions decrease as we approach the tight-binding limit and reduce the small parameter (c/a_e).

Figure 6.5 shows a detailed analysis of the dashed red cross-sections depicted in Fig. 6.3a. From these plots we learn how the energy behaves as we vary a_e at constant c , while also passing through the points discussed in the previous section. Most importantly, from the

⁶After a systematic analysis of data points, we conclude that evaluating the phase diagram at five shells is the best compromise between accuracy and computational expense.

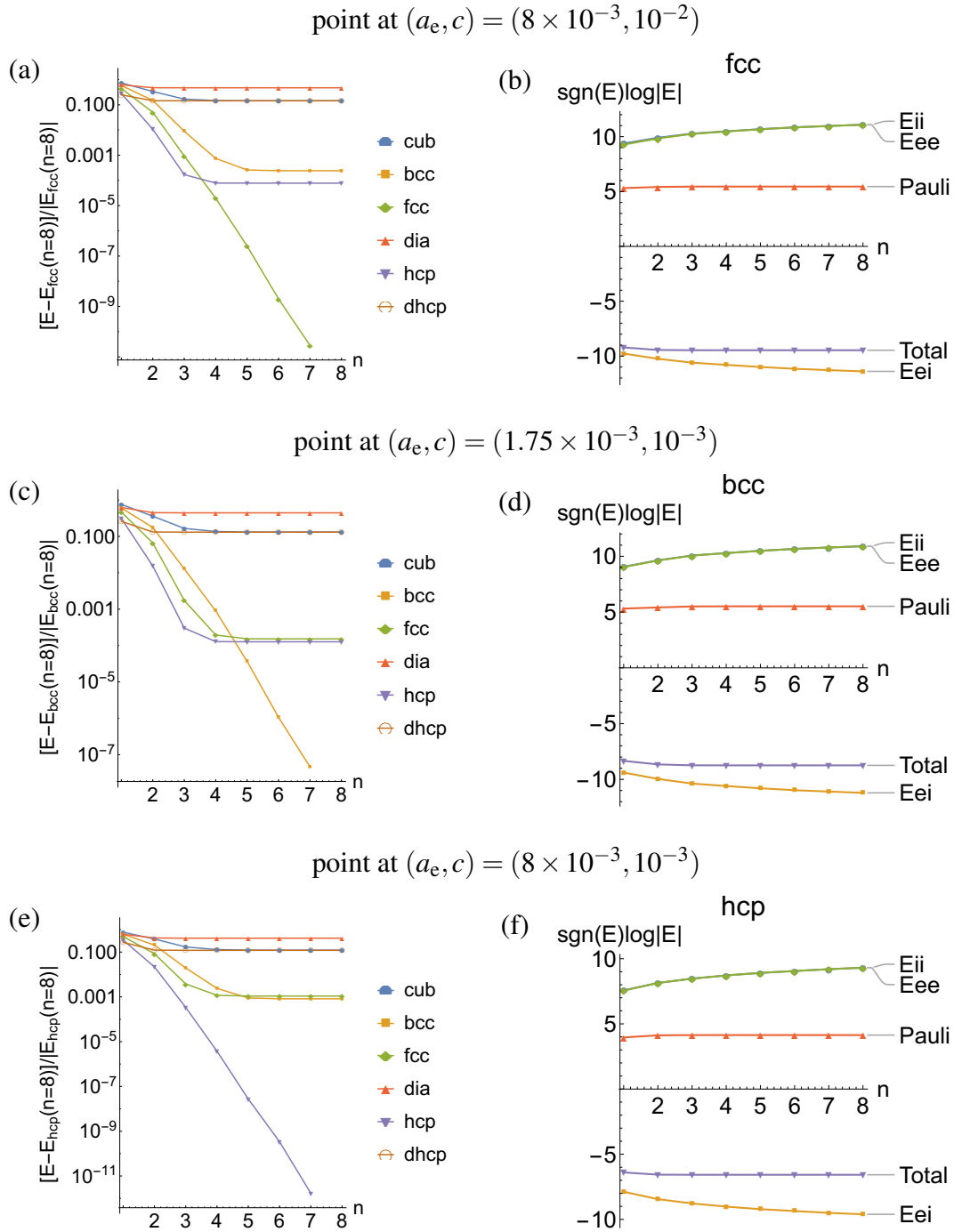


Fig. 6.4 Detailed analysis of the blue points depicted in Fig. 6.3a. [(a), (c), (e)] Fractional deviation of the energies from the lowest energy value at eight shells, $[E - E_{c.s.}(n=8)]/|E_{c.s.}(n=8)|$, against the number of shells, n . [(b), (d), (f)] Corresponding plots showing the breakdown of the contributions to the total energy for the most stable crystal structure. The total energy ('Total') is the sum of the ion-ion ('Eii'), electron-ion ('Eei'), electron-electron ('Eee'), and Pauli repulsion ('Pauli') contributions.

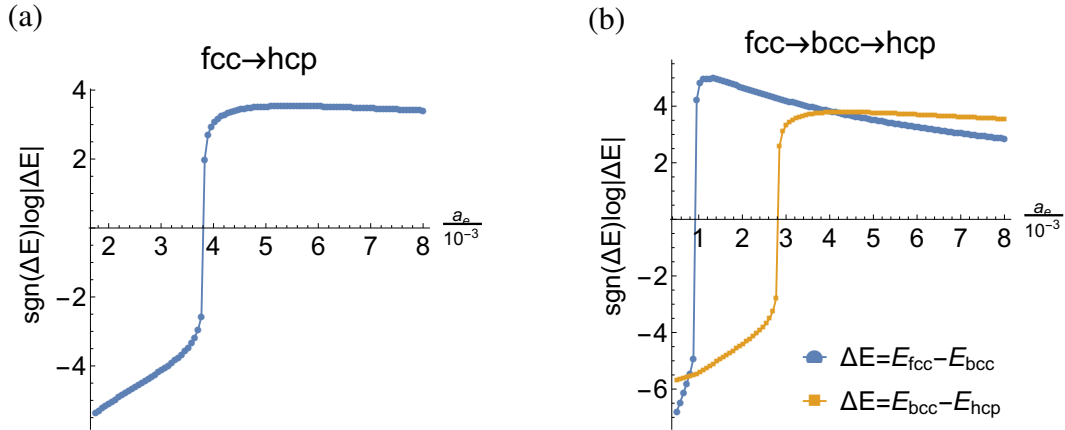


Fig. 6.5 Detailed analysis of the red dashed cross-sections depicted in Fig. 6.3a. (a) Difference in total energies between the fcc and hcp structures, $\Delta E = E_{\text{fcc}} - E_{\text{hcp}}$. (b) Difference in total energies between the fcc and bcc structures (blue) and between the bcc and hcp structures (orange). The cross sections are plotted to a resolution of 100 points.

plots of energy differences, in Figs. 6.5a & 6.5b we can identify the three transition lines. In Fig. 6.5a we can see the fcc-hcp transition at $a_e = 3.8 \times 10^{-3}$; and in Fig. 6.5b we can see the fcc-bcc transition at $a_e = 9 \times 10^{-2}$, and the bcc-hcp transition at $a_e = 2.8 \times 10^{-3}$. Away from the phase transition lines, the total energies remain free from fluctuations.

6.4.2 Discussion

In this section, we have progressed from the transient Coulomb model in Sec. 6.3 by adding electrons to stabilize the system. We increase the effect of the electron orbital gradually using a tight-binding toy model, so that we recover transient Coulomb physics in the appropriate limit. Here, we consider an unconfined two-component system [280]: the ionic crystal. As mentioned in Sec. 6.3.2, one-component repulsive crystals require either a charge neutralizing background, or a trap, to be stabilized; and in the cases with a charge neutralizing background, there are parallels between the condensed matter and plasma physics approaches. Here we consider an unconfined system in the extreme tight-binding limit, and look into results from the one-component plasma model, as well as the periodic table, to gain further insight.

It has been known for a long time that the ground state of a three-dimensional Coulomb crystal has a bcc symmetry [302], where the term ‘‘Coulomb crystal’’ in plasma physics refers to strongly-coupled charged particles with a neutralizing background [280]. In the extreme tight-binding limit ($c < a_e$, $c \ll 1$, $a_e \ll 1$), this is effectively equivalent to the system presented in Fig. 6.3. The particle interactions are Coulomb-like, since the effect of the well is still minimal, and the presence of the electrons provides the neutralizing background, albeit

highly concentrated around the ions. Therefore, we see the same bcc ground state crystal structure. As soon as we move into the region where $c > a_e$ we start to modify the effective interaction through screening. In this region ($c > a_e$, $c \ll 1$, $a_e \ll 1$), our tight-binding model breaks down and we effectively observe the behavior of screened Coulomb charges. Indeed, it has been shown by Hamaguchi et al. [308] that three-dimensional Yukawa crystals have a fcc and bcc phase. In their paper, they present a phase diagram of the Yukawa crystal parameterized by the coupling constant, the ratio of the Coulomb potential energy to the kinetic energy per particle, and the screening parameter, the ratio of the Wigner-Seitz radius to the Debye length. For large coupling constant, they show that there exist two solid phases for the Yukawa crystal: bcc at small screening parameter and a transition to fcc when the screening parameter is increased; which corresponds to moving vertically upwards in our phase diagram. This recovers the Coulomb results in the literature [302] and also accords with our toy model.

In addition to these extreme limits, our model provides insight into the transition from extreme matter to real materials. From Fig. 6.3, we can see that as a_e is increased, the hcp structure is the secondary dominant phase, for both $c < a_e$ and $c > a_e$. This shows that as the valence electron radius is increased and the tight-binding approximation is relaxed, the crystal lattice begins to favor high symmetry and packing factor. Here the theory becomes increasingly applicable to the solid state. Not only is the hcp crystal structure the most common crystal structure in the periodic table (despite not being a Bravais lattice – see Appendix D.3), it is also particularly common among elements further down in the periodic table, where the tight-binding approximation holds⁷, e.g. period 7. Moreover, the hcp structure has the maximal matrix of force constants out of the systems studied ($\{\text{cub}, \text{bcc}, \text{fcc}, \text{dia}, \text{hcp}, \text{dhcp}\}$) according to analytical calculations in the nearly free electron model (see Sec. 6.5).

6.5 Nearly Free Electron Model

In contrast to the tight-binding model, where the Bohr radii of the atoms are much smaller than the inter-atomic spacing, we now consider the opposite limit, where the Bohr radii mostly overlap. In the weak binding, or nearly free electron model, we perform 1st-order perturbation theory about the jellium model, where the electron density is uniform.

In this section we consider an ideal crystal, which is infinitely periodic in space. The details of the electron cloud densities in this model are presented in Appendix D.6.

⁷Further evidence to support this claim is in preparation at the time of writing.

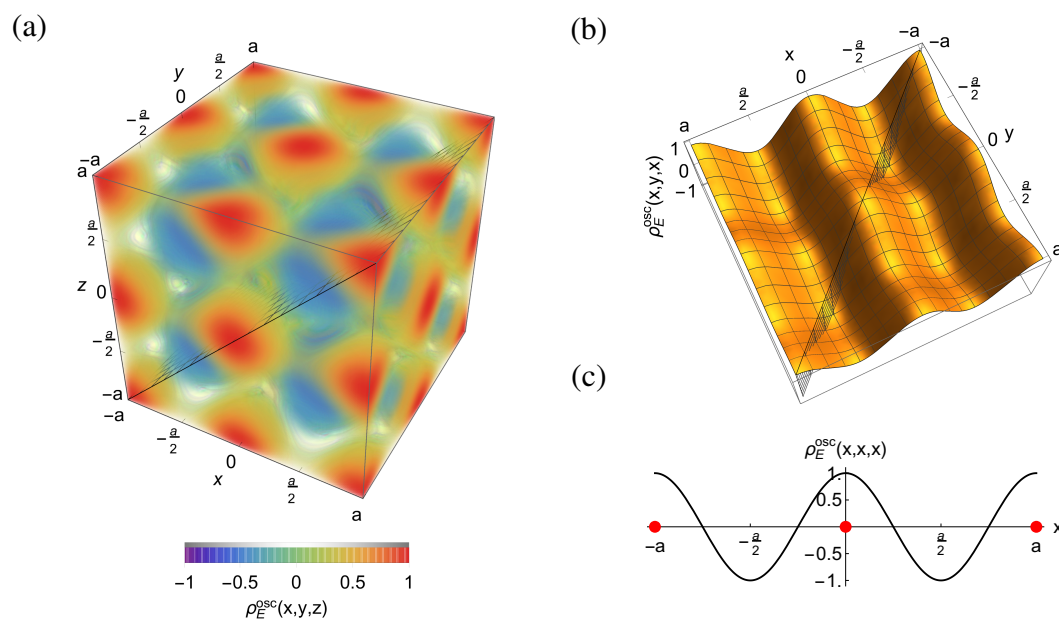


Fig. 6.6 (a) Three-, (b) two-, and (c) one-dimensional plots of the oscillatory part of the electron cloud density, $\rho_E^{\text{osc}}(x, y, z) = (\cos(kx) + \cos(ky) + \cos(kz))/3$ with $k = 2\pi/a$, for the cub lattice in the nearly free electron model. (a) Color and opacity both denote the magnitude of $\rho_E^{\text{osc}}(x, y, z)$. (b) Plot of the meshed cross-section depicted in (a), through the density extrema. (c) Plot of the meshed cross-section depicted in (b), through the density extrema. The red points illustrate the positions of the ions.

crystal	$a \frac{d^2 E_{i-i}}{d\mathbf{R}^2}$	$a \frac{d^2 E_{e-i}^{\text{const}}}{d\mathbf{R}^2} / \left(\frac{4\pi}{3}\right)$	$a \frac{d^2 E_{e-i}^{\text{osc}}}{d\mathbf{R}^2} / (2(2\pi)^{3/2} \tilde{u})$
cub	$\mathbf{0}$	\mathbf{I}	$\mathbf{I}/3$
bcc	$\mathbf{0}$	$2\mathbf{I}$	$\mathbf{I}/3$
fcc	$\mathbf{0}$	$4\mathbf{I}$	$\mathbf{I}/3$
dia	$\mathbf{0}$	$8\mathbf{I}$	$\mathbf{I}/3$
hcp	$0.16 \begin{pmatrix} 1 & 0 & 0 \\ 0 & 1 & 0 \\ 0 & 0 & -2 \end{pmatrix}$	$\sqrt{2}\mathbf{I}$	$\frac{1}{41} \begin{pmatrix} 16 & 0 & 0 \\ 0 & 16 & 0 \\ 0 & 0 & 9 \end{pmatrix}$
dhcp	$0.4 \begin{pmatrix} 1 & 0 & 0 \\ 0 & 1 & 0 \\ 0 & 0 & -2 \end{pmatrix}$	$2\sqrt{2}\mathbf{I}$	$\frac{1}{697} \begin{pmatrix} 218 & 0 & 0 \\ 0 & 218 & 0 \\ 0 & 0 & 261 \end{pmatrix}$

Table 6.4 Ion-ion and electron-ion contributions to the matrix of force constants in the nearly free electron model. \mathbf{I} and \tilde{u} denote the identity matrix and dimensionless oscillation strength, respectively. The oscillatory electron-electron contribution is zero for all structures, $E_{e-e}^{\text{osc}} = 0$.

The nearly free electron model, consists of a lattice of ions with a Coulomb repulsion, as studied in Sec. 6.3, together with an oscillatory and near-uniform electron cloud density, ρ_E . In accordance with 1st-order perturbation theory, this electron cloud density may be split into two parts, $\rho_E = \rho_E^{\text{const}} + \rho_E^{\text{osc}}$, with ρ_E^{const} corresponding to the uniform jellium-like density, and ρ_E^{osc} corresponding to the oscillatory density reflecting the geometry of the ionic lattice. An example of the oscillatory electron cloud density for the cub lattice is shown in Fig. 6.6. In each case, we ensure that the range is normalized such that $\max(\rho_E^{\text{osc}}) = u$, where u is the oscillation strength, and that the integral of ρ_E^{osc} over a unit cell is equal to zero.

In order to calculate the total matrix of force constants in the nearly free electron model, we proceed as before by summing the ion-ion, electron-ion, and electron-electron contributions. For the ion-ion contribution, we take results directly from Sec. 6.3. Note that when performing the summation over shells for the ion-ion contribution, the 0th-order contribution to the energy is divergent, whereas the matrix of constants converged to the results presented in Table 6.1. In fact, there will be divergent 0th-order contributions for the electron-ion and electron-electron contributions too, corresponding to the jellium-like term in the electron density. These divergent terms cancel in this limit, similar to the observation in Sec. 6.4.

The constant electron-ion contribution to the matrix of force constants is given by the Poisson equation for electrostatics: $\frac{d^2 E_{e-i}^{\text{const}}}{d\mathbf{R}^2} = \frac{4\pi}{3} \rho_E^{\text{const}} \mathbf{I}$. The neutralizing background stabilizes any crystal and its contribution is summarized in Table 6.4.

The oscillatory electron-ion contribution, $E_{e-i}(\mathbf{R}) = -2 \sum_I \int V_i(\mathbf{R}_I - \mathbf{R} + \mathbf{r}_e) \rho_E^{\text{osc}}(\mathbf{r}_e) d\mathbf{r}_e$, may be simplified by choosing an ion at the origin and noting that all ions are indistinguish-

able. Subsequently calculating the energy per atom allows us to drop the summation and write

$$E_{e-i}^{\text{osc}}(\mathbf{R}) = -2 \int V_i(-\mathbf{R} + \mathbf{r}_e) \rho_E^{\text{osc}}(\mathbf{r}_e) d\mathbf{r}_e, \quad (6.1)$$

where V_i is given by the Coulomb potential and the oscillatory part of the electron density is approximated by a cosine function (see Appendix D.6).

Finally, for the electron-electron contribution, $E_{e-e} = \sum_I \iint V_e(\mathbf{R}_I - \mathbf{r}_e - \mathbf{r}) \rho_E(\mathbf{r}_e) \rho_E(\mathbf{r}) d\mathbf{r}_e d\mathbf{r}$, we may drop the summation by the same argument. Note also that in the nearly free electron model the electron potential does not depend on the displacement of the central atom. Hence, excluding the 0th-order term and working to 1st-order in u , we may write the oscillatory contribution to the electron-electron energy as

$$E_{e-e}^{\text{osc}} = 2\rho_E^{\text{const}} \int_{\mathbf{r}_e \in \text{unit cell}} \int_{\mathbf{r} \in \mathbb{R}^3} V_e(\mathbf{r}_e - \mathbf{r}) \rho_E^{\text{osc}}(\mathbf{r}) d\mathbf{r} d\mathbf{r}_e, \quad (6.2)$$

where the factor of two appears from the addition of both cross terms, and V_e is again given by the Coulomb potential. The summation of the leading (non-zeroth) order terms from Sec. 6.3, Eq. 6.1, and Eq. 6.2 yields the total matrix of force constants and hence, a stability discriminant.

As an example, we consider the cub lattice with the oscillatory electron density shown in Fig. 6.6. Summing over electron-ion interactions, we find that

$$\frac{E_{e-i}^{\text{osc}}}{u} = -\frac{2}{3} \int \frac{\cos kx + \cos ky + \cos kz}{\sqrt{(x-X)^2 + (y-Y)^2 + (z-Z)^2}} dx dy dz.$$

for an ion displaced from the origin to position (X, Y, Z) , where $k = 2\pi/a$. In Fourier space, this expression reduces to

$$\frac{E_{e-i}^{\text{osc}}}{u} = -2 \int \frac{e^{iq_x X + iq_y Y + iq_z Z}}{q_x^2 + q_y^2 + q_z^2} dq_x dq_y dq_z \sum_{\alpha=x,y,z} \sqrt{\frac{\pi}{2}} (\delta(\mathbf{q} - k\hat{\mathbf{e}}_\alpha) + \delta(\mathbf{q} + k\hat{\mathbf{e}}_\alpha))$$

by Parseval's theorem, which ultimately yields

$$\begin{aligned} \frac{E_{e-i}^{\text{osc}}}{u} &= -\frac{4\sqrt{2}\pi^{3/2}}{3k^2} (\cos kX + \cos kY + \cos kZ) \\ &\sim \frac{2}{3} \sqrt{2}\pi^{3/2} (X^2 + Y^2 + Z^2), \end{aligned}$$

where the approximation is up to a constant and second order in small displacement, \mathbf{R} . Since cub crystal lattices have no contribution at second order from the ion-ion term (see Table 6.1)

and only have a constant contribution from the electron-electron term, we conclude that these systems are stable at second order in the nearly free electron model.

This example calculation is similarly extended to other crystal structures, as shown in Table 6.4. Since the oscillatory electron-electron contribution in Eq. 6.2 integrates to zero for all crystal structures, this table gives the complete information for the total matrices of force constants. We note that all of the electron-ion contributions are positive at this order. We can see that the cubic structures have isotropic matrices, whereas the hexagonal structures are only isotropic in the xy -plane, as expected by symmetry. Out of the crystals considered, hcp has the largest eigenvalue which implies that it is the most stable in this regime, when the oscillation strength is sufficiently large. This result accords with the secondary dominant phase observed in Sec. 6.4, as the opposing models agree in the far limits.

In this section, we have shown that all ionic crystals are stabilized with the addition of constant neutralizing background, and that a 1st-order oscillatory component to the background does not destabilize the system.

6.6 Conclusion

In this chapter, we have analyzed the lattice stability for unconfined crystal structures at zero temperature in the transient Coulomb, tight-binding, and nearly free electron models. We focused on the {cub,bcc,fcc,dia,hcp,dhcp} structures due to their prevalence in nature and distinctive properties.

In Sec. 6.3, we studied a transient one-component system of point Coulomb charges. We found that in this regime, cubic crystal structures have an instability at fourth order, whereas all other crystal structures have an instability at second order. We reviewed the history of the field, and noted that the bcc structure is special for being the stable crystal structure for both the low density Wigner crystal and the high density Coulomb crystal in the one-component plasma model. These findings motivated us to examine the preferred structure as we stabilize the system.

In Sec. 6.4, we stabilized the system through the addition of electron orbitals. For this, we constructed a tight-binding toy model, and introduced the electron orbitals to leading order around the tight-binding limit. We found that in the extreme tight-binding limit, the bcc structure is the most stable, as suspected from the results and discussion in Sec. 6.3. We also showed that if we tune the parameters to increase screening in our pseudopotential model of the nucleus, the fcc structure shows signs of stabilization with a lower energy. This is in agreement with theoretical studies of unconfined three-dimensional Yukawa crystals in the

literature. Finally, we report the second dominant phase to be hcp as we tune away from tight-binding, which accords to trends in the periodic table.

In Sec. 6.5, we briefly examined the stability of crystal structures in the opposite limit, nearly free electrons, which is representative of most common metals. In this model, we found that every crystal structure is stabilized with the addition of constant neutralized background, and that a 1st-order oscillatory perturbation to the background does not destabilize the system. The hcp structure showed the strongest stability, with respect to its matrix of force constants. This result is in agreement with the secondary phase shown in Sec. 6.4.

The work presented in this chapter is, in all sections, based on simplified theoretical models of matter. For real materials, there are a plethora of important effects which need to be taken into consideration to determine the optimal lattice structure e.g. the shape of the atomic orbitals, or the nature of the bonding. However, we have identified here the simplest models to illustrate some of the interesting physical effects at play. We hope that this more detailed look at the stability of three classes of toy model will instill a greater appreciation and understanding of the requirements for crystal stability, as well as their connection with lattice geometry.

Chapter 7

Conclusion

In this thesis, we have presented research in the fields of topological phases of matter, quantum Monte Carlo, and crystal structure. In Chapters 2 and 3, we reviewed the literature in these fields and set the scene for modern research. In Chapter 4, we studied the stability of fractional Chern insulators in higher Chern bands of the Hofstadter model. We showed that stable fractional Chern insulators exist in bands $|C| > 1$ for not only $r = 1$ composite fermion states but also $r = -1$, we presented potential evidence for stability at $|r| \neq 1$, and we analyzed the unexpected features of these exotic states. In Chapter 5, we presented a method for evaluating the matrix of force constants directly in quantum Monte Carlo and showed how this could be used to outperform the accuracy of existing computational methods. We verified the algorithm by stabilizing simple molecules to report their equilibrium bond lengths and eigenfrequencies. Finally, in Chapter 6, we found that cubic crystal structures have a zero 2nd-order matrix of force constants for purely ionic crystals with Coulomb interactions, and we commented on the implications of this result for the tight-binding and nearly free electron models. This observation allowed us revisit the current understanding of solid-state structure with new insight.

This thesis is the result of three years and three months of full-time postgraduate study under the supervision of Dr Gunnar Möller and Dr Gareth Conduit. During this time, the results and novel understanding of these topics has been disseminated at international conferences, workshops and seminars. Chapter 4 has been published in Physical Review B, Chapter 5 has been published in The Journal of Chemical Physics, and Chapter 6 is in preparation for submission. In this work, we have contributed to the field by computationally verifying the latest theories, enhancing state-of-the-art algorithms, and providing new perspectives on well-established knowledge.

The three areas of research presented in this thesis are vast, and usually distinct, and so the full details of each are beyond the scope of this work. However, we have showcased some

of the advancements in these fields, as well as the potential for unifying certain concepts. Future work in these areas could include: revisiting the simulations in Chapter 4 using the density matrix renormalization group; extending the algorithm in Chapter 5 to include the Pulay contribution; and constructing more detailed models of the atom in Chapter 6 to reach broader conclusions on the periodic table. In the long term, these techniques could be combined in the form of quantum Monte Carlo studies of the Hofstadter model, or the realization of three-dimensional fractional Chern insulators. The potential for future work in these fields in general, however, is practically limitless, and it will be exciting to see the developments that the next decade will bring.

Appendix A

Topological States of Matter

A.1 Classical Hall Effect

This section is based on the books by Mahan [125], Whelan & Hodgson [309], Janßen et al. [106], Phillips [108], and the notes by Tong [103]. The original paper is by Hall [98].

The equation of motion for an electron of mass m_e , charge $-e$, and velocity \mathbf{v} , in a magnetic field \mathbf{B} is

$$m_e \dot{\mathbf{v}} = -e\mathbf{v} \times \mathbf{B}. \quad (\text{A.1})$$

This equation may be solved to show that the electron moves in a circular trajectory with characteristic *cyclotron frequency*

$$\omega_B \equiv \frac{eB}{m_e}.$$

The equation of motion for the same electron in a two-dimensional sample with a longitudinal electric field \mathbf{E} is

$$m_e \dot{\mathbf{v}} = -e\mathbf{E} - \frac{m_e \mathbf{v}}{\tau}, \quad (\text{A.2})$$

where the *Drude model* of charge transport assumes that electrons collide elastically with an average *scattering time* τ . In this model, the current density is

$$\mathbf{J} = -n_e e \mathbf{v},$$

where n_e is the electron density. Hence, in equilibrium, Eq. A.2 takes the form of *Ohm's law*

$$\mathbf{J} = \sigma_{\text{DC}} \mathbf{E} \quad \text{with} \quad \sigma_{\text{DC}} \equiv \frac{n_e e^2 \tau}{m_e}.$$

Combining models A.1 & A.2, the equation of motion for electrons confined to a two-dimensional sample in a perpendicular magnetic field is

$$m_e \dot{\mathbf{v}} = -e\mathbf{E} - e\mathbf{v} \times \mathbf{B} - \frac{m_e \mathbf{v}}{\tau}. \quad (\text{A.3})$$

Considering an electron confined to the xy-plane, with a current flowing in the x-direction and a perpendicular magnetic field in the z-direction, Eq. A.3 may be rearranged in the form of Ohm's law; with conductivity and resistivity tensors:

$$\sigma = \frac{\sigma_{\text{DC}}}{1 + \omega_B^2 \tau^2} \begin{pmatrix} 1 & -\omega_B \tau \\ \omega_B \tau & 1 \end{pmatrix} \quad \text{and} \quad \rho = \frac{1}{\sigma_{\text{DC}}} \begin{pmatrix} 1 & \omega_B \tau \\ -\omega_B \tau & 1 \end{pmatrix}.$$

Note that:

1. $\rho_{xy} \propto \tau \Rightarrow$ transverse resistivity is a fundamental material property.
2. $R_{xy} \equiv V_y/I_x = -\rho_{xy} \Rightarrow$ we can measure transverse resistivity directly.

From the resistivity tensor, we deduce that

$$\begin{aligned} \rho_{xx} &= \frac{m_e}{n_e e^2 \tau} = \text{const.}, \\ \rho_{xy} &= R_H B \propto B, \end{aligned}$$

where the *Hall coefficient* is defined as

$$R_H \equiv \frac{\rho_{xy}}{B} = \frac{1}{n_e e}.$$

R_H is completely independent of the sample geometry. Hence, the transverse resistivity in the *classical Hall effect* is directly proportional to the magnetic field strength. The longitudinal resistivity is trivially constant.

A.2 Anyons

This section is based on the review by Nayak [139] and the notes by Tong [103]. The original papers are by Leinaas & Myrheim [310] and Wilczek [311].

Consider two indistinguishable particles with wave function $\psi(\mathbf{r}_1, \mathbf{r}_2)$. Since the particles are indistinguishable, we demand upon exchange

$$\psi(\mathbf{r}_1, \mathbf{r}_2) = e^{i\pi\alpha_s} \psi(\mathbf{r}_2, \mathbf{r}_1).$$

In three or more dimensions, exchanging the particles twice is equivalent to the identity and so

$$e^{2\pi i\alpha_s} = 1. \quad (\text{A.4})$$

This implies that

$$\alpha_s = \begin{cases} 0 & \text{for bosons,} \\ 1 & \text{for fermions.} \end{cases}$$

For this many dimensions, the particles' space-time trajectories may be continuously connected to their original world-lines. Hence, switching the particles twice corresponds to the identity transformation. In two dimensions, this is not the case.

In two dimensions, the particles' world-lines braid around each other as they are exchanged. Hence, their space-time trajectories cannot be continuously connected to their original world-lines. Consequently, in two-dimensions, any value of α_s is permitted in Eq. A.4, and so we postulate the existence of *anyons*.

Mathematically, in $d \geq 3$ dimensions, particle exchange is represented by the permutation group, whereas in $d = 2$ dimensions, it is represented by the braid group. As particles are exchanged in two dimensions, their world-lines make braids which are only distinguished by their topological class. All elements of the braid group B_n may be generated by the set of operations $\{R_1, \dots, R_{n-1}\}$, where R_i is the anticlockwise exchange of the i^{th} and $(i+1)^{\text{th}}$ particle. Hence, it may be shown that

$$\begin{aligned} R_i R_j &= R_j R_i, & |i-j| &\geq 3, \\ R_i R_{i+1} R_i &= R_{i+1} R_i R_{i+1}, & i &= 1, \dots, n-1. \end{aligned}$$

In terms of the original problem of particle exchange, in two dimensions, the unitary exchange operator in Hilbert space forms a one-dimensional representation of the braid group, with $R_i = e^{i\pi\alpha_{s,i}}$. The particles whose exchange may be represented using the one-dimensional

braid group are known as *Abelian anyons*, whereas particles whose exchange is represented by higher-dimensional braid groups are known as *non-Abelian anyons*.

Appendix B

Stability of Fractional Chern Insulators in the Effective Continuum Limit of Harper-Hofstadter Bands with Chern Number $|C| > 1$

B.1 Periodic Landau Gauge Vector Potential for Rectangular Lattices

Consider a general rectangular lattice with $\mathbf{l}_x = l_x \hat{\mathbf{e}}_x$ and $\mathbf{l}_y = l_y \hat{\mathbf{e}}_y$. In this basis, the absolute position vector may be written as

$$\mathbf{r} = \begin{pmatrix} x \\ y \end{pmatrix} = \xi_x \mathbf{l}_x + \xi_y \mathbf{l}_y$$

with $\xi_x = x/l_x$ and $\xi_y = y/l_y$. Following from Hasegawa & Kohmoto [201], we know that the periodic Landau gauge phase is given as

$$\chi(\mathbf{r}) = -SB[\xi_x]\xi_y,$$

where $S = |\mathbf{l}_x \times \mathbf{l}_y| = l_x l_y$. Hence, the phase may be written as

$$\chi(\mathbf{r}) = -Bl_x y \left\lfloor \frac{x}{l_x} \right\rfloor. \quad (\text{B.1})$$

Ultimately, we would like to calculate the periodic Landau gauge vector potential for rectangular lattices $\mathbf{A}^{(\text{p,rect})}$, which may be expressed in terms of the Landau gauge vector potential $\mathbf{A}^{(\text{L,rect})}$ for rectangular lattices as

$$\mathbf{A}^{(\text{p,rect})} = \mathbf{A}^{(\text{L,rect})} + \nabla\chi(\mathbf{r}). \quad (\text{B.2})$$

From Eq. B.1, we may write

$$\nabla\chi(\mathbf{r}) = -B \begin{pmatrix} y \sum_{n=-\infty}^{\infty} \delta(x/l_x - n + \varepsilon) \\ \lfloor x/l_x \rfloor \\ 0 \end{pmatrix}, \quad (\text{B.3})$$

where ε is an infinitesimal, added to avoid an ambiguity of the phase factor at lattice site positions. Now, given that the Landau gauge vector potential for rectangular lattices is

$$\mathbf{A}^{(\text{L,rect})} = \frac{SB}{2\pi} \xi_x \mathbf{F}_y, \quad (\text{B.4})$$

where

$$\mathbf{F}_y \equiv 2\pi \left(\frac{\hat{\mathbf{e}}_z \times \mathbf{l}_x}{(\mathbf{l}_x \times \mathbf{l}_y) \cdot \hat{\mathbf{e}}_z} \right) = \frac{2\pi}{l_y} \mathbf{e}_y,$$

we may substitute Eqs. B.4 & B.3 into Eq. B.2, which yields

$$\mathbf{A}^{(\text{p,rect})} = B \begin{pmatrix} -y \sum_{n=-\infty}^{\infty} \delta(x/l_x - n + \varepsilon) \\ x - \lfloor x/l_x \rfloor \\ 0 \end{pmatrix}.$$

Note that this potential reproduces the same discrete implementation of the finite-size Harper-Hofstadter Hamiltonian (Eq. 4.1), as would be obtained by applying the magnetic translation algebra with a basis of $\{T_M(\mathbf{l}_x), T_M(\mathbf{l}_y)\}$ (see, e.g., the supplementary material of Ref. 163).

B.2 Periodic Landau Gauge Transform in Fourier Space

As a gauge transform of the electromagnetic vector potential $\mathbf{A}(\mathbf{r}) \rightarrow \mathbf{A}(\mathbf{r}) + \nabla\chi(\mathbf{r})$ acts multiplicatively on the wave function in position space via $\psi(\mathbf{r}) \rightarrow \exp[i\chi(\mathbf{r})]\psi(\mathbf{r})$, its action in reciprocal space takes the form of a convolution with the gauge function. Let us therefore consider the Fourier transform of the gauge transforms between a periodic Landau gauge with respect to the standard Landau gauge to establish how momenta are transformed.

Consider a system with a total of $N_x N_y$ sites, $q = l_x l_y$ sites in each MUC, and $L_x L_y$ MUCs in the system. Let the system be pierced with a perpendicular magnetic field $\mathbf{B} = 2\pi n_\phi \hat{\mathbf{e}}_z$, where the lattice constant is set to one and sites in the MUC are labeled with a sublattice index $\alpha = 0, \dots, (q - 1)$. In the Landau gauge, the MUC is naturally $q \times 1$. To realize this gauge in a finite-size geometry, we require $N_x \bmod q = 0$, and hence we obtain momenta $k_x^{(L)} = 2\pi n^{(L)}/N_x$, with $n^{(L)} = 0, \dots, N_x/q - 1$ and $k_y^{(L)} = 2\pi m^{(L)}/N_y$, with $m^{(L)} = 0, \dots, N_y$. By contrast, the set of allowed momentum vectors in the periodic gauge are

$$\{\mathbf{k}^{(p)}\} = \left\{ \left(\frac{2\pi}{N_x} n, \frac{2\pi}{N_y} m \right) \right\},$$

with momentum indices $n = 0, \dots, L_x - 1$ and $m = 0, \dots, L_y - 1$. The resulting Brillouin zones (BZ) have different shapes, with the BZ for the Landau gauge spanning a narrow tall rectangle $\mathbf{k} \in [-\pi/q, \pi/q] \times [-\pi, \pi]$, whereas the periodic gauge yields a wider and shorter BZ geometry.

The absolute position vector $\mathbf{r}_{st\alpha} = \mathbf{R}_{st} + \rho_\alpha$ may be written as

$$\mathbf{r}_{st\alpha} = sl_x \hat{\mathbf{e}}_x + tl_y \hat{\mathbf{e}}_y + \rho_\alpha,$$

with spatial indices $s = 0, \dots, L_x - 1$ and $t = 0, \dots, L_y - 1$, and corresponding sublattice vectors

$$\rho_\alpha = \begin{pmatrix} \alpha \bmod l_x \\ \lfloor \alpha / l_x \rfloor \end{pmatrix}.$$

The magnetic field may be written as $\mathbf{B} = \nabla \times \mathbf{A}$, with a vector potential in the Landau gauge

$$\mathbf{A}^{(L)} = Bx \hat{\mathbf{e}}_y$$

that is independent of y . Other vector potentials may be obtained via a gauge transformation

$$\mathbf{A} \rightarrow \mathbf{A} + \nabla \chi(\mathbf{r}).$$

To ensure gauge periodicity, we take

$$\chi(\mathbf{r}) = -B[x]y,$$

which, with an arbitrary rectangular lattice basis $\{l_x \hat{\mathbf{e}}_x, l_y \hat{\mathbf{e}}_y\}$, becomes

$$\chi(\mathbf{r}) = -Bl_x \lfloor x/l_x \rfloor y,$$

as discussed by Hasegawa & Kohmoto [201]. We are interested in transforming to some arbitrary periodic Landau gauge, such that

$$\psi^{(p)} = G_\alpha \psi^{(L)},$$

where the gauge factor $G_\alpha \equiv e^{i\chi}$. In Fourier space, this may be written as

$$\hat{\psi}^{(p)} = \hat{G}_\alpha * \hat{\psi}^{(L,p)}, \quad (\text{B.5})$$

where $*$ denotes the convolution, and $\hat{\psi}^{(L,p)}$ indicates the wave function in the original Landau gauge Fourier transformed with respect to the BZ of the periodic gauge. Specifically, the Fourier transform with respect to the MUC in periodic gauge is defined as

$$\hat{f}(x,y) = \sum_{s=0}^{L_x-1} \sum_{t=0}^{L_y-1} e^{-i\mathbf{k}^{(p)} \cdot \mathbf{r}_{st\alpha}} f(x,y),$$

where $f(x,y)$ is an arbitrary function of x - and y -positions. The corresponding Fourier transform of the Landau gauge wave function in Eq. B.5 is of a general form, with functions given by solutions to the Harper equation. However, the Fourier transform of the gauge factor is analytically calculable, and we proceed by evaluating it here.

Noting that

$$\left\lfloor \frac{sl_x + \alpha \bmod l_x}{l_x} \right\rfloor = s,$$

and taking out constant factors, we find that

$$\hat{G}_\alpha = e^{-i\mathbf{k}^{(p)} \cdot \rho_\alpha} \sum_{s,t} \left(e^{-iBq} \right)^{st} \left(e^{-i(k_x^{(p)} l_x + B l_x \lfloor \alpha / l_x \rfloor)} \right)^s \left(e^{-ik_y^{(p)} l_y} \right)^t.$$

Since $B = 2\pi n_\phi = 2\pi p/q$, $\forall p \in \mathbb{Z}$, we make the simplification

$$\left(e^{-iBq} \right)^{st} = 1,$$

which allows us to separate the summation, such that

$$\hat{G}_\alpha = e^{-i\mathbf{k}^{(p)} \cdot \rho_\alpha} \sum_{s=0}^{L_x-1} \left(e^{-i(k_x^{(p)} l_x + B l_x \lfloor \alpha / l_x \rfloor)} \right)^s \sum_{t=0}^{L_y-1} \left(e^{-ik_y^{(p)} l_y} \right)^t.$$

Since $k_y^{(p)} = 2\pi m/l_y L_y$ for $m = 0, \dots, L_y - 1$, we deduce that

$$\sum_{t=0}^{L_y-1} \left(e^{-ik_y^{(p)} l_y} \right)^t = L_y \delta_{k_y^{(p)}, 0}.$$

Hence, our expression reduces to

$$\hat{G}_\alpha(\mathbf{k}^{(p)}) = L_y e^{-ik_x^{(p)}(\alpha \bmod l_x)} \sum_{s=0}^{L_x-1} e^{-i\frac{2\pi}{l_y}(l_y n + p L_x \lfloor \alpha/l_x \rfloor) \frac{s}{L_x}} \delta_{k_y^{(p)}, 0}.$$

Furthermore, since the total number sites in the x-direction is necessarily a multiple of q , it follows that $L_x \propto l_y$ in all cases. This allows us to make the simplification

$$\hat{G}_\alpha(\mathbf{k}^{(p)}) = L_x L_y \exp \left\{ -ik_x^{(p)}(\alpha \bmod l_x) \right\} \delta_{k_x^{(p)} N_x / 2\pi + p \kappa \lfloor \alpha/l_x \rfloor, 0} \delta_{k_y^{(p)}, 0}, \quad (\text{B.6})$$

where κ is the constant of proportionality such that $L_x = \kappa l_y$. Hence, the gauge factor may be explicitly expressed as a function of periodic gauge momentum in the x-direction. The k_y dependence in $\hat{\psi}^{(p)}$ comes solely from $\hat{\psi}^{(L,p)}$. Consequently, the k_y momentum in the periodic gauge equals the original k_y momentum in the Landau gauge modulo $2\pi/l_y$, while the transformation on the k_x dependence is non-trivial as ensues from Eq. B.6.

B.3 Scaling to the Continuum Limit at Fixed Flux Density

To cross-validate our scaling to the effective continuum at fixed aspect ratio, we additionally perform scaling for select cases at fixed flux density, n_ϕ .

In this procedure, we select a set of q values approximately geometrically distributed with common ratio 2, in the range $10 \lesssim q \lesssim 10^3$. This provides a spread of q values which reflects the distribution used in the scaling at fixed aspect ratio.¹ q defines the number of sites in each MUC, $l_x l_y$, which we factorize into all distinct pairs of factors. For each q value, we study N values in the range $N_{\min} \lesssim N \lesssim N_{\max}$, where N_{\min} and N_{\max} are the minimum and maximum number of particles studied in the fixed aspect ratio scaling. Here N/v defines the total number of MUCs in the system, $L_x L_y$, which we also factorize into all distinct pairs of factors. At this point, for each q, N configuration, we select the (l_x, l_y) and (L_x, L_y) pairs so as to minimize the deviation from a square system, ε . This minimization is performed only

¹Furthermore, q values with multiple factors are preferred during the selection process, and prime q immediately rejected, so as to maximize the chances of approximately square configurations for comparison.

as a subsidiary constraint to improve the comparison with the fixed aspect ratio scaling in the bulk of the chapter. In practice, ε may be as high as 50% for this scaling procedure.

To illustrate the mutual consistency of the scaling at fixed flux density ($\lim_{q,N \rightarrow \infty}$) and the scaling at fixed aspect ratio ($\lim_{N,q \rightarrow \infty}$), we provide data on the $r = 1$ Laughlin states, for both bosons (Fig. B.1a) and fermions (Fig. B.1b) in a $|C| = 1$ band. Here, we find extrapolated values of $\lim_{q,N \rightarrow \infty}(q\Delta) = 0.62 \pm (7.0 \times 10^{-4})$ for bosons and $\lim_{q,N \rightarrow \infty}(q^2\Delta) = 2.56 \pm (7.2 \times 10^{-3})$ for fermions, which is in close agreement with Sec. 4.3.1. We also examine the scaling at finite flux density for more fragile states in higher Chern number bands. Generally in these cases, we find that the effective continuum limit at constant aspect ratio provides a much smoother extrapolation that minimizes finite-size effects. Examples are shown in Fig. B.2.

B.4 Derivation of the Correlation Function

The two-particle correlation function may be written as the expectation value of the density operator, ρ , of a particle at site i with the density operator of a particle at site j :

$$\langle \rho_i \rho_j \rangle = \langle c_i^\dagger c_i c_j^\dagger c_j \rangle,$$

where c^\dagger , c are the creation and annihilation operators, respectively. We may normal order the expression such that, for bosons or fermions,

$$\langle : \rho_i \rho_j : \rangle = \langle c_i^\dagger c_j^\dagger c_j c_i + c_i^\dagger c_i \delta_{ij} \rangle.$$

From here, we substitute in the expression for the Fourier transform with respect to absolute position

$$c_{\mathbf{r}} = \frac{1}{\sqrt{N_c}} \sum_{n,\mathbf{k}} u_{n,\alpha}(\mathbf{k}) e^{i\mathbf{k}\cdot\mathbf{r}} c_{n,\mathbf{k}},$$

where N_c is the number of MUCs, n is the band index, α is the sublattice index corresponding to position \mathbf{r} , and \mathbf{k} is the momentum. This substitution yields

$$\begin{aligned} \langle : \rho_i \rho_j : \rangle &= \frac{1}{N_c^2} \sum_{\{n\}, \{\mathbf{k}\}} u_{n_1, \alpha_i}^*(\mathbf{k}_1) u_{n_2, \alpha_j}^*(\mathbf{k}_2) u_{n_3, \alpha_j}(\mathbf{k}_3) u_{n_4, \alpha_i}(\mathbf{k}_4) e^{i(-\mathbf{k}_1 \cdot \mathbf{r}_i - \mathbf{k}_2 \cdot \mathbf{r}_j + \mathbf{k}_3 \cdot \mathbf{r}_j + \mathbf{k}_4 \cdot \mathbf{r}_i)} \\ &\langle c_{n_1, \mathbf{k}_1}^\dagger c_{n_2, \mathbf{k}_2}^\dagger c_{n_3, \mathbf{k}_3} c_{n_4, \mathbf{k}_4} \rangle + \frac{1}{N_c} \sum_{\substack{n_1, n_4 \\ \mathbf{k}_1, \mathbf{k}_4}} u_{n_1, \alpha_i}^*(\mathbf{k}_1) u_{n_4, \alpha_i}(\mathbf{k}_4) e^{i(-\mathbf{k}_1 \cdot \mathbf{r}_i + \mathbf{k}_4 \cdot \mathbf{r}_i)} \langle c_{n_1, \mathbf{k}_1}^\dagger c_{n_4, \mathbf{k}_4} \rangle \delta_{ij}. \end{aligned}$$

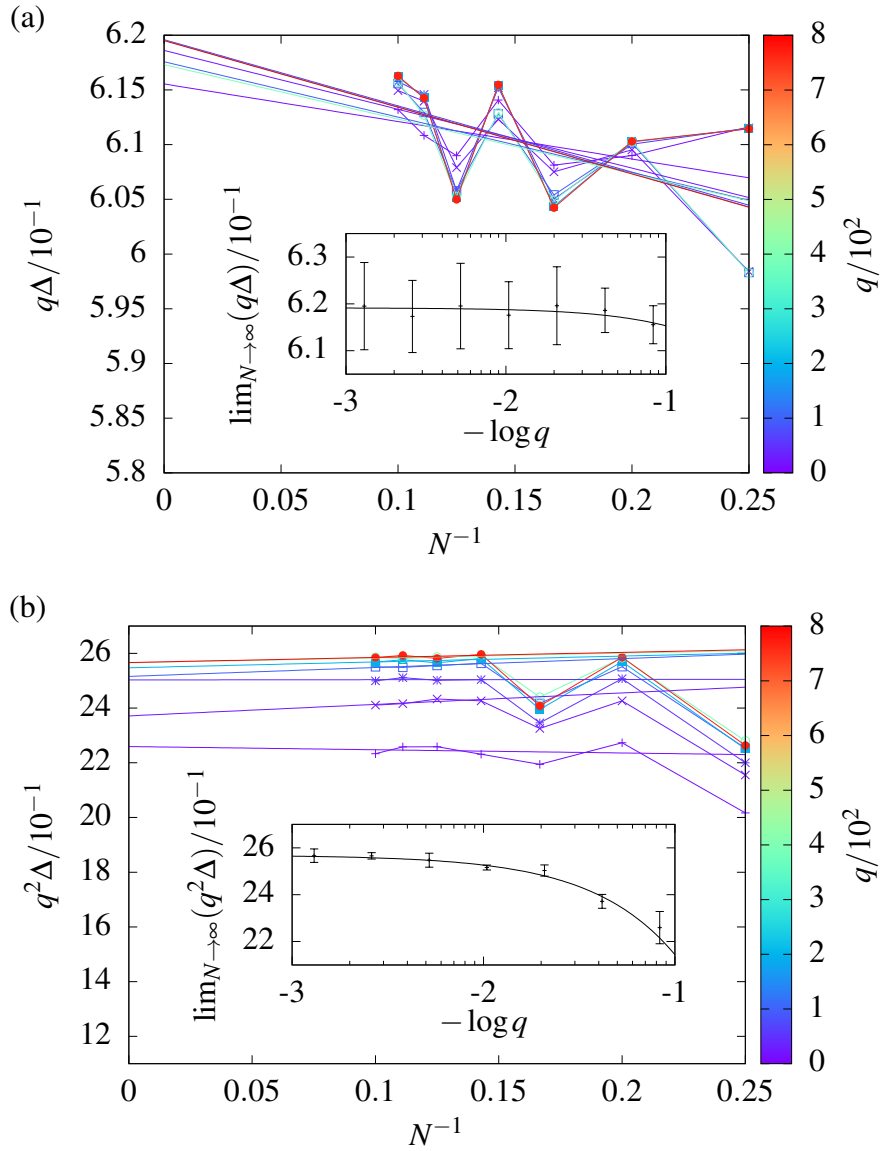


Fig. B.1 Finite-size scaling of the gap at fixed flux density. We show the finite-size gaps for flux densities $n_\phi = p/q$ with increasing values of denominator q given by the color scale as a function of the inverse system size for (a) the bosonic $\nu = 1/2$ states, and (b) the fermionic $\nu = 1/3$ states, in the $|C| = 1$ band. The extrapolations to the thermodynamic limit excludes outliers at small system sizes, i.e. excluding $N = 4$ in panel (a) and $N = 4, 5, 6$ in panel (b). The corresponding plots for the thermodynamic extrapolated gaps, for each finite q , are inset.

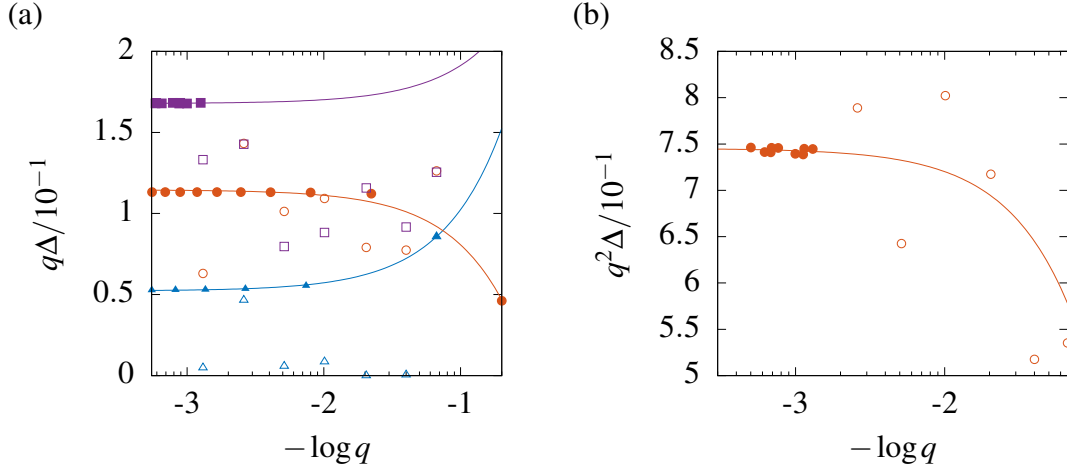


Fig. B.2 Finite-size scaling of the gap in the $C = 2$ band for (a) bosonic states, where squares, circles, and triangles denote states with $\{r = -3, N = 9; r = 2, N = 8; r = 3, N = 6\}$, respectively; and (b) fermionic states with $\{r = -1, N = 6\}$. The filled (hollow) symbols correspond to scaling with fixed aspect ratio (flux density). The linear trend-lines are shown for the scaling with fixed aspect ratio.

Introducing the single-particle wave function, $\phi_{n,\mathbf{k}}(\mathbf{r}_i) = u_{n,\alpha_i}(\mathbf{k})e^{i\mathbf{k}\cdot\mathbf{r}_i}$, this expression reduces to

$$\begin{aligned} \langle : \rho_i \rho_j : \rangle &= \frac{1}{N_c^2} \sum_{\{n\}, \{\mathbf{k}\}} \phi_{n_1, \mathbf{k}_1}^*(\mathbf{r}_i) \phi_{n_2, \mathbf{k}_2}^*(\mathbf{r}_j) \phi_{n_3, \mathbf{k}_3}(\mathbf{r}_j) \phi_{n_4, \mathbf{k}_4}(\mathbf{r}_i) \langle c_{n_1, \mathbf{k}_1}^\dagger c_{n_2, \mathbf{k}_2}^\dagger c_{n_3, \mathbf{k}_3} c_{n_4, \mathbf{k}_4} \rangle \\ &+ \frac{1}{N_c} \sum_{\substack{n_1, n_4 \\ \mathbf{k}_1, \mathbf{k}_4}} \phi_{n_1, \mathbf{k}_1}^*(\mathbf{r}_i) \phi_{n_4, \mathbf{k}_4}(\mathbf{r}_i) \underbrace{\langle c_{n_1, \mathbf{k}_1}^\dagger c_{n_4, \mathbf{k}_4} \rangle}_{\propto \delta_{\mathbf{k}_1, \mathbf{k}_4}} \delta_{ij}. \end{aligned}$$

Because of the proportionality relation of the density expectation value, the last sum reduces to a sum over a single momentum.

B.5 Accuracy of Correlation Functions

In order to verify the accuracy of the density-density correlation functions used in this project, we compare the correlation for the robust six-particle $\nu = 1/2$ state with the exact continuum result for a torus, shown in Fig. B.3. The derivation of the lattice correlation function in terms of single-particle eigenstates is shown in Appendix B.4, and the exact form of the correlation function on the continuum torus is discussed in many sources, for example, by Yoshioka et al. [312]. Note the slight deviation of the lattice result from the exact solution. Figures B.3a & B.3c show plots of the density-density correlation function with $p = 71$ and

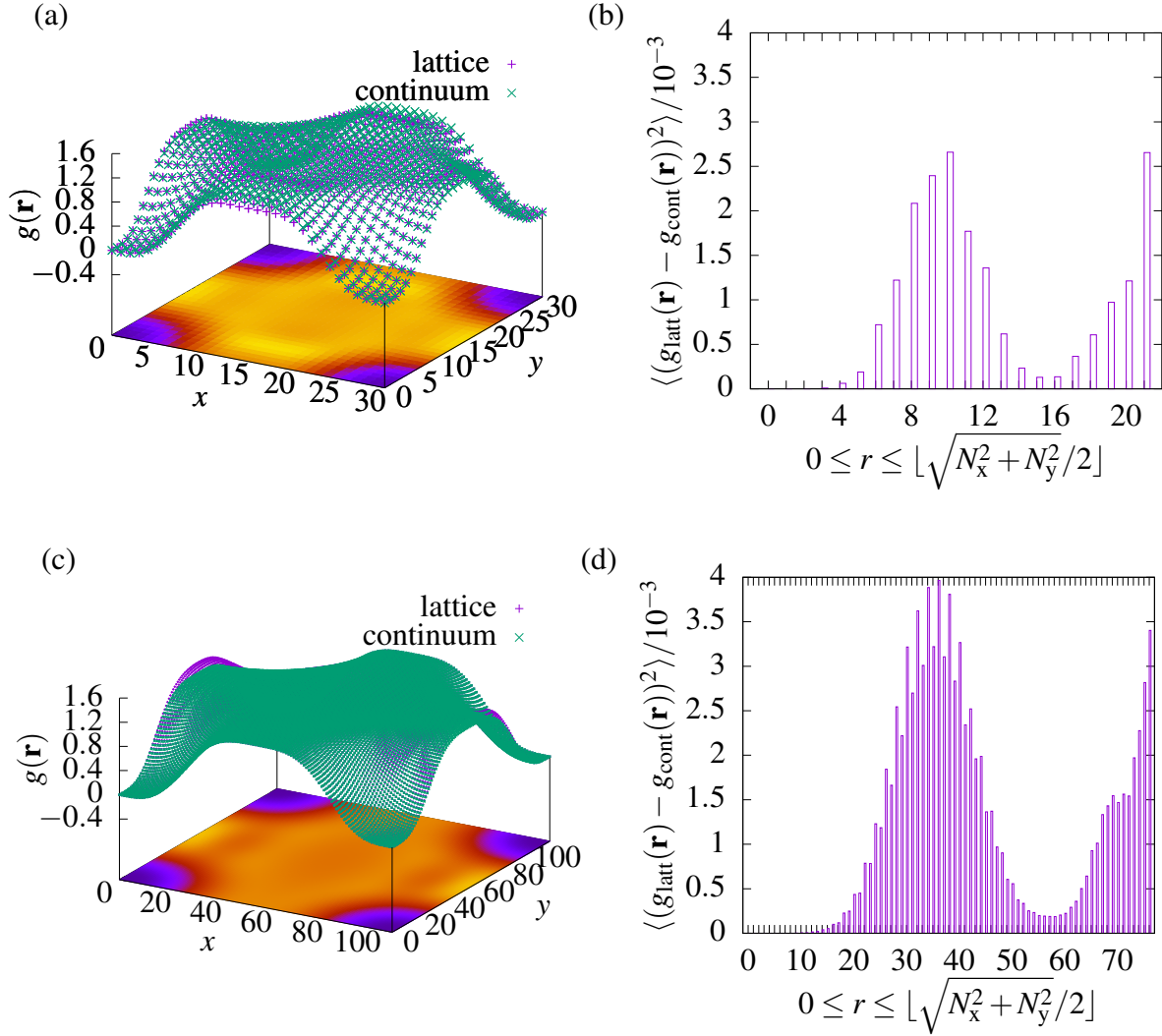


Fig. B.3 [(a), (c)] Two-particle correlation function for the bosonic six-particle $\nu = 1/2$ (Laughlin) state in the $|C| = 1$ band and $(k_x, k_y) = (0, 0)$ momentum sector, with (a) $p = 74$, and (c) $p = 971$. The lattice result is additionally projected to the base, and the exact continuum solution is plotted for comparison. [(b), (d)] Variance between the continuum and lattice results, with (b) $p = 74$, and (d) $p = 971$. The average is taken with respect to the points enclosed in origin-centric annuli of width $1.5a$, where a is the lattice spacing.

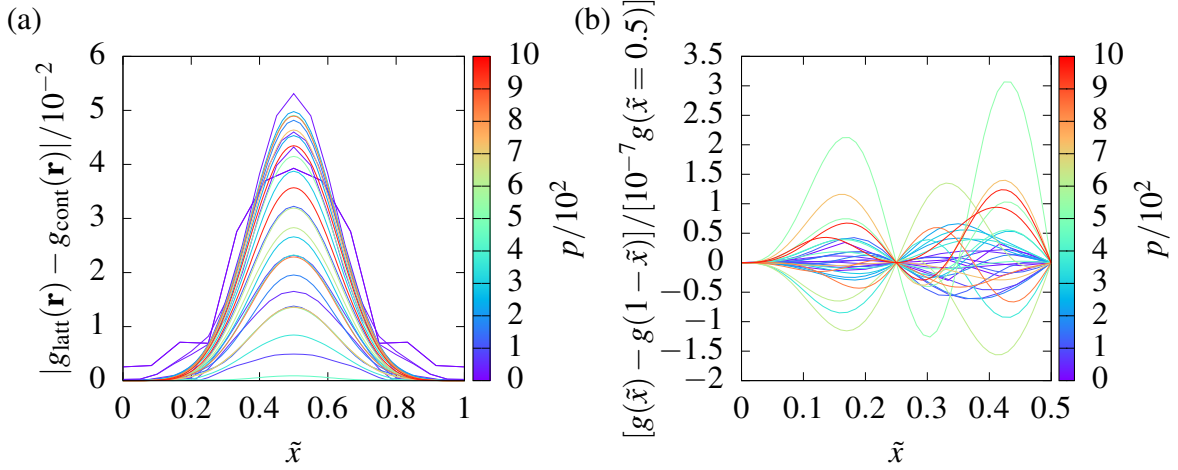


Fig. B.4 (a) Absolute deviation from the exact continuum torus solution and (b) asymmetry in the two-particle correlation function for the bosonic eight-particle $\nu = 1/2$ (Laughlin) state in the $|C| = 1$ band and $(k_x, k_y) = (0, 0)$ momentum sector, with $L_x = L_y = 4$. A $y = 0$ cross section is rescaled such that $\tilde{x} = x/N_x$.

$p = 971$, respectively, whereas Figs. B.3b & B.3d show the corresponding variance between the continuum and lattice results. We observe an agreement at the zero-separation correlation hole which oscillates with distance (note the small scale of the variance in Figs. B.3b & B.3d). Because of the lack of scaling with radius, this discrepancy is attributed to computational imprecision of the single-particle eigenvectors, which we obtain with standard diagonalization routines of the LAPACK library.

The same analysis is performed for the robust eight-particle state in the same Laughlin series. The asymmetry of the lattice results as well as their deviation from the continuum is shown in Fig. B.4. Since the continuum torus correlation function is symmetric by construction, we confirm that the lattice results obey the fundamental symmetry also, up to the scale of Fig. B.4a. In Fig. B.4b, we explicitly plot the asymmetry in the lattice results (note the small scale of the plot). The fact that we do not find a monotonic behavior of the asymmetry with p , supporting the view that the deviations are due to the numerical accuracy of the single-particle eigenstates.

B.6 Error Analysis

In order to obtain the thermodynamic (effective) continuum limit, we linearly extrapolated the data for the $q^{(2)}\Delta$ vs $1/q$ and $q^{(2)}\Delta$ vs $1/N$ plots. To determine this scaling, we rejected low- q/N outliers and focused only on high- q/N data points, since they are closer to the mode and also the limit of the distribution. As illustrated in the above discussion, occasionally data

for the limit is not precise. We define error bars relative to the linear trend-line. For most cases, this is the asymptotic standard error for the y-intercept fit parameter of a standard linear regression in N^{-1} . However, for $|C| > 1$ in the $q \rightarrow \infty$ limit, the error bars were read off on a case-by-case basis, by inspection, since they were often asymmetric and larger than the asymptotic standard error estimate.

Appendix C

Direct Evaluation of the Force Constant Matrix in Quantum Monte Carlo

C.1 Atomic Relaxation Calculation

In this section, we describe in detail how the configuration coordinates are adjusted on each step during the atomic relaxation process.

Let us define the atomic displacement on each Monte Carlo step as

$$\Delta\mathbf{R} = \Delta\mathbf{R}_e + \Delta\mathbf{R}_t + \Delta\mathbf{R}_r,$$

where $\Delta\mathbf{R}_e$ is the energy-minimizing term, $\Delta\mathbf{R}_t$ is the correction for global translations, and $\Delta\mathbf{R}_r$ is the correction for global rotations. We adjust the atomic displacements from \mathbf{R} to $\mathbf{R} + \Delta\mathbf{R}$ on each step, so as to minimize the total energy of the system. Once the equilibrium is reached, the anharmonic correction is applied.

C.1.1 Minimizing the energy

Consider a system of N_n atoms in three dimensions. Taylor expanding the total energy of the system as a function of atomic displacements, up to quadratic order, yields

$$E = E_0 + \sum_{I=1}^{N_n} \frac{dE}{d\mathbf{R}_I} \Delta\mathbf{R}_I + \frac{1}{2} \sum_{IJ} \frac{d^2E}{d\mathbf{R}_I d\mathbf{R}_J} \Delta\mathbf{R}_I \Delta\mathbf{R}_J,$$

where E_0 is a constant. Demanding that the sum of the 1st- and 2nd-order terms in the energy are zero at the minimum, gives

$$\left[\frac{1}{2} \Delta \mathbf{R}^T \mathbf{M} + \nabla_{\mathbf{R}} E \right] \cdot \Delta \mathbf{R} = 0,$$

which, excluding the trivial solution, implies

$$\Delta \mathbf{R}_e = -2\mathbf{M}^{-1} \nabla_{\mathbf{R}} E,$$

where \mathbf{M} is the matrix of force constants, and $\nabla_{\mathbf{R}} E$ is the multi-atom energy gradient with respect to the configuration atomic-displacement vector, \mathbf{R} . This is the bare estimate for the atomic-displacement correction, up to second order in the energy.

C.1.2 Correction for global translations

In order to ensure that the origin of our configuration is fixed and that we have no global translational mode, we explicitly subtract the center of mass motion of the configuration.

Given N_n atoms, each with mass m_I , this implies that the global translation correction term is

$$\Delta \mathbf{R}_t = - \frac{\sum_I m_I \mathbf{R}_I}{\sum_I m_I}.$$

This term is particularly important for non-symmetric molecules, such as hydrogen chloride in Sec. 5.4.2.

C.1.3 Correction for global rotations

Similarly, to ensure that the bond length corrections do not result in a rotation of the configuration, or atomic pair rotations, we explicitly subtract global rotational modes.

The law of moments states that the total moment about the center of mass of any atomic pair, as well as the total moment about the origin of the configuration, is zero, which gives $\sum_I m_I \mathbf{b}_I = \mathbf{0}$ and $\sum_I m_I \mathbf{R}_I = \mathbf{0}$, where \mathbf{b} is the half-bond length between an atomic pair. Together, these relations imply

$$\sum_I m_I \mathbf{R}_I \times (\mathbf{b}_I - \mathbf{R}_I \times \theta) = \mathbf{0}, \quad (\text{C.1})$$

where $\mathbf{b}_{r,I} \equiv \mathbf{b}_I - \mathbf{R}_I \times \theta$ is the corrected half-bond length to be found. Hence, an expression for the angular displacement of the molecule $\theta_I \equiv (\theta_{xI}, \theta_{yI}, \theta_{zI})$ is needed. Using the vector

triple product identity, we find that Eq. C.1 reduces to

$$\sum_I m_I \mathbf{R}_I \times \mathbf{b}_I = \sum_I [m_I \mathbf{R}_I (\mathbf{R}_I \cdot \boldsymbol{\theta}) - m_I \boldsymbol{\theta} (\mathbf{R}_I \cdot \mathbf{R}_I)],$$

which after rearrangement becomes

$$\underbrace{\sum_I m_I \begin{pmatrix} R_{yI} b_{zI} - R_{zI} b_{yI} \\ R_{zI} b_{xI} - R_{xI} b_{zI} \\ R_{xI} b_{yI} - R_{yI} b_{xI} \end{pmatrix}}_{\mathbf{a}} = \sum_I m_I \underbrace{\begin{pmatrix} -R_{yI}^2 - R_{zI}^2 & R_{yI} R_{xI} & R_{zI} R_{xI} \\ R_{xI} R_{yI} & -R_{xI}^2 - R_{zI}^2 & R_{zI} R_{yI} \\ R_{xI} R_{zI} & R_{yI} R_{zI} & -R_{xI}^2 - R_{yI}^2 \end{pmatrix}}_{\mathbf{B}} \begin{pmatrix} \theta_x \\ \theta_y \\ \theta_z \end{pmatrix}.$$

This implies that the atomic displacement correction for global rotations, is

$$\Delta \mathbf{R}_{r,I} = -\mathbf{R}_I \times \boldsymbol{\theta},$$

where $\boldsymbol{\theta} = \mathbf{B}^{-1} \mathbf{a}$.

C.1.4 Correction for anharmonicity

Up to this point in the analysis, we have assumed that the interaction between atomic pairs is harmonic. Although this is a valid approximation at short distances, at larger distances this approximation breaks down and so a correction term is necessary. One of the most well-studied models used to capture anharmonicity in the interaction between diatomic molecules is the Morse Hamiltonian, which we use as an approximation for our case studies. The Morse Hamiltonian is given by

$$\hat{H} = \frac{\hat{p}^2}{2\mu} + \hat{V}$$

with a Morse potential

$$\hat{V} = V(x) = D[1 - e^{-\alpha x}]^2, \quad (\text{C.2})$$

where D is the $x = x_0$ energy-minimum depth relative to the dissociation limit at $x \rightarrow \infty$, and α determines the curvature of the potential [313].

The eigenvalues of the Morse Hamiltonian are

$$E_n = \hbar\omega_0 \left[\left(n + \frac{1}{2} \right) - x_e \left(n + \frac{1}{2} \right)^2 \right],$$

where $\omega_0 \equiv \sqrt{2D\alpha^2/\mu}$ is the fundamental frequency, $x_e \equiv \hbar\omega_0/4D$ is the anharmonic constant, and $n \in \mathbb{Z}^+$ is the principal quantum number.

Note that the minima of the harmonic and Morse potentials are the same. However, due to the dissociative limit of the Morse potential, the expectation value of position is shifted in the positive x -direction in the Morse case. One of the main advantages of this model is that the majority of its properties can be expressed analytically.

By setting $D \equiv \frac{\hbar^2\alpha^2}{2\mu}(N + 1/2)^2$, the Morse Hamiltonian may be written as

$$\hat{H} = -\frac{\hbar^2}{2\mu} \frac{\partial^2}{\partial x^2} + \frac{\hbar^2\alpha^2}{2\mu} \left(N + \frac{1}{2}\right)^2 (e^{-2x} - 2e^{-x})$$

up to a constant term. The expectation value of position with respect to the ground-state Morse wave function is then

$$\langle 0|\hat{x}|0\rangle = \frac{\ln(2N+1) - \psi(2N)}{\alpha},$$

where ψ is the digamma function [314]. Expanding the expectation value of position gives

$$\langle 0|\hat{x}|0\rangle = \frac{3}{2} \sqrt{\frac{\hbar x_e}{2\mu\omega_0}}$$

up to leading order in x_e . This is the shift in the equilibrium bond length due to the anharmonicity of the Morse potential.

In order to evaluate this shift, an estimate for the anharmonic constant is needed. Expanding the Morse potential (Eq. C.2) about the equilibrium displacement $x = x_0$ in powers of x , we find that

$$V(x) = \frac{1}{2}\mu\omega_0^2x^2 + \sqrt{\frac{\mu^3x_e\omega_0^5}{2\hbar}}x^3 + \dots$$

up to a constant term. Comparing quadratic and cubic terms in x with the general form of the Taylor expansion, and solving simultaneously, yields

$$x_e = \frac{\hbar}{18\sqrt{\mu}} \left(\frac{d^3V}{dx^3} \Big|_{x_0} \right)^2 \left(\frac{d^2V}{dx^2} \Big|_{x_0} \right)^{-5/2}.$$

Conventionally, the third derivative of the energy is extracted from the curvature of the force, however now utilizing the new information available, we extract the anharmonic constant directly from the gradient of the force constant.

C.2 Vibrational Modes Calculation

In this section, we describe in detail the methods used to determine the vibrational modes and frequencies of atomic configurations, as well as their associated statistical uncertainties.

C.2.1 Existing computational approaches

In order to calculate an estimate for the frequency using the RHF and DFT methods, we use the default scheme, PBE and B3LYP exchange-correlation functionals, respectively, within the CRYSTAL program [58].

C.2.2 Matrix of force constants approach

The direct method to obtain the vibrational frequencies of a molecule is from an exact diagonalization of the matrix of force constants. Consider, for example, a diatomic molecule in one dimension, such as the hydrogen molecule discussed in Sec. 5.4.1. The matrix of force constants for this system may be written as

$$\mathbf{M} = \begin{pmatrix} \frac{d^2E}{dR_1^2} & \frac{d^2E}{dR_1dR_2} \\ \frac{d^2E}{dR_2dR_1} & \frac{d^2E}{dR_2^2} \end{pmatrix}. \quad (\text{C.3})$$

By exactly diagonalizing the matrix, we obtain the eigenmodes, and eigenfrequencies of the system given by

$$\omega^2 = \frac{1}{2} \left(\frac{d^2E}{dR_1^2} + \frac{d^2E}{dR_2^2} \right) \pm \sqrt{\frac{1}{4} \left(\frac{d^2E}{dR_1^2} - \frac{d^2E}{dR_2^2} \right)^2 + \left(\frac{d^2E}{dR_1dR_2} \right)^2}, \quad (\text{C.4})$$

where the positive frequencies are physical. The errors are calculated using Monte Carlo, as discussed in Sec. C.2.5.

There are two possible disadvantages of this method for obtaining the vibrational frequencies of a configuration. First, since it is a complete diagonalization method, it uses all of the entries in the matrix of force constants. However, many of these entries are related by symmetries, and so these calculations are potentially redundant. Second, due to numerical inaccuracy, Eq. C.4 may result in an overestimate of the frequencies if the diagonal terms in Eq. C.3 are not equal.

Following from the previous example, by imposing the known modes of a diatomic molecule in one dimension, we may write the matrix of force constants as

$$\mathbf{M}_{\text{KM}} = \frac{1}{2} \begin{pmatrix} \frac{d^2E}{d(R_1+R_2)} & 0 \\ 0 & \frac{d^2E}{d(R_1-R_2)} \end{pmatrix},$$

which now yields the eigenfrequencies

$$\omega_{\text{KM}}^2 = \frac{1}{2} \left(\frac{d^2E}{dR_1^2} + \frac{d^2E}{dR_2^2} \right) \pm \left(\frac{d^2E}{dR_1 dR_2} \right).$$

Notice that $|\omega_{\text{KM}}| \leq |\omega|$ due to the absence of the diagonal terms in the square root of Eq. C.4.

For a general system, we may input a set of known modes $\{\mathbf{x}\}$. These $3N_n$ -dimensional row vectors act on the $3N_n \times 3N_n$ dynamical matrix, \mathbf{D} , to extract the corresponding eigenfrequency, such that

$$\omega_{\text{KM},i} = \hat{\mathbf{x}}_i \mathbf{D} \hat{\mathbf{x}}_i^T,$$

with corresponding error

$$\sigma_{\text{KM},i} = \sqrt{\hat{x}_{ij}(2\Sigma_{jk}^2 - \Sigma_{jk}\delta_{jk})\hat{x}_i^k},$$

where the hats denote normalization, Σ is the standard error matrix corresponding to \mathbf{M} , and the dynamical matrix, \mathbf{D} , is the matrix of force constants weighted by the atomic masses.

By imposing known modes on the system, we can reduce the potential for numerical error and speed up the matrix diagonalization. However, these advantages only hold if the correct eigenmodes are known a priori, and therefore we do not employ this scheme as standard for our DMC calculations.

C.2.3 Approaches based on derivatives of the force and energy

Further to the methods based on the matrix of force constants, we also consider traditional techniques, for comparison.

We obtain an estimate of the frequency (ω_{FG}) from the gradient, κ , of the interatomic force against bond length graph. The error in the gradient of the slope is the asymptotic standard error from a linear regression, and this is propagated to the vibrational frequency in the usual way:

$$\sigma_{\omega}^2 = \left| \frac{\partial \omega}{\partial \kappa} \right|^2 \sigma_{\kappa}^2.$$

Similarly, an additional estimate of the vibrational frequency (ω_{EC}) is obtained by computing the second derivative of the energy at a series of displacements along the trajectory of an eigenmode. For this, we use a numerical central difference scheme. Since this result is based on a linear superposition of energy data points, the errors add in quadrature.

C.2.4 Correction for anharmonicity

All of the above methods for calculating the vibrational frequency rely on the harmonic potential approximation. However, there are certain cases where anharmonic vibration is dominant and a correction to these frequencies needs to be applied. As for atomic relaxation, we apply an approximate correction, due to a Morse potential, which for the fundamental vibrational frequency, is given as $\Delta\omega = -x_e/4$, where x_e is the anharmonic constant.

C.2.5 Monte Carlo uncertainty

The matrix of force constants \mathbf{M} comes with an associated standard error matrix, Σ , from the reblocking method in CASINO [315]. Calculating the errors in eigenvalues given the errors in the matrix elements is a non-trivial task and one which has been studied extensively in pure mathematics [316–321]. For the purposes of this project, we calculate the eigenvalue errors using Monte Carlo.

For each Monte Carlo run we generate a dynamical matrix, whose matrix elements are normally distributed, with a mean equal to the original matrix elements and a standard deviation equal to the corresponding standard errors. We then perform many runs until the average eigenvalues converge to the true eigenvalues, and we use the standard errors of these Monte Carlo runs as the errors in the eigenvalues.

Appendix D

Lattice Stability of Three-dimensional Crystals

D.1 Higher-order Derivative Test

For a single-variable, real-valued and sufficiently differentiable function, f , let the first $(n - 1)$ derivatives vanish such that

$$f'(c) = \dots = f^{(n-1)}(c) = 0 \quad \text{and} \quad f^{(n)}(c) \neq 0,$$

where c is a constant in the domain of the function, and $n \in \mathbb{Z}^+$. In this case, the n th derivative may be used as a discriminant to determine the nature of the turning points.

If n is even:

- $f^{(n)}(c) < 0 \Rightarrow c$ is a local maximum,
- $f^{(n)}(c) > 0 \Rightarrow c$ is a local minimum.

If n is odd:

- $f^{(n)}(c) < 0 \Rightarrow c$ is a strictly decreasing point of inflection,
- $f^{(n)}(c) > 0 \Rightarrow c$ is a strictly increasing point of inflection.

Hence, this test can classify the critical points of f in all cases, provided $f^{(n)}(c) \neq 0$ for some value of n [322].

The higher-order derivative test may be generalized to multi-dimensional problems. Denoting $D^{(p)}f$ as the p th-order multivariate derivative of f , it can be shown that under corresponding conditions:

- $D^{(p)}f(c)$ is negative definite $\Rightarrow c$ is a strict local maximum,
- $D^{(p)}f(c)$ is positive definite $\Rightarrow c$ is a strict local minimum,
- $D^{(p)}f(c)$ is indefinite $\Rightarrow c$ is a saddle point,
- $D^{(p)}f(c)$ is zero or semidefinite \Rightarrow the test is inconclusive.

Note that, unlike the single-variable test, this test is not conclusive in all cases [323].

D.2 Higher-order Matrices of Force Constants

In this project we consider the effect of displacing an atom at the origin, on its nearest neighbors, with a total interaction potential E and displacement \mathbf{R} . We may expand the total interaction potential about $\mathbf{R} = \mathbf{0}$, such that:

$$\begin{aligned}
 E(\mathbf{R}) = & E(\mathbf{0}) + \sum_{i=1}^3 \left. \frac{\partial E}{\partial R_i} \right|_{\mathbf{R}=\mathbf{0}} R_i + \frac{1}{2!} \sum_{i=1}^3 \sum_{j=1}^3 \left. \frac{\partial^2 E}{\partial R_i \partial R_j} \right|_{\mathbf{R}=\mathbf{0}} R_i R_j \\
 & + \frac{1}{3!} \sum_{i=1}^3 \sum_{j=1}^3 \sum_{k=1}^3 \left. \frac{\partial^3 E}{\partial R_i \partial R_j \partial R_k} \right|_{\mathbf{R}=\mathbf{0}} R_i R_j R_k \\
 & + \frac{1}{4!} \sum_{i=1}^3 \sum_{j=1}^3 \sum_{k=1}^3 \sum_{l=1}^3 \left. \frac{\partial^4 E}{\partial R_i \partial R_j \partial R_k \partial R_l} \right|_{\mathbf{R}=\mathbf{0}} R_i R_j R_k R_l + \dots
 \end{aligned}$$

The Hessian may be written in matrix form,

$$\frac{d^2 E}{d\mathbf{R}^2} = \begin{pmatrix} E_{xx} & E_{xy} & E_{xz} \\ E_{yx} & E_{yy} & E_{yz} \\ E_{zx} & E_{zy} & E_{zz} \end{pmatrix}, \quad (\text{D.1})$$

where we use the shorthand notation $E_{R_i R_j} \equiv \partial^2 E / \partial R_i \partial R_j$. Exploiting the symmetry of the system, we may additionally contract the 4th-order coefficient tensor, $E_{ijkl} \delta_j^i \delta_l^k = E_{iikk} \cong E_{ik}$, which in matrix form may be written as

$$\frac{d^4 E}{d\mathbf{R}^4} = \begin{pmatrix} E_{xxxx} & E_{xxyy} & E_{xxzz} \\ E_{yyxx} & E_{yyyy} & E_{yyzz} \\ E_{zzxx} & E_{zzyy} & E_{zzzz} \end{pmatrix}. \quad (\text{D.2})$$

Both matrices D.1 and D.2 are symmetric.

D.3 Crystal Structures in the Periodic Table

Sufficiently stable elements in the periodic table may be grouped in accordance with their crystal structure. A breakdown of the crystal structures (by Bravais lattice) in the periodic table is presented in Fig. D.1. In the cases where an element exhibits multiple crystal structures at standard temperature and pressure, the most thermodynamically stable allotrope is given.

In three-dimensions, all crystal structures are derived from fourteen possible Bravais lattices. However, some of the derived crystal structures are worth studying separately, either due to their ubiquity (e.g. in the case of the hcp structure: the most common crystal structure in nature) or interesting properties (e.g. in the case of diamond). The cub, bcc, fcc, dia, hcp, and dhcp crystal structures are studied in particular in this thesis because they only have one free parameter: the lattice constant. Furthermore, this group of crystal structures accounts for approximately 73% of the known crystal structures in the periodic table.

D.4 Numerical Model

In this section, we outline the numerical details of how the crystal structure summations were performed.

D.4.1 Cubic systems (cub, bcc, fcc, dia)

In this project, we consider unit cells with an atom situated at the origin in all cases. We refer to these as *origin-centric* unit cells, and we choose these in order to minimize finite system size error when summing radially outwards over many shells, as well as to simplify the computations. The unit cell for the simple cubic crystal consists of one atom situated at the origin. The unit cells for the bcc, fcc, and dia crystal lattices are shown in Fig. D.2.

In order to sum to n shells, we include all atoms in units cells whose origins are situated within a radius of n lattice constants, as illustrated in Fig. D.3. We continue to sum in this fashion until the properties of interest, such as the force constants, converge to the desired precision.

The coordinates of the unit cell sites for these cubic systems is shown in Table D.1a and the corresponding potentials are given in Table D.1b. Hence, the summation over n shells

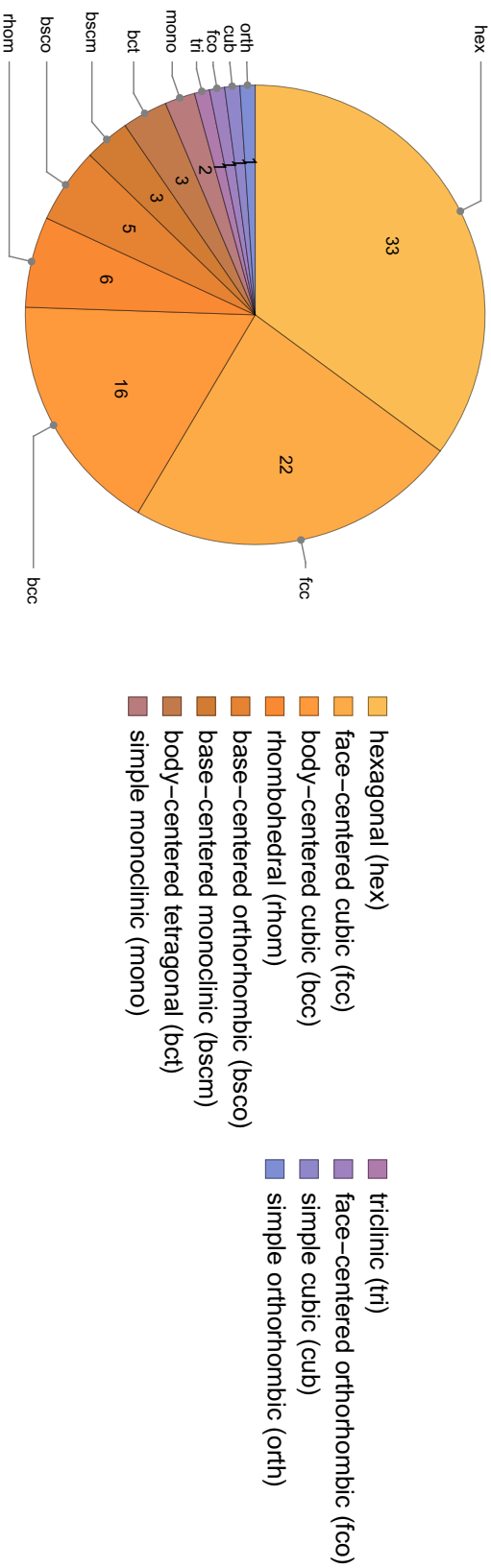


Fig. D.1 Breakdown of crystal structures (by Bravais lattice) for the most thermodynamically stable allotropes of elements in the periodic table, at standard temperature and pressure. The number of elements exhibiting each crystal structure is given in the corresponding section of the chart. Crystal structure data is provided for 94 out of the 118 elements, using Mathematica's ElementData function [324]. Note that, in the hexagonal Bravais lattice family, 23 elements form hcp, and 8 form dhcp structures. In the fcc family, 2 elements form dia structures.

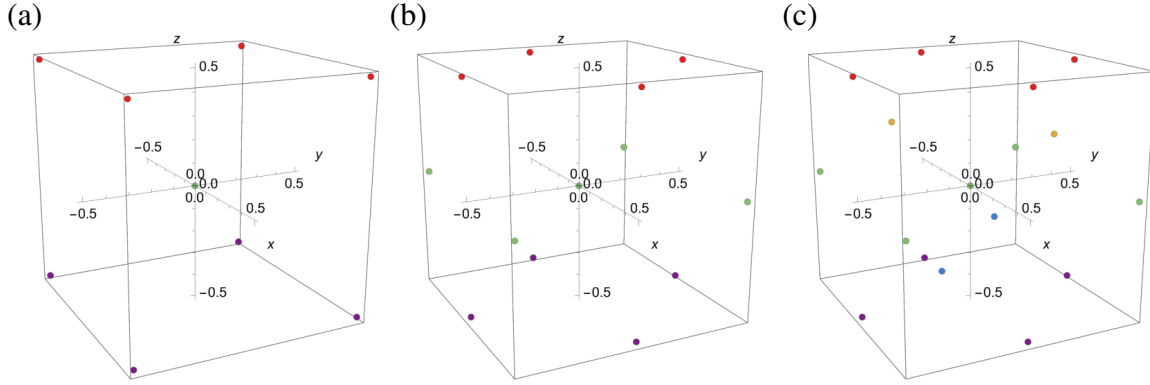


Fig. D.2 Origin-centric unit cells for the (a) bcc, (b) fcc, and (c) dia crystal structures. These structures have two, four, and eight atoms per unit cell, respectively. All lengths are given in units of the lattice constant, and the coloring distinguishes the position along the z -axis. The displacement vectors for these plots are given in Table D.1a.

may be written explicitly as

$$E_C = \sum_I V_C(\mathbf{R}_I - \mathbf{R}) = \sum_{i_x^2 + i_y^2 + i_z^2 \leq n^2} V_C \left(a \begin{pmatrix} i_x \\ i_y \\ i_z \end{pmatrix} - \begin{pmatrix} X \\ Y \\ Z \end{pmatrix} \right) - V \left(\begin{pmatrix} X \\ Y \\ Z \end{pmatrix} \right),$$

where $C \in \{\text{cub}, \text{bcc}, \text{fcc}, \text{dia}\}$ denotes the cubic crystal structure under consideration, and $\{i_x, i_y, i_z\}$ are integers. The summation yields the total potential energy of displacing the atom at the origin to a position \mathbf{R} . This expression can then be expanded to quadratic order in \mathbf{R} , for example, to extract the matrix of force constants.

D.4.2 Hexagonal systems (hcp, dhcp)

Hexagonal systems are treated in an analogous fashion to cubic systems, except now more care is needed since the vectors to neighboring unit cells are not orthogonal. The origin-centric unit cells for the hcp and dhcp crystal lattices are shown in Figs. D.4a & D.4b and the corresponding displacement vectors and potentials are presented in Table D.2. Hence for these systems, the (unnormalized) basis set, to go from one unit cell to another, may be denoted as

$$\{\mathbf{a}, \mathbf{b}, \mathbf{c}\} = \frac{a}{2} \left\{ \begin{pmatrix} 3 \\ -\sqrt{3} \\ 0 \end{pmatrix}, \begin{pmatrix} 3 \\ \sqrt{3} \\ 0 \end{pmatrix}, \begin{pmatrix} 0 \\ 0 \\ \frac{4\sqrt{6}}{3} \end{pmatrix} \right\},$$

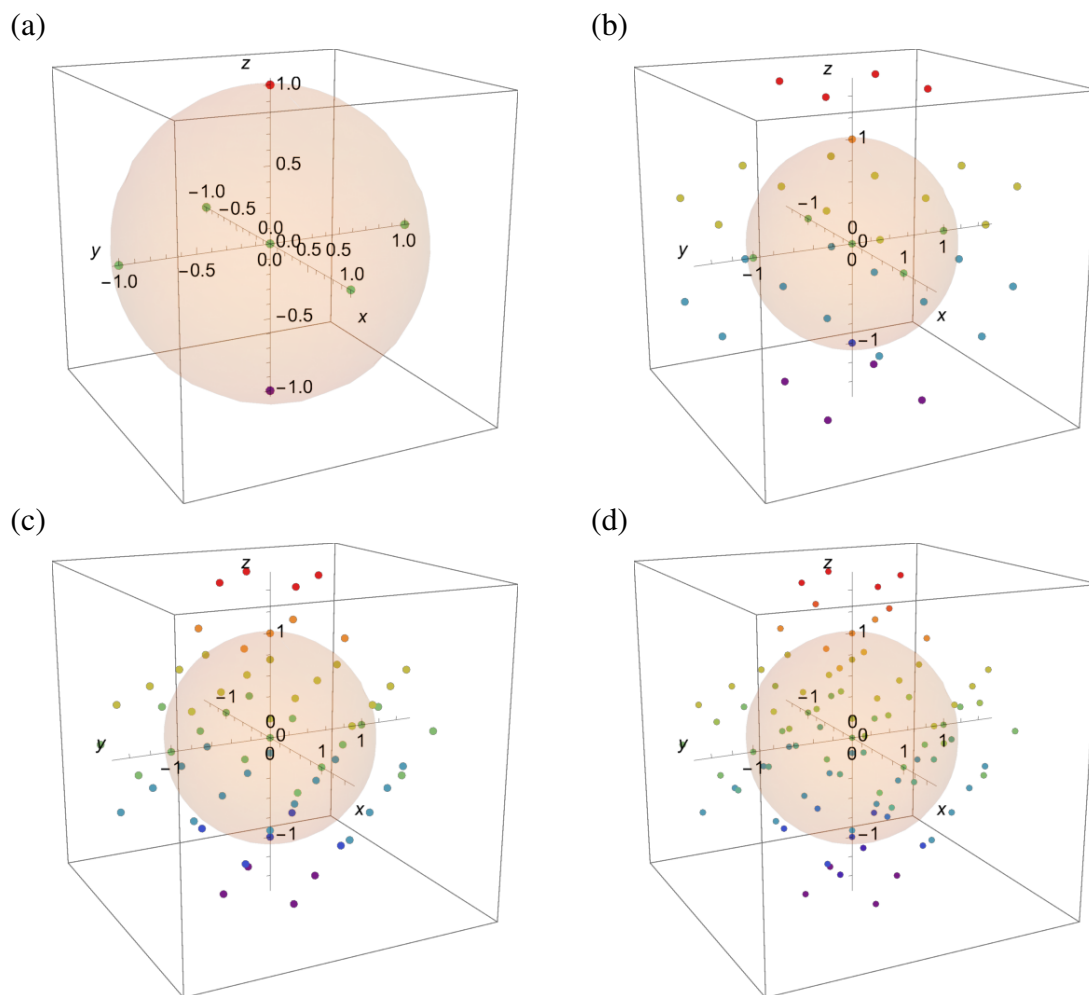


Fig. D.3 Illustration of the points included in a one-shell summation of the (a) cub, (b) bcc, (c) fcc, and (d) dia crystal structures. All points from the nearest-neighbor unit cells are considered. The centers of neighboring unit cells lie within a unit sphere (light orange). All lengths are given in units of the lattice constant, and the coloring of points distinguishes their position along the z-axis.

(a) displacement vectors

crystal	plane	displacement vectors of sites in the unit cell
bcc	$z = a/2$	$\mathbf{r}_1^{\text{bcc}} = \frac{a}{2}(1, 1, 1), \mathbf{r}_2^{\text{bcc}} = \frac{a}{2}(-1, 1, 1), \mathbf{r}_3^{\text{bcc}} = \frac{a}{2}(1, -1, 1), \mathbf{r}_4^{\text{bcc}} = \frac{a}{2}(-1, -1, 1),$ $\mathbf{r}_5^{\text{bcc}} = \frac{a}{2}(1, 1, -1), \mathbf{r}_6^{\text{bcc}} = \frac{a}{2}(1, -1, -1), \mathbf{r}_7^{\text{bcc}} = \frac{a}{2}(-1, 1, -1), \mathbf{r}_8^{\text{bcc}} = \frac{a}{2}(-1, -1, -1)$
	$z = 0$	$\mathbf{r}_1^{\text{fcc}} = \frac{a}{2}(1, 1, 0), \mathbf{r}_2^{\text{fcc}} = \frac{a}{2}(-1, 1, 0), \mathbf{r}_3^{\text{fcc}} = \frac{a}{2}(1, -1, 0), \mathbf{r}_4^{\text{fcc}} = \frac{a}{2}(-1, -1, 0),$ $\mathbf{r}_5^{\text{fcc}} = \frac{a}{2}(1, 0, 1), \mathbf{r}_6^{\text{fcc}} = \frac{a}{2}(-1, 0, 1), \mathbf{r}_7^{\text{fcc}} = \frac{a}{2}(1, 0, -1), \mathbf{r}_8^{\text{fcc}} = \frac{a}{2}(-1, 0, -1),$ $\mathbf{r}_9^{\text{fcc}} = \frac{a}{2}(0, 1, 1), \mathbf{r}_{10}^{\text{fcc}} = \frac{a}{2}(0, -1, 1), \mathbf{r}_{11}^{\text{fcc}} = \frac{a}{2}(0, 1, -1), \mathbf{r}_{12}^{\text{fcc}} = \frac{a}{2}(0, -1, -1)$
dia	$z = 0$	$\mathbf{r}_1^{\text{dia}} = \frac{a}{8}(4, 4, 0), \mathbf{r}_2^{\text{dia}} = \frac{a}{8}(-4, 4, 0), \mathbf{r}_3^{\text{dia}} = \frac{a}{8}(4, -4, 0), \mathbf{r}_4^{\text{dia}} = \frac{a}{8}(-4, -4, 0),$ $\mathbf{r}_5^{\text{dia}} = \frac{a}{8}(4, 0, 4), \mathbf{r}_6^{\text{dia}} = \frac{a}{8}(-4, 0, 4), \mathbf{r}_7^{\text{dia}} = \frac{a}{8}(4, 0, -4), \mathbf{r}_8^{\text{dia}} = \frac{a}{8}(-4, 0, -4),$ $\mathbf{r}_9^{\text{dia}} = \frac{a}{8}(0, 4, 4), \mathbf{r}_{10}^{\text{dia}} = \frac{a}{8}(0, -4, 4), \mathbf{r}_{11}^{\text{dia}} = \frac{a}{8}(0, 4, -4), \mathbf{r}_{12}^{\text{dia}} = \frac{a}{8}(0, -4, -4),$ $\mathbf{r}_{13}^{\text{dia}} = \frac{a}{8}(2, 2, 2), \mathbf{r}_{14}^{\text{dia}} = \frac{a}{8}(-2, -2, 2),$ $\mathbf{r}_{15}^{\text{dia}} = \frac{a}{8}(-2, 2, -2),$ $\mathbf{r}_{16}^{\text{dia}} = \frac{a}{8}(2, -2, -2)$
	$y = a/4$	
	$x = a/4$	

(b) potentials

crystal	atoms per unit cell	potential
bcc	2	$V_{\text{bcc}}(\mathbf{R}) = V(\mathbf{R}) + \frac{1}{8} \sum_{i=1}^8 V(\mathbf{R} + \mathbf{r}_i^{\text{bcc}})$
fcc	4	$V_{\text{fcc}}(\mathbf{R}) = V(\mathbf{R}) + \frac{1}{4} \sum_{i=1}^{12} V(\mathbf{R} + \mathbf{r}_i^{\text{fcc}})$
dia	8	$V_{\text{dia}}(\mathbf{R}) = V(\mathbf{R}) + \frac{1}{4} \sum_{i=1}^{12} V(\mathbf{R} + \mathbf{r}_i^{\text{dia}}) + \sum_{i=13}^{16} V(\mathbf{R} + \mathbf{r}_i^{\text{dia}})$

Table D.1 (a) Displacement vectors for sites in a unit cell, and (b) corresponding unit cell potentials, for the bcc, fcc, and dia crystal structures. For the displacement vectors, the site at the origin is omitted and all vectors are given in terms of the lattice constant, a .

where a is the lattice constant in the xy -plane. In this case, the summation over n shells may be explicitly written as

$$E_H = \sum_I V_H(\mathbf{R}_I - \mathbf{R})$$

$$= \sum_{\left(\frac{\sqrt{3}}{2}(i_x+i_y)\right)^2 + \left(\frac{i_y-i_x}{2}\right)^2 + i_z^2 \leq n^2} V_H \left(\frac{a}{2} \begin{pmatrix} 3(i_x + i_y) \\ \sqrt{3}(i_y - i_x) \\ \frac{4\sqrt{6}}{3}i_z \end{pmatrix} - \begin{pmatrix} X \\ Y \\ Z \end{pmatrix} \right) - V \left(\begin{pmatrix} X \\ Y \\ Z \end{pmatrix} \right),$$

where $H \in \{\text{hcp}, \text{dhcp}\}$ denotes the hexagonal crystal structure under consideration, and $\{i_x, i_y, i_z\}$ are integers. Figures D.4c & D.4d show the sites included in these summations up to eight shells, which is typically number at which the desired precision converged in Sec. 6.3. Note the approximate spherical symmetry of these systems.

D.4.3 Multi-parameter systems

Approximately one quarter of the periodic table is composed of elements which have crystal structures with more than one free parameter. The displacement vectors between unit cells for these structures is shown in Table D.3. Within our numerical model these systems are modeled in an analogous way, on a case-by-case basis, for the example parameters given.

D.5 Details of the Tight-binding Model

In this section, we outline the details of the tight-binding configuration discussed in Sec. 6.4. In our model, we have a crystal of ions with tightly-bound electrons at each site. We consider each atom to be composed of a pseudopotential, which takes into account the potential of the nucleus screened by the inner electrons, and one outermost electron.

D.5.1 Definitions

Wave function

We start by taking an simplified ansatz for the wave function of the valence electron orbital under the potential of the ion:

$$\Psi(\mathbf{R}; c, a_e) = A \sqrt{\frac{1}{1 + \exp\left(\frac{2(|\mathbf{R}|-c)}{a_e}\right)}},$$

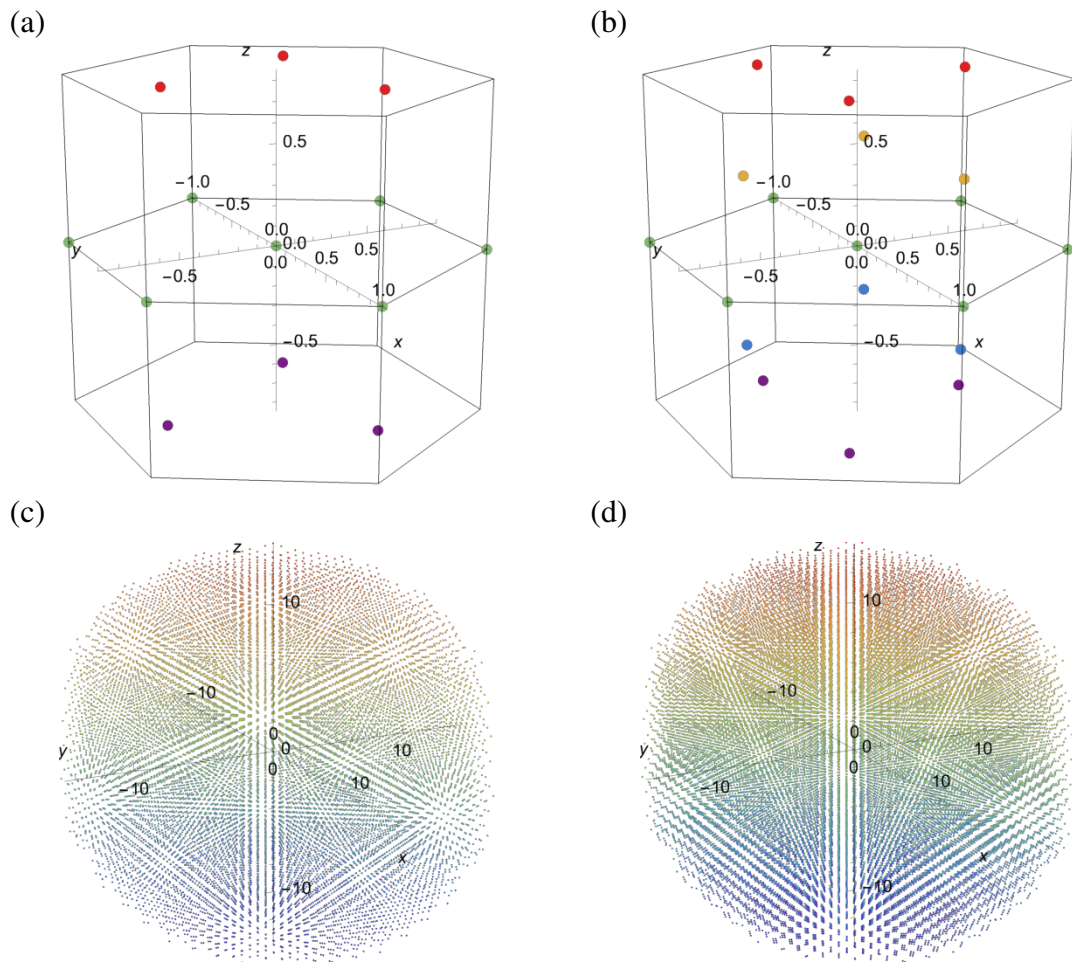


Fig. D.4 [(a), (b)] Origin-centric unit cells for the (a) hcp, and (b) dhcp crystal structures. These structures have six and twelve atoms per unit cell, respectively. [(c), (d)] Illustrations of the (c) hcp, and (d) dhcp crystal structures plotted up to eight shells. All lengths are given in units of the lattice constant, and the coloring of points distinguishes their position along the z-axis. The displacement vectors for these plots are given in Table D.2.

(a) displacement vectors

crystal	plane	displacement vectors of sites in the unit cell
hcp	$z = 0$	$\mathbf{r}_1^{\text{hcp}} = a(1, 0, 0), \mathbf{r}_2^{\text{hcp}} = \frac{a}{2}(1, \sqrt{3}, 0), \mathbf{r}_3^{\text{hcp}} = \frac{a}{2}(-1, \sqrt{3}, 0),$ $\mathbf{r}_4^{\text{hcp}} = a(-1, 0, 0), \mathbf{r}_5^{\text{hcp}} = \frac{a}{2}(-1, -\sqrt{3}, 0), \mathbf{r}_6^{\text{hcp}} = \frac{a}{2}(1, -\sqrt{3}, 0),$
	$z = 2\sqrt{6}/3$	$\mathbf{r}_7^{\text{hcp}} = \frac{a}{6}(3, \sqrt{3}, 2\sqrt{6}), \mathbf{r}_8^{\text{hcp}} = \frac{a}{6}(-3, \sqrt{3}, 2\sqrt{6}), \mathbf{r}_9^{\text{hcp}} = \frac{a}{3}(0, -\sqrt{3}, \sqrt{6}),$ $\mathbf{r}_{10}^{\text{hcp}} = \frac{a}{6}(3, \sqrt{3}, -2\sqrt{6}), \mathbf{r}_{11}^{\text{hcp}} = \frac{a}{6}(-3, \sqrt{3}, -2\sqrt{6}), \mathbf{r}_{12}^{\text{hcp}} = \frac{a}{3}(0, -\sqrt{3}, -\sqrt{6})$
	$z = 0$	$\mathbf{r}_1^{\text{dhcp}} = a(1, 0, 0), \mathbf{r}_2^{\text{dhcp}} = \frac{a}{2}(1, \sqrt{3}, 0), \mathbf{r}_3^{\text{dhcp}} = \frac{a}{2}(-1, \sqrt{3}, 0),$ $\mathbf{r}_4^{\text{dhcp}} = a(-1, 0, 0), \mathbf{r}_5^{\text{dhcp}} = \frac{a}{2}(-1, -\sqrt{3}, 0), \mathbf{r}_6^{\text{dhcp}} = \frac{a}{2}(1, -\sqrt{3}, 0),$ $\mathbf{r}_7^{\text{dhcp}} = \frac{a}{6}(3, \sqrt{3}, \sqrt{6}), \mathbf{r}_8^{\text{dhcp}} = \frac{a}{6}(-3, \sqrt{3}, \sqrt{6}), \mathbf{r}_9^{\text{dhcp}} = \frac{a}{3}(0, -\sqrt{3}, \frac{\sqrt{6}}{2}),$ $\mathbf{r}_{10}^{\text{dhcp}} = \frac{a}{6}(3, \sqrt{3}, -\sqrt{6}), \mathbf{r}_{11}^{\text{dhcp}} = \frac{a}{6}(-3, \sqrt{3}, -\sqrt{6}), \mathbf{r}_{12}^{\text{dhcp}} = \frac{a}{3}(0, -\sqrt{3}, -\frac{\sqrt{6}}{2}),$ $\mathbf{r}_{13}^{\text{dhcp}} = \frac{a}{6}(3, -\sqrt{3}, 2\sqrt{6}), \mathbf{r}_{14}^{\text{dhcp}} = \frac{a}{6}(-3, -\sqrt{3}, 2\sqrt{6}), \mathbf{r}_{15}^{\text{dhcp}} = \frac{a}{3}(0, \sqrt{3}, \sqrt{6}),$ $\mathbf{r}_{16}^{\text{dhcp}} = \frac{a}{6}(3, -\sqrt{3}, -2\sqrt{6}), \mathbf{r}_{17}^{\text{dhcp}} = \frac{a}{6}(-3, -\sqrt{3}, -2\sqrt{6}), \mathbf{r}_{18}^{\text{dhcp}} = \frac{a}{3}(0, \sqrt{3}, -\sqrt{6})$

(b) potentials

crystal	atoms per unit cell	potential
hcp	6	$V_{\text{hcp}}(\mathbf{R}) = V(\mathbf{R}) + \frac{1}{3} \sum_{i=1}^6 V(\mathbf{R} + \mathbf{r}_i^{\text{hcp}}) + \frac{1}{2} \sum_{i=7}^{12} V(\mathbf{R} + \mathbf{r}_i^{\text{hcp}})$
dhcp	12	$V_{\text{dhcp}}(\mathbf{R}) = V(\mathbf{R}) + \frac{1}{3} \sum_{i=1}^6 V(\mathbf{R} + \mathbf{r}_i^{\text{dhcp}}) + \sum_{i=7}^{12} V(\mathbf{R} + \mathbf{r}_i^{\text{dhcp}}) + \frac{1}{2} \sum_{i=13}^{18} V(\mathbf{R} + \mathbf{r}_i^{\text{dhcp}})$

Table D.2 (a) Displacement vectors for sites in a unit cell, and (b) corresponding unit cell potentials, for the hcp and dhcp crystal structures. For the displacement vectors, the site at the origin is omitted and all vectors are given in terms of the lattice constant, a .

crystal	atoms per unit cell	displacement vector between unit cells	example parameters
rhom	1	$a \begin{pmatrix} i_x - \cos \alpha (i_y + i_z) \\ \sin \alpha i_y + \cos \alpha i_z \\ \sin \alpha i_z \end{pmatrix}$	Boron $\alpha = \beta = \gamma = 1.0133$
bsco	2	(ai_x, bi_y, ci_z)	Gallium $(b, c) = (1.6955, 1.0014)a$
bscm	1	$(ai_x - c \cos \beta i_z, bi_y, c \sin \beta i_z)$	Oxygen $(b, c) = (0.6346, 0.9413)a$ $\beta = 2.3131$
bct	2	(ai_x, ai_y, ci_z)	Indium $c = 1.5208a$
mono	1	$(ai_x - c \cos \beta i_z, bi_y, c \sin \beta i_z)$	Plutonium $(b, c) = (0.7799, 1.7731)a$ $\beta = 1.7766$
hex	1	$(a(i_x - \frac{i_y}{2}), a\frac{\sqrt{3}}{2}i_y, ci_z)$	Hydrogen $c = 0.7234a$
tri	1	$\begin{pmatrix} ai_x - b \cos \gamma i_y - c \cos \beta i_z \\ b \sin \gamma i_y + c \cos \alpha i_z \\ c \sin \alpha i_z \end{pmatrix}$	Phosphorus $(b, c) = (0.4806, 0.9835)a$, $(\alpha, \beta, \gamma) = (1.2538, 1.5773, 1.2490)$
fco	4	(ai_x, bi_y, ci_z)	Sulphur $(b, c) = (1.2307, 2.3349)a$
orth	1	(ai_x, bi_y, ci_z)	Neptunium $(b, c) = (0.7088, 0.7335)a$

Table D.3 Displacement vectors between unit cells for less common Bravais lattices in the periodic table. We list example parameters in terms of the x-direction lattice constant, a . Standard definitions of the lattice constants (a, b, c) and angles (α, β, γ) are taken. Crystal structures are listed in order of ubiquity, as presented in Fig. D.1. All crystal structure data is obtained from Mathematica's ElementData function [324].

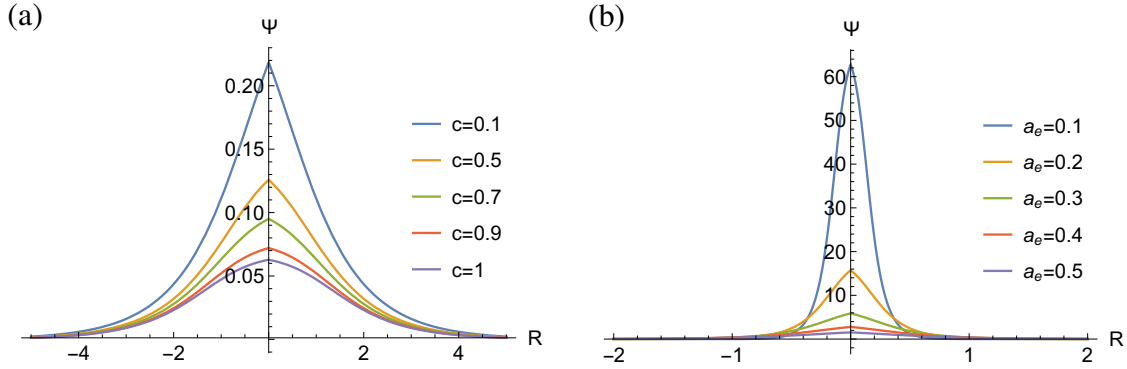


Fig. D.5 Plots of the normalized wave function of the valence electron under the pseudopotential of the ion, Ψ . The behavior of the wave function is shown as we (a) vary c with $a_e = 1$, and (b) vary a_e with $c = 0.1$.

where A is a normalization constant, $a_e \ll R_I$ is the width of the valence electron cloud, and $0 \leq c < a_e$ is the width of the core electron cloud. We choose this ansatz so that the electron density is analytically well behaved in subsequent calculations, and that in the limit of vanishing radius and large distances we recover the wave function of a particle in a Dirac delta potential well:

$$\lim_{c \ll a_e \ll |\mathbf{R}|} \Psi \propto e^{-|\mathbf{R}|/a_e}. \quad (\text{D.3})$$

This is the limit that we will expand around in the following sections. Plots of this wave function are shown in Fig. D.5. Since it not possible to analytically derive an expression for the normalized wave function, we expand the probability density, $|\Psi|^2$ up to 1st-order in the small parameter (c/a_e) and then solve the normalization condition $\int_{-\infty}^{\infty} |\Psi|^2 d\mathbf{R} = a_0/a_e$, where a_0 is the Bohr radius. This yields a normalization constant

$$A(c, a_e) = \frac{2\sqrt{a_0} (9a_e \zeta(3) - c\pi^2)}{9a_e^3 \sqrt{3\pi} \zeta(3)^{3/2}} + O\left[\left(\frac{c}{a_e}\right)^2\right],$$

where $\zeta(3)$ is Apéry's constant.

Electron cloud potential and density

The valence electron cloud (which we denote using a capital 'E') has a potential given by the Coulomb potential of the single electron, $V_e(\mathbf{R}) = |\mathbf{R}|^{-1}$, integrated over the density distribution of the electron cloud:

$$V_E(\mathbf{R}; c, a_e) = \int V_e(\mathbf{R} + \mathbf{r}_e) \rho_E(\mathbf{r}_e; c, a_e) d\mathbf{r}_e,$$

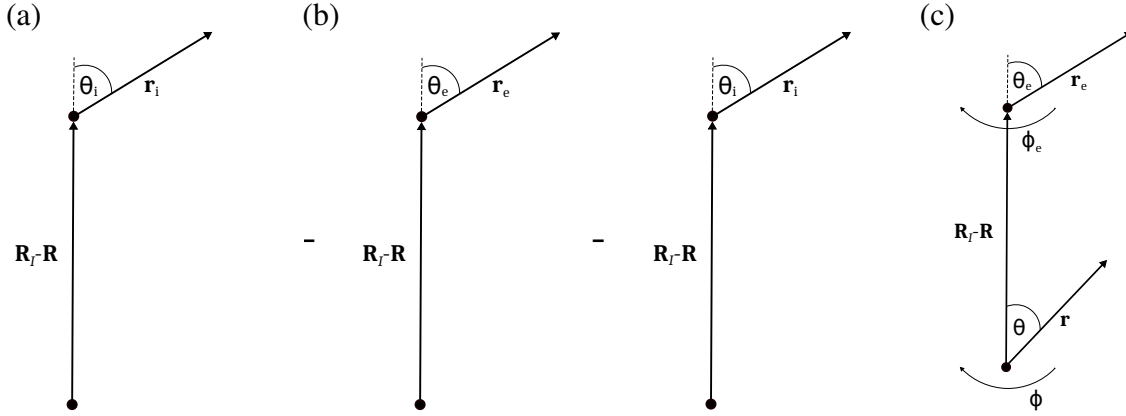


Fig. D.6 Diagrams corresponding to the (a) ion-ion, (b) electron-ion, and (c) electron-electron contribution calculations. The displacement vector between ions, $\mathbf{R} - \mathbf{R}_I$, is oriented along the north pole, and the polar and azimuthal angles are defined in the range $0 \leq \theta < \pi$ and $0 \leq \phi < 2\pi$, respectively.

where we calculate the density of the electron cloud using the normalized wave function defined in Sec. D.5.1:

$$\rho_E(\mathbf{r}_e; c, a_e) = |\Psi(\mathbf{r}_e; c, a_e)|^2.$$

Ion potential and density

The ion potential is obtained by solving the time-independent Schrödinger equation and subtracting the energy constant, such that

$$V_i(\mathbf{R}; c, a_e) = -a_0 \left(\frac{1}{\Psi} \frac{\nabla^2}{2} \Psi - \lim_{|\mathbf{R}| \rightarrow \infty} \left(\frac{1}{\Psi} \frac{\nabla^2}{2} \Psi \right) \right).$$

The ion density is then subsequently obtained from Poisson's equation:

$$\rho_i(\mathbf{r}_i; c, a_e) = -\frac{\nabla^2 V_i(\mathbf{r}_i; c, a_e)}{4\pi}.$$

Note that due to the norm-conserving property of our wave function ansatz, the ion density satisfies the normalization condition $\int_0^\infty \rho_i(r_i, c, a_e) 4\pi r_i^2 dr_i = a_0/a_e$ up to 1st-order in (c/a_e) .

D.5.2 Ion-ion contribution

First, we calculate the repulsive potential felt by an ion at position \mathbf{R}_I due to an ion being displaced from the origin to a position \mathbf{R} . An illustration of the set-up is shown in Fig. D.6a. Note that we orient the displacement vector between the two ions along the north pole to

simplify the calculations. In order to calculate the ion-ion potential for the whole system we then sum over all distinct atoms, such that

$$E_{i-i}(\mathbf{R}; c, a_e) = \sum_I \int V_i(\mathbf{R}_I - \mathbf{R} + \mathbf{r}_i; c, a_e) \rho_i(\mathbf{r}_i; c, a_e) d\mathbf{r}_i.$$

Rewriting the ion potential in terms of the scalar variables defined in Fig. D.6a, such that $V_i(|\mathbf{R}_I - \mathbf{R}|, \{r_i, \theta_i\}; c, a_e)$, we may Taylor expand the ion potential up to leading order in $(r_i/|\mathbf{R}_I - \mathbf{R}|)$:

$$\begin{aligned} E_{i-i}(\mathbf{R}; c, a_e) &= \sum_I V_i(|\mathbf{R}_I - \mathbf{R}|; c, a_e) \underbrace{\int \rho_i(\mathbf{r}_i; c, a_e) d\mathbf{r}_i}_{a_0/a} \\ &+ 2\pi \sum_I \int_{r_i=0}^{\infty} \int_{\theta_i=0}^{\pi} \left(\frac{\partial^2 V_i}{\partial r_i^2} \right) r_i^4 \rho_i(r_i; c, a_e) \sin(\theta_i) d\theta_i dr_i + O \left[\left(\frac{r_i}{|\mathbf{R}_I - \mathbf{R}|} \right)^3 \right]. \end{aligned}$$

Note that the 1st-order term in the expansion vanishes by symmetry. Hence the final expression for the ion-ion contribution is derived accurate to 1st-order in (c/a_e) and 2nd-order in $(r_i/|\mathbf{R}_I - \mathbf{R}|)$. Taken together, this forms the leading-order analytical expansion about the tight-binding limit introduced in Sec. D.5.1.

D.5.3 Electron-ion contribution

The next contribution is that due to the electron-ion interaction. There are attractive potentials felt by the electron cloud due to the ions, as well as those felt by the ion due to the electron clouds. A sketch of this scenario is shown in Fig. D.6b, where the minus signs indicate that this is an attractive interaction. As in the previous section, we set up the general form of the electron-ion contribution as

$$\begin{aligned} E_{e-i}(\mathbf{R}; c, a_e) &= - \sum_I \int V_i(\mathbf{R}_I - \mathbf{R} + \mathbf{r}_e; c, a_e) \rho_E(\mathbf{r}_e; c, a_e) d\mathbf{r}_e \\ &- \sum_I \int V_E(\mathbf{R}_I - \mathbf{R} + \mathbf{r}_i; c, a_e) \rho_i(\mathbf{r}_i; c, a_e) d\mathbf{r}_i. \end{aligned}$$

It can be shown, either by symmetry or integration by parts, that this expression reduces to

$$E_{e-i}(\mathbf{R}; c, a_e) = -2 \sum_I \int V_i(\mathbf{R}_I - \mathbf{R} + \mathbf{r}_e; c, a_e) \rho_E(\mathbf{r}_e; c, a_e) d\mathbf{r}_e.$$

Rewriting the ion potential in terms of scalar variables, as before, we may Taylor expand up to leading order in $(r_e/|\mathbf{R}_I - \mathbf{R}|)$:

$$\begin{aligned}
E_{e-i}(\mathbf{R}; c, a_e) &= -2 \sum_I V_i(|\mathbf{R}_I - \mathbf{R}|; c, a_e) \underbrace{\int \rho_E(\mathbf{r}_e; c, a_e) d\mathbf{r}_e}_{a_0/a} \\
&\quad - 4\pi \sum_I \int_{r_e=0}^{\infty} \int_{\theta_e=0}^{\pi} \left(\frac{\partial^2 V_i}{\partial r_e^2} \right) r_e^4 \rho_E(r_e; c, a_e) \sin(\theta_e) d\theta_e dr_e \\
&\quad + O \left[\left(\frac{r_e}{|\mathbf{R}_I - \mathbf{R}|} \right)^3 \right].
\end{aligned}$$

Analogously to before, the electron-ion contribution is derived to 1st-order in (c/a_e) and 2nd-order in $(r_e/|\mathbf{R}_I - \mathbf{R}|)$, which is the leading-order analytical expansion about the tight-binding limit in this model.

D.5.4 Electron-electron contribution

Finally, we compute the repulsive electron-electron contribution to the potential. Again the displacement vector between the ions is aligned along the north pole. The valence electrons are parameterized in spherical polar coordinates around each atom, as depicted in Fig. D.6c. The electron-electron contribution in this case may be written as

$$E_{e-e}(\mathbf{R}; c, a_e) = \sum_I \iint V_e(\mathbf{R}_I - \mathbf{R} + \mathbf{r}_e - \mathbf{r}) \rho_E(\mathbf{r}_e; c, a_e) \rho_E(\mathbf{r}; c, a_e) d\mathbf{r}_e d\mathbf{r}.$$

Due to the spherical symmetry of each electron cloud, this contribution reduces exactly to Coulomb repulsion, such that

$$E_{e-e}(\mathbf{R}; a_e) = \frac{a_0^2}{a_e^2} \sum_I \frac{1}{|\mathbf{R}_I - \mathbf{R}|}.$$

Note the total potential energy of the system at this stage, $E_{i-i} + E_{e-i} + E_{e-e}$, tends to zero as $(c/a_e) \rightarrow 0$ and $|\mathbf{R}| \gg a_e$. In this limit, the electrons are effectively on top of the ions and the whole system is neutral due to Gauss' theorem.

D.5.5 Pauli repulsion

To complement our result for the energy, we estimate the Pauli repulsion felt by the overlapping electron clouds. Since we only considering spherically symmetric (i.e. s-type) orbitals

in the toy model, this reduces to a one-dimensional problem. We consider a Dirac delta potential well, of depth g , inside an infinite square well, such that:

$$V_{\text{well}}(x) = \begin{cases} -g\delta(x), & |x| = 0, \\ 0, & 0 < |x| < L, \\ \infty, & |x| \geq L. \end{cases}$$

In this scenario, g determines how tightly bound the electrons are to their respective atoms, and L represents the effective radius for the electron clouds. As L is reduced, the bound state energy is increased – this represents the energy increase due to the Pauli repulsion of overlapping orbitals.

The wave function takes the form $\Psi \propto \sinh(k(L - |x|))$ inside the infinite well, where k is the wave number. Considering the derivative continuity of the wave function at the origin, we derive the transcendental equation $\tanh y = \chi y$, where we have defined $y \equiv kL$ and $\chi \equiv \hbar^2/mgL$. We can derive an analytical form for the solution, and hence the scaling behavior of the energy with L , by finding the lowest root with a Newton-Raphson scheme. The iterative equation for the root is then

$$y_{n+1} = y_n - \frac{\tanh y_n - y_n \chi}{\text{sech}^2 y_n - \chi},$$

where $n \in \mathbb{Z}^+$. Since we are interested in the regime where the wave function is significantly influenced by the boundary wall, we take y_n to be small. Additionally, we are interested in the limit when Pauli repulsion is dominant i.e. when L is small. Taking these limits together, we find that $y_\infty = \sqrt{3\chi/2}$. Hence the energy of the bound state is

$$E_{\text{Pauli}} = \frac{\hbar^2}{2mL^2} y_\infty^2 = \frac{3\hbar^2}{4m^{3/2} \sqrt{2E_b} L^3},$$

where we define the binding energy of an isolated Dirac delta potential well as $E_b \equiv mg^2/2\hbar^2$. In the tight-binding approximation, the wave function takes the form $\Psi \propto \exp(-m^{1/2} \sqrt{2E_b} L/\hbar)$. Comparing this to the form of the wave function in Eq. D.3 allows us to make the identification $E_b \sim a_e^{-2}$ up to physical constants. Hence, in atomic units, the energy gain due to Pauli repulsion becomes

$$E_{\text{Pauli}} = \frac{3a_e}{4L^3}.$$

Note that due to the differences in unit cell geometry, the lattice constant cannot be directly compared between the various crystal structures. For this, we may examine the optimal effective radius of each atom in a spherical packing, defined as

$$r_{\text{eff}} = \left(\frac{3}{4\pi} \frac{V_{\text{unit cell}}}{N_{\text{unit cell}}} \right)^{1/3},$$

where $V_{\text{unit cell}}$ is the optimal volume of the unit cell, and $N_{\text{unit cell}}$ is the number of atoms enclosed. In place of L , we evaluate E_{Pauli} at the effective optimum radius. This rudimentary approximation for the Pauli repulsion allows us to analytically capture the scaling behavior as the lattice constant is reduced.

D.5.6 Crystal relaxation

Let us define the total energy of the system as

$$E(\mathbf{R}; c, a_e) = E_{i-i}(\mathbf{R}; c, a_e) + E_{e-i}(\mathbf{R}; c, a_e) + E_{e-e}(\mathbf{R}; a_e) + E_{\text{Pauli}}(a, a_e).$$

Note that there is an implicit lattice constant dependence in the first three terms in the form of the potentials, as well as in the lattice summations. Once we have calculated an analytical form for the total energy of the system as a function of the displacement of the central atom, \mathbf{R} , and implicitly the lattice constant, a , we then compute the optimal lattice constant such that:

$$a_{\min} = \underset{a \in (a_e, \infty)}{\operatorname{argmin}} (E).$$

We subsequently relax the system to this lattice constant and re-evaluate the total energy at a given \mathbf{R} . This renders the total energy as a function of c and a_e only.

D.6 Oscillatory Electron Density in the Nearly Free Electron Model

In order to approximate the oscillatory part of the electron cloud density in the nearly free electron model, we consider Fourier transforms of the reciprocal lattices, as shown in Table D.4. For crystals with a single-atom basis, the resulting function has a simple form. However, for crystals with more than one atom in the basis, we consider a superposition of multiple offset lattices¹; with modulation along the z-axis, where appropriate. The functions,

¹Note that the offsets given in Table D.4 are not unique.

crystal	$\rho_E^{\text{osc}}(\mathbf{r})/u$
cub/bcc/fcc	$\frac{1}{\tilde{N}_{\text{c.s.}}} \sum_{i=1}^{\tilde{N}_{\text{c.s.}}} \cos(\mathbf{r} \cdot \tilde{\mathbf{r}}_i^{\text{c.s.}})$
dia	$\frac{1}{8} \left[\sum_{i=1}^8 \cos(\mathbf{r} \cdot \tilde{\mathbf{r}}_i^{\text{dia}}) + \sum_{i=1}^8 \cos\left(\left(\mathbf{r} - \mathbf{r}_{13}^{\text{dia}}\right) \cdot \tilde{\mathbf{r}}_i^{\text{dia}}\right) \right]$
hcp	$\frac{A_{\text{hcp}}}{6} \left[\sum_{i=1}^6 \cos(\mathbf{r} \cdot \tilde{\mathbf{r}}_i^{\text{hcp}}) \cos\left(\frac{3\pi}{\sqrt{6}a} z\right) \right.$ $\left. + \sum_{i=1}^6 \cos\left(\left(\mathbf{r} - \mathbf{r}_7^{\text{hcp}}\right) \cdot \tilde{\mathbf{r}}_i^{\text{hcp}}\right) \cos\left(\frac{3\pi}{\sqrt{6}a} \left(z - \frac{\sqrt{6}a}{3}\right)\right) \right]$
dhcp	$\frac{1}{6} \left[\frac{1}{3} \sum_{i=1}^6 \cos(\mathbf{r} \cdot \tilde{\mathbf{r}}_i^{\text{dhcp}}) \cos\left(\frac{3\pi}{\sqrt{6}a} z\right) \right.$ $\left. + \sum_{i=1}^6 \cos\left(\left(\mathbf{r} - \mathbf{r}_7^{\text{dhcp}}\right) \cdot \tilde{\mathbf{r}}_i^{\text{dhcp}}\right) \cos\left(\frac{\sqrt{6}\pi}{a} \left(z - \frac{a}{\sqrt{6}}\right)\right) \right.$ $\left. + \frac{1}{3} \sum_{i=1}^6 \cos\left(\left(\mathbf{r} - \mathbf{r}_{14}^{\text{dhcp}}\right) \cdot \tilde{\mathbf{r}}_i^{\text{dhcp}}\right) \cos\left(\frac{3\pi}{\sqrt{6}a} \left(z - \frac{\sqrt{6}a}{3}\right)\right) \right]$

Table D.4 Oscillatory part of the electron cloud density in the nearly free electron model, ρ_E^{osc} , in units of the oscillation strength, u . $\tilde{N}_{\text{c.s.}}$ is the number of displacement vectors, and $\{\tilde{\mathbf{r}}_i^{\text{c.s.}}\}$ the set of displacements in a unit cell of the reciprocal lattice. The vectors $\mathbf{r}_i^{\text{c.s.}}$ are defined in Tables D.1 and D.2. The normalization constant, $A_{\text{hcp}} = 2/3$, is chosen such that $\max\{\rho_E^{\text{osc}}\} = u$ for all crystal structures.

ρ_E^{osc} , are scaled such that $\max\{\rho_E^{\text{osc}}\} = u$ for all crystal structures. Over a unit cell, all of the functions integrate to zero.

References

- [1] B. Andrews and G. Möller. Stability of fractional Chern insulators in the effective continuum limit of Harper-Hofstadter bands with Chern number $|C| > 1$. *Phys. Rev. B*, 97:035159, Jan 2018.
- [2] Y. Y. F. Liu, B. Andrews, and G. J. Conduit. Direct evaluation of the force constant matrix in quantum Monte Carlo. *J. Chem. Phys.*, 150(3):034104, Jan 2019.
- [3] The Official Website of the Nobel Prize. On-line, <https://www.nobelprize.org/>. [Last accessed: 02/10/2018].
- [4] J. Perdew. Commentary on “the most cited physicists of the past 30 years” and “the most cited physics papers of the past 30 years”: Leadership role of density functional theory. On-line Article, Tulane University, New Orleans, USA, Sept 2010. [Last accessed: 02/10/2018].
- [5] I. Akasaki and H. Amano. Breakthroughs in improving crystal quality of GaN and invention of the p–n junction blue-light-emitting diode. *Jpn. J. App. Phys.*, 45(12R):9001, 2006.
- [6] V. Ryzhii and I. Khmyrova. Electron and photon effects in imaging devices utilizing quantum dot infrared photodetectors and light-emitting diodes. *Proc. SPIE*, 3948:3948 – 3948 – 14, 2000.
- [7] J. Kelly, R. Barends, A. G. Fowler, et al. State preservation by repetitive error detection in a superconducting quantum circuit. *Nature*, 519:66–69, Mar 2015.
- [8] D. Castelvecchi. Quantum computers ready to leap out of the lab in 2017. *Nature*, 541:9–10, Jan 2017.
- [9] K. v. Klitzing. For the Discovery of the Quantised Hall Effect. Nobel Prize in Physics, 1985.
- [10] R. B. Laughlin, H. L. Störmer, and D. C. Tsui. For their Discovery of a New Form of Quantum Fluid with Fractionally Charged Excitations. Nobel Prize in Physics, 1998.
- [11] D. J. Thouless, F. D. M. Haldane, and J. M. Kosterlitz. For Theoretical Discoveries of Topological Phase Transitions and Topological Phases of Matter. Nobel Prize in Physics, 2016.
- [12] M. Z. Hasan and J. E. Moore. Three-Dimensional Topological Insulators. *Annu. Rev. Condens. Matter Phys.*, 2:55–78, Mar 2011.

- [13] S.-Y. Xu, I. Belopolski, N. Alidoust, et al. Discovery of a Weyl fermion semimetal and topological Fermi arcs. *Science*, 349(6248):613–617, 2015.
- [14] V. Mourik, K. Zuo, S. M. Frolov, et al. Signatures of Majorana fermions in hybrid superconductor-semiconductor nanowire devices. *Science*, 336(6084):1003–1007, 2012.
- [15] Microsoft Station Q Website. On-line, <https://www.microsoft.com/en-us/research/group/microsoft-quantum-santa-barbara-station-q/>. [Last accessed: 02/10/2018].
- [16] L. Tung. Microsoft just upped its multi-million bet on quantum computing. On-line Article, Sep 2017. [Last accessed: 02/10/2018].
- [17] H. Zhang, C.-X. Liu, S. Gazibegovic, et al. Quantized Majorana conductance. *Nature*, 556:74–79, Apr 2018.
- [18] M. Franz and D. I. Pikulin. Quantized, finally. *Nat. Phys.*, 14:334–336, Apr 2018.
- [19] R. Süsstrunk and S. D. Huber. Observation of phononic helical edge states in a mechanical topological insulator. *Science*, 349(6243):47–50, 2015.
- [20] M. Xiao, G. Ma, Z. Yang, et al. Geometric phase and band inversion in periodic acoustic systems. *Nat. Phys.*, 11:240–244, Mar 2015.
- [21] P. Delplace, J. B. Marston, and A. Venaille. Topological origin of equatorial waves. *Science*, 358:1075–1077, Nov 2017.
- [22] H. Ochoa and Y. Tserkovnyak. Colloquium: Quantum skyrmionics. *ArXiv e-prints*, July 2018.
- [23] S. J. Clark, M. D. Segall, C. J. Pickard, et al. First principles methods using CASTEP. *Z. Kristallogr. Cryst. Mater.*, 220:567–570, May 2005.
- [24] F. Becca and S. Sorella. *Quantum Monte Carlo Approaches for Correlated Systems*. Cambridge University Press, Cambridge, UK, 2017.
- [25] A. Zen, S. Sorella, M. J. Gillan, A. Michaelides, and D. Alfè. Boosting the accuracy and speed of quantum Monte Carlo: Size consistency and time step. *Phys. Rev. B*, 93(24):241118, Jun 2016.
- [26] Y. Kamiya, Y. Kato, J. Nasu, and Y. Motome. Magnetic three states of matter: A quantum Monte Carlo study of spin liquids. *Phys. Rev. B*, 92:100403, Sep 2015.
- [27] V. A. Kashurnikov and A. V. Krasavin. Quantum Monte-Carlo simulation of FeAs-based superconductors. *J. Phys.: Conf. Ser.*, 490(1):012222, 2014.
- [28] Discussions with Richard Needs.
- [29] S. K. Shukla. *Tensor Network Representation of Many-Body Quantum States and Unitary Operators*. PhD thesis, California Institute of Technology, Pasadena, USA, 2018.

- [30] A. Geim and K. Novoselov. For Groundbreaking Experiments regarding the Two-dimensional Material Graphene. Nobel Prize in Physics, 2010.
- [31] D. Shechtman. For the Discovery of Quasicrystals. Nobel Prize in Chemistry, 2011.
- [32] K. Nagao, T. Inuzuka, K. Nishimoto, and K. Edagawa. Experimental observation of quasicrystal growth. *Phys. Rev. Lett.*, 115:075501, Aug 2015.
- [33] K. Kamiya, T. Takeuchi, N. Kabeya, et al. Discovery of superconductivity in quasicrystal. *Nat. Commun.*, 9(1):154, 2018.
- [34] H. Thomas, G. E. Morfill, V. Demmel, et al. Plasma crystal: Coulomb crystallization in a dusty plasma. *Phys. Rev. Lett.*, 73:652–655, Aug 1994.
- [35] R. J. Needs, M. D. Towler, N. D. Drummond, and P. López Ríos. Topical Review: Continuum variational and diffusion quantum Monte Carlo calculations. *J. Phys. Condens. Matter*, 22(2):023201, Jan 2010.
- [36] C.-K. Skylaris, P. D. Haynes, A. A. Mostofi, and M. C. Payne. Introducing ONETEP: Linear-scaling density functional simulations on parallel computers. *J. Chem. Phys.*, 122(8):084119, 2005.
- [37] M. Towler. An introductory guide to Gaussian basis sets in solid-state electronic structure calculations. Lecture Notes, European Summer School "Ab initio modelling in solid-state chemistry", Sept 2000.
- [38] D. C. Sherrill. Chemistry 4681 module: Electronic structure of small molecules background handout. Lecture Notes, Georgia Institute of Technology, Atlanta, USA, Jan 2000.
- [39] C.-K. Skylaris. Chem6085: Density functional theory, Lecture 8 Gaussian basis sets. Lecture Notes, University of Southampton, Southampton, UK, 2008.
- [40] J. C. Slater. Atomic shielding constants. *Phys. Rev.*, 36:57–64, Jul 1930.
- [41] S. F. Boys. Electronic Wave Functions. I. A General Method of Calculation for the Stationary States of Any Molecular System. *Proc. Royal Soc. Lond. A*, 200:542–554, Feb 1950.
- [42] D. Feller. The role of databases in support of computational chemistry calculations. *J. Comput. Chem.*, 17(13):1571–1586, 1996.
- [43] K. L. Schuchardt, B. T. Didier, T. Elsethagen, et al. Basis set exchange: A community database for computational sciences. *J. Chemical Inf. Model.*, 47(3):1045–1052, 2007.
- [44] F. Jensen. Atomic orbital basis sets. *Wiley Interdiscip. Rev. Comput. Mol. Sci.*, 3(3):273–295, 2013.
- [45] W. Kohn and L. J. Sham. Self-consistent equations including exchange and correlation effects. *Phys. Rev.*, 140:A1133–A1138, Nov 1965.
- [46] J.-L. Calais. Density-functional theory of atoms and molecules. *Int. J. Quant. Chem.*, 47(1):101–101, 1993.

- [47] J. Rychlewski. *Explicitly Correlated Wave Functions in Chemistry and Physics: Theory and Applications*. Kluwer Academic, Dordrecht, The Netherlands, 2003.
- [48] J. P. Perdew. Accurate density functional for the energy: Real-space cutoff of the gradient expansion for the exchange hole. *Phys. Rev. Lett.*, 55:1665–1668, Oct 1985.
- [49] J. Tao, J. P. Perdew, V. N. Staroverov, and G. E. Scuseria. Climbing the density functional ladder: Nonempirical meta-generalized gradient approximation designed for molecules and solids. *Phys. Rev. Lett.*, 91:146401, Sep 2003.
- [50] K. Burke. The ABC of DFT. Lecture Notes, Department of Chemistry, University of California, Irvine, USA, Apr 2007.
- [51] A. D. Becke. A new mixing of Hartree-Fock and local density-functional theories. *J. Chem. Phys.*, 98(2):1372–1377, 1993.
- [52] J. P. Perdew, M. Ernzerhof, and K. Burke. Rationale for mixing exact exchange with density functional approximations. *J. Chem. Phys.*, 105(22):9982–9985, 1996.
- [53] J. P. Perdew, K. Burke, and M. Ernzerhof. Generalized gradient approximation made simple. *Phys. Rev. Lett.*, 77:3865–3868, Oct 1996.
- [54] S. H. Vosko, L. Wilk, and M. Nusair. Accurate spin-dependent electron liquid correlation energies for local spin density calculations: a critical analysis. *Can. J. Phys.*, 58(8):1200–1211, 1980.
- [55] A. D. Becke. Density-functional exchange-energy approximation with correct asymptotic behavior. *Phys. Rev. A*, 38:3098–3100, Sep 1988.
- [56] C. Lee, W. Yang, and R. G. Parr. Development of the Colle-Salvetti correlation-energy formula into a functional of the electron density. *Phys. Rev. B*, 37:785–789, Jan 1988.
- [57] A. D. Becke. Density-functional thermochemistry. iii. the role of exact exchange. *J. Chem. Phys.*, 98(7):5648–5652, 1993.
- [58] R. Dovesi, R. Orlando, A. Erba, et al. CRYSTAL14: A program for the ab initio investigation of crystalline solids. *Int. J. Quant. Chem.*, 114(19):1287–1317, 2014.
- [59] J. Toulouse, R. Assaraf, and C. J. Umrigar. Introduction to the variational and diffusion Monte Carlo methods. *ArXiv e-prints*, Aug 2015.
- [60] M. D. Towler. The quantum Monte Carlo method. *Phys. Status Solidi (b)*, 243(11):2573–2598, 2006.
- [61] B. M. Austin, D. Yu. Zubarev, and W. A. Lester. Quantum Monte Carlo and related approaches. *Chem. Rev.*, 112(1):263–288, 2012.
- [62] W. M. C. Foulkes, L. Mitas, R. J. Needs, and G. Rajagopal. Quantum Monte Carlo simulations of solids. *Rev. Mod. Phys.*, 73:33–83, Jan 2001.
- [63] J. Kolorenč and L. Mitas. Applications of quantum Monte Carlo methods in condensed systems. *Rep. Prog. Phys.*, 74(2):026502, Feb 2011.

- [64] M. Hjorth-Jensen, M. P. Lombardo, and U. van Kolck, editors. *An Advanced Course in Computational Nuclear Physics: Bridging the Scales from Quarks to Neutron Stars*, volume 936 of *Lecture Notes in Physics*, chapter 9. Springer, Heidelberg, Germany, 2017.
- [65] A. Badinski. *Forces in Quantum Monte Carlo*. PhD thesis, University of Cambridge, Cambridge, UK, July 2008.
- [66] P. Kent. *Techniques and Applications of Quantum Monte Carlo*. PhD thesis, University of Cambridge, Cambridge, UK, Aug 1999.
- [67] W. L. McMillan. Ground state of liquid He^4 . *Phys. Rev.*, 138:A442–A451, Apr 1965.
- [68] D. M. Ceperley and B. J. Alder. Ground state of the electron gas by a stochastic method. *Phys. Rev. Lett.*, 45:566–569, Aug 1980.
- [69] N. Metropolis, A. W. Rosenbluth, M. N. Rosenbluth, A. H. Teller, and E. Teller. Equation of state calculations by fast computing machines. *J. Chem. Phys.*, 21(6):1087–1092, 1953.
- [70] W. K. Hastings. Monte Carlo sampling methods using Markov chains and their applications. *Biometrika*, 57(1):97–109, 1970.
- [71] R. Assaraf and M. Caffarel. Zero-variance principle for Monte Carlo algorithms. *Phys. Rev. Lett.*, 83:4682–4685, Dec 1999.
- [72] R. Assaraf, M. Caffarel, and A. Scemama. Improved Monte Carlo estimators for the one-body density. *Phys. Rev. E*, 75:035701, Mar 2007.
- [73] J. Toulouse, R. Assaraf, and C. J. Umrigar. Zero-variance zero-bias quantum Monte Carlo estimators of the spherically and system-averaged pair density. *J. Chem. Phys.*, 126(24):244112, 2007.
- [74] F. R. Petruzielo, J. Toulouse, and C. J. Umrigar. Approaching chemical accuracy with quantum Monte Carlo. *J. Chem. Phys.*, 136(12):124116, 2012.
- [75] S. M. Rothstein and J. Vrbik. A Green’s function used in diffusion Monte Carlo. *J. Chem. Phys.*, 87(3):1902–1903, 1987.
- [76] J. B. Anderson and D. R. Garmer. Validity of random walk methods in the limit of small time steps. *J. Chem. Phys.*, 87(3):1903–1904, 1987.
- [77] P. J. Reynolds, R. K. Owen, and W. A. Lester. Is there a zeroth order time-step error in diffusion quantum Monte Carlo? *J. Chem. Phys.*, 87(3):1905–1906, 1987.
- [78] M. Iazzi, A. A. Soluyanov, and M. Troyer. Topological origin of the fermion sign problem. *Phys. Rev. B*, 93:115102, Mar 2016.
- [79] J. B. Anderson. A random-walk simulation of the Schrödinger equation: H_3^+ . *J. Chem. Phys.*, 63(4):1499–1503, 1975.
- [80] J. B. Anderson. Quantum chemistry by random walk. $\text{H } ^2P$, $\text{H}_3^+ D_{3h} ^1A'_1$, $\text{H}_2 ^3\Sigma_u^+$, $\text{H}_4 ^1\Sigma_g^+$, $\text{Be } ^1S$. *J. Chem. Phys.*, 65(10):4121–4127, 1976.

- [81] D. J. Klein and H. M. Pickett. Nodal hypersurfaces and Anderson's random-walk simulation of the Schrödinger equation. *J. Chem. Phys.*, 64(11):4811–4812, 1976.
- [82] G. H. Booth, A. Grüneis, G. Kresse, and A. Alavi. Towards an exact description of electronic wavefunctions in real solids. *Nature*, 493:365, Dec 2012.
- [83] C. J. Umrigar, M. P. Nightingale, and K. J. Runge. A diffusion Monte Carlo algorithm with very small time-step errors. *J. Chem. Phys.*, 99(4):2865–2890, 1993.
- [84] M. Calandra Buonauro and S. Sorella. Numerical study of the two-dimensional Heisenberg model using a Green's function Monte Carlo technique with a fixed number of walkers. *Phys. Rev. B*, 57:11446–11456, May 1998.
- [85] R. Assaraf, M. Caffarel, and A. Khelif. Diffusion Monte Carlo with a fixed number of walkers. *Phys. Rev. E*, 61:4566–75, 05 2000.
- [86] M. P. Nightingale and H. W. J. Blöte. Gap of the linear spin-1 Heisenberg antiferromagnet: A Monte Carlo calculation. *Phys. Rev. B*, 33:659–661, Jan 1986.
- [87] D. M. Ceperley and M. H. Kalos. *Monte Carlo Methods in Statistical Physics*. Springer, Berlin, Germany, 1979.
- [88] M. P. Nightingale and C. J. Umrigar. *Monte Carlo Methods in Chemical Physics*, volume 105 of *Advances in Chemical Physics*, chapter 4. Wiley, University of Minnesota, Minnesota, USA, Nov 1998.
- [89] R. N. Barnett, P. J. Reynolds, and W. A. Lester. Monte Carlo algorithms for expectation values of coordinate operators. *J. Comput. Phys.*, 96(2):258 – 276, 1991.
- [90] R. Assaraf and M. Caffarel. Computing forces with quantum Monte Carlo. *J. Chem. Phys.*, 113:4028–4034, 09 2000.
- [91] S. Moroni, S. Sacconi, and C. Filippi. Practical schemes for accurate forces in quantum Monte Carlo. *J. Chem. Theory Comput.*, 10(11):4823–4829, 2014.
- [92] A. Badinski, P. D. Haynes, J. R. Trail, and R. J. Needs. Methods for calculating forces within quantum Monte Carlo simulations. *J. Phys.: Condens. Matter*, 22(7):074202, 2010.
- [93] D. M. Ceperley. Top ten list of reasons why quantum Monte Carlo is not used in chemistry. On-line Article. [Last accessed: 06/10/2018].
- [94] J. Vrbik and S. M. Rothstein. Infinitesimal differential diffusion quantum Monte Carlo study of diatomic vibrational frequencies. *J. Chem. Phys.*, 96(3):2071–2076, 1992.
- [95] P. Belohorec, S. M. Rothstein, and J. Vrbik. Infinitesimal differential diffusion quantum Monte Carlo study of CuH spectroscopic constants. *J. Chem. Phys.*, 98(8):6401–6405, 1993.
- [96] C. Filippi and C. J. Umrigar. Correlated sampling in quantum Monte Carlo: A route to forces. *Phys. Rev. B*, 61:R16291–R16294, Jun 2000.

- [97] P. Delplace, J. B. Marston, and A. Venaille. Topological origin of equatorial waves. *Science*, 358:1075–1077, Nov 2017.
- [98] E. H. Hall. On a new action of the magnet on electric currents. *Am. J. Math.*, 2(3):287–292, 1879.
- [99] K. v. Klitzing, G. Dorda, and M. Pepper. New method for high-accuracy determination of the fine-structure constant based on quantized Hall resistance. *Phys. Rev. Lett.*, 45:494–497, Aug 1980.
- [100] D. C. Tsui, H. L. Störmer, and A. C. Gossard. Two-dimensional magnetotransport in the extreme quantum limit. *Phys. Rev. Lett.*, 48:1559–1562, May 1982.
- [101] D. J. Thouless, M. Kohmoto, M. P. Nightingale, and M. den Nijs. Quantized Hall conductance in a two-dimensional periodic potential. *Phys. Rev. Lett.*, 49:405–408, Aug 1982.
- [102] S. Huber. Topological Quantum Numbers in Condensed Matter Systems. Lecture Notes, ITP, ETH, Zürich, Switzerland, 2016.
- [103] D. Tong. Quantum Hall Effect. Lecture Notes, DAMTP, University of Cambridge, Cambridge, UK, 2016.
- [104] M. O. Goerbig. Quantum Hall effects. *ArXiv e-prints*, Sep 2009.
- [105] J. K. Jain. *Composite Fermions*. Cambridge University Press, Cambridge, UK, 2007.
- [106] M. Janßen, O. Viehweger, U. Fastenrath, and J. Hajdu. *Introduction to the Theory of the Integer Quantum Hall Effect*. VCH, Weinheim, Germany, 1994.
- [107] X.-G. Wen. *Quantum Field Theory of Many-Body Systems*. Oxford University Press, Oxford, UK, 2004.
- [108] P. Phillips. *Advanced Solid State Physics*. Cambridge University Press, Cambridge, UK, 2nd edition, 2012.
- [109] L. D. Landau and D. M. Lifschitz. *Quantum Mechanics: Non-relativistic Theory. Course of Theoretical Physics*. Pergamon Press, London, UK, 3rd edition, 1977.
- [110] E. Witten. Three lectures on topological phases of matter. *ArXiv e-prints*, Oct 2015.
- [111] B. A. Bernevig and T. L. Hughes. *Topological Insulators and Topological Superconductors*. Princeton University Press, Princeton, USA, 2013.
- [112] M. V. Berry. Quantal phase factors accompanying adiabatic changes. *Proc. R. Soc. A*, 392(1802):45–57, 1984.
- [113] M. Born and V. Fock. Beweis des Adiabatenatzes. *Z. Phys.*, 51:165–180, Mar 1928.
- [114] P. A. M. Dirac. Quantised singularities in the electromagnetic field. *Proc. Royal Soc. Lond. A*, 133(821):60–72, 1931.

- [115] C. Nayak. Quantum Condensed Matter Physics. Lecture Notes, Hard Condensed Matter, UCLA, Los Angeles, USA, 2004.
- [116] S. M. Girvin. Course 2: The quantum Hall effect: Novel excitations and broken symmetries. In A. Comtet, T. Jolicoeur, S. Ouvry, and F. David, editors, *Topological Aspects of Low Dimensional Systems*, page 53, 1999.
- [117] R. B. Laughlin. Quantized Hall conductivity in two dimensions. *Phys. Rev. B*, 23:5632–5633, May 1981.
- [118] B. I. Halperin. Quantized Hall conductance, current-carrying edge states, and the existence of extended states in a two-dimensional disordered potential. *Phys. Rev. B*, 25:2185–2190, Feb 1982.
- [119] E. Fradkin. *Field Theories of Condensed Matter Physics*. Cambridge University Press, Cambridge, UK, 2013.
- [120] J. Zak. Magnetic translation group. *Phys. Rev.*, 134:A1602–A1606, Jun 1964.
- [121] P. Streda. Theory of quantized Hall conductivity in two dimensions. *J. Phys. C*, 15(22):L717, 1982.
- [122] P. G. Harper. The general motion of conduction electrons in a uniform magnetic field, with application to the diamagnetism of metals. *Proc. R. Soc. A*, 68(10):879, 1955.
- [123] D. R. Hofstadter. Energy levels and wave functions of bloch electrons in rational and irrational magnetic fields. *Phys. Rev. B*, 14:2239–2249, Sep 1976.
- [124] R. B. Laughlin. Anomalous quantum Hall effect: An incompressible quantum fluid with fractionally charged excitations. *Phys. Rev. Lett.*, 50:1395–1398, May 1983.
- [125] G. D. Mahan. *Many-Particle Physics*. Kluwer Academic, New York, USA, 3rd edition, 2000.
- [126] R. de Picciotto, M. Reznikov, M. Heiblum, et al. Direct observation of a fractional charge. *Physica B Condens. Matter*, 249:395–400, Jun 1998.
- [127] F. D. M. Haldane. Fractional quantization of the Hall effect: A hierarchy of incompressible quantum fluid states. *Phys. Rev. Lett.*, 51:605–608, Aug 1983.
- [128] G. Möller and N. R. Cooper. Composite fermion theory for bosonic quantum Hall states on lattices. *Phys. Rev. Lett.*, 103:105303, Sep 2009.
- [129] J. K. Jain. The composite fermion: A quantum particle and its quantum fluids. *Physics Today*, 53(4):39–45, 2000.
- [130] J. K. Jain. Composite-fermion approach for the fractional quantum Hall effect. *Phys. Rev. Lett.*, 63:199–202, Jul 1989.
- [131] B. I. Halperin, P. A. Lee, and N. Read. Theory of the half-filled Landau level. *Phys. Rev. B*, 47:7312–7343, Mar 1993.

- [132] S. A. Parameswaran, R. Roy, and S. L. Sondhi. Fractional quantum Hall physics in topological flat bands. *C. R. Phys.*, 14(9):816–839, 2013.
- [133] T. Neupert, C. Chamon, T. Iadecola, L. H. Santos, and C. Mudry. Fractional (Chern and topological) insulators. *Phys. Scr. T*, 164(1):014005, Dec 2015.
- [134] E. J. Bergholtz and Z. Liu. Topological flat band models and fractional Chern insulators. *Int. J. Mod. Phys. B*, 27:1330017, Sep 2013.
- [135] T. Neupert. Fractional Chern Insulators. On-line Lecture, Perimeter Institute, Waterloo, Canada, 2012. [Last accessed: 03/06/16].
- [136] N. Regnault and B. A. Bernevig. Fractional Chern insulator. *Phys. Rev. X*, 1(2):021014, Oct 2011.
- [137] F. D. M. Haldane. Model for a quantum Hall effect without Landau levels: Condensed-matter realization of the "parity anomaly". *Phys. Rev. Lett.*, 61:2015–2018, Oct 1988.
- [138] G. Möller and N. R. Cooper. Fractional Chern insulators in Harper-Hofstadter bands with higher Chern number. *Phys. Rev. Lett.*, 115:126401, Sep 2015.
- [139] C. Nayak, S. H. Simon, A. Stern, M. Freedman, and S. Das Sarma. Non-Abelian anyons and topological quantum computation. *Rev. Mod. Phys.*, 80:1083–1159, Jul 2008.
- [140] G. Möller. Lectures on Numerical Methods. Lecture Notes, TCM, University of Cambridge, Cambridge, UK, 2014.
- [141] E. Koch. The Lanczos Method. Lecture Notes, Computational Materials Science, German School for Simulation Sciences, Jülich, Germany, 2011.
- [142] D. Poilblanc. Introduction to Numerical Techniques for Correlated Models. Lecture Notes, Laboratory of Theoretical Physics, CNRS & University of Toulouse, Toulouse, France, 2011.
- [143] T. Neupert, L. Santos, C. Chamon, and C. Mudry. Fractional quantum Hall states at zero magnetic field. *Phys. Rev. Lett.*, 106(23):236804, Jun 2011.
- [144] S. Kourtis, T. Neupert, C. Chamon, and C. Mudry. Fractional Chern insulators with strong interactions that far exceed band gaps. *Phys. Rev. Lett.*, 112:126806, Mar 2014.
- [145] A. G. Grushin, J. Motruk, M. P. Zaletel, and F. Pollmann. Characterization and stability of a fermionic $\nu = 1/3$ fractional Chern insulator. *Phys. Rev. B*, 91:035136, Jan 2015.
- [146] Y. J. Lin, R. L. Compton, K. Jimenez-Garcia, J. V. Porto, and I. B. Spielman. Synthetic magnetic fields for ultracold neutral atoms. *Nature*, 462(7273):628–632, 2009.
- [147] M. Aidelsburger, M. Atala, M. Lohse, et al. Realization of the Hofstadter Hamiltonian with ultracold atoms in optical lattices. *Phys. Rev. Lett.*, 111(18):185301, 2013.

- [148] H. Miyake, G. A. Siviloglou, C. J. Kennedy, W. C. Burton, and W. Ketterle. Realizing the Harper Hamiltonian with laser-assisted tunneling in optical lattices. *Phys. Rev. Lett.*, 111(1):185302, 2013.
- [149] G. Jotzu, M. Messer, R. Desbuquois, et al. Experimental realization of the topological Haldane model with ultracold fermions. *Nature*, 515(7526):237–240, 2014.
- [150] M. E. Tai, A. Lukin, M. Rispoli, et al. Microscopy of the interacting Harper–Hofstadter model in the two-body limit. *Nature*, 546(7659):519–523, 2017.
- [151] J. Dalibard, F. Gerbier, G. Juzeliūnas, and P. Öhberg. Colloquium: Artificial gauge potentials for neutral atoms. *Rev. Mod. Phys.*, 83(4):1523–1543, 2011.
- [152] N. Goldman, G. Juzeliūnas, P. Öhberg, and I. B. Spielman. Light-induced gauge fields for ultracold atoms. *Rep. Prog. Phys.*, 77(12):126401, 2014.
- [153] N. Goldman, J. C. Budich, and P. Zoller. Topological quantum matter with ultracold gases in optical lattices. *Nat. Phys.*, 12(7):639–645, 2016.
- [154] T. Oka and H. Aoki. Photovoltaic Hall effect in graphene. *Phys. Rev. B*, 79(8):081406, 2009.
- [155] N. Goldman and J. Dalibard. Periodically driven quantum systems: Effective Hamiltonians and engineered gauge fields. *Phys. Rev. X*, 4(3):031027, 2014.
- [156] N. Goldman, N. Cooper, and J. Dalibard. Preparing and probing Chern bands with cold atoms. In N. Proukakis, D. Snoke, and P. Littlewood, editors, *Universal Themes of Bose-Einstein Condensation*, pages 274–298. Cambridge University Press, Cambridge, UK, 2017.
- [157] C. L. Kane and E. J. Mele. Quantum spin Hall effect in graphene. *Phys. Rev. Lett.*, 95(22):226801, 2005.
- [158] E. Tang, J.-W. Mei, and X.-G. Wen. High-temperature fractional quantum Hall states. *Phys. Rev. Lett.*, 106(2):236802, 2011.
- [159] A. Kol and N. Read. Fractional quantum Hall effect in a periodic potential. *Phys. Rev. B*, 48(1):8890–8898, 1993.
- [160] R. N. Palmer and D. Jaksch. High-field fractional quantum Hall effect in optical lattices. *Phys. Rev. Lett.*, 96(18):180407, 2006.
- [161] G. Möller and N. R. Cooper. Composite fermion theory for bosonic quantum Hall states on lattices. *Phys. Rev. Lett.*, 103(1):105303, 2009.
- [162] A. Sterdyniak, C. Repellin, B. A. Bernevig, and N. Regnault. Series of Abelian and non-Abelian states in $C > 1$ fractional Chern insulators. *Phys. Rev. B*, 87(20):205137, 2013.
- [163] G. Möller and N. R. Cooper. Fractional Chern insulators in Harper-Hofstadter bands with higher Chern number. *Phys. Rev. Lett.*, 115(12):126401, 2015.

- [164] E. M. Spanton, A. A. Zibrov, H. Zhou, et al. Observation of fractional Chern insulators in a van der Waals heterostructure. *Science*, 360(6384):62–66, 2018.
- [165] N. Regnault and B. A. Bernevig. Fractional Chern insulator. *Phys. Rev. X*, 1(2):021014, 2011.
- [166] F. D. M. Haldane. Model for a quantum Hall effect without Landau levels: Condensed-matter realization of the "parity anomaly". *Phys. Rev. Lett.*, 61(18):2015–2018, 1988.
- [167] N. R. Cooper. Rapidly rotating atomic gases. *Adv. Phys.*, 57(6):539–616, 2008.
- [168] T. Neupert, L. Santos, C. Chamon, and C. Mudry. Fractional quantum Hall states at zero magnetic field. *Phys. Rev. Lett.*, 106(2):236804, 2011.
- [169] K. Sun, Z.-C. Gu, H. Katsura, and S. Das Sarma. Nearly flatbands with nontrivial topology. *Phys. Rev. Lett.*, 106(23):236803, 2011.
- [170] D. N. Sheng, Z.-C. Gu, K. Sun, and L. Sheng. Fractional quantum Hall effect in the absence of Landau levels. *Nat. Commun.*, 2:389, 2011.
- [171] E. J. Bergholtz and Z. Liu. Topological flat band models and fractional Chern insulators. *Int. J. Mod. Phys. B*, 27(24):1330017, 2013.
- [172] S. A. Parameswaran, R. Roy, and S. L. Sondhi. Fractional quantum Hall physics in topological flat bands. *Comptes Rendus Phys.*, 14(9):816–839, 2013.
- [173] T. Scaffidi and G. Möller. Adiabatic continuation of fractional Chern insulators to fractional quantum Hall states. *Phys. Rev. Lett.*, 109(24):246805, 2012.
- [174] Y.-H. Wu, J. K. Jain, and K. Sun. Adiabatic continuity between Hofstadter and Chern insulator states. *Phys. Rev. B*, 86(16):165129, 2012.
- [175] Y.-L. Wu, N. Regnault, and B. A. Bernevig. Bloch model wave functions and pseudopotentials for all fractional Chern insulators. *Phys. Rev. Lett.*, 110(10):106802, 2013.
- [176] M. Barkeshli and X.-L. Qi. Topological nematic states and non-Abelian lattice dislocations. *Phys. Rev. X*, 2(3):031013, 2012.
- [177] M. Barkeshli, C.-M. Jian, and X.-L. Qi. Twist defects and projective non-Abelian braiding statistics. *Phys. Rev. B*, 87(4):045130, 2013.
- [178] Z. Liu, G. Möller, and E. J. Bergholtz. Exotic non-Abelian topological defects in lattice fractional quantum Hall states. *Phys. Rev. Lett.*, 119(10):106801, 2017.
- [179] P. G. Harper. Single band motion of conduction electrons in a uniform magnetic field. *Proc. Phys. Soc. A*, 68(10):874–878, 1955.
- [180] M. Y. Azbel. Energy spectrum of a conduction electron in a magnetic field. *J. Exp. Theor. Phys.*, 19:634, 1964.
- [181] D. R. Hofstadter. Energy levels and wave functions of Bloch electrons in rational and irrational magnetic fields. *Phys. Rev. B*, 14(6):2239–2249, 1976.

- [182] D. J. Thouless, M. Kohmoto, M. P. Nightingale, and M. den Nijs. Quantized Hall conductance in a two-dimensional periodic potential. *Phys. Rev. Lett.*, 49(6):405–408, 1982.
- [183] V. Kalmeyer and R. B. Laughlin. Equivalence of the resonating-valence-bond and fractional quantum Hall states. *Phys. Rev. Lett.*, 59(18):2095–2098, 1987.
- [184] E. Fradkin. Jordan-Wigner transformation for quantum-spin systems in two dimensions and fractional statistics. *Phys. Rev. Lett.*, 63(3):322–325, 1989.
- [185] E. Fradkin. Superfluidity of the lattice anyon gas and topological invariance. *Phys. Rev. B*, 42(1):570–586, 1990.
- [186] J. K. Jain. Composite-fermion approach for the fractional quantum Hall effect. *Phys. Rev. Lett.*, 63(2):199–202, 1989.
- [187] A. S. Sørensen, E. Demler, and M. D. Lukin. Fractional quantum Hall states of atoms in optical lattices. *Phys. Rev. Lett.*, 94(8):086803, 2005.
- [188] M. Hafezi, A. S. Sørensen, M. D. Lukin, and E. Demler. Characterization of topological states on a lattice with Chern number. *EPL*, 81(1):10005, 2008.
- [189] M. Aidelsburger, M. Lohse, C. Schweizer, et al. Measuring the Chern number of Hofstadter bands with ultracold bosonic atoms. *Nat. Phys.*, 11(2):162–166, 2015.
- [190] M. Barkeshli, N. Y. Yao, and C. R. Laumann. Continuous preparation of a fractional Chern insulator. *Phys. Rev. Lett.*, 115(2):026802, 2015.
- [191] Y.-C. He, F. Grusdt, A. Kaufman, M. Greiner, and A. Vishwanath. Realizing and adiabatically preparing bosonic integer and fractional quantum Hall states in optical lattices. *Phys. Rev. B*, 96(20):201103, 2017.
- [192] J. Motruk and F. Pollmann. Phase transitions and adiabatic preparation of a fractional Chern insulator in a boson cold-atom model. *Phys. Rev. B*, 96(16):165107, 2017.
- [193] T. Scaffidi and S. H. Simon. Exact solutions of fractional Chern insulators: Interacting particles in the Hofstadter model at finite size. *Phys. Rev. B*, 90(11):115132, 2014.
- [194] D. Bauer, T. S. Jackson, and R. Roy. Quantum geometry and stability of the fractional quantum Hall effect in the Hofstadter model. *Phys. Rev. B*, 93(23):235133, 2016.
- [195] S. A. Parameswaran, R. Roy, and S. L. Sondhi. Fractional Chern insulators and the w_∞ algebra. *Phys. Rev. B*, 85(24):241308, 2012.
- [196] M. O. Goerbig. From fractional Chern insulators to a fractional quantum spin Hall effect. *Eur. Phys. J. B*, 85:15, 2012.
- [197] R. Roy. Band geometry of fractional topological insulators. *Phys. Rev. B*, 90(1):165139, 2014.
- [198] T. S. Jackson, G. Möller, and R. Roy. Geometric stability of topological lattice phases. *Nat. Commun.*, 6:8629, 2015.

- [199] M. Claassen, C. H. Lee, R. Thomale, X.-L. Qi, and T. P. Devereaux. Position-momentum duality and fractional quantum Hall effect in Chern insulators. *Phys. Rev. Lett.*, 114(23):236802, 2015.
- [200] C. H. Lee, M. Claassen, and R. Thomale. Band structure engineering of ideal fractional Chern insulators. *Phys. Rev. B*, 96(16):165150, 2017.
- [201] Y. Hasegawa and M. Kohmoto. Periodic Landau gauge and quantum Hall effect in twisted bilayer graphene. *Phys. Rev. B*, 88(1):125426, 2013.
- [202] A. Eckardt. Colloquium: Atomic quantum gases in periodically driven optical lattices. *Rev. Mod. Phys.*, 89(1):311, 2017.
- [203] L. Hormozi, G. Möller, and S. H. Simon. Fractional quantum Hall effect of lattice bosons near commensurate flux. *Phys. Rev. Lett.*, 108(2):256809, 2012.
- [204] Y.-F. Wang, H. Yao, Z.-C. Gu, C.-D. Gong, and D. N. Sheng. Non-Abelian quantum Hall effect in topological flat bands. *Phys. Rev. Lett.*, 108(12):126805, 2012.
- [205] Z. Liu, E. J. Bergholtz, H. Fan, and A. M. Läuchli. Fractional Chern insulators in topological flat bands with higher Chern number. *Phys. Rev. Lett.*, 109(18):186805, 2012.
- [206] N. Read and E. H. Rezayi. Beyond paired quantum Hall states: Parafermions and incompressible states in the first excited Landau level. *Phys. Rev. B*, 59(12):8084–8092, 1999.
- [207] G. Möller and N. R. Cooper. Condensed ground states of frustrated Bose-Hubbard models. *Phys. Rev. A*, 82(6):063625, 2010.
- [208] S. S. Natu, E. J. Mueller, and S. Das Sarma. Competing ground states of strongly correlated bosons in the Harper-Hofstadter-Mott model. *Phys. Rev. A*, 93(6):063610, 2016.
- [209] D. Hügél, H. U. R. Strand, P. Werner, and L. Pollet. Anisotropic Harper-Hofstadter-Mott model: Competition between condensation and magnetic fields. *Phys. Rev. B*, 96(5):054431, 2017.
- [210] F. Kozarski, D. Hügél, and L. Pollet. Quasi-one-dimensional Hall physics in the Harper-Hofstadter-Mott model. *New J. Phys.*, 20(4):043001, Apr 2018.
- [211] G. Möller and N. R. Cooper. Correlated phases of bosons in the flat lowest band of the dice lattice. *Phys. Rev. Lett.*, 108(4):045306, 2012.
- [212] N. R. Cooper, N. K. Wilkin, and J. M. F. Gunn. Quantum phases of vortices in rotating Bose-Einstein condensates. *Phys. Rev. Lett.*, 87(12):120405, 2001.
- [213] N. Regnault and T. Jolicoeur. Quantum Hall fractions in rotating Bose-Einstein condensates. *Phys. Rev. Lett.*, 91(3):030402, 2003.
- [214] G. Möller and S. H. Simon. Composite fermions in a negative effective magnetic field: A Monte Carlo study. *Phys. Rev. B*, 72(4):045344, 2005.

- [215] S. C. Davenport and S. H. Simon. Spinful composite fermions in a negative effective field. *Phys. Rev. B*, 85(24):245303, 2012.
- [216] N. R. Cooper and E. H. Rezayi. Competing compressible and incompressible phases in rotating atomic Bose gases at filling factor $\nu=2$. *Phys. Rev. A*, 75(1):013627, 2007.
- [217] T. Senthil and M. Levin. Integer quantum Hall effect for bosons. *Phys. Rev. Lett.*, 110(4):046801, 2013.
- [218] N. Regnault and T. Senthil. Microscopic model for the boson integer quantum Hall effect. *Phys. Rev. B*, 88(16):161106, 2013.
- [219] Y.-C. He, S. Bhattacharjee, R. Moessner, and F. Pollmann. Bosonic integer quantum Hall effect in an interacting lattice model. *Phys. Rev. Lett.*, 115(11):116803, 2015.
- [220] E. H. Rezayi, N. Read, and N. R. Cooper. Incompressible liquid state of rapidly rotating bosons at filling factor $3/2$. *Phys. Rev. Lett.*, 95(16):160404, 2005.
- [221] Y.-L. Wu, B. A. Bernevig, and N. Regnault. Zoology of fractional Chern insulators. *Phys. Rev. B*, 85:075116, 2012.
- [222] A. Sterdyniak, N. R. Cooper, and N. Regnault. Bosonic integer quantum Hall effect in optical flux lattices. *Phys. Rev. Lett.*, 115(11):116802, 2015.
- [223] R. N. Palmer, A. Klein, and D. Jaksch. Optical lattice quantum Hall effect. *Phys. Rev. A*, 78(1):013609, 2008.
- [224] G. Möller, L. Hormozi, J. Slingerland, and S. H. Simon. Josephson-coupled Moore-Read states. *Phys. Rev. B*, 90(23):235101, 2014.
- [225] F. Harper, S. H. Simon, and R. Roy. Perturbative approach to flat Chern bands in the Hofstadter model. *Phys. Rev. B*, 90(7):075104, 2014.
- [226] B. A. Bernevig and N. Regnault. Emergent many-body translational symmetries of Abelian and non-Abelian fractionally filled topological insulators. *Phys. Rev. B*, 85(7):075128, 2012.
- [227] T. S. Cubitt, D. Perez-Garcia, and M. M. Wolf. Undecidability of the spectral gap. *Nature*, 528(7581):207–211, 2015.
- [228] R. J. Wheatley, A. S. Tulegenov, and E. Bichoutskaia. Intermolecular potentials from supermolecule and monomer calculations. *Int. Rev. Phys. Chem.*, 23(1):151–185, 2004.
- [229] R. J. Wheatley and T. C. Lillestolen. Calculating intermolecular potentials with SIMPER: the water–nitrogen and water–oxygen interactions, dispersion energy coefficients, and preliminary results for larger molecules. *Int. Rev. Phys. Chem.*, 26(3):449–485, 2007.
- [230] J. Kolorenč and L. Mitás. Applications of quantum Monte Carlo methods in condensed systems. *Rep. Prog. Phys.*, 74(2):026502, 2011.

- [231] M. W. Lee, S. V. Levchenko, and A. M. Rappe. Force calculation of polyatomic molecules in quantum Monte Carlo using Pulay's corrections. *Mol. Phys.*, 105(19-22):2493–2497, 2007.
- [232] C. Filippi and C. J. Umrigar. Interatomic forces and correlated sampling in quantum Monte Carlo. In W. A. Lester, S. M. Rothstein, and S. Tanaka, editors, *Recent Advances in Quantum Monte Carlo Methods*, volume II, pages 12–29. World Scientific, Singapore, 2002.
- [233] R. Assaraf and M. Caffarel. Computing forces with quantum Monte Carlo. *J. Chem. Phys.*, 113(10):4028–4034, 2000.
- [234] C. Attaccalite and S. Sorella. Stable liquid hydrogen at high pressure by a novel ab initio molecular-dynamics calculation. *Phys. Rev. Lett.*, 100:114501, Mar 2008.
- [235] C. Filippi, R. Assaraf, and S. Moroni. Simple formalism for efficient derivatives and multi-determinant expansions in quantum Monte Carlo. *J. Chem. Phys.*, 144(19):194105, 2016.
- [236] D. R. Hartree. The wave mechanics of an atom with a non-Coulomb central field. part ii. some results and discussion. *Math. Proc. Camb. Philos. Soc.*, 24(1):111–132, 1928.
- [237] J. C. Slater. The self consistent field and the structure of atoms. *Phys. Rev.*, 32:339–348, Sep 1928.
- [238] V. Fock. Näherungsmethode zur Lösung des quantenmechanischen Mehrkörperproblems. *Z. Phys.*, 61(1):126–148, Jan 1930.
- [239] P. Hohenberg and W. Kohn. Inhomogeneous electron gas. *Phys. Rev.*, 136:B864–B871, Nov 1964.
- [240] N. D. Drummond, J. R. Trail, and R. J. Needs. Trail-Needs pseudopotentials in quantum Monte Carlo calculations with plane-wave/blip basis sets. *Phys. Rev. B*, 94:165170, Oct 2016.
- [241] A. D Becke. Density-functional thermochemistry. iii. the role of exact exchange. *J. Chem. Phys.*, 98(7):5648–5652, 1993.
- [242] P. J. Stephens, F. J. Devlin, C. F. N. Chabalowski, and M. J. Frisch. Ab initio calculation of vibrational absorption and circular dichroism spectra using density functional force fields. *J. Phys. Chem.*, 98(45):11623–11627, 1994.
- [243] S. H. Vosko, L. Wilk, and M. Nusair. Accurate spin-dependent electron liquid correlation energies for local spin density calculations: a critical analysis. *Can. J. Phys.*, 58(8):1200–1211, 1980.
- [244] F. Weigend and R. Ahlrichs. Balanced basis sets of split valence, triple zeta valence and quadruple zeta valence quality for H to Rn: Design and assessment of accuracy. *Phys. Chem. Chem. Phys.*, 7(18):3297–3305, 2005.
- [245] M. Ernzerhof and G. E. Scuseria. Assessment of the Perdew–Burke–Ernzerhof exchange-correlation functional. *J. Chem. Phys.*, 110(11):5029–5036, 1999.

- [246] N. Mardirossian and M. Head-Gordon. Thirty years of density functional theory in computational chemistry: an overview and extensive assessment of 200 density functionals. *Mol. Phys.*, 115(19):2315–2372, 2017.
- [247] J. Paier, M. Marsman, and G. Kresse. Why does the B3LYP hybrid functional fail for metals? *J. Chem. Phys.*, 127(2):024103, 2007.
- [248] N. D. Drummond and R. J. Needs. Variance-minimization scheme for optimizing Jastrow factors. *Phys. Rev. B*, 72:085124, Aug 2005.
- [249] C. J. Umrigar, K. G. Wilson, and J. W. Wilkins. Optimized trial wave functions for quantum Monte Carlo calculations. *Phys. Rev. Lett.*, 60:1719–1722, Apr 1988.
- [250] C. J. Umrigar, J. Toulouse, C. Filippi, S. Sorella, and R. G. Hennig. Alleviation of the fermion-sign problem by optimization of many-body wave functions. *Phys. Rev. Lett.*, 98:110201, Mar 2007.
- [251] M. D. Brown, J. R. Trail, P. López Ríos, and R. J. Needs. Energies of the first row atoms from quantum Monte Carlo. *J. Chem. Phys.*, 126(22):224110, 2007.
- [252] R. M. Lee, G. J. Conduit, N. Nemec, P. López Ríos, and N. D. Drummond. Strategies for improving the efficiency of quantum Monte Carlo calculations. *Phys. Rev. E*, 83:066706, Jun 2011.
- [253] D. M. Ceperley and M. H. Kalos. Monte Carlo methods in Statistical Physics. In K. Binder, editor, *Topics in Current Physics*, volume 7. Springer, Berlin, Germany, 1979.
- [254] M. Casalegno, M. Mella, and A. M. Rappe. Computing accurate forces in quantum Monte Carlo using Pulay’s corrections and energy minimization. *J. Chem. Phys.*, 118(16):7193–7201, 2003.
- [255] M. W. Lee, S. V. Levchenko, and A. M. Rappe. Force calculation of polyatomic molecules in quantum Monte Carlo using Pulay’s corrections. *Mol. Phys.*, 105(19-22):2493–2497, 2007.
- [256] Á. Ruiz-Serrano, N. D. M. Hine, and C.-K. Skylaris. Pulay forces from localized orbitals optimized in situ using a psinc basis set. *J. Chem. Phys.*, 136(23):234101, 2012.
- [257] R. Assaraf and M. Caffarel. Zero-variance zero-bias principle for observables in quantum Monte Carlo: Application to forces. *J. Chem. Phys.*, 119(20):10536–10552, 2003.
- [258] J. R. Trail. Heavy-tailed random error in quantum Monte Carlo. *Phys. Rev. E*, 77:016703, Jan 2008.
- [259] L. K. Wagner and J. C. Grossman. Quantum Monte Carlo calculations for minimum energy structures. *Phys. Rev. Lett.*, 104:210201, May 2010.
- [260] R. J. Needs, M. D. Towler, N. D. Drummond, and P. López Ríos. Continuum variational and diffusion quantum Monte Carlo calculations. *J. Phys. Condens. Matter*, 22(2):023201, 2009.

- [261] W. A. Al-Saidi. Variational and diffusion Monte Carlo study of post-d group 13–17 elements. *J. Chem. Phys.*, 129(6):064316, 2008.
- [262] R. N. Barnett and K. B. Whaley. Variational and diffusion Monte Carlo techniques for quantum clusters. *Phys. Rev. A*, 47(5):4082, 1993.
- [263] N. D. Drummond, P. López Ríos, A. Ma, et al. Quantum Monte Carlo study of the Ne atom and the Ne⁺ ion. *J. Chem. Phys.*, 124(22):224104, 2006.
- [264] L. E. Sutton, editor. *Tables of Interatomic Distances and Configuration in Molecules & Ions*. Special Publication No.18, The Chemical Society, London, UK, 1965. Supplement 1956-1959.
- [265] G. D. Dickenson, M. L. Niu, E. J. Salumbides, et al. Fundamental vibration of molecular hydrogen. *Phys. Rev. Lett.*, 110:193601, May 2013.
- [266] K. P. Huber and G. Herzberg. *Molecular Spectra and Molecular Structure*, volume IV. Constants of Diatomic Molecules. Van Nostrand Reinhold, New York, USA, 1979.
- [267] T. Shimanouchi. *Tables of Molecular Vibrational Frequencies*, volume I. National Bureau of Standards, Gaithersburg, USA, 1972.
- [268] R. Peverati and D. G. Truhlar. Communication: A global hybrid generalized gradient approximation to the exchange-correlation functional that satisfies the second-order density-gradient constraint and has broad applicability in chemistry. *J. Chem. Phys.*, 135(19):191102, 2011.
- [269] C. W. McCluskey and D. S. Stoker. Raman observations of quantum interference in the $\nu_1/2\nu_2$ Fermi dyad region of carbon dioxide. *ArXiv e-prints*, Jan 2006.
- [270] M. Born. On the stability of crystal lattices. i. *Math. Proc. Cam. Philos. Soc.*, 36(2):160–172, 1940.
- [271] J. L. Ericksen. On the Cauchy-Born rule. *Math. Mech. Solids*, 13(3-4):199–220, 2008.
- [272] G. Grimvall, B. Magyari-Köpe, V. Ozoliņš, and K. A. Persson. Lattice instabilities in metallic elements. *Rev. Mod. Phys.*, 84:945–986, Jun 2012.
- [273] D. Brown. *The Chemical Bond in Inorganic Chemistry*. Oxford University Press, Oxford, UK, 2002.
- [274] M. Born and J. E. Mayer. Zur Gittertheorie der Ionenkristalle. *Z. Phys.*, 75(1):1–18, Jan 1932.
- [275] A. F. Kapustinskii. Lattice energy of ionic crystals. *Q. Rev. Chem. Soc.*, 10:283–294, 1956.
- [276] K. P. Driver, R. E. Cohen, Z. Wu, et al. Quantum Monte Carlo computations of phase stability, equations of state, and elasticity of high-pressure silica. *Proc. Natl. Acad. Sci. U.S.A.*, 107(21):9519–9524, 2010.
- [277] J. Ahn, I. Hong, Y. Kwon, et al. Phase stability and interlayer interaction of blue phosphorene. *Phys. Rev. B*, 98:085429, Aug 2018.

- [278] J. P. Hansen. Statistical mechanics of dense ionized matter. i. equilibrium properties of the classical one-component plasma. *Phys. Rev. A*, 8:3096–3109, Dec 1973.
- [279] J. H. Chu and I. Lin. Direct observation of Coulomb crystals and liquids in strongly coupled rf dusty plasmas. *Phys. Rev. Lett.*, 72:4009–4012, Jun 1994.
- [280] M. Bonitz, P. Ludwig, H. Baumgartner, et al. Classical and quantum Coulomb crystals. *Phys. Plasmas*, 15(5):055704, 2008.
- [281] E. Madelung. Das elektrische Feld in systemen von regelmäßig angeordneten Punktladungen. *Phys. Z.*, 19:524–532, 1918.
- [282] E. Wigner. On the interaction of electrons in metals. *Phys. Rev.*, 46:1002–1011, Dec 1934.
- [283] E. Wigner. Effects of the electron interaction on the energy levels of electrons in metals. *Trans. Faraday Soc.*, 34:678–685, 1938.
- [284] J. R. Trail, M. D. Towler, and R. J. Needs. Unrestricted Hartree-Fock theory of Wigner crystals. *Phys. Rev. B*, 68:045107, Jul 2003.
- [285] J. Solanpaa, P. J. J. Luukko, and E. Räsänen. Many-particle dynamics and intershell effects in Wigner molecules. *J. Phys. Condens. Matter*, 23(39), Oct 2011.
- [286] L. Bonsall and A. A. Maradudin. Some static and dynamical properties of a two-dimensional Wigner crystal. *Phys. Rev. B*, 15:1959–1973, Feb 1977.
- [287] P. G. Silvestrov and P. Recher. Wigner crystal phases in bilayer graphene. *Phys. Rev. B*, 95:075438, Feb 2017.
- [288] M. Hinarejos, A. Pérez, and M. C. Bañuls. Wigner function for a particle in an infinite lattice. *New J. Phys.*, 14(10):103009, 2012.
- [289] R. A. Coldwell-Horsfall and A. A. Maradudin. Zero-point energy of an electron lattice. *J. Math. Phys.*, 1(5):395–404, 1960.
- [290] W. J. Carr. Energy, specific heat, and magnetic properties of the low-density electron gas. *Phys. Rev.*, 122:1437–1446, Jun 1961.
- [291] G. Goldoni and F. M. Peeters. Stability, dynamical properties, and melting of a classical bilayer Wigner crystal. *Phys. Rev. B*, 53:4591–4603, Feb 1996.
- [292] G. Goldoni, V. Schweigert, and F. M. Peeters. Stability and dynamical properties of a double-layer Wigner crystal in two dimensions. *Surf. Sci.*, 361-362:163 – 166, 1996.
- [293] R. R. Palanichamy and K. Iyakutti. Structural stability analysis of Wigner crystal with Gaussian and Yukawa-type positive background. *Int. J. Quantum Chem.*, 86(5):478–486, 2001.
- [294] I. J. Zucker. Stability of the Wigner electron crystal on the perovskite lattice. *J. Phys. Condens. Matter*, 3(15):2595, 1991.

- [295] N. D. Drummond, Z. Radnai, J. R. Trail, M. D. Towler, and R. J. Needs. Diffusion quantum Monte Carlo study of three-dimensional Wigner crystals. *Phys. Rev. B*, 69:085116, Feb 2004.
- [296] X. Zhu and S. G. Louie. Variational quantum Monte Carlo study of two-dimensional Wigner crystals: Exchange, correlation, and magnetic-field effects. *Phys. Rev. B*, 52:5863–5884, Aug 1995.
- [297] D. Ceperley. Ground state of the fermion one-component plasma: A Monte Carlo study in two and three dimensions. *Phys. Rev. B*, 18:3126–3138, Oct 1978.
- [298] L. Cândido, B. Bernu, and D. M. Ceperley. Magnetic ordering of the three-dimensional Wigner crystal. *Phys. Rev. B*, 70:094413, Sep 2004.
- [299] G. Ortiz, M. Harris, and P. Ballone. Zero temperature phases of the electron gas. *Phys. Rev. Lett.*, 82:5317–5320, Jun 1999.
- [300] S. Ciccariello. On the crystalline states of the dilute jellium model. *Annal. Phys.*, 18(2-3):157–173, 2009.
- [301] S. Ichimaru. Strongly coupled plasmas: high-density classical plasmas and degenerate electron liquids. *Rev. Mod. Phys.*, 54:1017–1059, Oct 1982.
- [302] D. H. E. Dubin and T. M. O’Neil. Trapped nonneutral plasmas, liquids, and crystals (the thermal equilibrium states). *Rev. Mod. Phys.*, 71:87–172, Jan 1999.
- [303] R. W. Hasse and V. V. Avilov. Structure and Madelung energy of spherical Coulomb crystals. *Phys. Rev. A*, 44:4506–4515, Oct 1991.
- [304] J. P. Schiffer. Melting of crystalline confined plasmas. *Phys. Rev. Lett.*, 88:205003, May 2002.
- [305] S. Mavadia, J. Goodwin, G. Stutter, et al. Control of the conformations of ion Coulomb crystals in a Penning trap. *Nat. Commun.*, 4:2571, 10 2013.
- [306] L. Hornekær, N. Kjærgaard, A. M. Thommesen, and M. Drewsen. Structural properties of two-component Coulomb crystals in linear Paul traps. *Phys. Rev. Lett.*, 86:1994–1997, Mar 2001.
- [307] R. C. Ashoori. Electrons in artificial atoms. *Nature*, 379:413–419, Feb 1996.
- [308] S. Hamaguchi, R. T. Farouki, and D. H. E. Dubin. Triple point of Yukawa systems. *Phys. Rev. E*, 56:4671–4682, Oct 1997.
- [309] P. M. Whelan and M. J. Hodgson. *Essential Principles of Physics*. Arrowsmith, Bristol, UK, 1978.
- [310] J. M. Leinaas and J. Myrheim. On the theory of identical particles. *Il Nuovo Cimento B (1971-1996)*, 37(1):1–23, 1977.
- [311] F. Wilczek. Quantum mechanics of fractional-spin particles. *Phys. Rev. Lett.*, 49:957–959, Oct 1982.

- [312] D. Yoshioka, B. I. Halperin, and P. A. Lee. The ground state of the 2D electrons in a strong magnetic field and the anomalous quantized Hall effect. *Surf. Sci.*, 142(1-3):155–162, 1984.
- [313] P. M. Morse. Diatomic molecules according to the wave mechanics. ii. vibrational levels. *Phys. Rev.*, 34:57–64, Jul 1929.
- [314] E. F. de Lima and J. E. M. Hornos. Matrix elements for the Morse potential under an external field. *J. Phys. B*, 38(7):815, 2005.
- [315] H. Flyvbjerg and H. G. Petersen. Error estimates on averages of correlated data. *J. Chem. Phys.*, 91(1):461–466, 1989.
- [316] G. Alefeld and H. Spreuer. Iterative improvement of componentwise errorbounds for invariant subspaces belonging to a double or nearly double eigenvalue. *Computing*, 36(4):321–334, Dec 1986.
- [317] H. Behnke. Inclusion of eigenvalues of general eigenvalue problems for matrices. In U. Kulisch and H. J. Stetter, editors, *Scientific Computation with Automatic Result Verification*, pages 69–78, Springer, Vienna, Austria, 1988.
- [318] J. J. Dongarra, C. B. Moler, and J. H. Wilkinson. Improving the accuracy of computed eigenvalues and eigenvectors. *SIAM J. Numer. Anal.*, 20(1):23–45, 1983.
- [319] S. M. Rump. Guaranteed inclusions for the complex generalized eigenproblem. *Computing*, 42(2):225–238, Jun 1989.
- [320] T. Yamamoto. Error bounds for computed eigenvalues and eigenvectors. *Numer. Math.*, 34(2):189–199, Jun 1980.
- [321] T. Yamamoto. Error bounds for computed eigenvalues and eigenvectors. ii. *Numer. Math.*, 40(2):201–206, Jun 1982.
- [322] E. Gkioulekas. Generalized local test for local extrema in single-variable functions. *Int. J. Sci. Math. Educ.*, 45(1):118–131, 2014.
- [323] M. A. H. Nerenberg. The second derivative test for constrained extremum problems. *Int. J. Sci. Math. Educ.*, 22(2):303–308, 1991.
- [324] Wolfram Research Inc. Mathematica, Version 11.3, Champaign, IL, USA, 2018.